JAERI-M
8661

ANNUAL REPORT OF THE FUSION RESEARCH AND DEVELOPMENT CENTER FOR THE PERIOD OF APRIL 1, 1978 TO MARCH 31, 1979

March 1980

Fusion Research and Development Center

日本原子力研究所
Japan Atomic Energy Research Institute

この報告書は，日本原子力研究所がJAERI-Mレポートとして，不定期に刊行している研究報告書です．入手，複製などのお問合わせは，日本原子力研究所技術情報部（茨城県那珂郡東海村）あて，お申しこしください．

JAERI-M reports, issued irregularly, describe the results of research works carried out in JAERI. Inquiries about the availability of reports and their reproduction should be addressed to Division of Technical Information, Japan Atomic Energy Research Institute, Tokai-mura, Naka-gun, Ibaraki-ken, Japan.

JAERI-M 8661

Annual Report of the Fusion Research and Development Center for the period of April 1, 1978 to March 31, 1979

Fusion Research and Development Center
Tokai Research Establishment, JAERI

(Received December 25, 1979)

Research and development activities of the Fusion Research and Development Center (Division of Thermonuclear Fusion Research and Division of Large Tokamak Development) from April 1978 to March 1979 are described.

(1) Theoretical studies continued on tokamak confinement with more emphasis on computations. A fluid model numerical code system for tokamak equilibrium, stability and transport progressed as planned.

(2) In JFT-2, efforts were concentrated on the study of LH heating physics. Installation of remodeled JFT-2 was started in December 1978. In JFT-2a/DIVA, very low q discharge ($q_a \gtrsim 1.3$), confinement scaling, ICRF heating were studied after reducing the impurity content with poloidal divertor or titanium coated surface. Diagnostic researches in JFT-2 and DIVA are as follows: evaluation of pseudo-continuum radiation from gold impurity, effect of oxygen ion sputtering on metal impurity release, and determination of ion temperature during RF heating.
A medium-size tokamak of JFT-2M is under design, aiming at a high β plasma with D shaped cross section.

(3) JFT-2, JFT-2a/DIVA and motor-generator operated as planned. Improvements were made on Taylor type discharge cleaning and preionization.

(4) In the development of a neutral beam system, hydrogen beam of 70 keV, 5.5 A, 0.1 sec duration was extracted from a two-stage ion source of diameter 10 cm. Final design of the prototype JT-60 NBI unit was started for completion in summer of 1979. In JFT-2 LH heating, the transmitted RF power density was raised up to 1.2 kw/cm^2 by means of a new waveguide coupler of stainless steel whose inner surface was plated with copper and gettered with titanium. Power of the JFT-2 LH heating system was increased to 300 kw at 750 MHz in March 1979. A conceptual design of the LH heating system for JT-60 was made.

(5) In particle-surface interaction research, a special scanning electron microscope was developed to observe sample surfaces under ion bombardment, and a conceptual design of an ion source for refractory elements was made.

(6) In superconducting magnets development, the following were done: construction of a conductor testing facility and of a cluster testing facility including helium liquefier/refrigerator, detailed design of Japanese coil for Large Coil Task, and winding test of Japanese LCT conductor.

(7) In the process technology of fuel recirculation and tritium production, thermal diffusion experiment using H_2-He system and permeation test of H_2 and D_2 gas with Pd-Ag alloy membrane were made, and preliminary conceptual design of a tritium handling facility of 10^4 Ci level was made.

(8) A second preliminary design of the experimental tokamak fusion reactor was started in April 1977, and finished in March 1979, with emphasis on realistic and credible solutions of the design problems.

(9) On JT-60 construction of the tokamak machine was started in April 1978. The poloidal field power supply was also ordered in early 1979. Design study of the diagnostic equipment continued. Design of experimental and control buildings was completed, and design of the power supply building continued.

(10) The research program of JAERI's noncircular cross sectioned tokamak was revised in a Fusion Council meeting in 1978. In place of JT-4, a possibility was pursued to conduct the experimental studies of Doublet III of General Atomic, and the preliminary design study of JFT-2M.

(11) Design study of the PETF (Plasma Engineering Test Facility) was started in April 1978, first with its physical aspect to look into the possibility of self-ignition. Along with this, conceptual design study of the hardware was also made under contracts of three industrial firms.

(12) IAEA organized an International Workshop of INTOR (International Tokamak Reactor) by IFRC's recommendation. Delegates to the workshop are from four tokamak advanced countries; Japan, U.S.A., U.S.S.R., and E.C. Its first session was held in February 1979.

Keywords: Annual Report, Plasma Confinement, Plasma Physics, JFT-2 tokamak, JFT-2a(DIVA) tokamak, Diagnostics, Neutral Beam Injector, RF Heating, Surface Study, Superconducting Magnet, Reactor Design, JT-60 Tokamak, JT-4 Tokamak, Impurity Emission, Tritium Production.

核融合研究開発推進センター年報
（昭和53年度）

日本原子力研究所　東海研究所
核融合研究開発推進センター

（1979年12月25日受理）

核融合研究開発推進センター（核融合研究部および大型トカマク開発部）における研究開発の現況とその成果をとりまとめた*。概要は次のとおり。

1）トカマク閉じ込めの解析を，計算に力点をおいて進めている。トカマクの平衡，安定性，輸送に関する磁気流体的ふるまいを扱う計算機コードシステムが進歩した。

2）JFT－2では，低域ハイブリッド加熱の物理を追求した。改造後の据付が1978年12月から開始された。JFT－2a（DIVA）では，ポロイダルダイバータまたはチタン蒸着第1壁により不純物を低減して，極低安定係数（$q_a \gtrsim 1.3$），閉じ込め比例則，ICRF加熱の研究を行った。JFT－2，2aに関連した計測では，金不純物線の擬似連続光，RF加熱時のイオン温度の測定等の研究を行った。

JFT－2Mの設計が進行した。非円形度1.7のD型高ベータプラズマを，ハイブリッド電流制御方式により得ることを目的としている。そのために，プラズマ容積3 m^3に対し，4 MWのNBIと1～2MWのRF加熱，およびポロイダル磁気リミタを採用する。

3）JFT－2，JFT－2a，およびその共用電源は，大きな故障もなく，計画通り運転された。また，低電流放電洗浄，予備電離等の技術改良を行った。

4）直径10 cmの2段加速イオン源により，70 keV，55 A，0.1秒の水素イオンビームを得た。JT－60用NBIの最終設計が始められた。1979年夏までに完了する予定である。

JFT－2用低域ハイブリッド（LH）加熱実験では，ランチャーとしてSUS 304を母材とし，内面に銅メッキおよびチタン蒸着をしたものを使用し，電力密度1.2 kW/cm^2までの実験が可能となった。LH加熱装置の300 kW増力工事に着手し，54年3月に完了した。JT－60用LH加熱装置の概念設計を行った。

5）プラズマと真空壁との相互作用に関連して，スパッタ表面同時観察装置の設置と，セルフ・スパッタリングを研究するためのイオン源についての調査と概念設計を行った。

6）超電導磁石の開発研究は，導体試験装置およびヘリウム液化・冷凍機の製作を含むクラス

---

*）既刊されている年報は，昭和54年度以降，それぞれJAERI－M 4654，5029，5564，5888，6359，6926，7479および8059である。

ター・テスト装置の製作と，日本のLCTコイルの詳細設計と巻線予備試験，ならびに，導体開発およびその試験等が行われた。

7）トリチウム・プロセス技術の開発においては，主として水素を用いたコールド実験を行っており，H_2－He系の分離特性を研究している。また，10^4Ciレベルのトリチウム施設の概念設計を行った。

8）1977年4月より開始したトカマク型核融合実験炉第2次予備設計は，1979年3月に完了した。より現実的な炉を目指した設計を行った。

9）JT－60の建設は，1978年4月にトカマク装置の本体を発注することによって途についた。ポロイダルコイル電源についても，1979年の初期に契約が成立した。計測系に関する設計検討が進められた。実験棟および制御棟の設計が完了し，引き続き電源棟の設計が行われている。

10）原研における非円形断面トカマクの研究計画は，1978年の核融合会議において変更された。JT－4の代わりにGAでのダブレットⅢの実験に参加し，また原研ではJFT－2Mの予備設計検討を進めることとなった。

11）1978年4月，炉心工学試験装置の設計検討が物理的側面から始められた。平行して，本体装置の概念検討も産業界3社と契約して行われた。

12）IAEAは，IFRCの勧告によってINTORに関する国際作業部会を創立した。作業部会の委員は，トカマク先進国である日本，米，ソ連，ヨーロッパから派遣され1978年2月に第1回作業部会が開かれた。

PREFACE

A brief summary of activities in the Fusion Research and Development Center during the fiscal year 1978 is as follows.*

JT-60: In April 1978 construction of JT-60 was started. The JT-60 program was formally initiated in 1973 succeeding the scoping studies made since 1970. The program went through the conceptual design (1973), preliminary design (1974～5), engineering development (1975-7), and preconstruction design (1976).

The Tokamak machine is being constructed starting from the toroidal field coils. Order was also placed for the poloidal field power supply.

JT-4: In the past years JT-4 program went through stages of designs and engineering development. Those activities were summarized and evaluated to complete the specification of JT-4 device. In parallel, a possibility was pursued to conduct experimental studies of dee=shaped plasmas in Doublet III now in operation in USA.

JFT-2: Lower hybrid resonance heating experiments were successfully continued. A phase-controlled 4-wave guides launcher worked well yielding a good coupling efficiency about 90% up to the maximum power of 200 kW. The ion temperature increase was proportional to the RF power, the heating efficiency being 0.6-1.4 eV/kW. Remodelling of the device was initiated from the end of 1978.

JFT-2a: The most remarkable experiment in 1978 was the realization of very low q stable discharges by reducing the impurity content in the plasma. Plasma parameters in a q = 1.7 discharge were; the toroidal field 12.5 kG, plasma current of 64 kA, electron temperature of 190 eV, mean density $1.1 \times 10^{14}/cm^3$, beta of 0.8%, and energy confinement time of 5.7 ms. It was indicated also that disruptive instabilities were completely eliminated in the discharge with q less than 2.

Another major achievement was concerned on the origin of metal impurities in the plasma. Careful experiment showed convincingly that metal impurity release in the quiet discharges was dominantly due to the ion sputtering.

---

* The preceding annual reports are JAERI-M 4654 (FY 1970), 5029, 5564, 5888, 6359, 6926, 7479 and 8059.

Theory and Computation: The TRITON system, a fluid model code system for tokamak confinement, advanced well.

Plasma Heating Technology: Works aiming at NBI and RF heating systems for JT-60 were continued. Hydrogen beams of 70 keV, 5.5A and of 0.1 sec duration were extracted from a two-stage ion source of 10 cm in diameter. Full-sized models of the JT-60 ion source, duopigatron and bucket sources, were successfully tested. In lower hybrid heating experiments on JFT-2 a new launcher of stainless steel plated with copper, and gettered with titanium on its inner surface worked well, the transmitted RF power density being increased up to 1.2 kW/cm^2.

Surface Science and Vacuum Technology: Two accelerators (0.1 - 6 keV and 50 - 400 keV) are actively operated to study the particle-surface interactions. In-situ and continuous observation of the surface during ion bombardment was done using a scanning electron microscope. Precise measurements of the sputtering yield, and angular distribution of molybdenum were done.

Superconducting Magnet: Developmental works aiming at the superconducting toroidal coil system for a device after JT-60 were started from 1976. In 1978 superconductor test facility was installed, and actively used in the high field, large current tests of several NbTi and Nb_3Sn conductor samples. The design of the cluster test facility and its helium refrigerator was completed.

JAERI signed on IEA-Implementing Agreement for a Program of Research and Development on Superconducting Magnet for Fusion in April 1978. A design work of the LCT coil was started.

Reactor System Design: The second preliminary design of JXFR (JAERI Experimental Fusion Reactor) was completed with emphasis on the realistic solutions to the design problems revealed in the first preliminary design (1975 - 1976). The design covered plasma characteristics, reactor structure, blanket neutronics and shielding, magnets, NBI systems, power supplies, fuel circulating and tritium recovery systems, and maintenance scheme.

(Sigeru MORI)

CONTENTS

目　　次

I. PLASMA THEORY AND COMPUTATION

1. Introduction

Theoretical studies have been continued on tokamak confinement with increasing emphasis on computation.

The TRITON system, a fluid model numerical code system for the tokamak equilibrium, stability, and transport, advanced well. Several versions of the constituent codes were completed.

Toroidal effects on the collisionless drift-mode were examined in detail. The mode-mode coupling leads the mode ballooning and reduced shear damping. Resistive instabilities in a low q tokamak discharge were studied numerically in collaboration of the Institute of Plasma Physics.

A new algorithm to solve the Poisson equation in toroidal geometry was devised. The maximum entropy method was applied successfully to the spectrum analysis appearing in particle model simulations.

2. Stability and transport

2.1 Toroidal effects on the shear stabilization of drift waves[1)]

The drift motion of ions due to the magnetic curvature causes a mode-mode coupling, i.e., mode of poloidal mode number m with m±1. The influence of this mode coupling on the Pearlstein-Berk solution is examined in the weak coupling approximation. It is found that the mode coupling causes real frequency shift and mode ballooning, and also reduces the shear damping.

2.2 Anomalous ion loss by low frequency instabilities[2)]

The ambipolarity formula of the cross-field flux of the nonuniform plasma in the presence of the low frequency ($\omega \ll$ ion gyrofrequency) electromagnetic fluctuations is studied. It is shown that owing to the ion polarization drift the ions are pulled out by the diffusing electrons.

2.3 Computer simulation of resistive MHD instabilities in a low-q tokamak discharge[3)]

Resistive MHD instabilities in a low-q tokamak discharge are studied by using a three-dimensional one fluid MHD model. The basic

equations of the model are:

$$\frac{\partial \rho}{\partial t} + \mathrm{div}(\rho \vec{v}) = 0 \ ,$$

$$(\frac{\partial}{\partial t} + \vec{v}\cdot\nabla)\vec{v} = \frac{1}{\rho}(-\nabla P + \vec{j} \times \vec{B}) \ ,$$

$$(\frac{\partial}{\partial t} + v\cdot\nabla)P = -(\gamma-1)P \ \mathrm{div}\ \vec{v} + (\gamma-1)\eta j^2 - P/\tau \ ,$$

$$\frac{\partial \vec{B}}{\partial t} = \mathrm{rot}(-\eta\vec{j} + \vec{v} \times \vec{B}) \ ,$$

$$\mathrm{rot}\ \vec{B} = \mu_o \vec{j} \ ,$$

where η is the resistivity which has the classical temperature dependence, that is, $\eta=\bar{\eta}\ T^{-3/2}$, P/τ represents the energy loss with $\tau=\tau(r)$, $r^2=x^2+y^2$, and $\gamma=5/3$. The above equations are solved numerically by the two step Lax-Wendroff method in the cartesian coordinates ($-a\leq x\leq a$, $-a\leq y\leq a$). Fixed boundary conditions are imposed on the plasma. That is,

$\vec{B}(t) = \vec{B}(t=0)$ at the boundary,

$\vec{v} = 0$ at the boundary.

In the z-direction, the periodic boundary condition with periodicity $2\pi R$ is assumed.

Figures I.2-1∿3 show the vector plots of (v_x, v_y) and the magnetic flux at typical times of the run. Time is normalized by a/v_A, where v_A is the Alfven velocity. The parameters are: $q_o=0.7$, $q_a=1.7$, $\bar{\eta}=10^{-4}$, and mesh size 26×26×12. The sawtooth oscillation by m/n=1 resistive instability are developing. Figure I.2-1 shows the growth of the magnetic island. Figure I.2-2 corresponds to the saturation of the instability and Fig. I.2-3 to the decay of the mode (cf. Fig. I.2-4). Figure I.2-4 shows the time development of the fundamental and higher harmonics of the m/n=1 mode. As the fundamental mode grows, higher harmonics are excited, and as the fundamental mode is stabilized, all harmonics are stabilized. Other mode $m/n\neq 1$ are not at all excited. If $q_a<2$, the sawtooth oscillation appears but the coupling among different m/n modes which may be regarded as a mechanism of the disruption does not occur.

2.4 Anomalous plasma transport due to electron temperature gradient instability[4)]

The collisionless drift wave instability driven by an electron temperature inhomogeneity (electron temperature gradient instability) and the enhanced transport processes associated with it are studied using a two-and-a-half dimensional particle simulation code.

The simulation shows that the quasilinear diffusion in phase space is an important mechanism for the saturation of the electron temperature gradient instability. Also, the instability yields particle fluxes toward the hot plasma regions. The heat conductivity for the electron temperature perpendicular to the magnetic field, $T_{e\perp}$, is not reduced by magnetic shear but remains high, whereas the heat conductivity for the parallel temperature, $T_{e//}$, is effectively reduced, and the instability stabilized.

2.5 Orbit loss of 3.5 MeV alpha particles[5)]

Alpha particles generated by D-T reactions are expected to heat a plasma in fusion reactors. However, the displacement of their orbits from the magnetic surface is so large even in a large tokamak device such as INTOR that alpha particles generated near the plasma surface are lost directly from the plasma. Numerical evaluation is made on the orbit loss of 3.5 MeV alpha particles in a tokamak with elliptical cross-section.

The equations of the guiding center motion is solved in the cylindrical cooldinates system (R, ψ, z). We assume the magnetic axis at $(R_0, \psi, 0)$, and nested elliptical magnetic surfaces described by

$$\frac{b}{a}(R-R_0)^2 + \frac{a}{b} z^2 = ab\rho^2 \ , \quad 0 \leq \rho \leq 1$$

where a, b are semi-axes of the plasma surface. The magnetic field is given by

$$B_R = -\frac{a}{b}\frac{z}{\sqrt{ab}}\frac{R_0}{R}\tilde{B}(\rho) \ , \ B_\psi = \frac{B_0}{R} B_0 \ , \ B_z = \frac{b}{a}\frac{R-R_0}{\sqrt{ab}}\frac{R_0}{R}\tilde{B}(\rho) \ ,$$

where

$$\tilde{B}(\rho) = \frac{\mu_0 I_p}{2\pi r_{eff}}\frac{1+\gamma}{1+\gamma\rho^m} \ , \ r_{eff} \simeq \frac{a^2+b^2}{2\sqrt{ab}} \ , \ m = \left(\frac{b}{a}+\frac{a}{b}\right)\frac{1+\gamma}{\gamma} \ ,$$

and the coefficient γ is related to the safety factor $q(\rho)$ as $1+\gamma=q(1)/q(0)$.

In Fig. I.2-5(a) the fraction of the confined alpha particles is shown as a function of ρ for various plasma current I_p, where a/R_0=0.24, b/a=1.5 and γ=0.6. The same is shown in Fig. I.2-5(b) for various a/R_0, where I_p=4.7 MA, b/a=1.5, and γ=0.6.

We summarize the results: (1) The orbit loss is determined mainly by I_p and a/R_0. (2) Peaked current profile yields good confinement, but the gain is insignificant. (3) The elliptic tokamak is good for alpha confinement compared with the circular tokamak with the same volume.

References

1) K. Ito*, T. Tuda, and S. Inoue*, submitted for publication in Nuclear Fusion
2) S. Inoue*, T. Tange*, K. Ito*, and T. Tuda, IPPJ-334 (1979)
3) S. Tokuda, T. Kamimura*, and Sanuki*, in preparation
4) S. Tokuda, T. Kamimura*, and H. Ito, IPPJ-369 (1979)
5) T. Takizuka, in preparation

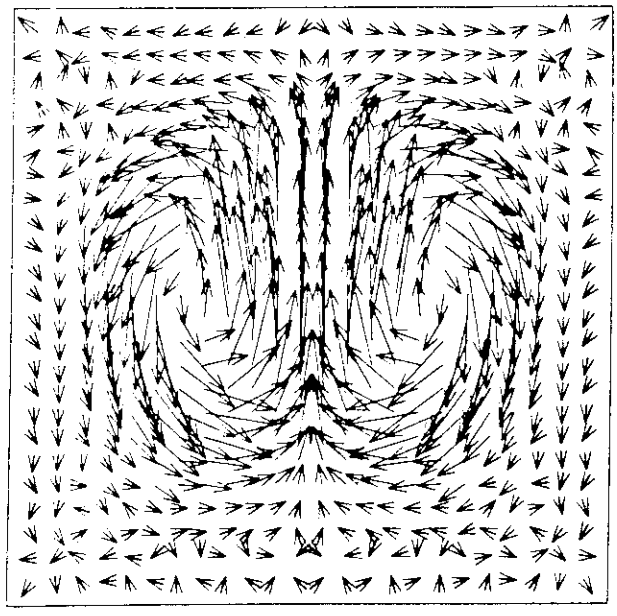

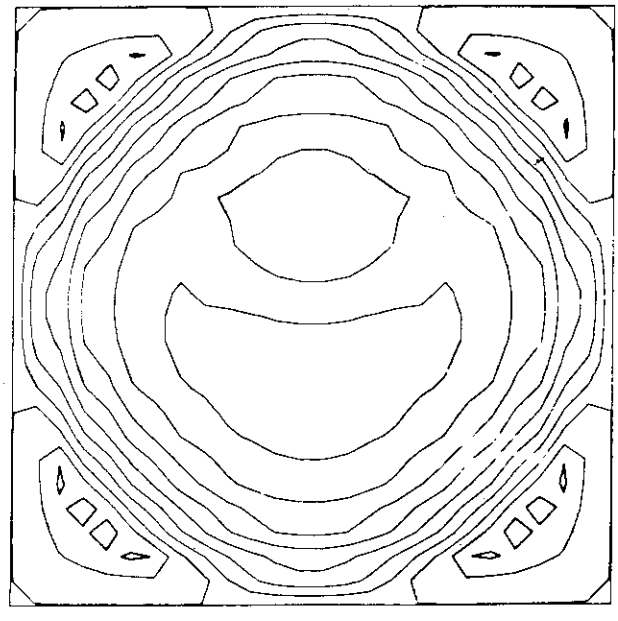

Fig. I.2-1 Vector plot of (V_x, V_y) and magnetic flux at time=170

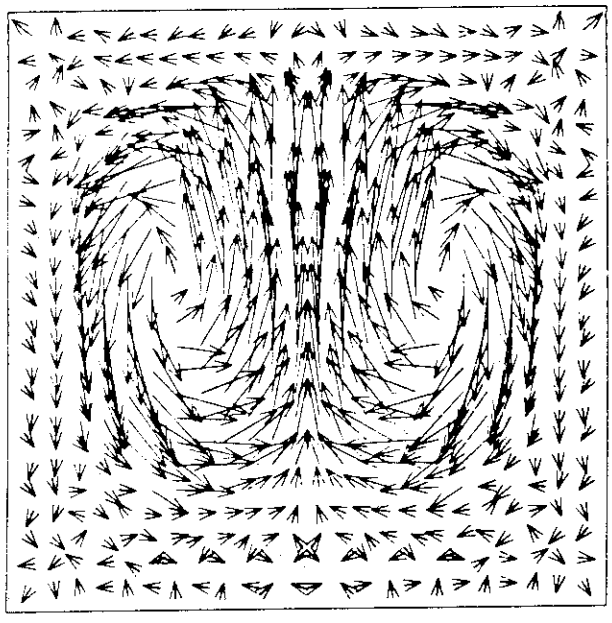

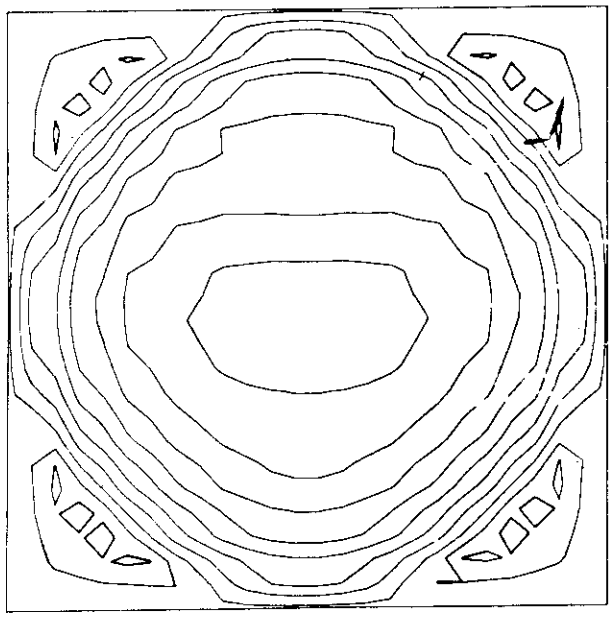

Fig. I.2-2 Vector plot of (V_x, V_y) and magnetic flux at time=210

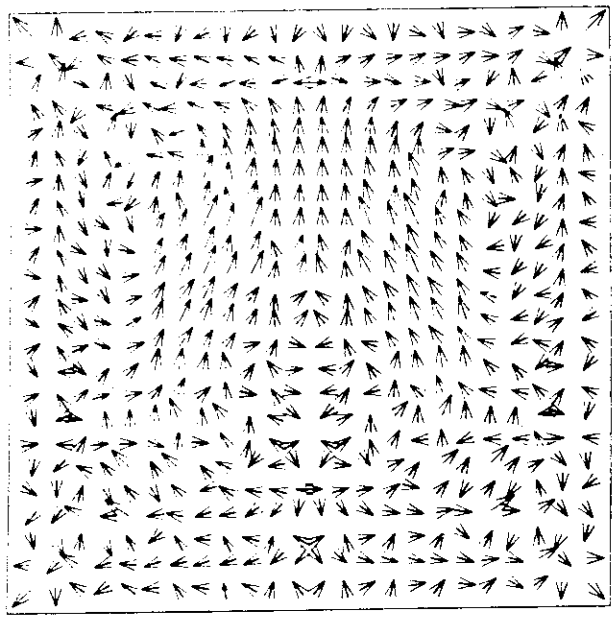

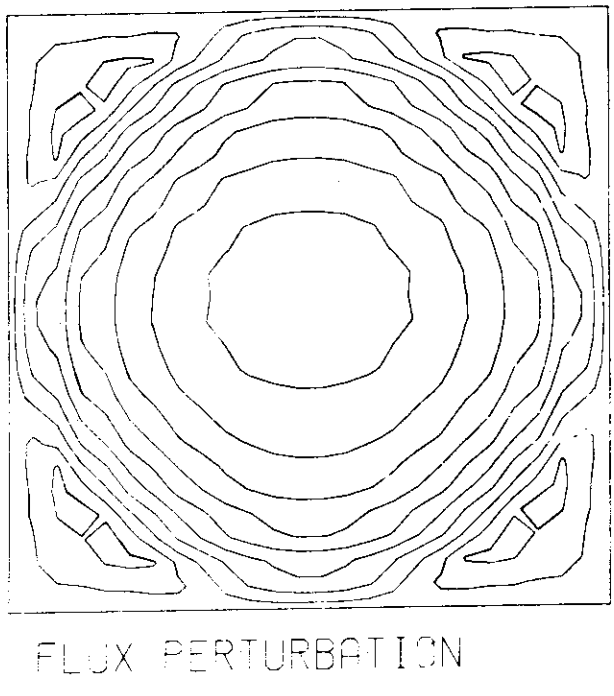

Fig. I.2-3 Vector plot of (V_x, V_y) and magnetic flux at time=280

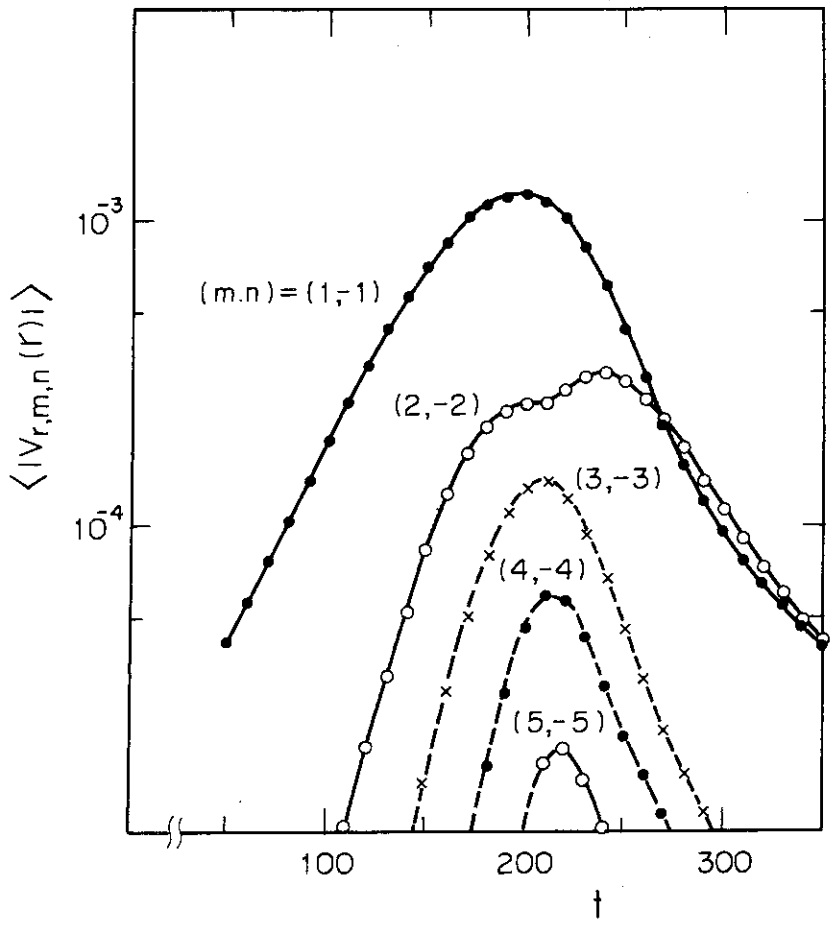

Fig. I.2-4 Time development of the fundamental and higher harmonics of the m/n=1 mode

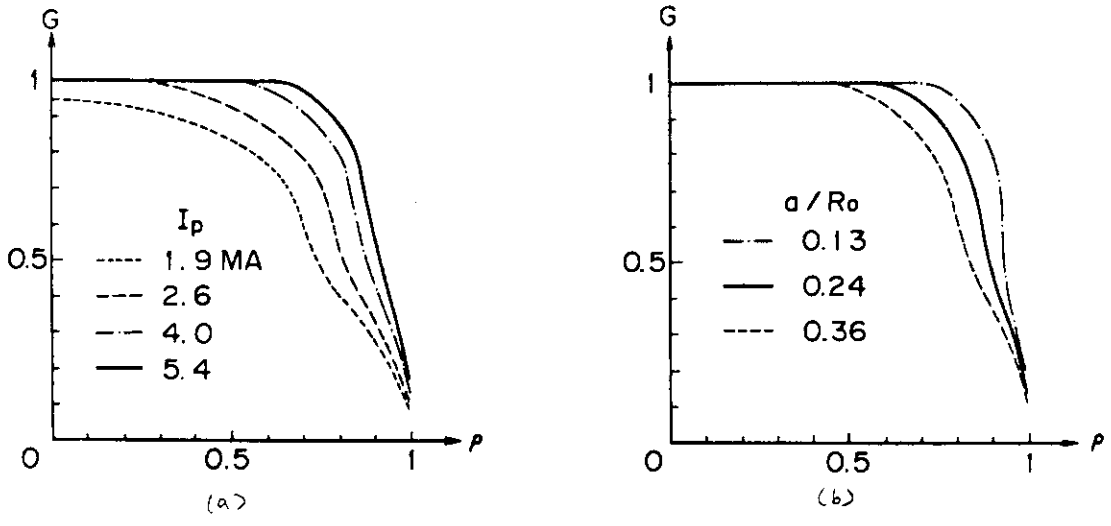

Fig. I.2-5 Orbit Losses of 3.5 MeV Alpha particles

3. Computing

3.1 3D potential calculation in the axisymmetric toroidal boundary[1)]

We devise a new numerical method to solve Poisson's equation in the cylindrical coordinates

$$\frac{1}{r}\frac{\partial}{\partial r} r \frac{\partial \phi}{\partial r} + \frac{1}{r^2}\frac{\partial^2 \phi}{\partial \theta^2} + \frac{\partial^2 \phi}{\partial z^2} = -\rho$$

with an axisymmetric toroidal boundary condition, $\phi=0$ on S (see Fig. I.3-1). This problem frequently appears in the numerical simulation of a plasma in tokamaks. The above equation is approximated by the "seven-point" difference equations, and Fourier-expanded in the θ direction. Introducing the potential $\tilde{\phi}$ which vanishes on the surface, $r=r_1$, r_2 and $z=z_1$, z_2, we also apply Fourier-sine-expansion to the difference equations in the z direction. Then we obtain a set of equations of the form.

$$A(r)\tilde{\phi}_{mn}(r+\Delta_r) - B_{mn}(r)\tilde{\phi}_{mn}(r) + C(r)\tilde{\phi}_{mn}(r-\Delta_r) = D_{mn}(r)$$

with the boundary condition $\tilde{\phi}_{mn}(r_1)=\tilde{\phi}_{mn}(r_2)=0$, where $\tilde{\phi}_{mn}$ denotes the Fourier coefficient (suffix m for the θ direction and n for z), $A=1+\Delta_r/2r$, $B_{mn}=2+(\alpha_m/r^2+\beta_n)/\Delta_r^2$, $C=1-\Delta_r/2r$, $D_{mn}=-\rho_{mn}\Delta_r^2$, $\alpha_m=2\{1-\cos(2\pi m/M)\}$, $\beta_n=2\{1-\cos(\pi n/N)\}$. Note that $\tilde{\phi}$ does not vanish on S. Next we assign a source ρ^*_m along the curve s of the cross-section of S, and make $\tilde{\phi}^*_m$ to be equal to $-\tilde{\phi}_m$. Then the potential ϕ due to the source $\rho+\rho^*$ satisfies the boundary condition, $\phi=0$ on S. The fictitious source ρ^*_m can be calculated as follows. The curve s is approximated by a series of K grid points. It is not necessary to use in the series all grid points near s, because Poisson's equation with Dirichlet's boundary condition is stable with respect to small fluctuations of the boundary values. The potential $\tilde{\phi}^{*kj}_m$ on a grid point j, which is due to the source ρ^{*k}_m on a grid point k, can be written as $\tilde{\phi}^{*kj}_m=\Phi^{kj}_m\ \rho^{*k}_m$, where Φ^{kj}_m depends only on positions (r_k, z_k) and (r_j, z_j). Since $\tilde{\phi}^{*j}_m=\sum_{k=1}^{K}\Phi^{kj}_m\ \rho^{k}_m$ and $\tilde{\phi}^{*j}_m=-\tilde{\phi}^{j}_m$, the value of ρ^{*k}_m is given by

$$\rho^{*k}_m = -\sum_{j=1}^{K}(\Phi^{kj}_m)^{-1}\ \tilde{\phi}^{j}_m$$

where Φ^{-1} denotes the inverse matrix of Φ, and needs to be prepared once initially in the simulation.

The method described above may provide a simple and time-saving procedure in the plasma simulation. The ratio of CPU times is estimated

as, (rectangular cross-section): (curved cross-section): (preparation of ϕ^{-1})=1:1.2:K.

3.2 Applications of the maximum entropy method to the plasma simulation[2)]

The maximum entropy method (MEM) is applied to the spectral analysis of the electric fluctuations in an equilibrium plasma and of the large amplitude electron plasma waves to test the applicability of the method to the plasma simulation. Particle simulations using a CIC model is used to obtain time series data. The results show that the MEM performs the spectral estimate with high resolution from a short length data record. The MEM spectrum can also resolve the multiplet structures of the large amplitude electron plasma waves.

References

1) T. Takizuka, in preparation.

2) S. Tokuda, submitted for publication in J. Comp. Phys.

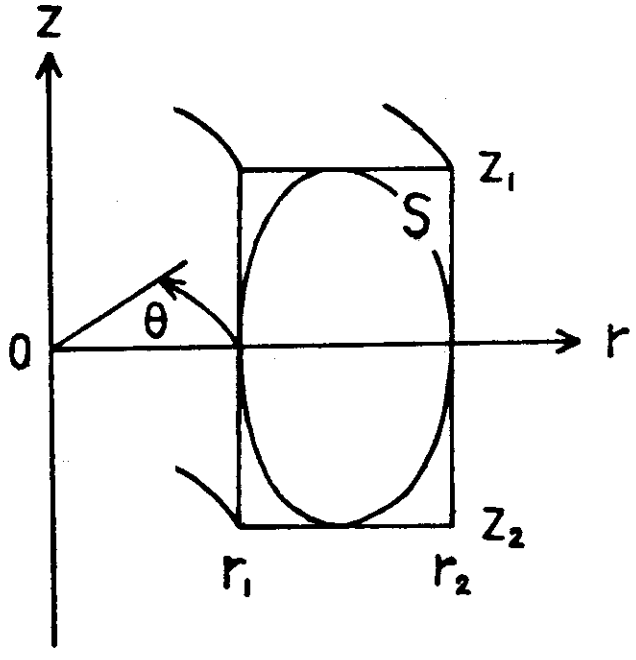

Fig. I.3-1 Three-dimensional Potential Calculation

4. Project TRITON

4.1 Introduction

In the second year of the project TRITON, we made necessary modifications and amendments on the details of the time schedule and of the constituent codes of the system (Fig. I.4-1). We have had in mind to keep the balance between the physics codes, supporting codes, and their applications.

1) The ASTRAEA subsystem, a fluid code system for tokamak plasmas

Main code in the subsystem are shown in Table I.4-1, each of which consists of several versions with different levels.

2) ARGUS, PARIS, PEGASUS, supporting systems.

We have also placed an emphasis on the development of the supporting codes, which are concerned with, e.g. graphic presentation of computational results, handling of large-scale matrices, management of the codes developed.

3) Utilization of the codes

We have endevoured also to the application of the codes, several versions of them being now in the stage for the actual applications. Especially, the equilibrium codes (SELENE) and low n stability code (TRITON-ERATO, JAERI version of ERATO originally developed by the Lausanne group) are actively used in design works.

4.2 A numerical code "SELENE" to calculate axisymmetric toroidal MHD equilibria[1)]

A new algorithm to calculate a MHD equilibrium of axisymmetric toroidal plasmas has been devised on the basis of the Grad-Shafranov equation and applied successfully to the case of a fixed boundary nonlinear eigenvalue problem[2)]. The algorithm is based on a combination of a usual finite element method and a new iteration scheme whereby the mesh structure for calculation is corrected for the finite elements always to be along magnetic surfaces (Fig. I.4-2). Very high accuracy is thus attained in the vicinity of the magnetic axis and in the regions were magnetic surfaces are closely located.

4.3 MHD stability

1) Numerical analysis of linear MHD stability of a toroidal plasma

The relation between the stabilizing effect of a conducting shell on low n mode and the poloidal beta β_p was studied in detail for a plasma of circular cross-section using the ERATO. We adopt a class of toroidal equilibria described by

$$P = \beta_J P_0\{(\psi-\psi_b) - \frac{\alpha}{z}[(\psi-\psi_m)^2 - (\psi_b-\psi_m)^2]$$

$$+ \frac{\gamma}{L+1}\{(\psi-\psi_m)^{L+1} - (\psi_b-\psi_m)^{L+1}\}, \qquad L\geq 4,$$

$$\gamma = -[1+\alpha(\psi_m-\psi_b)]/(\psi_b-\psi_m)^L$$

where ψ_m and ψ_b are ψ values at the plasma boundary and the magnetic axis, respectively, α and β_J are parameters determining the width of the current column and β_p, respectively. The computations yield (see Fig. I.4-3):

(1) The n=1 mode is completely stabilized by the conducting shell. The shell should be placed closer to the plasma for higher β_p.

(2) When the shell is placed far from the plasma both n=1, 2 modes are less stable for higher β_p.

(3) The stabilizing effect of the shell on the n=2 mode becomes significant with increasing β_p, when the shell is placed sufficiently close to the plasma.

2) Numerical analysis of nonlinear MHD phenomena of a toroidal plasma

We have been developing nonlinear MHD codes. As for the resistive nonlinear code a system of so-called reduced equations is solved as an initial value problem. The leap-frog method for the convective term, and the Crank-Nicholson implicit method for the resistive term are used to improve the restriction of the time step. A test calculation of the resistive mode of single helicity was done. The time step can be made larger compared with the fully explicit code, the CPU time being reduced to 1/5 for S=1000. The multi-helicity code is now under development.

3) Numerical analysis of nonlinear MHD pheneomena of a toroidal plasma (a free boundary code)

Prior to the full nonlinear 3D code we are now developing a 2D axisymmetric code to study the nonlinear behavior of the tokamak plasma with a divertor. The ideal MHD equation are expressed in a weak form

by the finite element method. The resulting equations are in conservative form. The grid velocity is determined so that the Jacobian is spatially constant. This reduces the deformation of the elements and simplifies volume integration. All the equations are solved in the explicit scheme except the equation for the total pressure to remove fast wave pheneomena, which limit the maximum time step in the explicit scheme[3]. Procedure of the calculation is shown in Fig. I.4-4.

4.4 2D tokamak transport code "APOLLO"

The basic version of a 2D transport code was completed by using the finite element method. In this version simplified transport models are adopted to check the accuracy of the computation. The density profile is fixed in time. The Pfirsch-Schluter or pseudoclassical electron heat conductivity is assumed, and the ion heat conductivity is the neoclassical one in the plateau region. The model yields no numerical instability nor evident accumulation of numerical errors[4]. In Fig.. I.4-5 time evolution of the electron temperature is shown. Incorporation of more realistic transport coefficients and source terms is now under way.

4.5 Graphic utility system "ARGUS"

The ARGUS-VI subsystem is designed to facilitate programming of graphic output of computational results. All the subroutines are written in FORTRAN and the user is required only to call necessary subroutines.

The most significant feature of the systme is that input data are divided into two classes of clearly defined data sets, i.e. "Graphic Data Set (GDS)" and "Control Data Set (CDS)". Other features of the system are as follows.

(1) Each figure is identified by a figure identifier (IDENT).

(2) In order to prepare a GDS the user needs only to call the corresponding GDS subroutine. It is not required to take care how the GDS data are stored in the memory. Allocation of the memory and the disk file are automatically carried out.

(3) When the user is satisfied by a figure which is drawn by the default values of CDS data, it is not necessary to call CDS subroutines. In this case the user can draw a complicated figure by calling a GDS subroutine and a DISPLAY subroutines.

Examples of graphic display of a 3D object and its projection to

a plane are shown in Fig. I.4-6(a),(b). Figure I.4-6 (a) is drawn by calling only two ARGUS subroutine, STORE2N and BRDEYE.

4.6 Convergence studies of the ICCCG method

This work belongs to the development of codes in PARIS subsystem. In our equilibrium code "SELENE" large-scale simultaneous equations are frequently solved. The coefficient matrix is very large, but very sparse and narrow. The matrix size is $N \simeq 10^4$, $M \simeq 10^2$, to obtain a highly accurate equilibrium for the stability calculation, where N, M are the dimension and band width of the matrix, respectively. Since the matrix is symmetric and positive, iterative methods are more useful than decomposition methods. We compare the number of operations of ICCCG (Incomplete Cholesky-Conjugate Gradient) method[5] with the ordinary Cholesky method for our matrix and studied the convergence properties. Figure I.4-7 shows that the ICCCG method is superior to the Cholesky method if the iterations are completed within 10 times. We also tested two methods of the initial decompositions, one is to use only the diagonal and nearest elements, and the other the method given in reference 5). Figure I.4-8 shows the latter is preferable, the iterations being completed only 6 times.

4.7 A subroutine package "BELLERphone" for editing output data

This package belongs to PEGASUS and is used to rearrange the output data to the line printer. "BELLERphone" is a kind of the extended system of the OLYMPUS utility routines CYCLOPS. It contains five classes of subroutines written in FORTRAN.

(1) Basic class: initialization, line-feed, page-feed.
(2) Scalar class: output of values in variables.
(3) Tabulation class: tabulation of variables.
(4) Graph class: writing simple graphs on line-printer sheets.
(5) Matrix class: writing patterns and elements of matrices.

In Fig. I.4-9 the examples are shown, output of messages (class 1), tabulation (class 3), simple graphs (class 4), and pattern of a sparse matrix (class 5). The package also contains physical and mathematical constants (i.e. π, e, h, etc.) and diagnostic routines for the tokamak transport code (i.e. calculation of fluxes, energy sources and confinement time etc.).

References

1) Takeda T. and Tsunematsu T., A numerical code "SELENE" to calculate axisymmetric toroidal mhd equilibria, JAERI-M 8042 (1978).
2) Lachner K., Comput. Phys. Commun. 12 33 (1976).
3) Jardin S.C., Johnson J.L., Greene J.M., and Grimm R.C., J. Comp. Phys. 29 101 (1978).
4) Takeda T., Tsunematsu T., and Kurita G., unpublished.
5) Kershaw D.S., J. Comp. Phys. 26 43 (1978).

Table I.4.1 Codes in ASTRAEA subsystem.

SELENE	MHD equilibrium analysis
NOTUS ERATO	Linear ideal MHD stability analysis for the low wave number modes
BOREAS	Ballooning mode analysis for the high wave number modes
AEOLUS	Nonlinear MHD behabior analysis
APOLLO	2-dimensional tokamak transport analysis

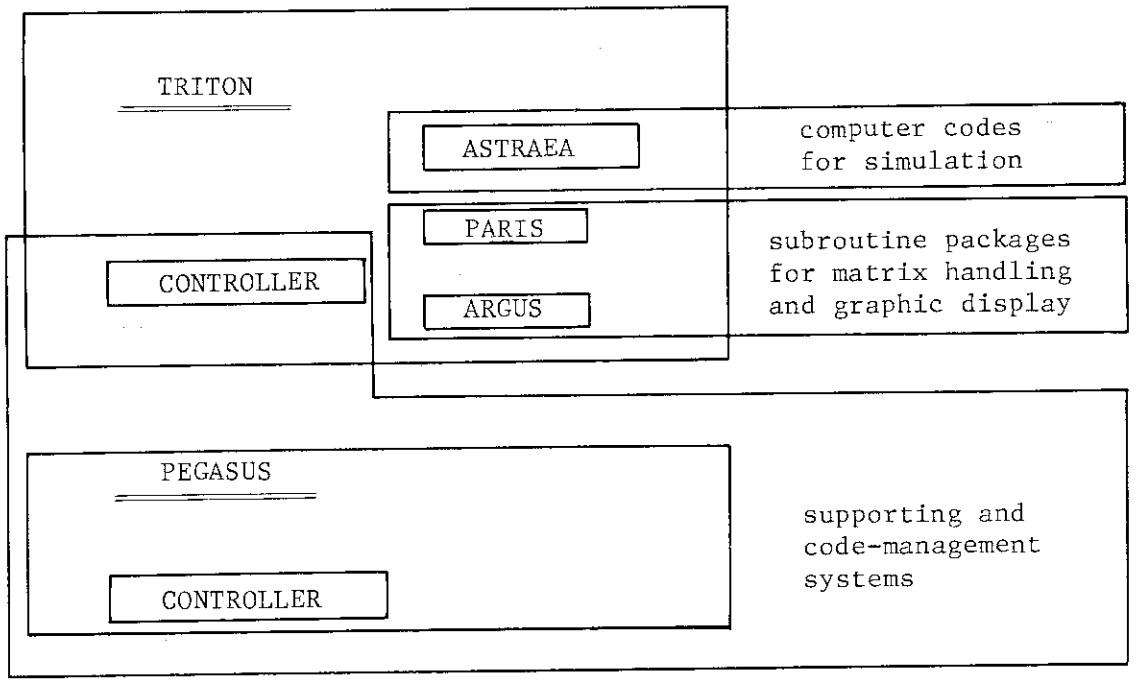

Fig. I.4-1 TRITON system.

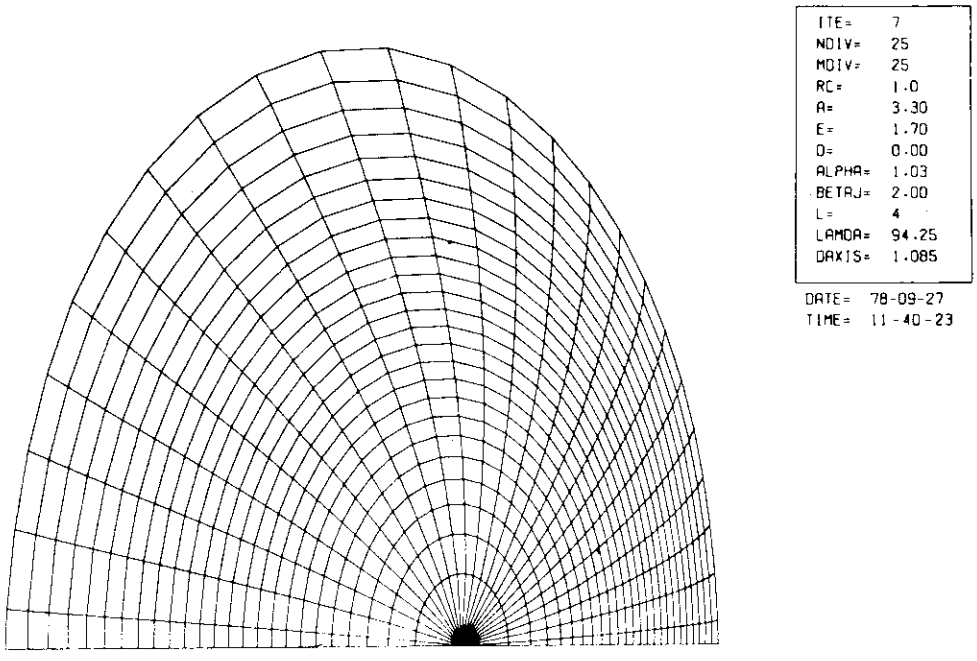

Fig. I.4-2 Numerical equilibrium obtained by using SELENE code. Mesh points are always placed on the magnetic surfaces.

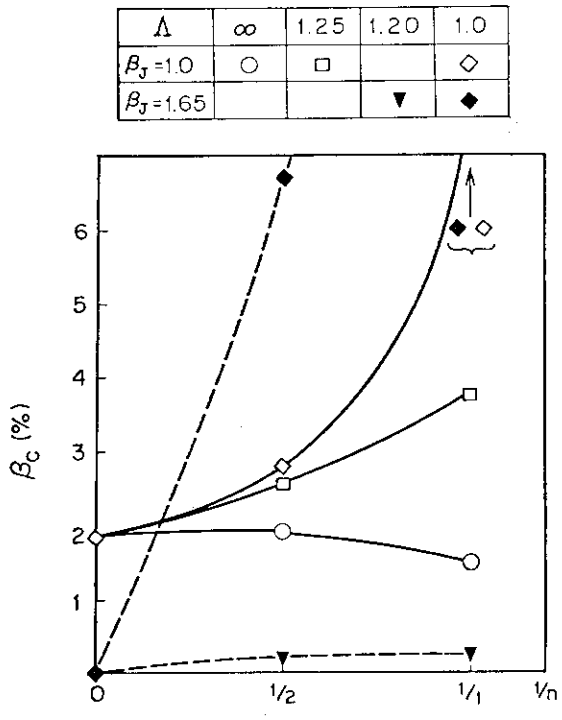

Fig. I.4-3 Critical beta values versus the toroidal mode number n. The parameter Λ denotes the ratio of the radii of a shell and a plasma.

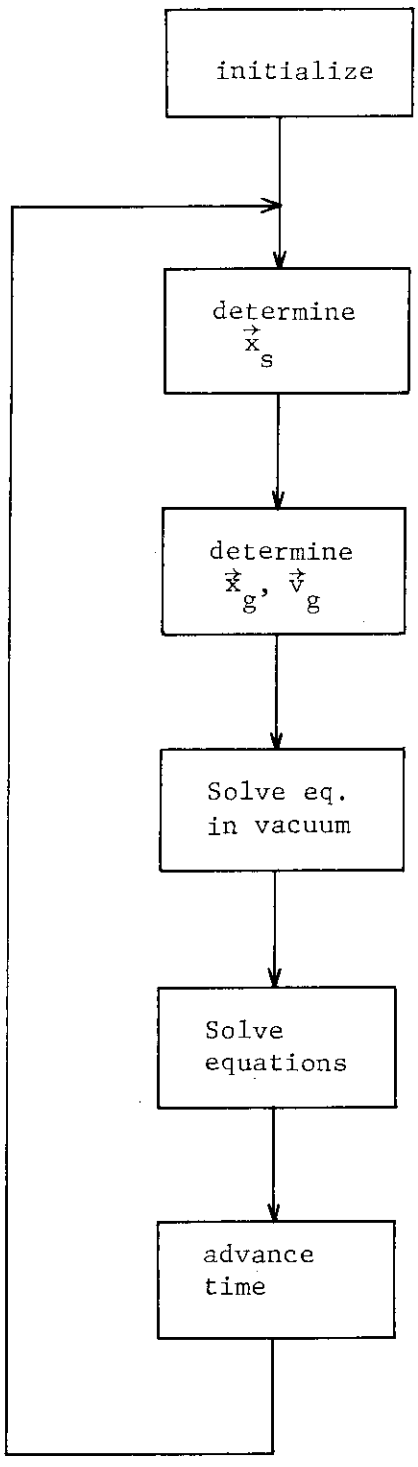

$\vec{x}_s$: position of a plasma surface

$\vec{x}_g$: positions of grid points

$\vec{v}_g$: grid velocity

Fig. I.4-4 Procedure of the calculation of 2D nonlinear MHD behavior.

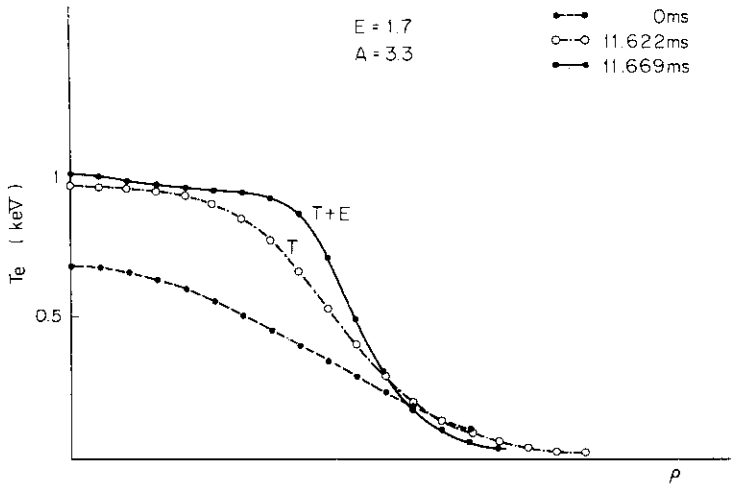

Fig. I.4-5 The time evolution of the electron temperature profile for the Pfirsh-Schlüter's heat conductivity. T+E and T denote the two-dimensional (transport + equilibrium) and the one-dimensional (only transport) operations respectively. E and A are the ratio of elongation and the aspect ratio respectively.

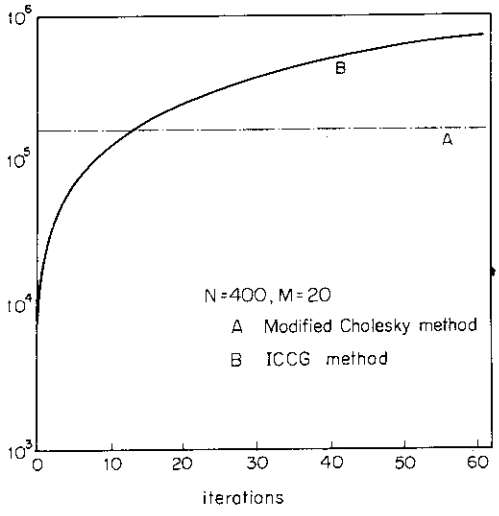

Fig. I.4-7 The number of operations versus the number of iterations.

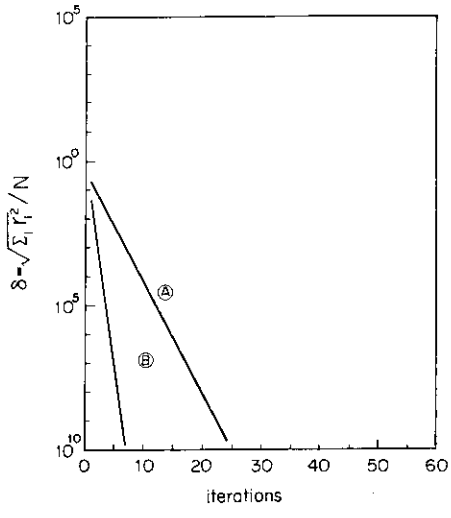

Fig. I.4-8 The convergence properties of ICCCG method. A and B denote that the initial decompositions are done for the tri-diagonal elements and by using Kershaw's method respectively.

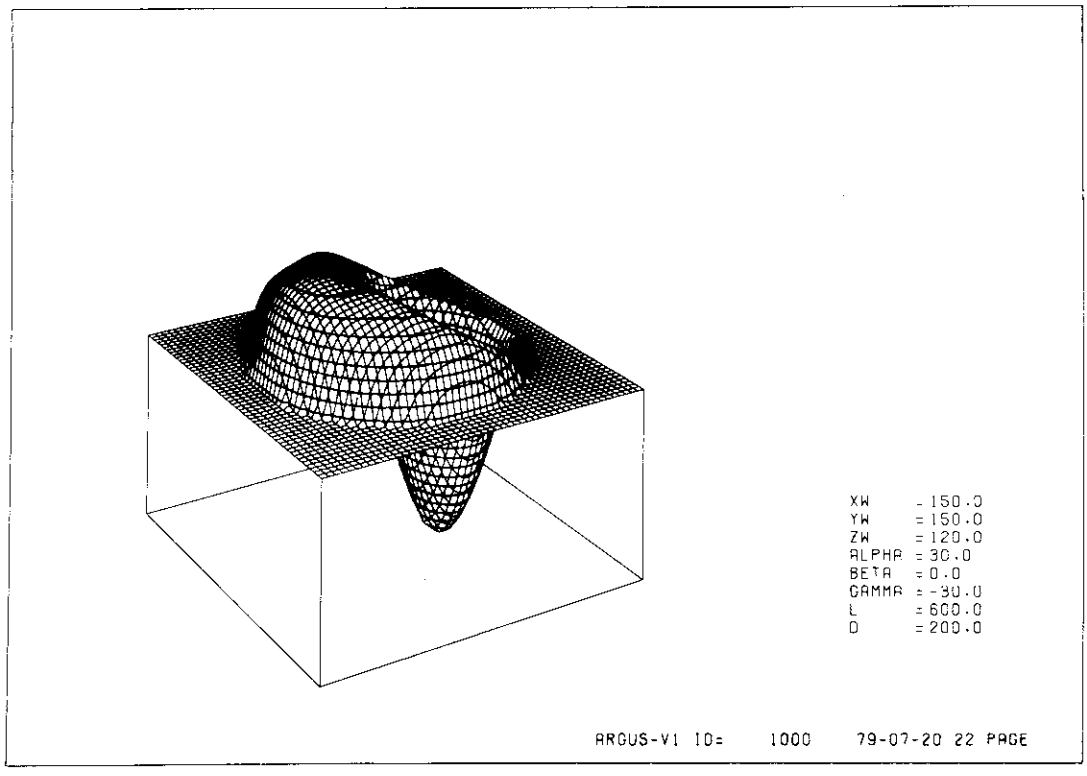

Fig. I.4-6(a) Graphic display of a three-dimensional object by ARGUS-VI.

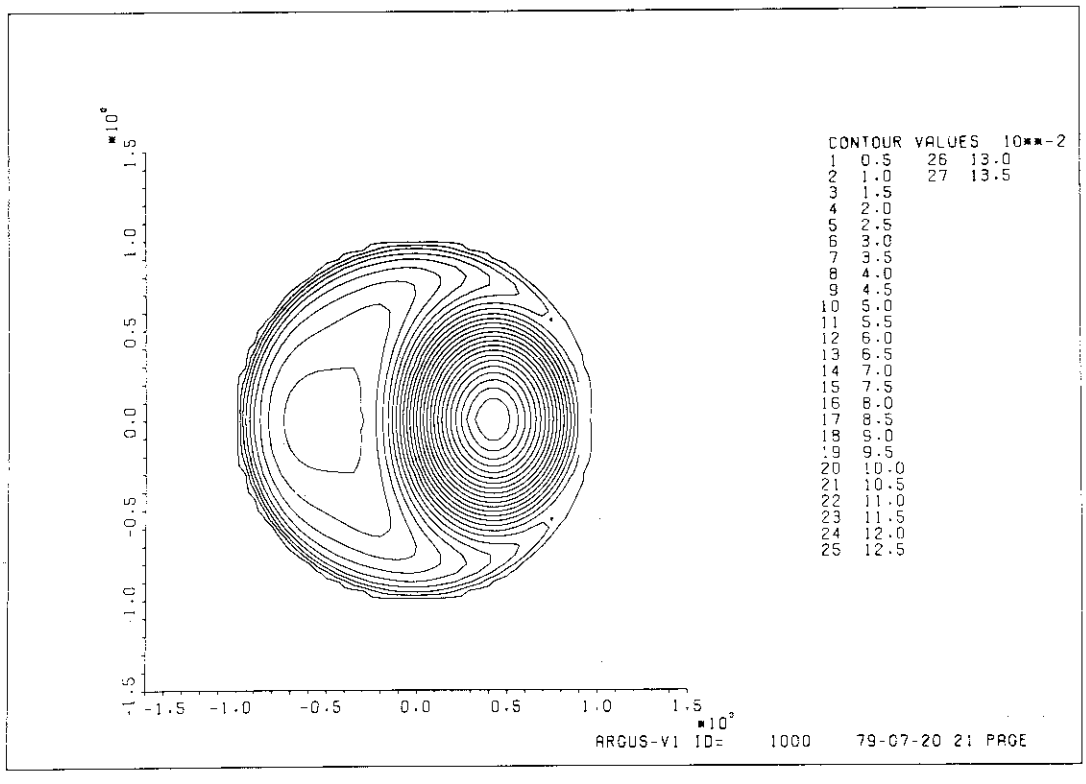

Fig. I.4-6(b) The projection of Fig. I.4-6(a) to a plane.

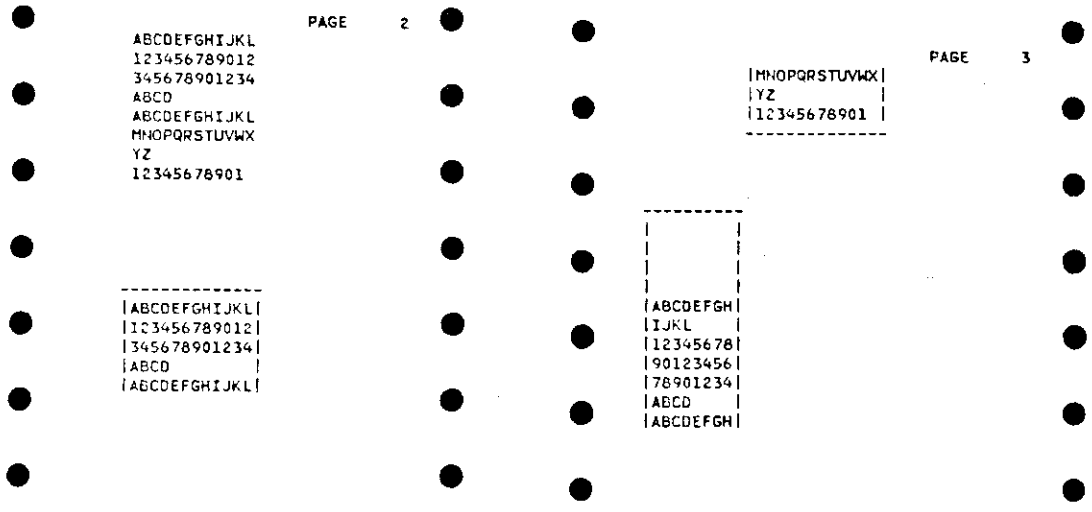

Fig. I.4-9(a) The output of messages

PAGE 1

	1	2	3
A1 =	0.11000E+01	0.18000E+01	0.18000E+01
A2 =	0.900	0.800	0.100
A3=	0.1000E+02	0.1000E+02	0.1000E+02
	4	5	6
A1 =	0.18000E+01	0.27000E+01	0.27000E+01
A2 =	0.400	0.500	1.000
A3=	0.1000E+02	0.1000E+02	0.1000E+02
	7	8	9
A1 =	0.27000E+01	0.27000E+01	0.27000E+01
A2 =	0.700	0.200	0.600
A3=	0.1000E+02	0.1000E+02	0.1000E+02
	10	11	12
A1 =	0.19000E+01	0.19000E+01	0.17000E+01
A2 =	0.300	0.0	0.0
A3=	0.1000E+02	0.1000E+03	0.1000E+03
	13	14	15
A1 =	0.16000E+01	0.15000E+01	0.14000E+01
A2 =	0.0	0.0	0.0
A3=	0.1000E+03	0.1000E+03	0.1000E+03
	16	17	18
A1 =	0.20000E+01	0.20000E+01	0.20000E+01
A2 =	0.0	0.0	0.0
A3=	0.1000E+03	0.1000E+03	0.1000E+03
	19	20	
A1 =	0.20000E+01	0.20000E+01	
A2 =	0.0	0.0	
A3=	0.1000E+03	0.1000E+03	

Fig. I.4-9(b) Tabulation

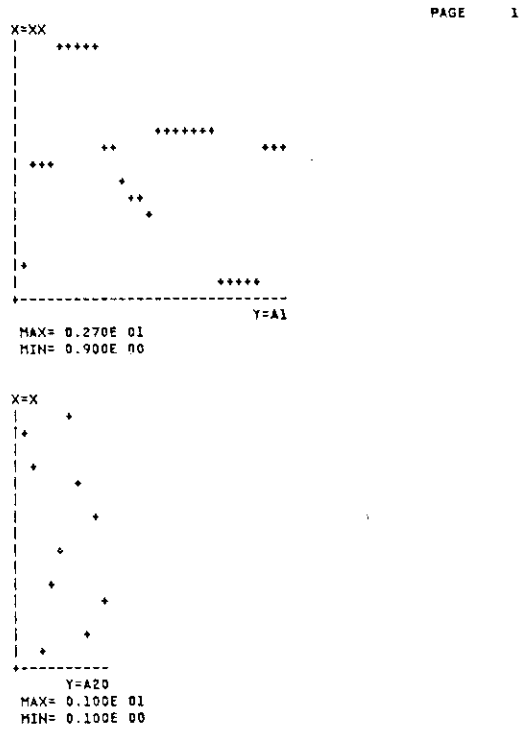

Fig. I.4-9(c) The simple graphs

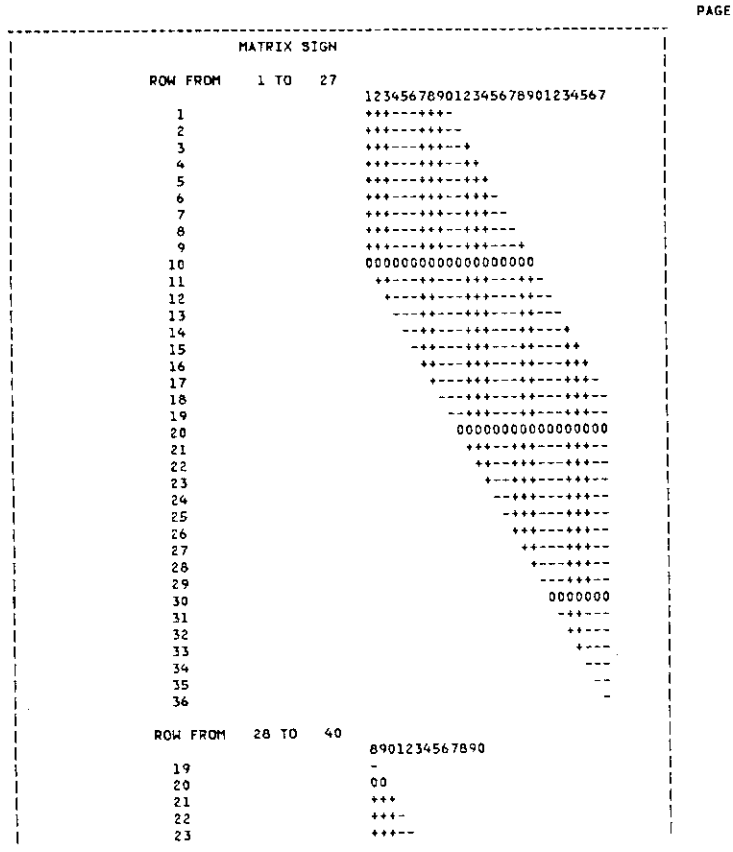

Fig. I.4-9(d) The pattern of a sparse matrix

II. TOROIDAL CONFINEMENT EXPERIMENT

1. Introduction

JFT-2 (conventional circular tokamak) and JFT-2a/DIVA (tokamak with a poloidal divertor) are under investigation with relevant research on diagnostics. Furthermore, following a revised plan of JAERI for research on high beta tokamak, the design of JFT-2M (medium size noncircular tokamak) is started from 1978.

In JFT-2, after the promissing first result of lower hybrid heating (LHH) in the last year, intensive efforts had been made on the study of LHH physics and technical development of the launcher. The outline of experimental results of LHH is described in Section 2 with relevant subject on the impurity control.

The installation of JFT-2 was commenced from December 1979. The main objectives of this remodeling are; 1) improvement of vacuum condition by the use of a cryogenic panel (15°K) for pumping, metal O ring seal and rather higher baking temperature (350°C) of the vacuum vessel, 2) feedback and feedforward position control. Furthermore, large radial ports which can afford the high power density heating (NBI and/or RF, 1.5 MW/m^3) experiments with appropriate diagnostic equipments are also supplemented. The setup is to be completed in July 1979.

In JFT-2a/DIVA the experiment to study the tokamak plasma with extremely low impurity level is being continued. Meanwhile, we have gotten almost impurity free plasma by both the poloidal divertor and titanium coating on the wall surface. In addition to the experimental results obtained in the last year, stable low q discharges (q_a=1.3 to 1.7) and good efficiency of ion cyclotron range of frequency (ICRF) heating are demonstrated. The former result indicated the possibility of increase of beta on future large tokamaks, and in the latter effectiveness of ICRF as a supplementary heating for present tokamaks was proved. In order to assess the divertor effect on future large tokamaks, intensive study on the role of boundary layer plasma is carried out. Those results are described in Section 3.

The main topics of diagnostic research relevant to JFT-2 and JFT-2a/DIVA are; evaluation of pseudo-continuum radiation from gold impurity emission, effect of titanium coated wall on metal impurity emission and determination of ion temperature during RF heating (LHH and ICRF).

In addition to these physical topics, by improvement of electronics in the Thomson scattering system, temporal behavior of electron temperature profile during the internal disruption can be investigated. The summary of these works are described in Sections 3 and 4.

JFT-2M is a medium size tokamak under design. The characteristic feature of JFT-2M are; 1) hybrid current control of the poloidal field to realize D shape plasma whose elongation ratio is 1.7 with simple arrangement of poloidal coils, 2) high power supplementary heating by coupled NBI (net 4 MW) and RF (1∿2 MW) for the plasma volume of 3 m^3, 3) poloidal magnetic limiter, 4) capabilities of long pulse opearation (1.5 T, 30 sec) or high current discharge (4.5 T, 1 MA) in the upgraded phase II.

JFT-2M program is intended to form a complementray part of Doublet-III D shape experiment, i.e. the objective of the Doublet-III D shape experiment is to demonstrate the scaling of high temperature, high beta tokamak confinement. On the other hand the main objective of JFT-2M is to investigate the advanced subjects crucial for future tokamak reactor, e.g. to establish control methods for sustaining a high bata plasma (>5 %) and to achieve effective plasma heating including the optimization of radial profile, current sustaining and fueling system. Outline of the design is described in Section 5.

2. JFT-2

2.1 RF heating experiments near lower hybrid resonance frequency

The lower hybrid heating (LHH) experiments have been carried out successfully in the JFT-2 Tokamak using a phased array of four waveguides as a launcher. An effective ion heating has been obtained by applying up to 160 kW net RF input power of frequency 750 MHz or 650 MHz in impurity-free condition with titanium gettering on the limiter and the wall. The heating rate of 0.6 to 1.4 eV/kW in the range of the average electron density $(1\text{-}3)\times10^{13}$ cm^{-3} is demonstrated.

Typical operational conditions of JFT-2 and its plasma parameters are; toroidal magnetic field B_t of up to 18 kG, plasma current I_p of 100 kA, electron temperature T_{eo} at the center of 0.6-1 keV, ion temperature at the center T_{io} of 200-400 eV, major radius R of 90 cm, minor radius of 25 cm and effective Z above 2. The mean plasma density was varied from 0.3×10^{13} cm^{-3} to 3.5×10^{13} cm^{-3}, and the density region

was divided into four regions depending on the heating characteristics.

A) very high density region of $\omega_0/\bar{\omega}_{LH}<<1$, where ω_0 is the incident wave frequency and $\bar{\omega}_{LH}$ is the lower hydrid resonance frequency for the mean density. In this case, even though the turning point of the wave is at the outer edge of the plasma column, the appreciable ion heating is observed[1].

B) high density region of $\omega_0/\bar{\omega}_{LH}<1$. In this case, the turning point is still at the mid point of the radius and the condition of $\omega_0/\omega_{pi}^s<2$ is compatible in JFT-2, where ω_{pi}^s is ion plasma frequency at the plasma surface (scrape-off region). Meanwhile, the decay spectra which are observed at the plasma surface are rather weak and high-efficiency ion heating is obtained.

C) intermediate density region of $1<\omega_0/\bar{\omega}_{LH}<2$. The turning point is at near the center and ion heating is also observed with strong decay spectra. Simultaneously, an intense high-energy tail is observed in the charge exchanged particle analysis. This suggests some nonlinear heating mechanisms.

D) low density region of $2<\omega_0/\bar{\omega}_{LH}$. There is no turning point of the wave in the plasma and then interaction between the wave and electrons is predominant. In this case, with application of RF power, the remarkable enhancement of emission of 2nd harmonics electron cyclotron frequency and the decrease in the loop voltage are observed.

In the following subsection, the specific subjects on heating efficiency, decay spectra, behavior of scrape-off plasma and high energy tail in the density regions of B) and C) are described.

2.1.1 Ion heating efficiency of the core plasma. [2]

Ion heating efficiencies of the core plasma for various experimental conditions are investigated. A typical example of local ion heating efficiency is shown in Fig. II.2-1 as a function of net input RF power. The local heating efficiency is defined by

$$\eta_{ex} = \frac{P_{di}}{P_{in}} = \frac{3\ \Delta T_i}{T_{io}} P_{ei}$$

where P_{in} is net input power, P_{di} power deposit during the steady state, $\Delta T_i/T_{io}$ relative increase of ion temperature to the central ion temperature and P_{ei} classical energy transfer from electrons to ion.

The ion heating efficiency calculated from linear ion and electron Landau damping rates near the turning point of the wave is shown in Fig. II.2-1 by dotted lines. Apparently the experimental result deviates from the linear theory especially in case (b) of Fig. II.2-1.

In order to evaluate the nonlinear effect, we calculate the local electric field of the incident wave in the plasma column. Using nonlinear spatial damping rate of nonresonant quasi mode and linear Landau damping rate for respective radial position, we can get the heating efficiency for the core plasma by integration over r=0 to a/2, by WKB approximation. The calculated results are shown in Fig. II.2-1 by solid lines. The calculated results as well as $\omega_0/\omega_{LH}(x)$ for references are shown in Fig. II.2-2, in which (a) describes the case of no turning point of the dominant waves in the plasma, (b) the case of the turning point near the central region in the plasma. When the higher RF power was irradiated to the plasma, it is seen from Fig. II.2-2 that the central ion heating for the case of (a), where the ion heating by the linear Landau damping of the externally generated slow waves is very small, is due to the nonlinear heating caused by the excitation of nonresonant quasi-modes, and in the case of (b), where the most effective ion heating is expected by the linear mode conversion in the hot plasma, the nonlinear absorption of the slow waves at the outer region (r=15∿25 cm) leads to less ion heating of the central plasma.

When the density is smaller than 1.7×10^{13} cm^{-3} (corresponding to $\omega_0/\omega_{LH}(0)\leq1.13$) the parameter dependence of ion heating is explained by the theoretical model including the nonlinear absorption due to the excitation of non-resonant quasi-modes at the outer region of the plasma column in addition to the linear wave damping. Then, it is expected from this model that the ion heating of the central plasma may be improved as the electron temperature at the outer region could be raised up.

2.1.2 Parametric instabilities near the plasma surface [3)]

Parametric decay spectra were observed during the RF pulse. Characteristics of the decay spectra and its effect on plasma heating were investigated in order to identify the decay instabilities and

mechanism of the plasma heating.

Typical frequency spectra during the RF pulse are shown in Fig. II.2.2-3. The low frequency and sideband modes satisfy a usual frequency conservation law. The frequencies of the decay waves and threshold of the onset of parametric instabilities were studied in detail. We concluded that the observed decay was parametric decay of the incident lower hybrid wave into the cold lower hybrid wave and the electrostatic ion cyclotron wave excited in the plasma in front of the launcher.

Dependences of the frequency spread $\Delta\omega$ and gross ion heating efficiency on plasma density were also investigated. Under the condition $(\omega_{pi}/\omega_{\Omega})^2>0.25$ remarkable reduction of the decay instabilities as well as the maximum ion heating was obtained, where $\omega_{pi}^{(s)}$ is the ion plasma frequency at the plasma surface. This situation is shown in Fig. II.2-4. The reduction of the decay spectra amplitude is clearly explained by the theory [4]. Maximum ion heating was obtained when the parametric instabilities in the surface plasma were reduced. This indicates that some fraction of the RF power was absorved at the surface. But surface absorption was not fatal because fairly good heating efficiency was maintained at a power far higher than the threshold of parametric instabilities. More efficient ion heating will be expected if parametric instabilities in the surface plasma are well controlled.

2.1.3 Scrape-off plasma parameters during lower hybrid heating [5,6]

The cross field particle and heat transport coefficicents are estimated from the density and temperature profiles in the scrape-off plasma, and particle and heat losses to the limiter and wall are also estimated both with and without RF power.

We can solve the transport equation in the scrape-off layer substituting experimental values obtained by the probe measurement and assuming plausible boundary conditions. And then we can get the particle and heat fluxes, which are related to gross particle confinment time and average heating efficiency.

The results obtained are; the lower hybrid wave increases the particle and heat fluxes parallel and perpendicular to the magnetic field line. However, when the effective ion heating occurs in the core plasma, these losses are compatible with the classical loss of ions. Figure II.2-5 shows the increment of perpendicular ion temperature from the charge

exchanged neutral analysis, ΔT_i, and the gross particle confinement time τ_p during the lower hybrid heating as a function of the density n_e, the toroidal magnetic field B_t, the phase difference of RF $\Delta\phi$ and the RF power P_{rf}.

The mean heating efficiency is about 30 %, which is almost consistent with those obtained from the method described in the previous section.

2.1.4 Behavior of high energy tail of ions produced by lower hybrid heating[7)]

Important and interesting feature of lower hybrid heating is fast ion production. In perpendicular energy spectrum in charge exchanged neutrals, fast ion component is always observed above the energy of 3 keV and the decay time of the fast ions after RF turns off is 200-400 μsec.

The estimated characteristic times for the fast ion loss through four mechanisms; pitch angle scattering into loss cone, charge exchange, pitch angle scattering into ripple loss cone and slowing down process are summarized in Table II.2-1.

The Table shows that the pitch angle scattering into loss cone or ripple loss cone is a plausible loss process of energetic ions. Furthermore, the observed fast ion is considered to be in the region $0.6 \leq r/a \leq 0.9$, where r is the radial position and a is the plasma radius.

It is important to note two experimental observations about the fast ion; (1) the fast ions have energy above 3 keV, (2) as the electron density was increased, the amount of charge exchange particles decreased by an order of magnitude. This indicates that stochastic heating due to the parametric decayed wave is one of the possible causes of the generation of the energetic ions during the RF pulse.

2.2 Impurity ion sputtering for introducing metal impurities.[8)]

Three mechanisms responsible for introducing metal impurity were discussed, that is, ion sputtering, unipolar arcing, and evaporation.

Evaporation is not a predominant source because the surface temperature of Mo limiter was 400 to 600 °C at the end of discharge. As for remaining two processes, dependences on the electron temperature of scrape-off plasma T_{es} and ion species are investigated.

Firstly, the electron temperature of scrape-off plasma was varied by adjusting the injection rate of working gas. Secondary, light

impurities can be decreased with T_i titanium gettering. Thirdly, under the same operation condition, working gas was changed from H_2 to He. Finally, in order to simulate the effect of light impurity and T_{es}, neon gas was injected into a clean hydrogen plasma. Impurity densities were measured with a VUV monochrometer and checked by the soft X-ray emission. The T_{es} was measured with an electrostatic probe.

These results are summerized as follows; under the same T_{es} the metal impurity concentration is just proportional to the light impurity one. This means the dominant process of the metal impurity in JFT-2 is sputtering by the light impurity. On the otherhand, the self sputtering is considered to give minor effect because the T_{es} was kept to be low (10 to 30 eV) in all discharge condition of JFT-2. The arcing was not observed in these experiments of stable steady state operation.

2.3 Experimental study on limit of the safety factor[9)]

In order to realize higher beta tokamaks, stable low-q discharge is one of the attractive ways. However, the maximum plasma current in the present tokamak is limited by the major current disruption.

In JFT-2, titanium gettering on the wall surface is effective to reduce impurities and total radiation loss caused by them (See II.4-2). As a result, the total radiation loss can be decreased from 80 to 15 % of the Joule input. In those situations, we study the attainable minimum safety factor as a function of total radiation. The result is shown in Fig. II.2-6.

In medium q_a ($q_a \approx 3$) discharges, enhanced radiation loss power due to increased plasma-wall interaction plays an important role in the growth of low frequency oscillations. The m=2 tearing mode seems to be the most plausible cause of the disruption. The reduction of the impurity is essential in realizing stable discharges of medium q_a. Attainable q_a is reduced with decreasing radiation loss power. In low q_a ($q_a < 2$) discharges, no enhancement of the radiation loss power was observed until the disruption. The plasma disrupts at $q_a \lesssim 2$. The m=2 kink mode is a probable cause of the disruption. Attainable q_a is reduced with decreasing the ratio of shell radius to plasma radius. The possibility of the shell stabilization against the m=2 kink mode is proposed.

2.4 Low power discharge cleaning

Recently it has been shown that the discharge cleaning by a weakly ionized hydrogen plasma with low plasma current and low plasma temperature is more effective than the conventional discharge cleaning with high current. Table II.2-2 shows the results of Low power Discharge Cleaning (LDC) and High current Discharge Cleaning (HDC) experiments in the JFT-2 tokamak. LDC can clean the first wall faster than HDC by a factor of ten. After LDC the macroscopic plasma parameters do not deteriorate during about ten shots, though the surface is contaminated shot by shot as shown in Fig. II.2-7.

In LDC water molecules are formed on wall surfaces by chemical reaction between the adsorbed oxygen or the oxidized layer and protons or radical atomic hydrogen. After particle-induced desorption and/or thermal desorption, these moleculars are evacuated through the vacuum system. Therefore, it is most important that these molecules should not be dissociated and/or ionized in the plasma. Optimum plasma temperature in LDC should be in such a region,

$$[\text{Dissociation energy of } H_2] < T_e < [\text{Dissociation energy of } H_2O] ,$$

$$4.5 \text{ eV} < T_e < 9.6 \text{ eV}.$$

The results shown in Fig. II.2-8 agree well with the above condition.

Table II.2-1

r/a	0.9	0.8	0.7	0.6	0.5
pitch-angle scatter into loss cone	14 μs 3.4 ms	75 μs 1.2 ms	130 μs 780 μs	190 μs 630 μs	－
charge exchange loss	1.1 ms	2.0 ms	3.3 ms	4.9 ms	7.3 ms
pitch-angle scattering into ripple loss cone	40 μs 3 ms	60 μs 840 μs	70 μs 430 μs	－	－
slowing down process	22 ms	6.1 ms	3.0 ms	1.9 ms	1.4 ms

References

1) Fujii, T., et al.: Plasma physics and controlled Nuclear Fusion Research 1978 Vol.1, 85.
Nagashima, T. and Fujisawa, N.: Joint Varenna-Grenoble Int. Symp. on Heating in Toroidal Plasmas (Grenoble, 1978) Vol.II, 281.

2) Yamamoto, T., Imai, T., Shimada, M., Takeuch, H., et al.: Unpublished.

3) Imai, T., Nagashima, T., Yamamoto, T., Uehara, K., Konoshima, S., Takeuchi, H., Yoshida, H. and Fujisawa, N.: to be submitted to Phys. Rev. Letters.

4) Porkolab, M.: Phys. Fluids 20 (1977) 2085.

5) Uehara, K., et al.: Unpublished.

6) Uehara, K., et al.: Plasma Phys. 21 (1979) 89.

7) Shimada, M., et al.: Unpublished.

8) Suzuki, N., Fujisawa, N., Konoshima, S., Maeno, M., Shimada, M., et al.: to be presented at 8th Europ. Conf. on Controlled Fusion and Plasma Physics (September 1979).

9) Maeno, M., Suzuki, N., Konoshima, S., Yamamoto, T., Shimada, M., et al.: Symp. on Current Disruption in Toroidal Devices (Garching, 1979).

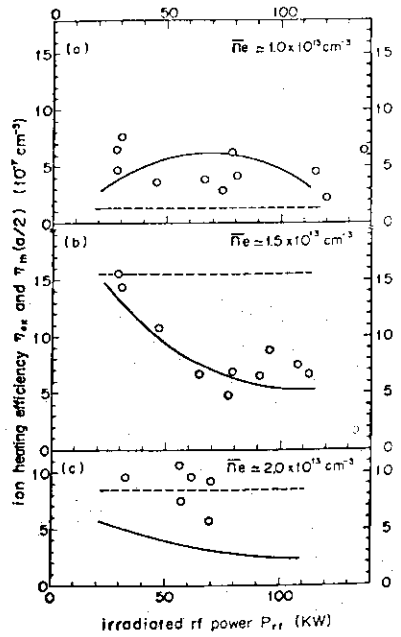

Fig. II.2-1 The local ion heating efficiency versus the net irradiated RF power for B_t=13 kG and f_0=650 MHz. The circles represent the experimental values η_{ex} and the dotted and solid lines show the theoretical values $\eta_{th}(a/2)$ calculated from the linear and linear plus nonlinear models, respectively.

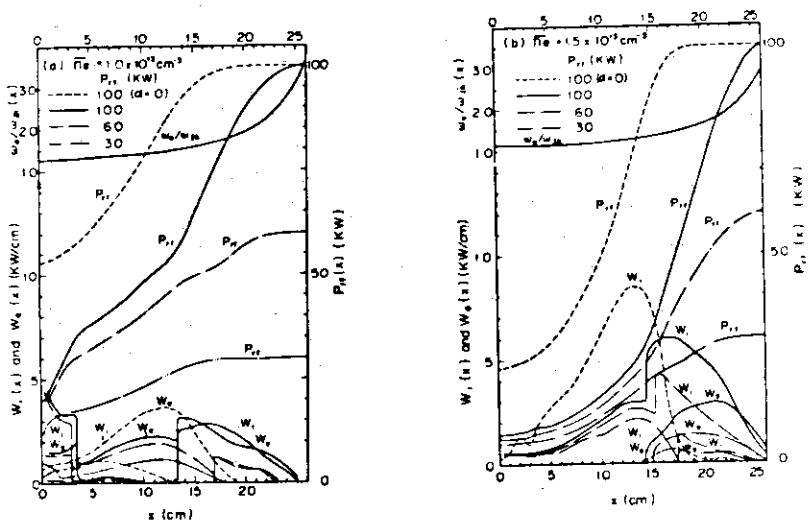

Fig. II.2-2 The radial distribution of the local RF power and the deposited power fluxes of ions and electrons, W_i and W_e, calculated from the theoretical model for the conditions corresponding to Fig. II.2-1. The pump frequency normalized by the local lower hybrid frequency is also shown for references.

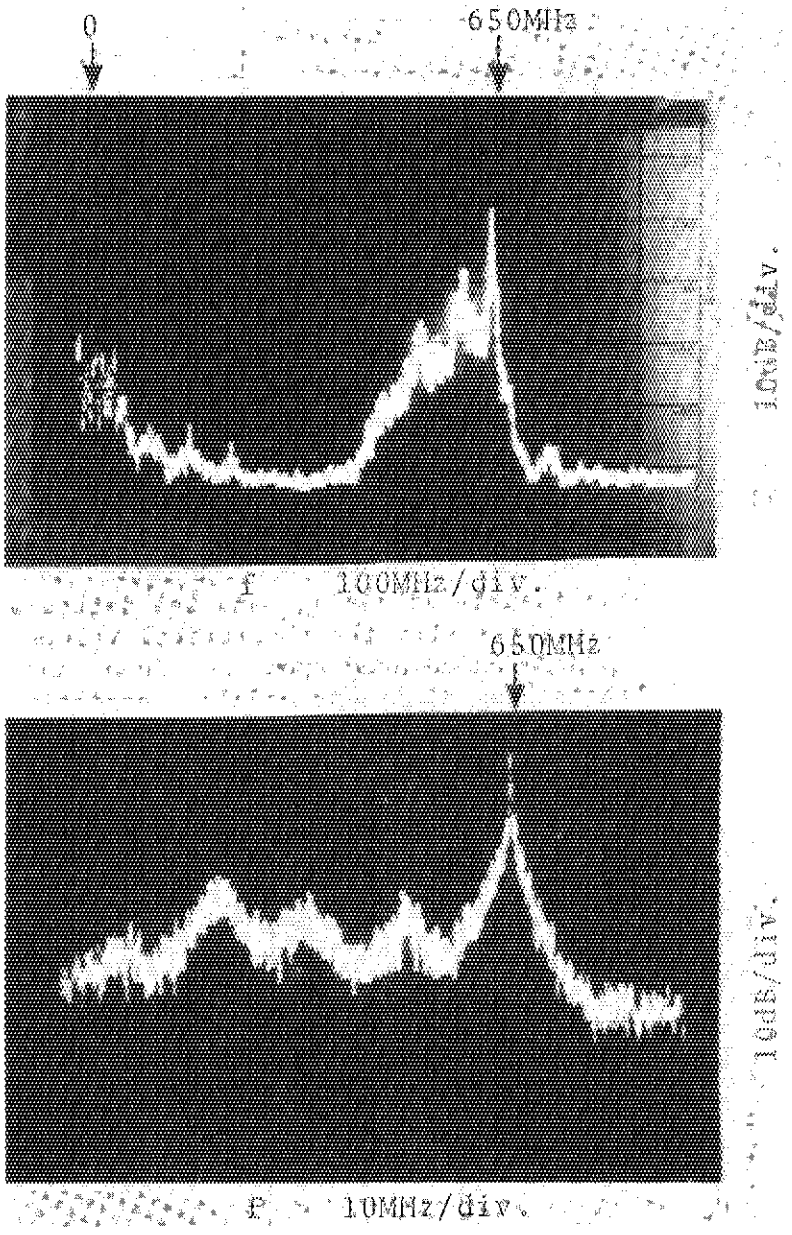

Fig. II.2-3 Typical decay spectra during the RF pulse.

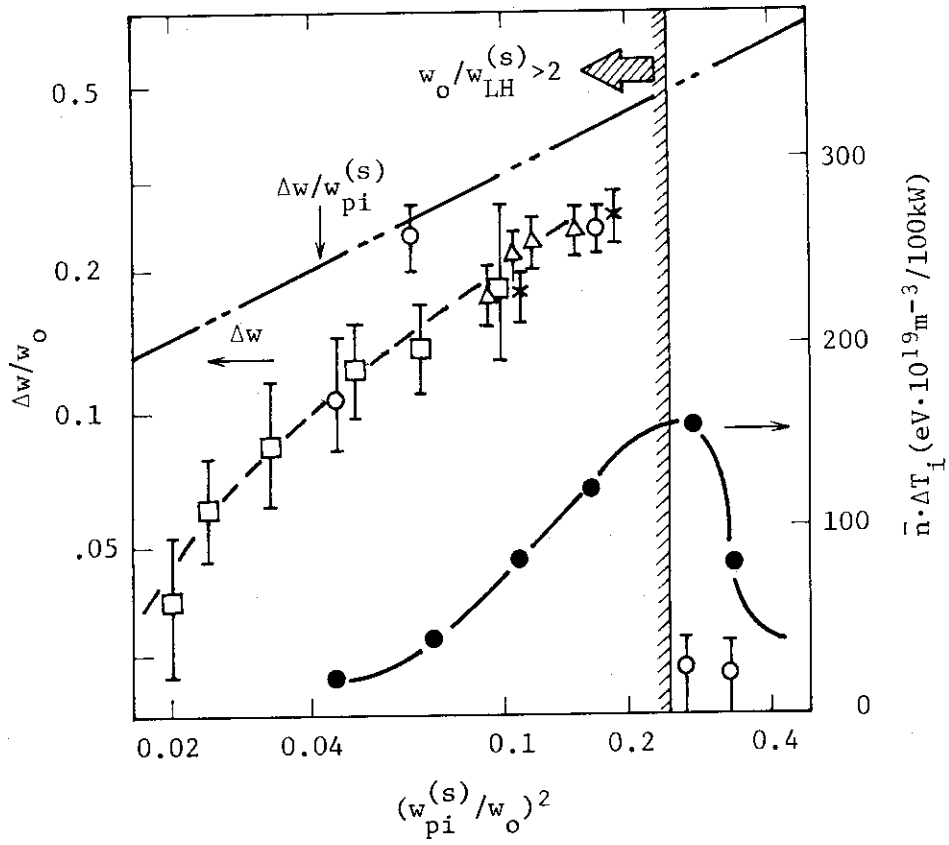

Fig. II.2-4 Dependence of frequency spread ($\Delta\omega/\omega_0$) and heating rate ($\bar{n}\Delta T_i$) as a function of normalized surface density $(\omega_{pi}^s/\omega_0)^2$

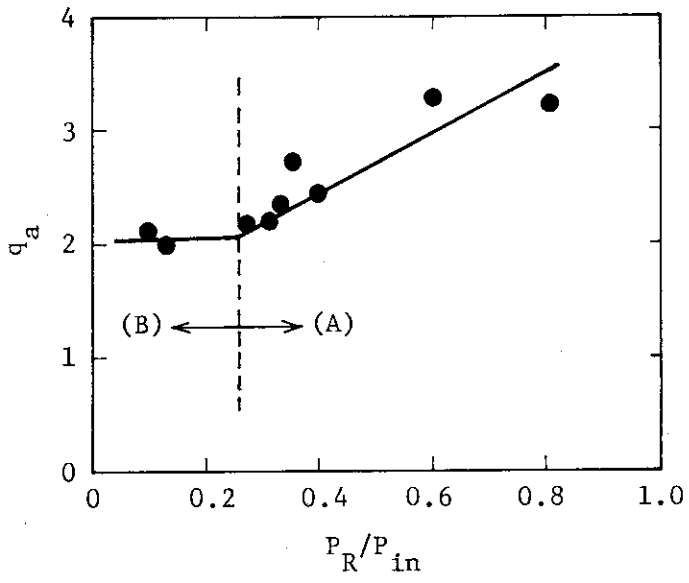

Fig. II.2-6 The dependence of the attainable q_a on radiation loss power. P_R is the radiation loss power and P_{in} is Joule input power. P_R/P_{in} is the value just before the disruption.

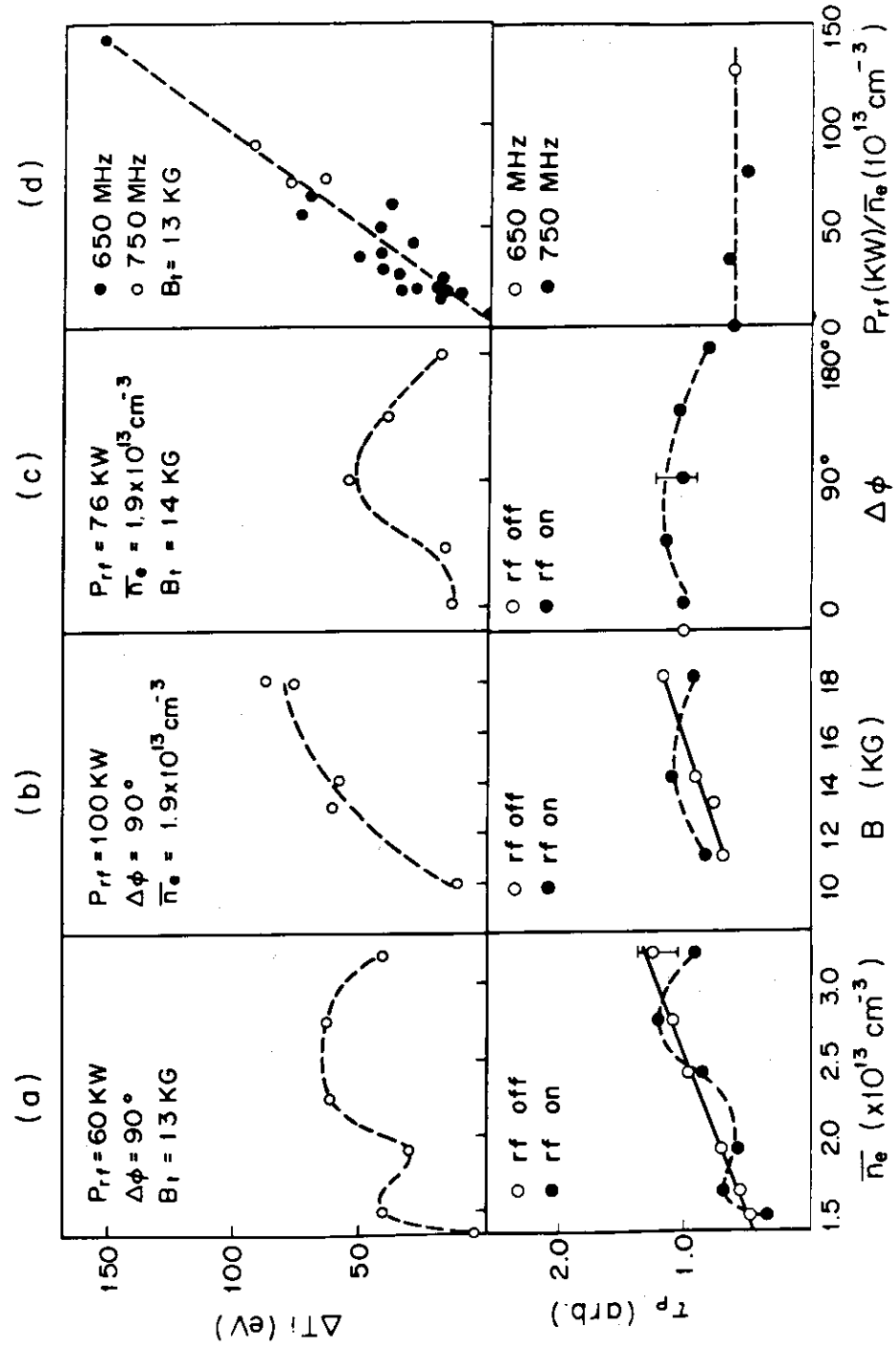

Fig. II.2-5 Increment of perpendicular ion temperature derived from the charge exchange neutral analyser, ΔT_i, and the gross particle confinement time, τ_p, during the lower hybrid heating experiments against the density, $\bar{n}_e$, the toroidal magnetic field, B_t, the phase difference of RF, $\Delta\phi$, and the RF power, P_{rf}.

Table II.2-2 Improved plasma parameters by LDC and HDC

	V_ℓ (volt)	Z_{eff}	t (hrs.)
LDC	1.9	3.2 ∿ 4.3	3 ∿ 4
HDC	2.2 ∿ 2.4	3.8 ∿ 5.6	40 ∿ 60

Notation t indicates required time to obtain steady, stable discharges by discharge cleaning, after the vaccum chamber was exposed to air. V_ℓ and Z_{eff} are one-turn voltage and mean ionic charge of the plasma. Respective plasma parameters in LDC and HDC are:

LDC $I_p \sim 5$ kA, $P_f \sim 2\times10^{-4}$ Torr, Rep. rate=1/0.7 PPS, Duty cycle of discharges=1/28, $T_e \sim 5$ eV ;

HDC I_p=50 ∿ 100 kA, $P_f \sim 2\times10^{-4}$ Torr, Rep. rate=1/60 PPS, Duty cycle of discharges=1/1200, T_e=200 ∿ 300 eV.

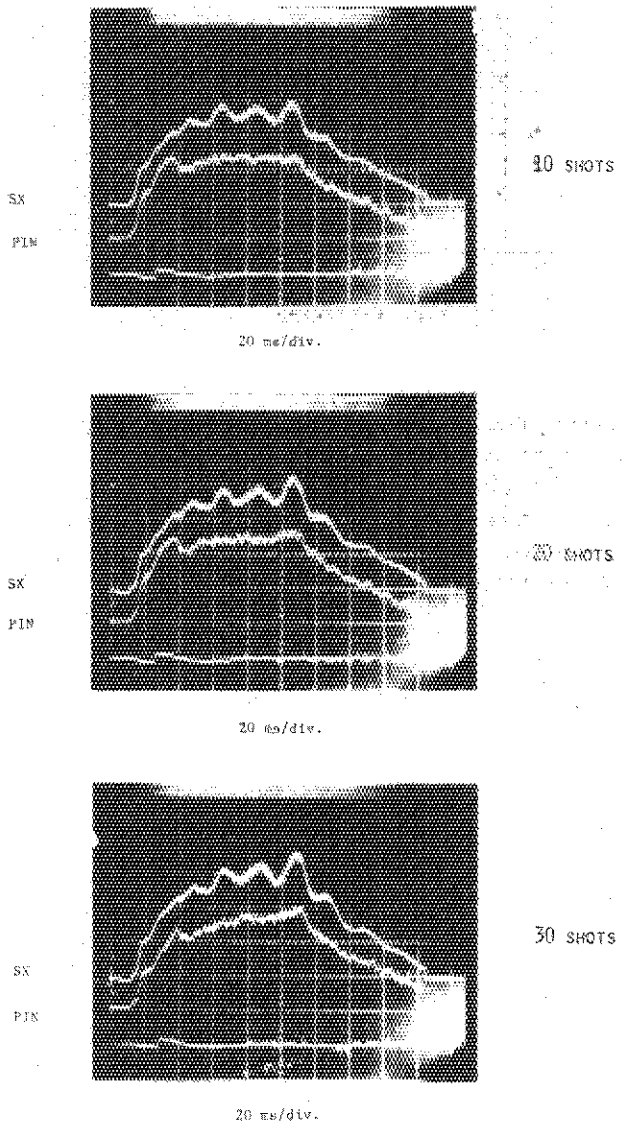

Fig. II.2-7 Time behavior of the signals from SX and PIN diode. These signals show that the clean surface is contaminated shot by shot.

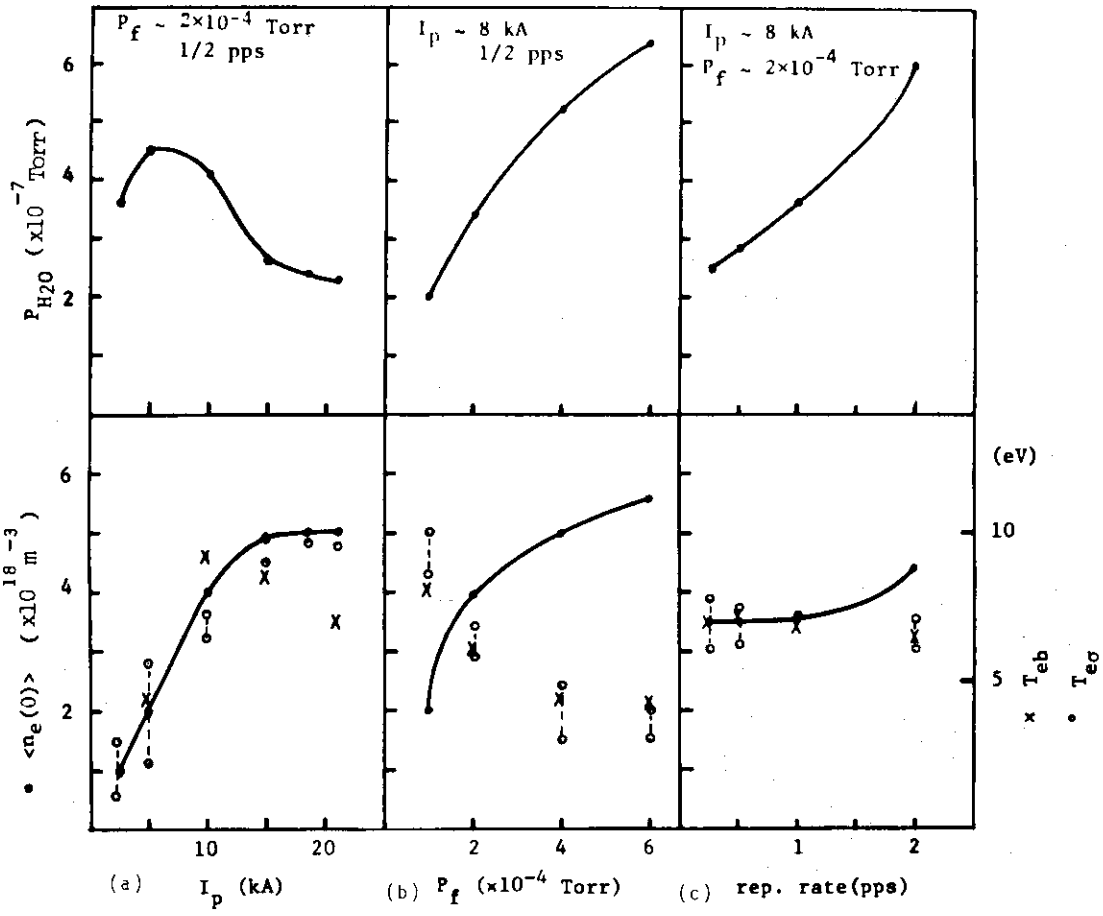

Fig. II.2-8 Dependency of water molecule production on LDC parameters: plasma current (I_p), filling pressure (P_f) and repetion rate of discharge. $\langle n_e(0)\rangle$ is the electron density of central line average. T_{eb} is the boundary electron temperature measured by a double probe. $T_{e\sigma}$ is the conductivity temperature on the assumition that Z_{eff}=1.

3. JFT-2a (DIVA)

3.1 Introduction

Very low q discharges, confinement scaling, ICRF heating have been studied in DIVA after reducing the impurity content with the poloidal divertor or the fresh titanium surface. Major results are summarized as follows.

A) Very low q discharges

(1) Stable plasmas with good confinement properties are obtained with $q_a \geq 1.3$.

(2) Noncircular magnetic surface inside the plasma column is obtained.

(3) Energy balance during the sawtooth oscillation is clarified and it is shown that the energy confinement time can be improved by a factor of a few.

(4) Major disruption can not be excited.

(5) Very high density plasmas are obtained, i.e. $n_e = 5\times10^{13}\ B_T(T)/R(m)$.

(6) Average toroidal beta $\bar{\beta}=0.8$ % is obtained with $q_a=1.7$.

B) mhd activities

(1) Large m=2/n=1 fluctuations induced by impurity injection and by internal disruption are direct course of the major disruption with $q_a \gtrsim 2$.

(2) Separatrix does not affect the major disruption.

(3) Reducing impurity level, the $q_a<2$ discharges are stably obtained with $\bar{b}/\bar{a}=1.2$ and probably with $\bar{b}/\bar{a}=1.35$.

(4) Increase of loop voltage and m=2/n=1 mode, probably kink mode, are observed when q_a is near 2. The fluctuation level of the mode is reduced by the separatrix magnetic surface.

(5) Internal disruptions are observed but major disruption cannot be excited in the $q_a<2$ discharges.

C) Confinement scaling

(1) Modified Alcator scaling, i.e. $\tau_E = 1.8\times10^{-15}\ \bar{n}_e\ (cm^{-3})\ a^2_{half}(cm)ms$, describes well observed confinement time of various discharge conditions without large mhd activities where a_{half} is the half radius of an electron temperature profile.

D) ICRF heating

In the preliminary experiment, the ion temperature increased, but impurity increase was also observed in a dirty discharge as in ST or ATC. Therefore ICRF heating experiment using 2 ω_{CD} frequency for a deuteron

plasma with a minority proton ccmponent was performed under the extremely pure wall condition ($Z_{eff}\simeq 1$).

(1) RF net power was up to 140 KW. RF net energy of 1 KJ was applied.

(2) No change of one turn loop voltage and electron density was observed.

(3) The maximum $\Delta T_i/P_{Net}$ was observed at B_T=18 kG and ε_p=5∿10 %. Ion heating efficiency is 40 % and ion temperature increases from 180 eV up to 290 eV.

E) Conditions of boundary plasma in a large device.

Recycling of self-sputtered impurities from a limiter or a divertor neutralizer plate was numerically investigated based on the experimental results. An upper limit for the boundary plasma temperature was determined from the condition that wall material impurity ions did not increase. This temperature is shown to be very low in a conventional tokamak but not limited in a divertor tokamak with a molybdenum neutralizer plate.

These results are discussed in detail in the following subsections.

3.2 Confinement characteristics of very low q discharges[1)2)3)]

Very low q discharges, i.e. $q_a<2$, are investigated in DIVA. No current disruption is observed with $q_a<2$. Average energy confinement time is dominated by sawtooth oscillations but Alcator scaling continues to hold with a larger numerical factor in front of $a^2\bar{n}_e q_a{}^{1/2}$ when $q_a\geq 1.3$. It is shown that suppression of the sawtooth oscillations is important and desirable because of the following reasons: the energy confinement time has a possibility to increase by a factor of a few by suppressing the oscillations.

Figure II.3-1 shows measured radiation loss power v.s. plasma current: (●) corresponds to discharges with gold walls without divertor, (○) with gold walls and divertor and (▲,△) with titanium walls in this experiment. The radiation loss power is very low, typically 10-20 %. in this experiment which is the same level as that with poloidal divertor with gold walls[4)]. In these discharges with low level of impurities, stable very low q plasmas are obtained with good reproducibility.

Typical discharge characteristics with $q_a<2$ are shown in Fig. II.3-2, i.e. time behavior of loop voltage V_L and current I_p, and profiles of density n_e, radiation loss power density P_{py} including charge exchange loss, and electron temperature at the top and bottom of the sawtooth oscillations.

Energy loss by the internal disruption dominates the average energy confinement time. The average energy confinement, however, is 5.7 ms with the plasma radius of only 10 cm and average β is 0.8 % in this case. Therefore it can be mentioned that a $q_a<2$ discharge is stably obtained.

The next interest is the attainable minimum q_a value. A $q_a=1.3$ discharge has similar characteristics to those in the $q_a=1.7$ discharge shown in Fig. II.3-2. No large voltage spike is observed also in $q_a\approx1$ discharge but the average energy confinement time is drastivally reduced, i.e. the average confinement time is only about 50 μs at $q_a=1.05$ with $n_{eo}=2\times10^{13}$ cm^{-3} and $T_{eo}=130$ eV. This poor confinement time may be due to the wide area of $q<1$ as discussed below. When q_a is reduced down to 1 or a less value, large increase of the loop voltage which may be due to m=1/n=1 kink mode is observed and the current cannot increase any more. Therefore it can be said that a good confined plasma is obtained with $q_a\gtrsim1.3$, a poor confined plasma with $q_a\approx1$ and an unstable discharge with $q_a\lesssim1$.

Mean plasma density $\bar{n}_e$ and safety factor q_a are summarized in Fig. II.3-3 following Murakami scaling. The density limitation has not been investigated in DIVA because of its short discharge duration but the obtained density in high q discharges is almost comparable to those obtained in DITE or JFT-2. In very low q discharges, the density can be increased, e.g. $\bar{n}_e/(B_T/R_o)=4$-5. Therefore it can be said that the very low q discharges are suitable for obtaining a high density plasma.

In order to investigate the parameter dependence of the energy confinement time, the following discharges are studied: 1) fixing B_T and $\bar{n}_e$ and changing q_a, i.e. $q_a=1.8$ and 2.5; 2) fixing B_T and q_a and changing $\bar{n}_e$, i.e. $\bar{n}_e=1.1\times10^{14}$ cm^{-3} and 6×10^{13} cm^{-3}. The results show that the energy confinement time is almost proportional to $\bar{n}_e$ and roughly proportional to $q_a^{1/2}$. Therefore confinement time is well described by Alcator scaling. Confinement time in various discharge conditions are summarized in Fig. II.3-4. (▲, △) show data in this experiment, and (●) without divertor and (○) with divertor in the previous experiment[4]. The very low q discharges seem to increase the energy confinement time because the old confinement time (●) without the divertor is almost equal to Alcator scaling. The provious experiment, however, shows that the energy confinement is improved by reducing impurities as shown by (○)[4)5)]. Therefore it seems reasonable that the reduction of impurities improves

the energy confinement also in very low q discharges.

It is very interesting to know the energy confinement time excluding the effect of the internal disruption because sawtooth oscillations have a possibility to be suppressed in a device with high power additional heating and because the energy confinement time excluding the effect becomes important. Figure II.3-5 shows a typical energy balance in the sawtooth oscillations. The average energy confinement time is 5.7 ms and dominated by the internal disruptions, i.e. energy loss due to the internal disruptions is the major loss from the plasma column. When X-ray intensity increases, the energy loss is only about 40 J during 0.82 ms and the confinement time is about 20 ms. During the internal disruption, the energy loss is about 125 J during only 0.18 ms and the confinement time is only about 0.8 ms. Therefore the energy confinement time excluding the effects of the sawtooth oscillations is about 20 ms, i.e. the confinement time can be improved by a factor of a few if the sawtooth oscillations are suppressed. And the energy confinement time excluding the internal disruption is much longer than the value given by Alcator scaling.

The above result suggests that Alcator scaling has to be modified. Alcator scaling describes well the observed data except the numerical factor in front of $a^2 \bar{n}_e q_a^{1/2}$ and the previous experiment shows that the numerical factor increases by increasing the radius of the hot column. In the very low q discharges, the radius of the hot column is large. Therefore it seems reasonable that the long confinement time during the slow rise of the sawtooth oscillations is explained by the same reason, i.e. the large effective radius gives the long confinement time. Energy confinement time without large mhd activities are summarized in Fig. II.3-6 as a function of $\bar{n}_e q_a^{1/2} a_{half}^2$ where a_{half} is a half radius of an electron temperature profile. In the figure, (●) shows old data with gold walls without the divertor, (○) with gold walls with the divertor and (▲) with $q_a<2$. The modified Alcator scaling describes well the observed confinement time in various discharge conditions.

3.3 MHD characteristics of very low q discharges[2)3)]

Disruptive instabilities are investigated in tokamak discharges near $q_a=2$. It is shown that excitation of large m=2/n=1 fluctuations by impurity injection are a dominant trigger of the major disruption when

$q \gtrsim 2$. Reducing impurity radiation loss, very low q, typically $2.5 \gtrsim q_a \gtrsim 1.3$, discharges are stably obtained with good confinement property. It is demonstrated that very low q discharges with $q_a < 2$ are free from major disruptions even with impurity injection.

In order to observe the disruptive instability in low q discharges, neon gas is injected into a stable discharge with $2 < q_a \lesssim 2.5$. The radiation loss increases from about 15 % of ohmic input power to about 100 %. The disruptive instability is excited with good reproducibility, and the events immediately proceding the negative voltage spike are observed in order to clarify the cause of the disruption. Examples of the loop voltage and the magnetic fluctuation immediately preceding the negative voltage spike are shown in Fig. II.3-7. Traces (a) to (d) are cases to lead the major disruption without divertor, (e) is with divertor and (f) is an example of minor disruption. The experimental observation shows that a m=2 tearing mode grows up to 4∿6 % at rapid decreasing phase of loop voltage, even if the behavior of precursor oscillations are different. If the m=2 tearing mode cannot grow sufficiently, the voltage spike is rather small and results in a minor disruption as shown in trace (f). Operating the divertor the disruption can be also triggered by injecting neon gas but the amount of neon to induce the disruption is 2∿3 times larger than that without the divertor. The disruptive instability in a plasma with separatrix configuration is shown in trace (e). The behavior of the precursor oscillation is the same as the trace (b). The negative spike appears at $\tilde{B}_p/B_p = 4$ %. It should be noted that the separatrix does not affect the major disruption, which is consistent with the previous experiment[6].

Figure II.3-8 shows an events immediately before and during the negative voltage spike. About 100 μs before the negative spike, mhd activity gradually increases, and soft X-ray signal at central chord decreases and at the outer chord slowly increases. This means a spread of a hot column and flattening of the current profile. The events in this phase is the same as minor disruption and/or internal disruption. Then m=2/n=1 mode suddenly grows up to 5.5 % within 30 μs, and loop voltage drops steeply. The radiation loss including charge exchange loss is 40 kW before the disruption and increases gradually up to 250 kW at the negative voltage spike which is almost equal to the total input power. These results suggest that internal or minor disruption and

impurity cooling enhance the m=2 mode up to several % which triggers the negative spike. Therefore the observed behavior of the current disruption in this experiment with $q_a \gtrsim 2$ is very similar to that in high-q discharges[6].

In the experiment, sudden growth of m=2/n=1 mode is observed, i.e. the level of the mode grows up to 5-7 % during about 30∿300 μs just before the disruption. To understand this behavior it is necessary to show how the m=2/n=1 mode grows by the impurity injection. Combining one dimensional transport code and linear helical symmetric tearing code, the observed large m=2/n=1 mode is well simulated. Figure II.3-9 gives the calculated results, i.e. electron temperature profiles in Fig. II.3-9(a), current profiles in Fig. II.3-9(b), fluctuation level and island width in Fig. II.3-9(c) and the dominant power balance in Fig. II.3-9(d). Plasma near q=2 is drastically cooled by the radiation loss during 1.5 ms (Fig. II.3-9(a)) and sudden growth of m=2/n=1 mode is observed after the drastic cooling (Fig. II.3-9(c)) because of the change of the current profile (Fig. II.3-9(b)). The level of the m=2/n=1 mode is 5.5 % at 1.5 ms after the injection and the island width is 28 % of the plasma radius (Fig. II.3-9(c)). The large m=2/n=1 fluctuations seem easy to disrupt the plasma, which may be combined by other modes. The radiation loss is almost equal to the total input power at 1.5 ms from the injection. The following characteristics obtained from the calculations are very similar to those of the experimental results: 1) the level of the m=2/n=1 mode is 5.5 % at 1.5 ms after injection, and 2) the input power equals to the radiation loss power at 1.5 ms after the injection. It should be noted that these results are obtained in the case with both the sawtooth oscillations and the impurity injection. The calculated level of the m=2/n=1 mode with only sawtooth oscillations or only impurity injection is a few times less than the observed level. In conclusion, the direct cause of the disruptive instability is mainly the large m=2 mode induced by the impurity injection and the internal disruption.

When the discharge fall into $q_a<2$ region, fluctuations including m=3/n=2 are observed by magnetic probes but the level is very low, i.e. $\tilde{B}_p/B_p \simeq 0.05$ %. Large sawtooth oscillations are observed in soft X-ray signal and loop voltage and the energy replacement time τ_E is dominated by these internal disruptions. The average energy confinement time,

however, follows Alcator scaling with an higher numerical factor in front of $a^2 \bar{n}_e q_a^{1/2}$. Therefore q_a 2 discharge with good confinement property is obtained. Reduction of the radiation loss has dominant role to obtain $q_a<2$ discharges. The sum of the radiation loss and the charge exchange loss is 32 kW for 280 kW joule input in the case of Fig. II.3-2 and the $Z_{eff}\simeq 1$. When the plasma current is crossing through $q_a=2$, m=2 which may be kink mode grows up to $\tilde{B}_p/B_p=4$ % and the loop voltage rises, but negative voltage spike is not usually observed. The characteristic feature of the mhd activity is not changed by changing the current rising rate dI_p/dt from 10 to 28×10^6 (A/sec). When the plasma has a separatrix in the shell at the case with divertor operation, the duration of the voltage increase is much shorter than the case without divertor, and the mhd activity is smaller than that without the divertor by a factor of 4 as shown in Fig. II.3-10. Therefore the separatrix stabilizes the kink mode.

An example of neon injection into the $q_a<2$ discharge is shown in Fig. II.3-11. The radiation loss including charge exchange loss is about 30 kW before the neon injection and increases up to 250 kW by the injection in all cases. It should be noted that no disruptive instability occurs in $q_a<2$ region which is contrast with a disruption in $q_a>2$ region.

From these results, the control of the m=2/n=1 tearing mode is necessary tc supress the disruptive instability. The best way to supress the m=2 mode is to achieve a $q_a<2$ discharge, because there is no q=2 resonant surface in the plasma. And other modes cannot cause the major disruption with $q_a<2$.

3.4 ICRF heating of a D^+ plasma with a minority H^+ component[7)8)].

Preliminary experiment was affected by impurity influx[7)]. Therefore ICRF heating of impurity free tokamak plasmas is studied in DIVA. The frequency is fixed at 25 MHz, which is the second harmonic cyclotron frequency of deuteron with a toroidal magnetic field of 16.4 KG. The toroidal field B_T and the ratio of proton to deuteron density ε_p are varied over ranges of $12\leq B_T\leq 19$ KG and $2\lesssim\varepsilon_p\lesssim 40$ %, respectively. The most favorable ion heating is obtained at $B_T=18$ KG and $\varepsilon_p=5\sim10$ %. Ion temperature increases from 200 to 300 eV measured with charge exchange neutral analysis and also spectroscopy with the application of 100 KW RF net power. The result is consistent with the mode conversion theory.

The RF power was applied for 3∿8 ms. The maximum RF net power was

140 KW, limited by breakdown at the antenna. Although breakdown took place, the RF power could be raised gradually from a low level to the maximum power as before. One turn loop voltage did not change even with the application of the maximum RF power. Change of the electron density was also within shot-to-shot reproducibilities of the base plasma, that is, less than 10 %. We first examined the response of charge exhcange neutral spectra, varying the toroidal field, i.e. the position of the fundamental cyclotron resonance layer for hydrogen. Figure II.3-12 shows some examples of charge exchange neutral spectra and corresponding cyclotron resonance layers. In these examples, ε_p was kept to be 5∿10 %. The features of these spectra are as follows: (A) —— the cyclotron resonance layer was located on the inner side of the plasma cross section - ΔT_i was medium and no high energy tail was present. (B) —— the cyclotron resonance layer was located on the outer side of the plasma cross section - ΔT_i was large and also no high energy tail was present. (C) —— the cyclotron resonance layer was located on the outer edge of the plasma cross section - ΔT_i was medium and remarkable high energy tail was built. Figure II.3-13 compares temporal evolutions of count numbers of charge exchange neutrals at 1.5 KeV in these cases. The 1/e decay times of count numbers after terminating the RF pulse were (A) 0.7 ms, (B) 1.5 ms and (C)<0.3 ms, respectively. This indicates that heating took place in the most central region in case B. It is consistent with the fact that the two-ion hybrid resonance layer was located most closely to the plasma center in case B, since the two-ion hybrid resonance layer lies on little high field side of the cyclotron resonance layer and strong wave damping occures near the two-ion hybrid resonance layer, following the mode conversion theory.

Next we examined the response of charge exchange neutral spectra to the ratio of proton to deuteron density ε_p, keeping the toroidal field at 18 KG and 16.4 kG. Figure II.3-14 shows some examples of charge exchange neutral spectra for different values of ε_p. Here the toroidal field was fixed at 18 kG. Profiles of L_α lines of deuterium and hydrogen were measured with the monochromator for each case. They are also shown in Fig. II.3-14, where curves are normalized at the peak corresponding to deuterium. ε_p was determined as

$$\varepsilon_p = \frac{2\ P_H}{\alpha\ P_D} \ ,$$

where P_D and P_H are peak values of L_α lines of deuterium and hydrogen, respectively, assuming same temperatures, and α is a correction factor for absorption effect of the deuterium L_α line by ground levels of deuterium. Rough calculation shows α is about 1.3 for the present experiment. We make ε_p simply to be obtained from P_H/P_D for convenience. This procedure includes error within 20 %. The features of spectra shown in Fig. II.3-14 are as follows: (D) For ε_p<5 %, a remarkable high energy tail was build and ΔT_i was medium. (B) For ε_p=5∿10 %, a high energy tail disappeared and ΔT_i was large. (E) For ε_p>10 %, a high energy tail was also absent but ΔT_i was small. A decay time of the high energy tail in case D was 1.2 ms, which was comparable with that of the bulk ion temperature 1.5 ms. In addition, the former is much longer than that of the high energy tail in case C, 0.3 ms. $\Delta T_i/P_{Net}$ has the maximum value of 1.2 eV/kW with ε_p=5∿10 %. It can be concluded that the most favorable heating is realized at ε_p=5∿10 % for B_T=18 KG.

Radial profile of ion temperature in the case of ε_p=5∿10 % and B_T=18 KG was determined from the Doppler broadening of OVII (1623 Å), CV (2271 Å) and CIV (1548 Å) lines and from the localization of line intensities (Fig. II.3-15). The localization of the impurity emissions was experimentally confirmed by measuring spatial distributions of their total line intensities. The spatial distributions of the total line emission coefficient were obtained by using an Abel inversion method from the radiances observed along different horizontal chords. For the central ion temperature, data from the charge exchange were adopted. Ion temperatures in the scrape-off layer were measured with the multigrid analyser[9] and the Katsumata probe[10]. Ion heating in the overall plasma cross section was shown in Fig. II.3-15. Radial profiles of electron temperature are also measured. Peripheral electron heating was observed. When ε_p was smaller than 5 %, no electron heating occured in the whole plasma cross section.

We consider power balances using the radial profile shown in Fig. II.3-15 and the electron temperature profile. Steady state power balances for ions with and without the RF power are as follows.

$$Q'_{ei} + Q^i_{rf} - \frac{W'_i}{\tau'_{Ei}} = 0 \quad \text{with RF power} \tag{1}$$

$$Q_{ei} - \frac{W_i}{\tau_{Ei}} = 0 \quad \text{without RF power,} \tag{2}$$

where Q_{ei}, Q^i_{rf}, W_i and τ_{Ei} are power transferred from electrons to ions, the RF power to ions, energy of ions and ion energy confinement time, respectively, and (') denotes quantities with RF power. W_i, W'_i, Q_{ei} and Q'_{ei} are calculated from the observed radial profiles of $T_i(r)$, $T_e(r)$ and $n_e(r)$, assuming same values of perpendicular and parallel temperatures. Those are tabulated in Table II.3-1. The RF power to ions Q^i_{rf} can be estimated from

$$Q^i_{rf} = \frac{W'_i - W_i}{\tau_s}$$

Here τ_s is a decay time of bulk ion temperature after terminating the RF pulse, and was 1.5 ms (Fig. II.3-13). Then, Q^i_{rf}=38 kW. An ion heating efficiency η_i is defined as the ratio of Q^i_{rf} to the RF net power P_{Net}. The efficiency is about 40 %. From Eq. (1) and (2) τ_{Ei} and τ'_{Ei} are calculated to be 4.8 ms and 3.7 ms, respectively. They are in agreement within experimental error (±25 %).

Steady state power balances for electrons with and without the RF power are given below.

$$P_{OH} - Q'_{ei} + Q^e_{rf} - \frac{W'_e}{\tau'_{Ee}} = 0 \qquad \text{with RF power} \qquad (3)$$

$$P_{OH} - Q_{ei} - \frac{W_e}{\tau_{Ee}} = 0 \qquad \text{without RF power,} \qquad (4)$$

where P_{OH}, Q^e_{rf}, W_e and τ_{Ee} are the ohmic input power, the RF power to electrons, energy of electrons and electron energy confinement time, respectively. Values of P_{OH}, W_e and W'_e are shown in Table II.3-1. Q^e_{rf} is unknown, since time evolution of electron temperature after terminating the RF pulse did not measured. τ_{Ee} and τ'_{Ee} are calculated to be 2.2 ms and 1.9 ms, respectively, assuming Q^e_{rf}=0. Thus, the RF heating causes no change in the ion and electron energy confinements. The rest of the RF power presumably went to the edge plasma, although the detail has not yet been clarified.

3.5 Conditions of boundary plasma in a large device[11)12)]

Evaporation, arcing and ion sputtering were observed in an actual tokamak. Evaporation may be excluded by spreading the heat flux and by reducing runaway electrons. Arcing is important in a dirty, unstable

discharge and in an early phase of the plasma formation. However, in the steady state of a discharge, impurity ion sputtering, especially self-sputtering, was shown to be the dominant process in the origin of heavy impurities in some present day tokamaks[1)13)14)15)] and will become more important in future large tokamaks. The self sputtering yield can be very high, typically higher than unity, since multi-ionized ions are accelerated to high energy by the sheath potential, and the number of the high-Z imputities sputtered from a limiter increases if the temperature is high in the scrape-off layer. Increased impurities enhance the radiation loss and decrease the temperature of the scrape-off layer. Therfore, the temperature of a scrape-off layer plasma is limited to a very low value in a steady state plasma. A low temperature plasma can carry only a small portion of the power loss from a high temperature plasma to material surface[16)], and consequently the main portion of the power must be lost by other processes. Generally, the other loss processes, especially radiation, give adverse effects on the plasma characteristics, especially the energy confinement time.

It is very important tc know the maximum values for the temperature of a scrape-off layer plasma and the power loss to a limiter, and to study possible methods of increasing the permissible temperature and also increasing the other losses near the plasma boundary, i.e. cooling the boundary plasma, without introducing adverse effects on plasma confinement. These were qualitatively investigated in Ref. 17. The process of heavy impurity recycling due to self-sputtering including ionization, coulomb scattering and diffusion in a given plasma with and without a divertor is investigated by using Monte-Calro method, and the permissible value for the boundary temperature in a future tokamak, e.g. JT-60, is discussed. The numerical model follows the experimental results in DIVA.

In the given plasma, motion of impurity particles and self-sputtering were calculated with and without a divertor (Fig. II.3-16). For the Monte-Carlo calculation presented here, a sufficient number of incident particle histories were processed at each energy to yield at least 10,000 sputtered atoms. Some portion of the impurity ions moving through the background plasma reach molybdenum limiters or neutralizer plates and sputter out molybdenum atoms becoming impurity sources for the next generation. Calculations show that the charge states increase continuously

as the temperature of the scrape-off plasma increases when the divertor is off. However, when the divertor is on, the average charge state of molybdenum atoms is lowered due to a decrease of the number of impurity ions going to the hot plasma region, because the neutralizer plates are removed from the main plasma. By the same reason, impurity ions flow back to the neutralizer plate in a short time due to the particle flow and the pre-sheath field. This effect is enhanced when the boundary temperature increases. Therefore, the average charge states saturate at around five when divertor is on. Hence, a divertor lowers the incident energy, and thus the number of sputtered atoms decreases. Because the neutralizer plates are well separated from the main plasma, the number of impurity ions, N_Z, which arrive at the neutralizer plates decreases, i.e. more impurity ions are captured in the burial chamber. Decreasing E_I and N_Z leads to a lower impurity growth rate γ, as shown in Fig. II.3-18, as compared with the case of divertor off.

In the cade with divertor, owing to the increase in the flow velocity and the diffusion coefficient, the number of impurity ions that anihilate at the burial chamber increases when the temperature increases. In addition to this, the sputtering yield saturates at energies above $E_I \sim 1$ KeV, i.e. $T_{ev} \sim 60$ eV. Therefore, the growth rate decreases at temperatures above $T_{ev} \sim 60$ eV and is always less than unity, as shown in Fig. II.3-18. The result shows that the maximum temperature is very low, ~ 45 eV without the divertor, but is infinete with a divertor.

In this calculation, only self-sputtering was assumed and the effect of secondary electron emission was neglected. However, sputtering by protons and modifying the sheath potential cannot be neglected in a high temperature boundary plasma. To investigate these effects, calculation was repeated with the addition of proton-sputtering and the effect of secondary electron emission. The growth rate, including proton- and self-sputtering, $\gamma(Mo^+, H^+)$, is then given analytically as follows

$$\gamma(Mo^+, H^+) = \{1 + \frac{1}{f} \frac{S_0(H^+)}{S_0(Mo^+)}\} \gamma(Mo^+) \quad , \qquad (10)$$

where f ($\equiv N_{Mo}+/N_H+$) is the fraction of molybdenum ions, $S_0(H^+)$ is the calculated proton sputtering yield. This calculation gives a maximum in the temperature of the scrape-off plasma, without the divertor, of 80∿140 eV with f=0.1 % (allowable concentration for molybdenum in the

main plasma). And $\gamma(Mo^+, H^+)$ is always less than 0.5 with the divertor.

Impurity recycling including self-sputtering in a large tokamak was numerically investigated. The condition for equilibrium of the recycling gives a maximum temperature for a boundary plasma and it is shown that the equilibrium temperature is very low, 80∿140 eV, without a divertor. This value is much lower than the temperature of the main plasma in a large tokamak. Therefore, most of the energy loss from the main plasma must be converted into radiation or charge exhcange losses to maintain such the equilibrium of the hot core with a cold boundary. If this conversion results in large adverse effects on the main plasma, the permissible maximum boundary temperature should be increased by some method, such as employing a material of low self sputtering yield or a divertor. Impurity recycling employing a material of low self sputtering yield, such as carbon, for neutralizer plates or limiters will be reported in the near future. When a divertor is employed, the maximum boundary temperature is infinite. In such a system, other mechanisms, such as evaporation, could possibly limit the boundary temperature. The fraction f can have a range of values, because few sputtered impurity ions can flow back into the main plasma and the fraction near the neutralizer plate is almost independent of that of the main plasma. Therefore, the fraction must be given by a self-consistent method to discuss the impurity recycling and the permissible boundary temperature in detail. This study will be reported in the near future.

Table II.3-1 Power balances with and without the rf power.
$P_{OH}\simeq 85$ kW, $P_{Net}\simeq 100$ kW, $\varepsilon_p = 5\sim 10$ %, $B_T = 18$ KG.

W_e	W_i	Q_{ei}	τ_{Ee}	τ_{Ei}					WITHOUT RF
141 Joule	95 Joule	20 kW	2.2 ms	4.8 ms					
W'_e	W'_i	Q'_{ei}	τ'_{Ee}	τ'_{Ei}	Q^e_{rf}	Q^i_{rf}	η_e	η_i	WITH RF
158 Joule	151 Joule	3 kW	≲1.9 ms	3.7 ms	?	38 kW	?	∿40 %	

Reference

1) MAEDA, H., SENGOKU, S., KIMURA, H., OHTSUKA, H., OHASA, K., et al., 7th International Conference on Plasma Physics and Controlled Nuclear Fusion Research (Innsbruck, 1978)., 1 (1979) 377.
2) ODAJIMA, K., et al., Symposium on Current Disruption in Toroidal Devices (Garching, 1978)
3) DIVA Group, JAERI-M 8205 (1979).
4) DIVA Group, Nuclear Fusion, 18 (1978) 1619.
5) YAMAMOTO, S., et al., in Controlled Fusion and Plasma Physics (Proc. 8th Europ. Conf., Prague, 1977) 2 (1977) 234.
6) SHIMOMURA, Y., MAEDA, H., OHTSUKA, H., KITSUNEZAKI, A., NAGASHIMA, T., Phys. of Fluids, 19 (1976) 1635.
7) DIVA Group, Joint Varrenna-Grensble International Symposium on Heating in Toroidal Plasmas, (Grenoble, 1978) 441.
8) KIMURA, H., et al., to be published in Nuclear Fusion.
9) KIMURA, H., ODAJIMA, K., SUGIE, T., MAEDA, H., Application of Multigrid Energy Analyzer to the Scrape-off Layer Plasma in DIVA, to be published in Japan J. Appl. Phys..
10) ODAJIMA, K., KIMURA, H., MAEDA, H., OHASA, K., Japan J. Appl. Phys. 17 (1978) 1281.
11) SENGOKU, S., et al., JAERI-M 7918 (1978).
12) SENGOKU, S., et al., to be published in Nuclear Fusion.
13) OHASA, K., MAEDA, H., YAMOMOTO, S., NAGAMI, M., OHTSUKA, H., KASAI, S., ODAJIMA, K., KIMURA, H., SENGOKU, S. and SHIMOMURA, Y., Nucl. Fusion 18 (1978) 872.
14) OHASA, K., et al., JAERI-M 7935 (1979).
15) OHASA, K., et al., Journal of Physical Sociaty of Japan 46 (1979) 1979.
16) KIMURA, H., MAEDA, H., UEDA, N., SEKI, M., KAWAMURA, H., YAMAMOTO, S., NAGAMI, M., ODAJIMA, K., SENGOKU, S. and SHIMOMURA, Y., Nucl. Fusion 18 (1978) 1195.
17) SHIMOMURA, Y., Nucl. Fusion 17 (1977) 1377.

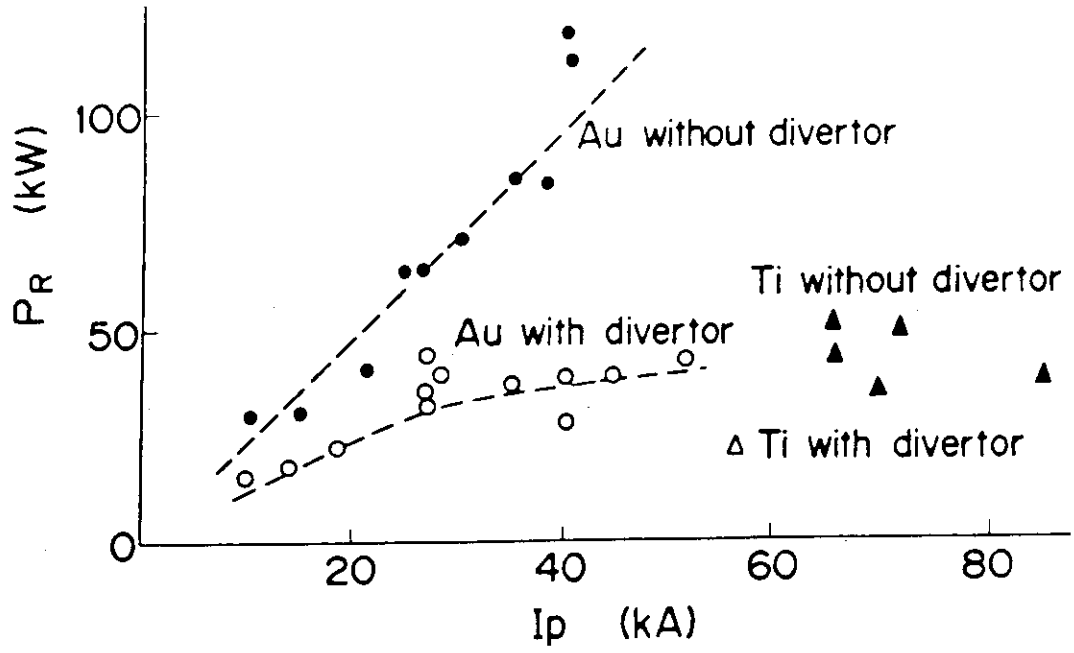

Fig. II.3-1 Radiation loss power v.s. plasma current. (▲) and (△) show the present data

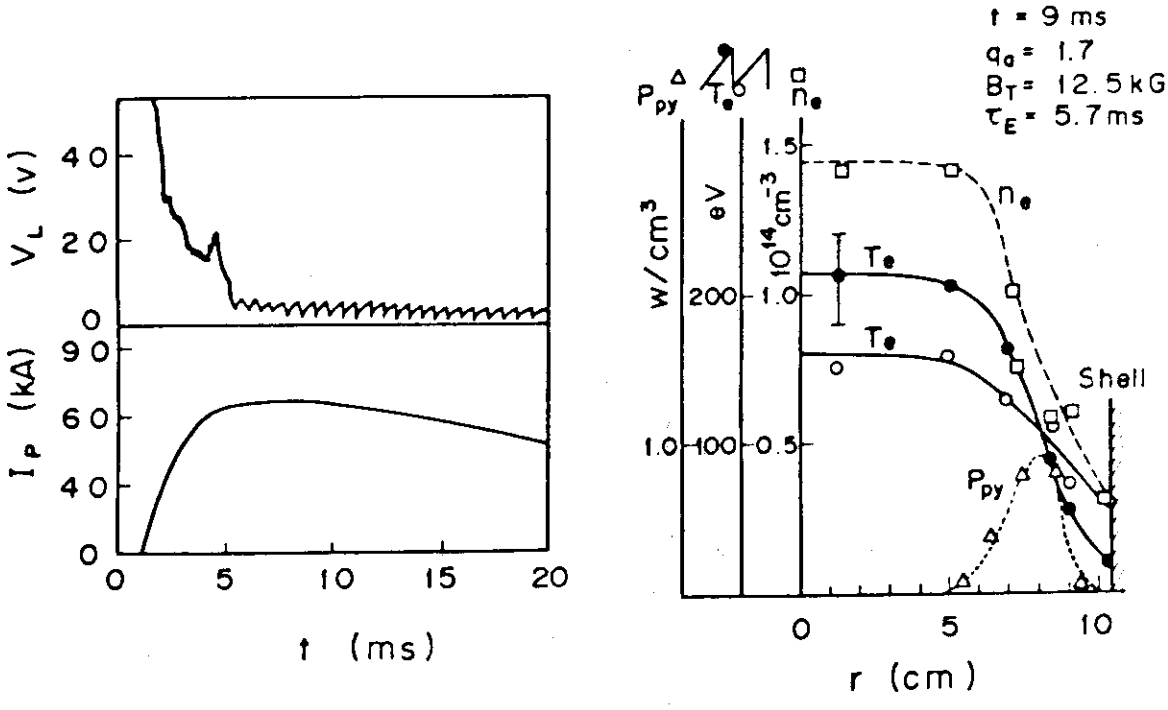

Fig. II.3-2 Typical plasma characteristics in a q_a<2 discharge.

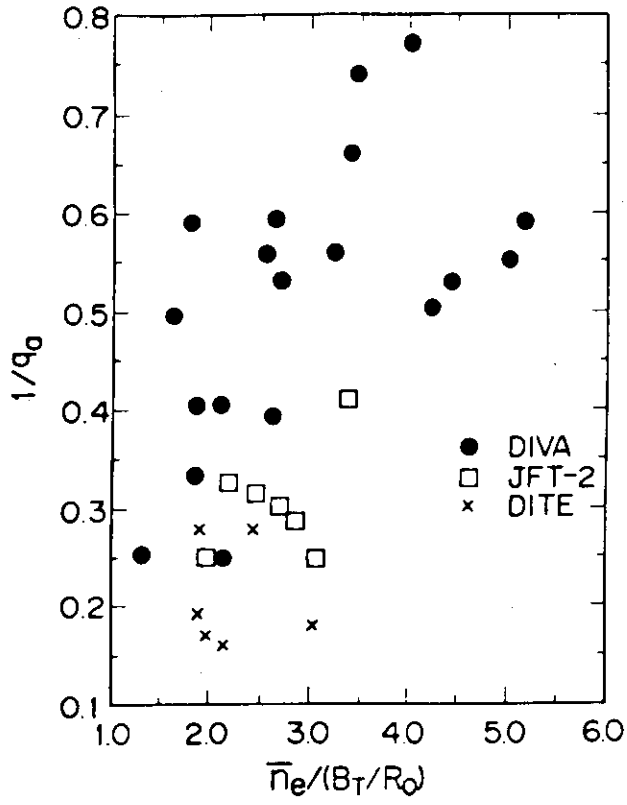

Fig. II.3-3 Typical plasma density v.s. $\bar{n}_e/(B_T/R_o)$ where $\bar{n}_e$ is mean electron density in 10^{13} cm^{-3}, B_T toroidal field in T and R_o major radius in m.

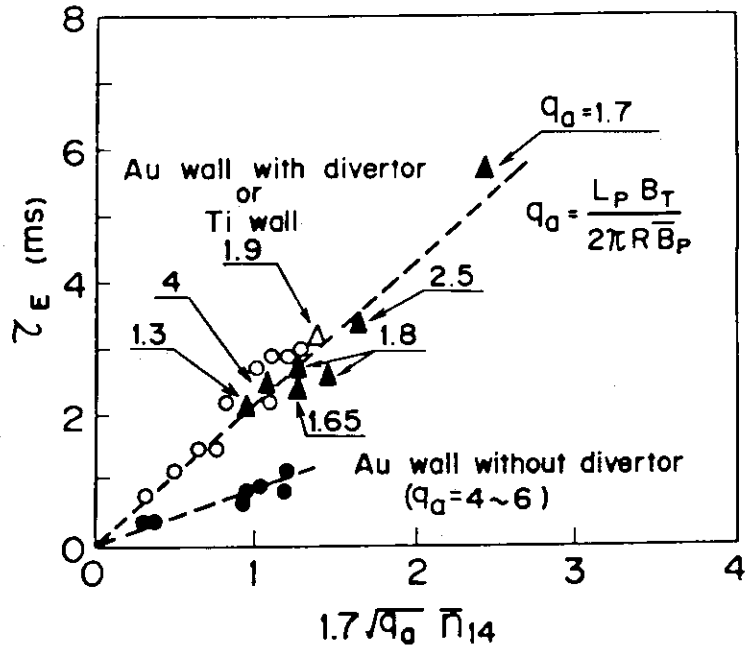

Fig. II.3-4 Energy confinement time v.s. $q_a^{1/2}\bar{n}_{14}$ where $\bar{n}_{14}$ is mean electron density in 10^{14} cm^{-3}.

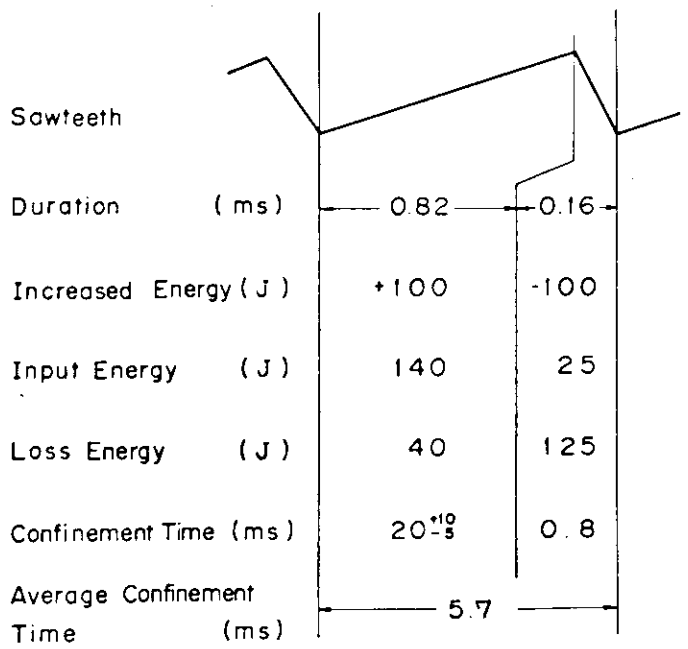

Fig. II.3-5 Energy balance in a sawtooth oscillation.

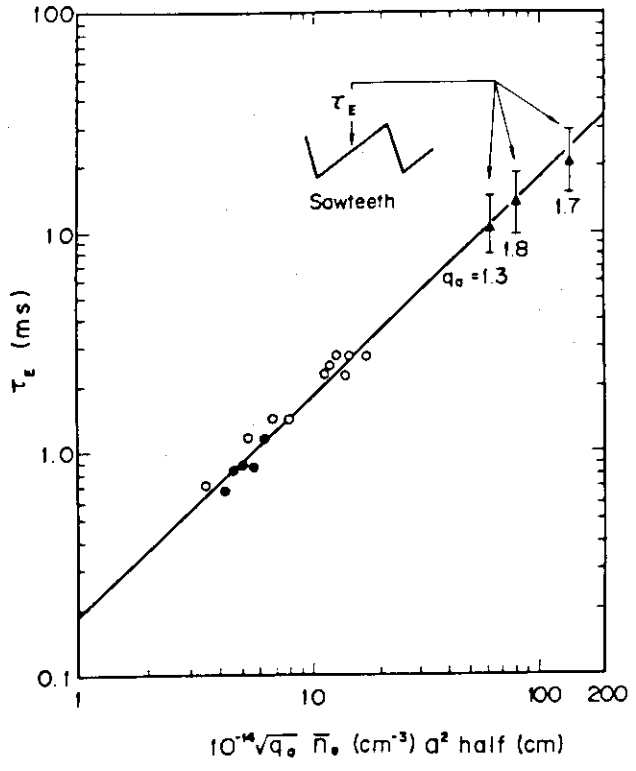

Fig. II.3-6 Energy confinement time v.s. $q_a{}^{1/2}\bar{n}_e a^2_{half}$ where a_{half} is a half radius of an electron temperature profile. q_a and $\bar{n}_e$ correspond to those shown in Fig. II.3-4.

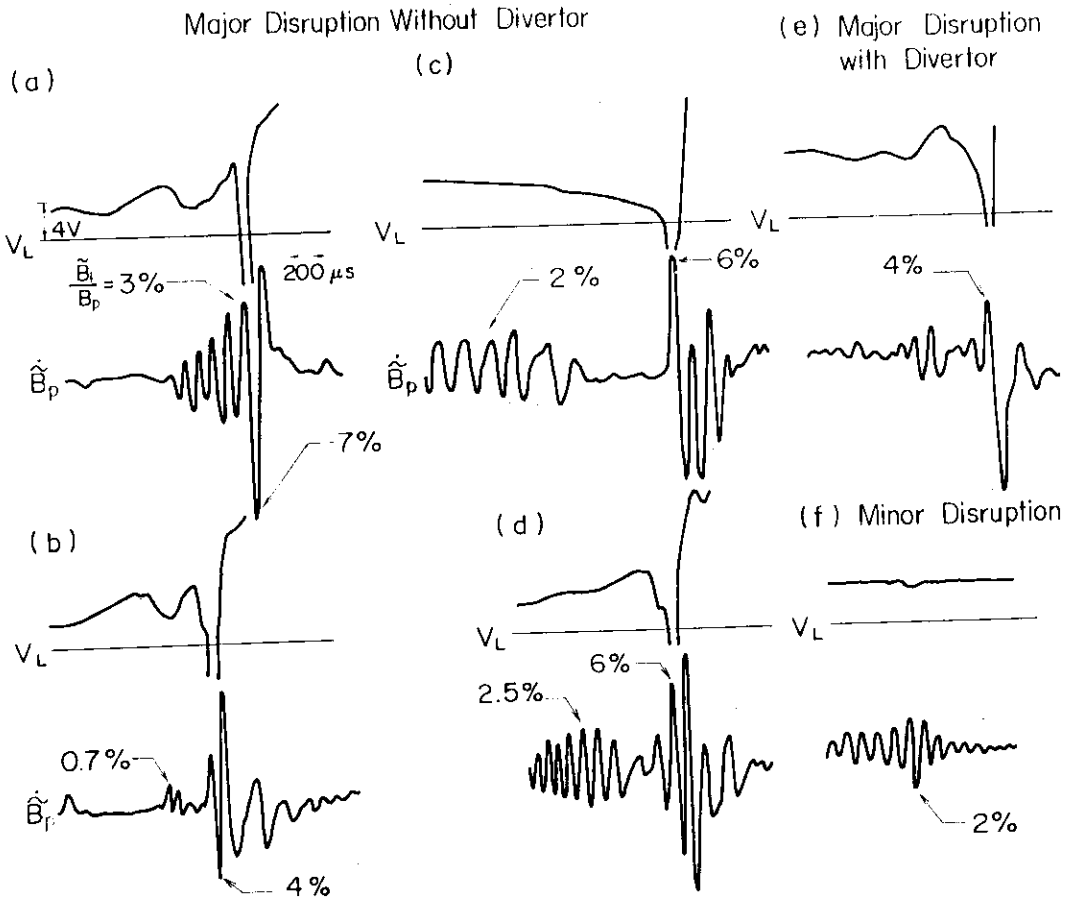

Fig. II.3-7 Examples of the loop voltages and mhd activities immediately preceding the negative voltage spike with the neon injection. Trace (a) to (d) are cases to lead the major disruption without divertor, while (e) is with the divertor. Trace (f) is an example of minor disruption without divertor.

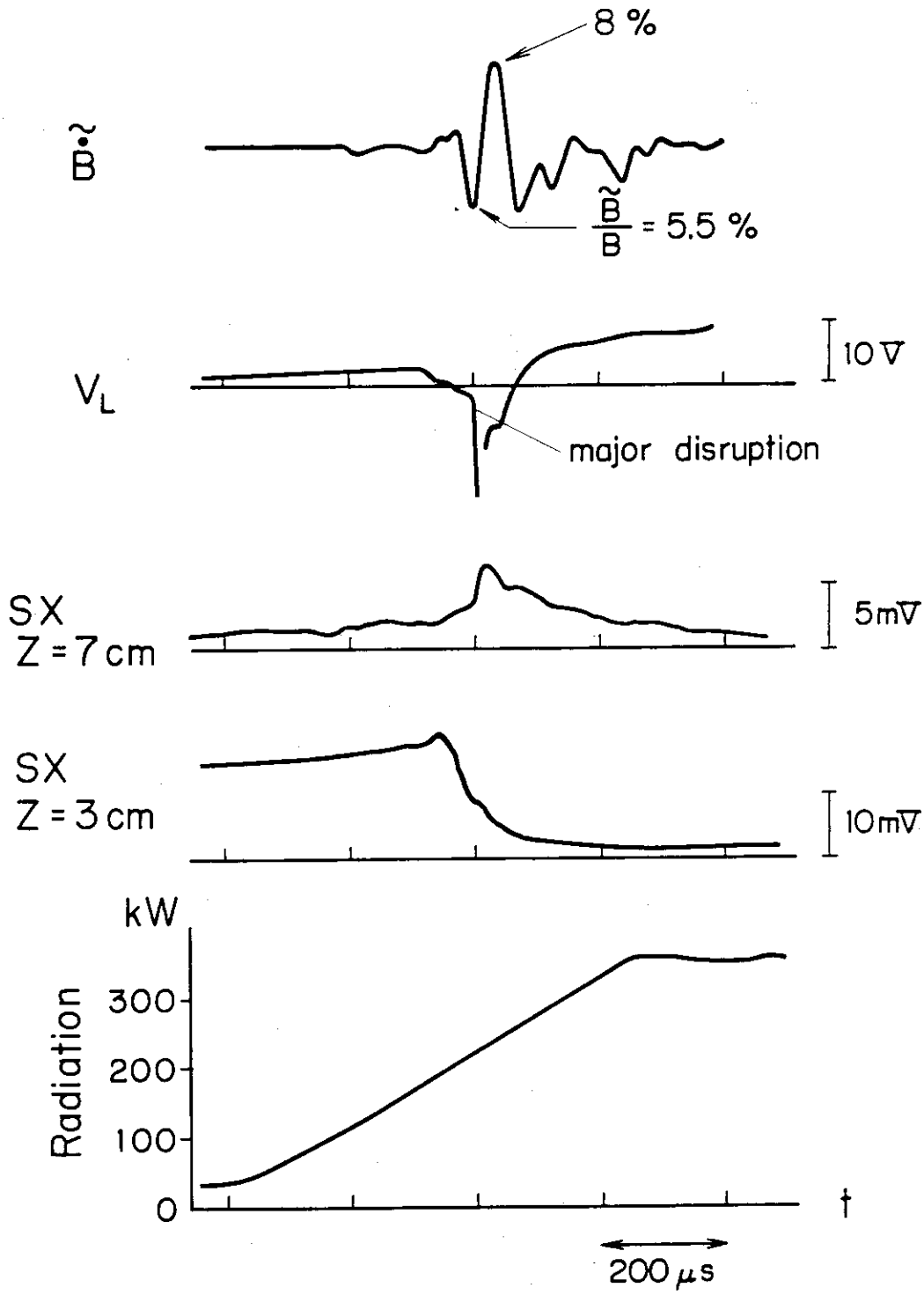

Fig. II.3-8 Evolution of mhd activity $\tilde{B}_p$, loop voltage V_L, soft X-ray signal of two different chords, and total radiation loss before and during the disruptive instability. The q=1 surface is located at about r=5 cm before the disruption.

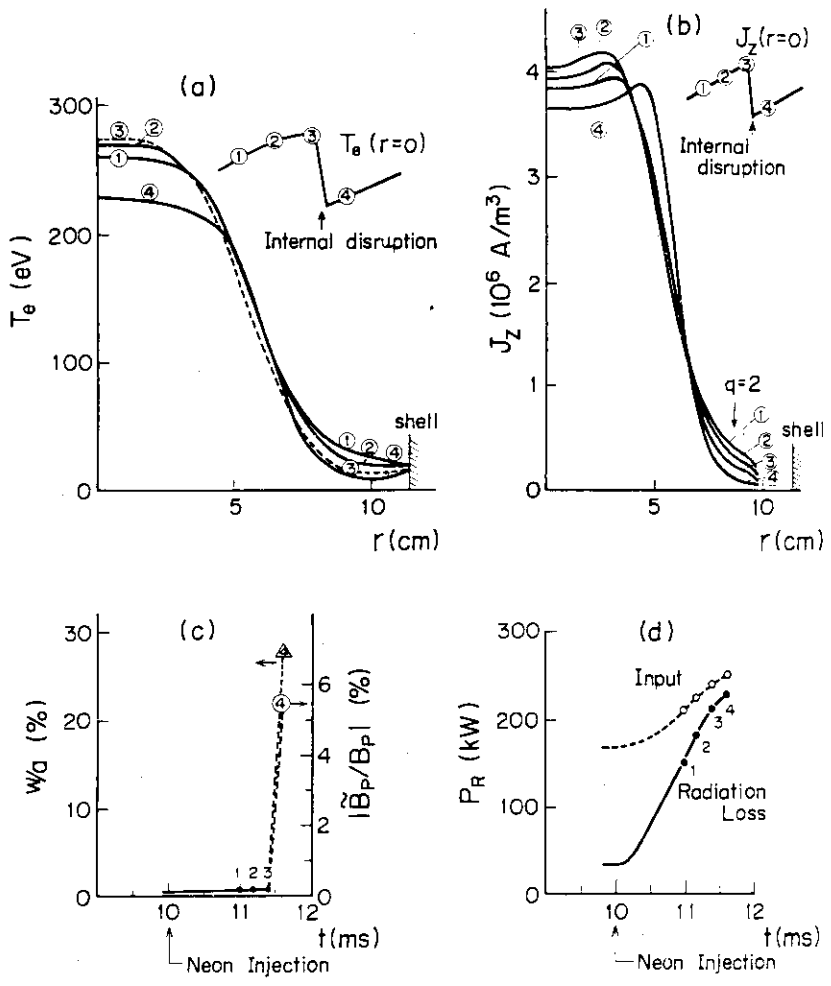

Fig. II.3-9 Results of simulation for a m=2/n=1 tearing mode using one dimensional transport code and linear helical symmetric tearing code. Increase of radiation loss due to neon injection and artificial sawtooth are included.

Fig. II.3-9(a) Time evolution of temperature profiles from the start of neon injection to the disruption, plotted at 150 μsec spacings. The initial temperature and density profiles are given from the experimental results. Time evolution of the radiation loss profile and repetition time of sawtooth oscillation (500 μs) are also given from the experimental data but other profiles are calculated by the transport code.

Fig. II.3-9(b) Corresponding time evolution of current profile;

Fig. II.3-9(c) Time evolution of current profile;

Fig. II.3-9(d) Time evolution of joule input and total radiation loss power.

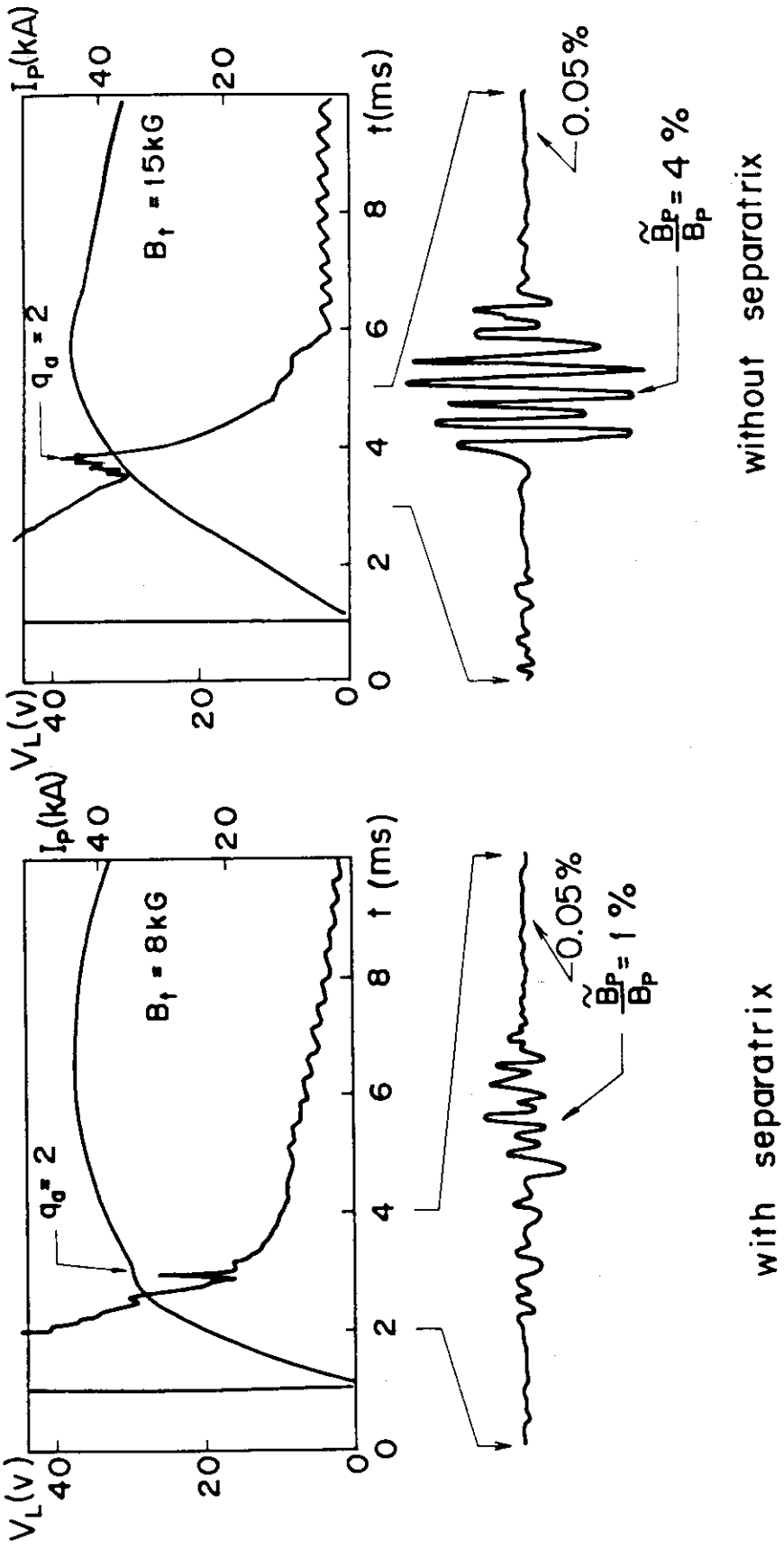

Fig. II.3-10 Oscillogram of plasma current I_p and loop voltage V_L and expanded scan of magnetic fluctuations during the current rise phase at $q_a \sim 2$ for discharges with and without separatrix. These figures show separatrix has a stabilizing effects on the kink mode.

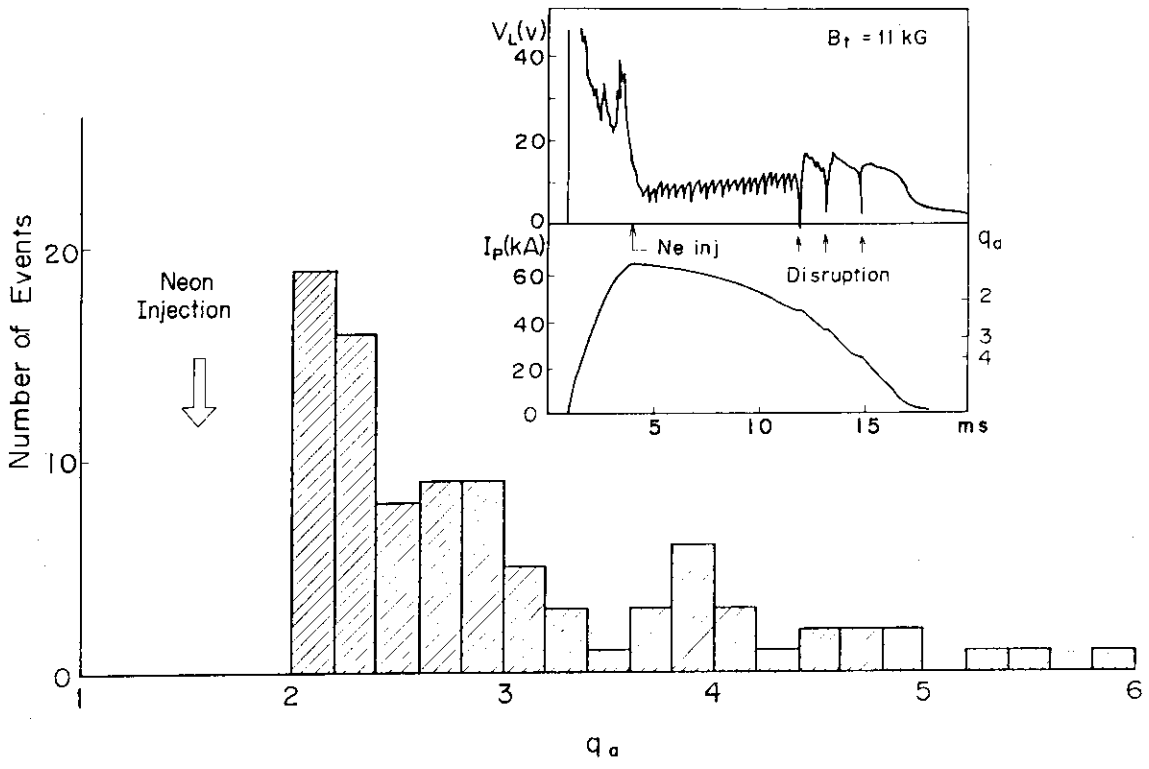

Fig. II.3-11 Neon injection into stable q_a=1.6 discharges. Major disruptions do not occur in q_a<2 region.

Fig. II.3-11(a) Time behavior of loop voltage and plasma current with neon injection at 4 ms into the stable q_a=1.6 discharge. The loop voltage increases at increasing radiation loss, and the plasma current decreases due to increasing resistivity. After the safety factor q_a becomes larger than two, the first major disruption occurs, and a series of voltage spikes appears on the loop voltage.

Fig. II.3-11(b) The number of occurrences of observed disruption at different q_a. Disruptions are frequently observed near q_a=2, but are not observed in q_a<2.

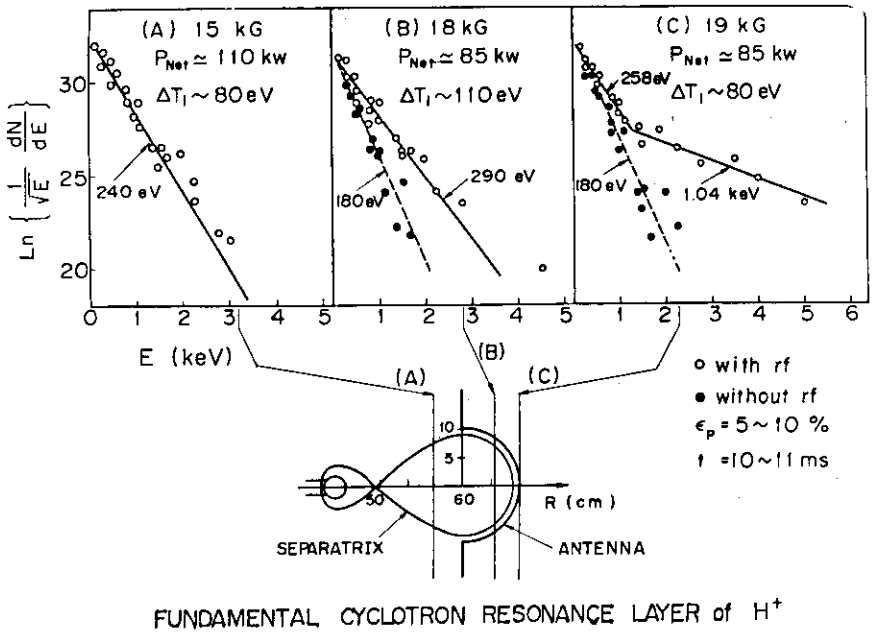

Fig. II.3-12 Charge exchange neutral spectra for different toroidal fields and corresponding fundamental cyclotron resonance layers for hydrogen. ε_p was kept to be 5∿10 %.

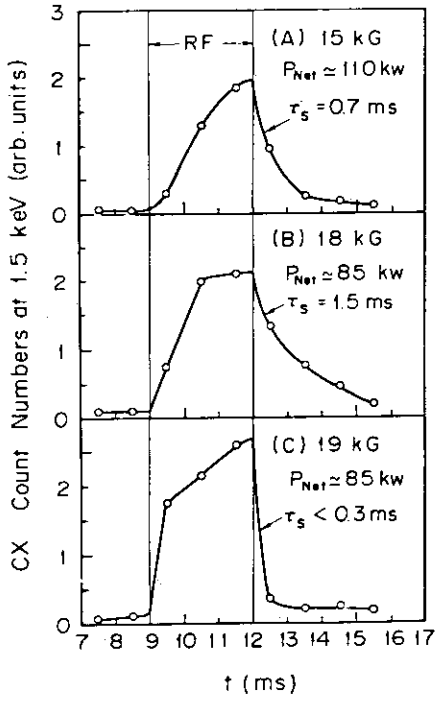

Fig. II.3-13 Temporal evolutions of count numbers of charge exchange neutrals at 1.5 KeV corresponding to the spectra shown in Fig. II.3-12.

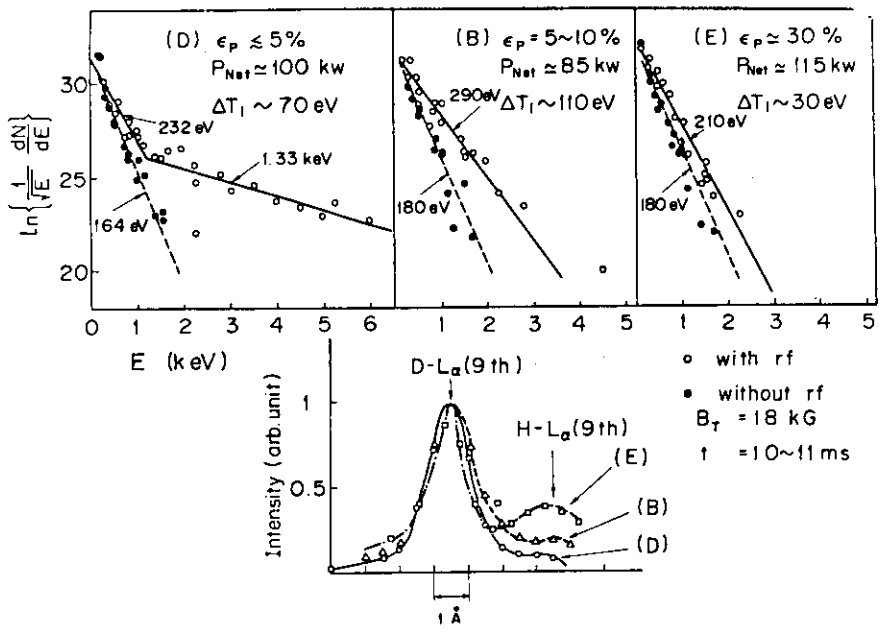

Fig. II.3-14 Charge exchange neutral spectra for different values of ε_p and corresponding profiles of L_α lines of deuterium and hydrogen. The toroidal field was fixed at 18 kG.

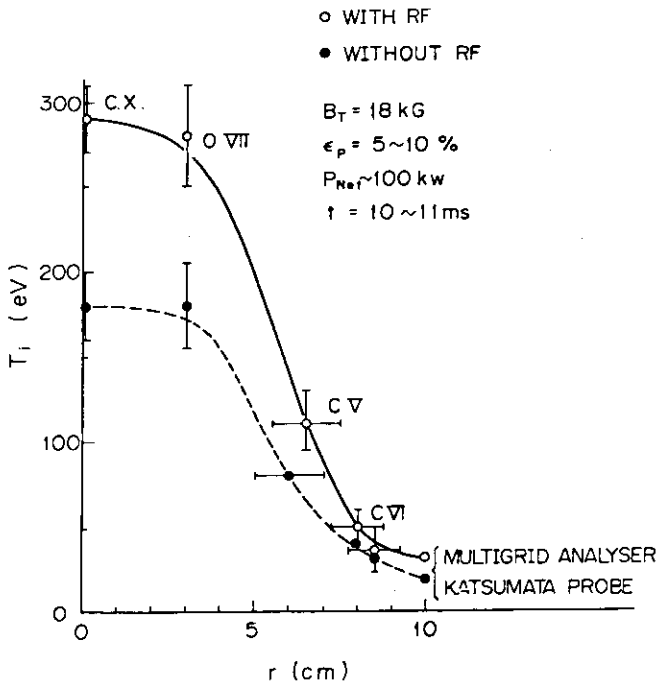

Fig. II.3-15 Radial profiles of ion temperature with and without RF power in the case of ε_p=5∿10 % and B_T=18 kG.

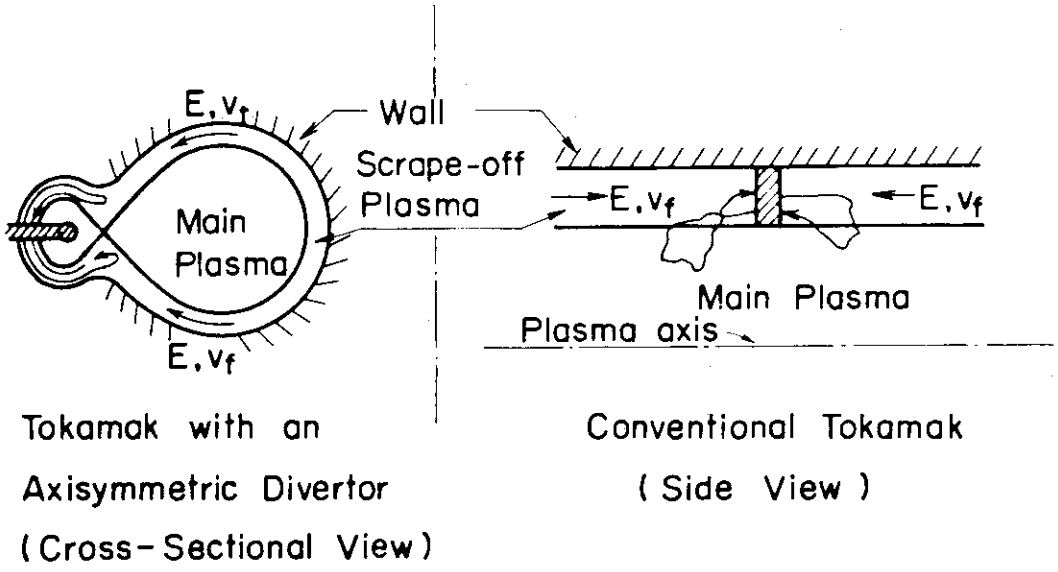

a

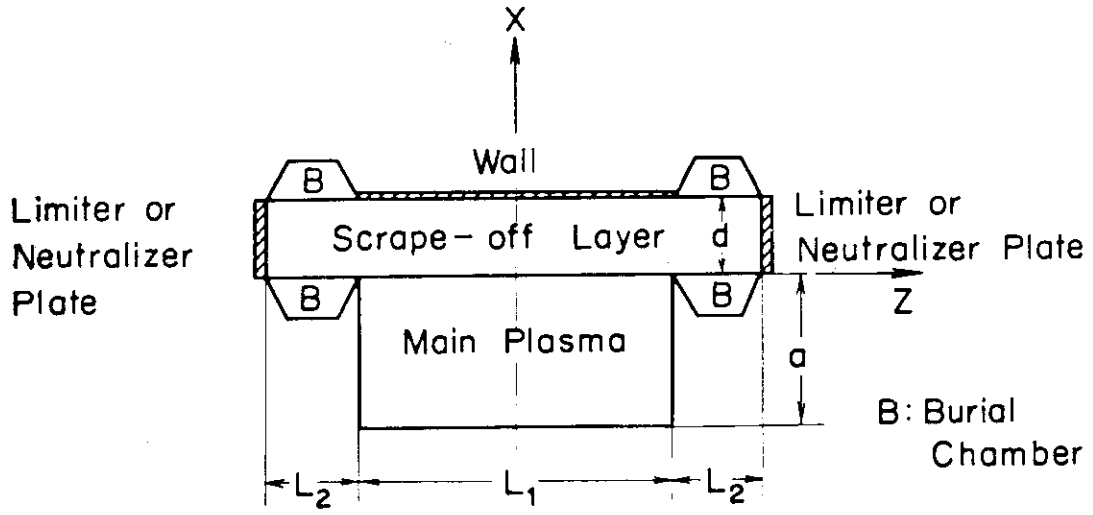

b

Fig. II.3-16 a) Plasma configurations with and without the divertor. b) Sheet model of the tokamak plasma. Ordinate is taken to be in the direction of the thickness of the sheet and abscissa in the direction of the magnetic field lines. The thickness of the scrape-off plasma is denoted by d and the main plasma by a, respectively. The length along the field line of the scrape-off plasma is $L=L_1+2L_2$ and of the main plasma is L_1.

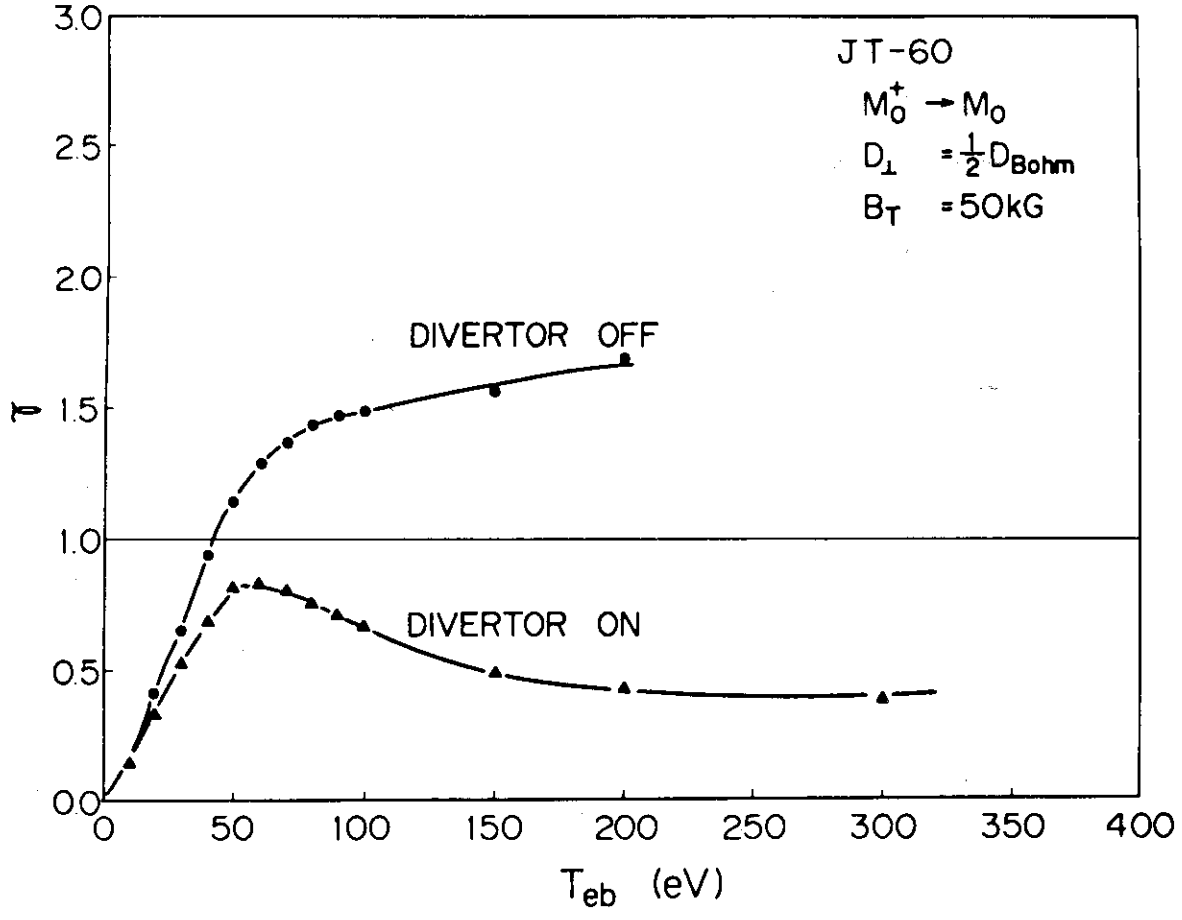

Fig. II.3-17 Growth of the number of impurity atoms due to self-sputtering for the case of divertor off and T_{eb}=50 eV. Numbers in each area indicate the number of arrived impurity ions. The total numbers of initial impurity atoms, N_I, at each generation are indicated in the squares and their sources are shown by the arrows. The number N_S denotes the number of sputtered molybdenum atoms. The growth rate of the impurity atoms, N_S/N_I, is denoted by γ.

4. Diagnostics

4.1 Pseudo-continuum radiations from gold impurity

The emission spectrum of the many lines was found to be just like a continuum spectrum in the region of 42 to 200 Å[1] in the DIVA hydrogen plasma under the experimental condition with a toroidal magnetic field of 20 kG and a plasma current of 40 kA and with a divertor. In this plasma, the central electron and ion temperatures were 700 and 270 eV, respectively, and the central electron density was 8.2×10^{13} cm^{-3}. The Joule input power of the plasma was 140 kW.

We describe here the time-resolved spatial distribution of the pseudo-continuum radiation and the time-evolution of the radiation power.

Figure II.4-1 shows the time-resolved spatial distributions of the power density of the pseudo-continuum radiation at 175 and 60 Å. During the early phase, where the central electron temperature (T_{eo}) is less than 200 - 300 eV, the spatial distribution of the radiation at 175 Å indicates a broadened profile at 4 msec, with a small central deposition developing at 5 msec, as shown in Fig. II.4-1(a). The spectrum distributed in the region from 120 to 240 Å. As the electron temperature increases in time, emission of the pseudo-continuum spectrum above 120 Å is intensified, and simultaneously the spectrum extended towards a shorter-wavelength region. For T_{eo} above 400 - 500 eV (after 6 msec), the spatial distribution of the 175 Å radiation power density became hollow as shown in Fig. II.4-1(a). After 8 msec, where T_{eo} was higher than 600 eV, the emission of pseudo-continuum was distinctly found in the region below 110 Å, in addition to that in the region of 120 - 200 Å. The radiation power at 60 Å peaked in the central region of the plasma as shown in Fig. II.4-1(b), while the power at 175 Å was increased in the intermediate region. In Fig. II.4-2, the solid curves show the distributions of the radiation power density per unit wavelength at 10 msec measured for four typical wavelengths, i.e. at 60, 98, 150 and 175 Å. The electron temperature and density distributions are shown in the inset of the figure. The broken curve shows the spatial distribution of the total (integrated) radiation power density emitted in the 120 - 200 Å region. The power density was found to be peaked at 4 - 5 cm, where the electron temperature was 200 - 300 eV. The spatial distribution of the radiation power density in the 42 - 110 Å region is indicated by a dotted curve, with the power loss peaked near the plasma center. The dot-and-

dashed curve shows the distribution of the total radiated power density in the 42 - 200 Å region.

Figure II.4-3 shows the radiation power measured at times from 4 to 14 msec. The solid line represents the total power radiated from highly ionized gold ions. The dot-and-dashed curve shows the time-evolution of the line radiation power due to low-Z impurities (oxygen and carbon). The radiation power due to low-Z impurities in DIVA plasma had been reported in detail in ref. 2. The radiation power due to the pseudo-continuum (42 - 200 Å) corresponded to 40 - 50 % at 5 - 10 msec and to approximately 70 % at 14 msec of the total (low-Z and high-Z impurity) radiation power loss from the plasma volume, respectively. From the figure, the radiation power due to low-Z impurities was found to increase linearly up to 10 msec with an increase of the electron density and was saturated at a value of 30 - 35 kW at 10 - 11 msec. Subsequently, the radiation power showed a tendency to decrease. While the power due to the low-Z impurities was decreasing, the power radiated from the gold impurities continued to rise with a gradient steeper than the gold impurity or the low-Z impurity radiation power before 10 msec. Dotted and broken curves in Fig. II.4-3 show the time-evolutions of the radiation power in the 42 - 110 Å region and in the 120 - 200 Å region, respectively. The latter increased with a time-evolution similar to that of the total power due to the pseudo-continuum (42 - 200 Å). On the other hand, the former increased slowly and appeared to saturate at a level of 10 kW at 12 - 14 msec. If we compare these power losses in the two separated wavelength regions, we see that the power loss in the 120 - 200 Å region is dominant during the whole discharge and is several times larger than that in the 42 - 110 Å region. Since the radiation in the 120 - 200 Å region concentrated in the intermediate region, the radiation cooled more strongly the intermediate region than the central region of DIVA plasma.

The observed increase in the emission of the pseudo-continuum after 10 msec was coming from an enhancement of gold influx into the plasma from the gold protection plates and/or the shell surface. The most plausible explanation of the enhanced gold influx was considered to be sputtering by multi-charged impurity ions[3]. Very frequently, the DIVA plasma was disruptive after about 14 msec. The plasma disruption may be caused by the emission of the pseudo-continuum due to increased gold impurities, which play an important role in excess cooling of the intermediate plasma column region in the DIVA tokamak.

4.2 Effect of titanium coated wall on metal impurity emission

We studied metal impurity emissions in the JFT-2 hydrogen plasma with and without titanium coating.

Figure II.4-4[4] shows characteristics of discharges under the toroidal magnetic field of 17 kG and a minor radius of the plasma of 20 cm. The discharge without titanium coating as shown in Fig. II.4-4(a) was obtained in the JFT-2 device without titanium gettering on the wall. The discharge with titanium coating in Fig. II.4-4(b) was obtained after the OVI(λ1031.95 Å) line intensity was saturated to a lower value by gettering titanium on the part of the torus wall near limiters. In both cases, the plasma current I_p and the line-average electron density $\bar{n}_e$ were 110 kA and about 1.3×10^{13} cm^{-3} during a current flat top phase. Figure II.4-4(c) shows measured electron temperature at 70 msec in discharges with (open circles) and without (full circles) titanium coating. Solid and dotted lines indicate curves fitting to experimental values.

On the discharge in Fig. II.4-4(a), a dominant impurity was oxygen and the content was about 12 % of the line-average electron density. The effective ionic charge Z_{eff} is about 6 as we estimated from population density of oxygen ions, whose value could explain the plasma conductivity. On the other hand, the concentration of molybdenum, which was material of limiters, was about 2.5×10^9 cm^{-3}, being less than 0.1 % of the line-average electron density. The iron concentration was smaller than or at most comparable to the molybdenum one. In the discharge, the pseudo-continuum spectrum (solid curve) was obtained in the wavelength region from 65 to 120 Å as shown in Fig. II.4-5. The emission peaks strongly at 72 Å. Most of the pseudo-continuum emission may be due to highly ionized ions of molybdenum. The total radiation power due to this continuum spectrum was at most 1 kW in the quasi-steady state.

On the discharge with titanium coating in Fig. II.4-4(b), line intensities of the OVI(λ1031.95 Å), MoXIII(λ341 Å) and FeXV(λ284 Å) decreased to a considerably lower level, i.e. to about 1/10. The oxygen concentration was decreased to 1 - 2 % of the line-average electron density. Also, the molybdenum and iron concentrations diminished by a factor of 10 to 20. The concentration of titanium (a new additional impurity) was less than 10^8 - 10^9 cm^{-3}, which was estimated from intensities of TiXIV(λ=122 Å, I.P.=861 eV) and TiXI(λ=386 Å, I.P.=265 eV) lines. Thus the titanium contamination in the plasma was concluded to

be very low. In this discharge, the effective ionic charge was about 2 and still governed by the oxygen impurity. Intensity of the pseudo-continuum radiation was decreased to approximately 1/16 of that without titanium coating.

With titanium coating, there was correlation between the reduction of the pseudo-continuum emission and molybdenum and oxygen contents. The correlation may be explained by the sputtering process between oxygen and molybdenum impurities. By gettering titanium, the amount of the sputtered particles (oxygen) were reduced and consequently the molybdenum content and the pseudo-continuum emission were suppressed to a lower level. Recent experiments on the JFT-2 tokamak have confirmed from measurements on temperatures of the limiter surface and the scrape-off plasma in addition to spectroscopic measurements that the predominant mechanism introducing the metal impurities into the plasma is the sputtering by light impurities, and that the self-sputtering by the metal impurity and the thermal evaporation are not to play an important role[5].

4.3 Measurements of increases in ion temperatures during RF heating

Ion temperature in the RF heating experiments was measured by energy spectra of charge-exchanged atoms and Doppler broadening of impurity-ion lines (OVII, CV and CIV). Ion heating is studied on Lower hybrid heating (LHH) in JFT-2 (see Section II.2) and ion cyclotron range of frequencies (ICRF) in DIVA (see Section II.3).

In LHH of JFT-2 experiments, the measurements of charge-exchanged neutrals were performed perpendicularly to the toroidal magnetic field. The obtained charge-exchange spectrum and time variation of perpendicular bulk ion temperature ($T_{\perp bulk}$) are shown in Fig. II.4-6, where the operational conditions are also indicated. The application of the lower hybrid wave yields the higher component ($E \geq 2$ keV) of protons, as shown in the figure. The value of $T_{\perp bulk}$ was determined from the spectrum in the energy range of 0.6 to 2 keV. A series of the JFT-2 LHH experiments[6,7] has shown that $T_{\perp bulk}$ increases linearly with input power, and that the heating efficiency of ion temperature is approximately 1 eV/kW.

In the ICRF experiments on DIVA, the charge-exchanged atoms and Doppler broadening of OVII(1623 Å), CV(2271 Å) and CIV(1548 Å) lines were measured during the RF heating[8]. The typical time variations of ion temperature obtained by these two methods are shown Fig. II.4-7(a) and

(b). The operational conditions are also given in the figure. The radial distributions of ion temperature are shown in Fig. II.4-8 with and without the RF wave. This figure shows that the ion temperature is increased over the wide plasma volume and that an increment of central temperature is 250 eV for the RF input power of 150-180 kW.

4.4 Impurity blow-off technique by means of a laser beam

In order to get a clear evidence about impurity behaviors in tokamak plasmas, the blow-off techniques is quite useful[9]. We describe the experimental arrangement and the experimental results obtained from the blow-off techniques[10,11] applied to the DIVA plasma. The injected metal is aluminium or gold. The metal (Al or gold) film with nearly 0.2 μm in thickness is adsorbed on a pyrex glass plate, on which a Q-switched ruby laser beam is irradiated. The metal film irradiated by laser beam is shown in Fig. II.4-9. Metal materials adsorbed on a circular glass plate are the aluminium at the outside and the gold at the inside. As shown in Fig. II.4-10, a parallel beam from the Q-switched ruby oscillator (the typical operationing power density $\sim$100 MW/cm^2) is irradiated upon the metal surface after passing through prisms and an aperture. It is possible to inject the metal impurity more than five hundreds shots for the laser beam diameter of 2 mm by using the present blow-off method. As the vaporized metal is weakly ionized, the velocity of the injected metal is determined from the measurement of ion velocity of the weakly ionized gas with two double probes separated with the distance of 15 mm, since gas velocity is nearly equal to the ion velocity within about a factor of two. Ion saturation currents of the ionized aluminium measured with the probes are shown in Fig. II.4-11. The aluminium ion velocity calculated from the measurement of the time of flight between those probes becomes, $V_{Al} = 5.2 \times 10^5$ cm/sec, when the laser power density of 84 MW/cm^2 is irradiated upon the aluminium surface.

Experimental results for the DIVA plasma with a total electron density Ne = (3-4) $\times 10^{18}$ and loop voltage V_L = 4-5 V are shown in the following. Total number of aluminium ($N_{Al} = 8 \times 10^{16}$) is injected at the time of 7 msec after the discharge breakdown as shown in Fig. II.4-11, where the loop voltage has risen by several percents within the time from 7 to 10 msec. The increment of an average electron density $\bar{n}_e$ measured with a microwave interferometer is approximately 8 percents. A typical

time-evolution of the AlXI 550 Å spectral line is shown in Fig. II.4-13. The present blow-off system has found to be very reliable, because of the reproducibility of the injected metal line signal[12,13].

The injected-metal flux of vaporized-metal expansion is given by

$$F(x,r,t) = n_s \cdot d \cdot (1-\exp(-(V/x)\cdot t)) \cdot (S_1/S_3)$$

$$S_1/S_3 = (1 + x\cdot\theta/r_o)^{-2}, \quad r = x\cdot\theta + r_o \qquad (1)$$

where, n_s metal density on the pyrex plate, d foil thickness, V vapor velocity, x distance measured from the metal foil, r radius of expanding vapor at the distance of x, t time elapsed from the incidence of laser beam, r_o radius of laser beam irradiated on the metal surface, θ a half angle of divergence at a half maximum of vapor profile, S_1 area of evaporation and S_3 area of expanding vapor at the distance of x. The experimental result agrees within a factor of two with the calculation as shown in Fig. II.4-14.

References

1) Kasai, S., Funahashi, A., Nagami, M., and Sugie, T.: Nucl. Fusion 19 (1979) 195.
2) Kasai, S., Funahashi, A., Nagami, M., Sugie, T., and Yamauchi, T.: J. Phys. Soc. Japan 46 (1978) 3277.
3) Shimomura, Y.: Nucl. Fusion : 17 (1977) 1377.
4) Konoshima, S., et al.: J. Nucl. Materials 76 & 77 (1978) 581.
5) Suzuki, N., et al.: Submitted to 9th Europ. Conf. on Controlled Fusion and Plasma Physics.
6) Nagashima, T. and Fujisawa, N.: Joint Varenna-Grenoble International Symposium on Heating in Toroidal Plasma (1978).
7) Fujii, T., et al.: 7th International Conference on Plasma Physics and Controlled Nuclear Fusion Research in Innsbruck, Austria from 23 to 30 August 1978 IAEA-CN-A-4-2.
8) Kimura, H., et al.: to be published in Nuclear Fusion.
9) Marmap, E.S., Cecchi, T.L. and Cohen, S.A.: P.P.L. MATT-1138 (1975).
10) Yamauchi, T., Okuda, T. and Ishikawa, N.: Electr. Eng. Jpn. 95 (1975) 15.
11) Yamauchi, T., Asano, C., Kobayashi, T. and Okuda, T.: Electr. Eng. Jpn. 99A-8 (1979) 41.

12) Nagami, M., Shimimura, Y., Maeda, H., Kasai, S., Yamauchi, T. and et al.: Nucl. Fusion 9 (1978) 1347.

13) Kasai, S., Funahashi, A., Nagami, M., Sugie, T. and Yamauchi, T.: J. Phys. Soc. Japan 46 (1979) 241.

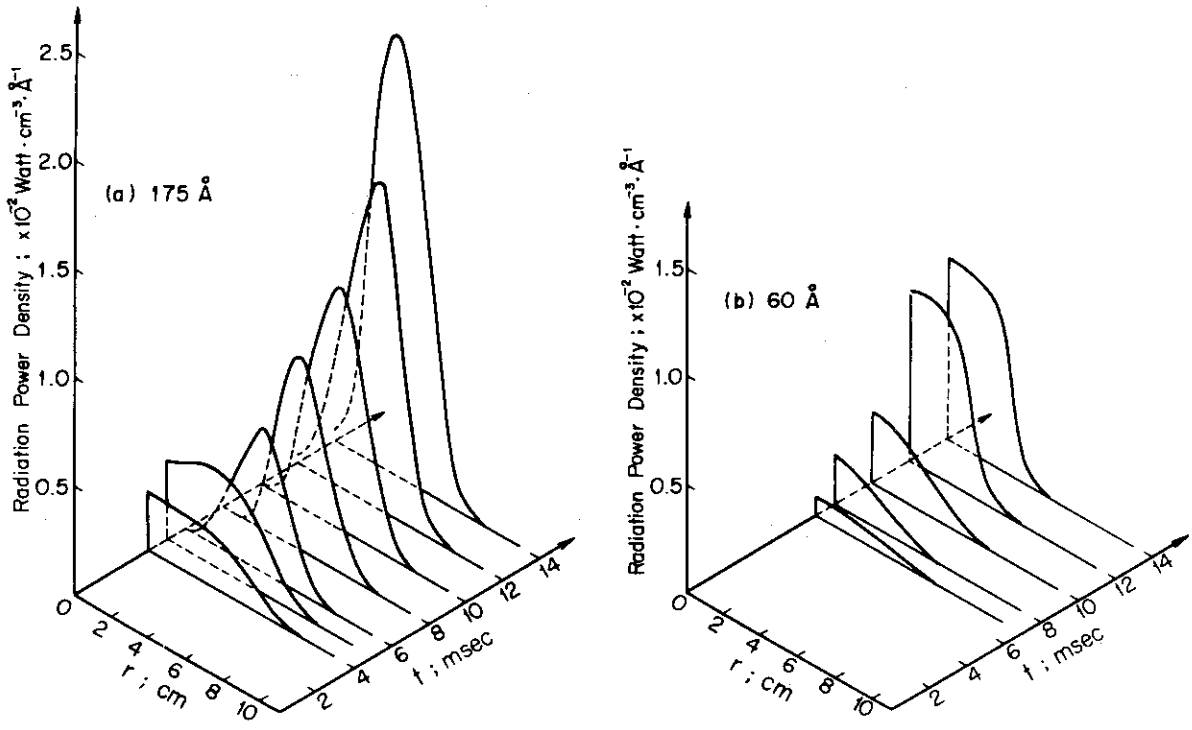

Fig. II.4-1 Time-resolved spatial distributions of radiation power density per unit wavelength of the pseudo-continuum at (a) 175 Å and (b) 60 Å.

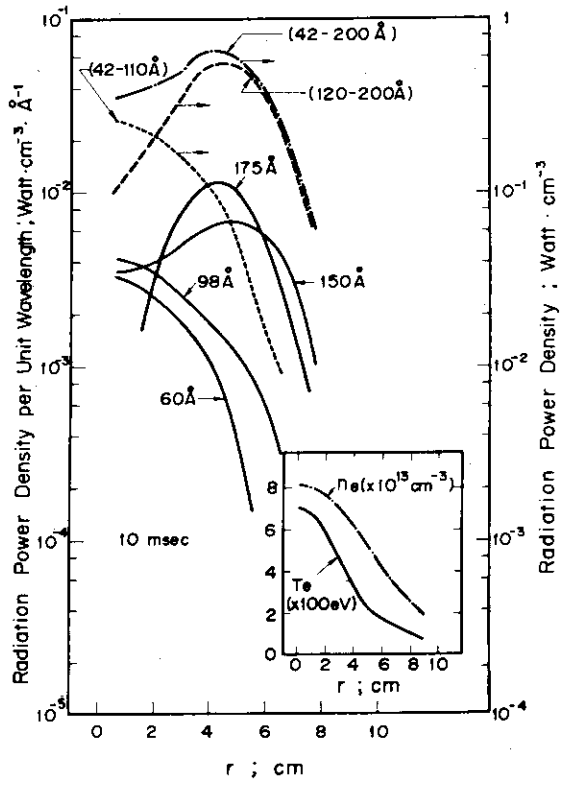

Fig. II.4-2 Spatial distributions of radiation power density per unit wavelength for pseudo-continuum at 60, 98, 150 and 175 Å (solid curves) at 10 msec. Spatial distributions of radiation power density for pseudo-continuum in 42 - 110 Å (dotted curve), 120 - 200 Å (broken curve) and 42 - 200 Å (dot-and-dashed curve) regions.

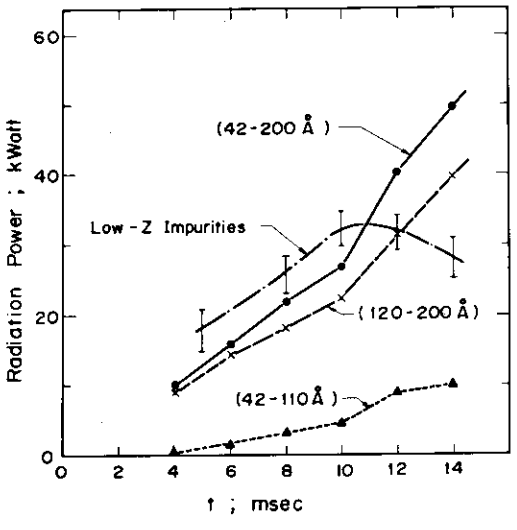

Fig. II.4-3 Time-evolutions of radiation power due to pseudo-continuum in 42 - 200 Å (solid curve), 42 - 110 Å (dotted curve) and 120 - 200 Å (broken curve) regions, and due to low-Z impurities (dot-and-dashed curve).

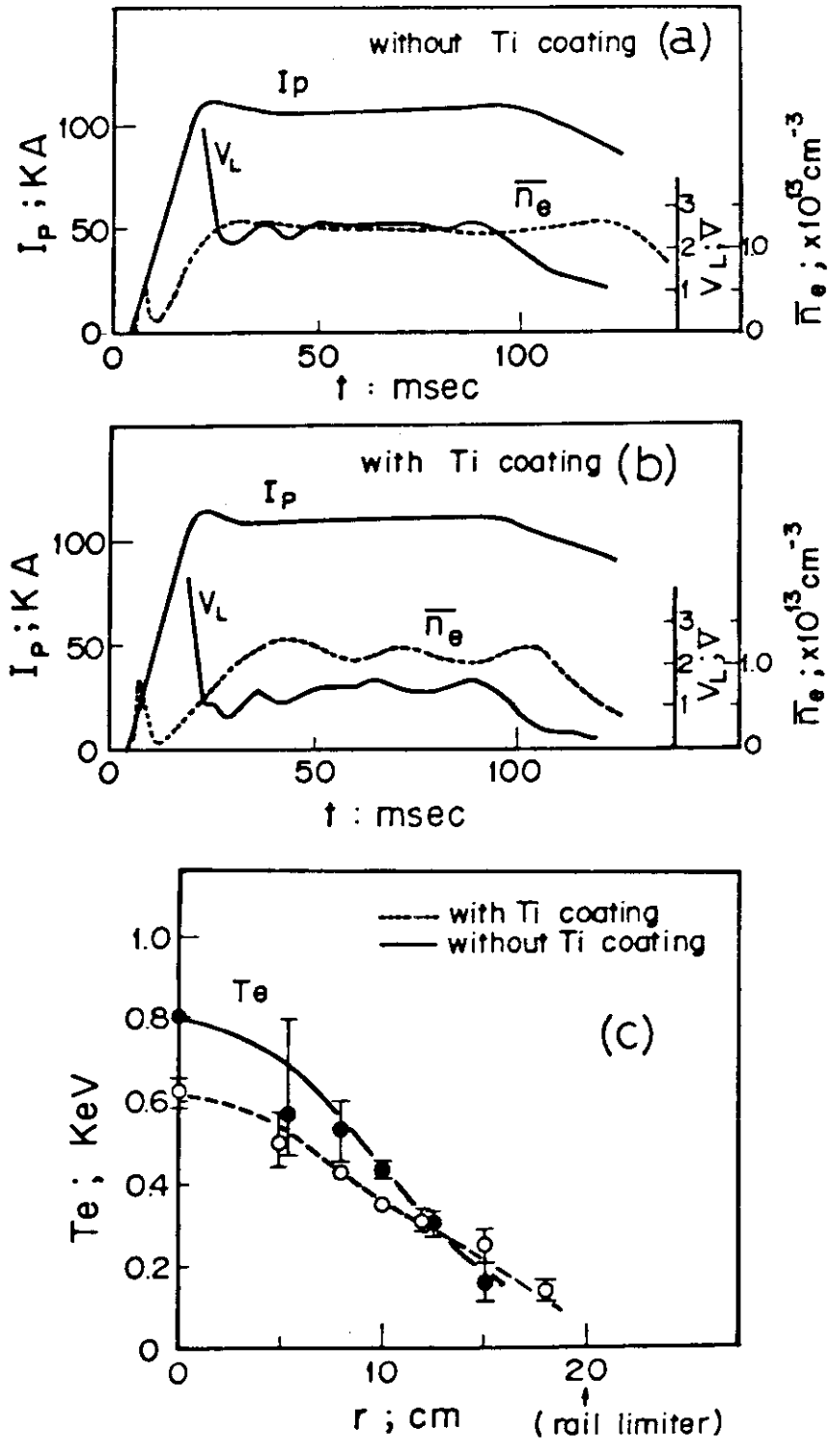

Fig. II.4-4 Characteristics of the hydrogen discharge without titanium coating (a), with titanium coating (b) and the radial distributions of the electron temperature at 70 msec with and without titanium coating (c)[4].

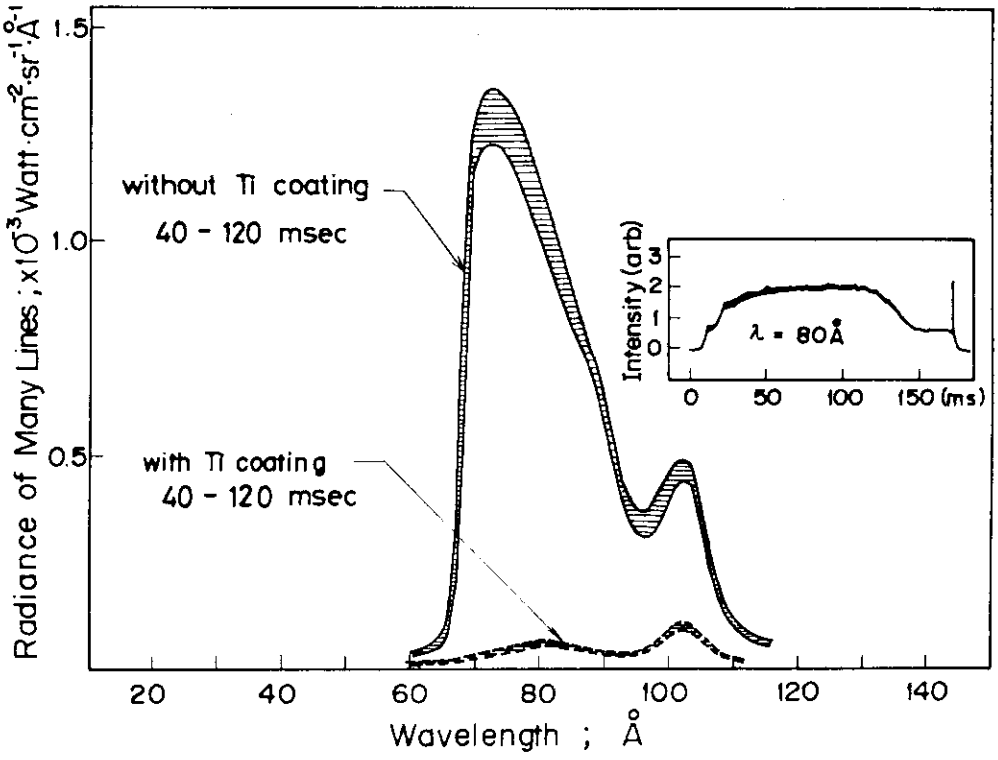

Fig. II.4-5 Radiation of the pseudo-continuum emission on the JFT-2 plasma by titanium coating.

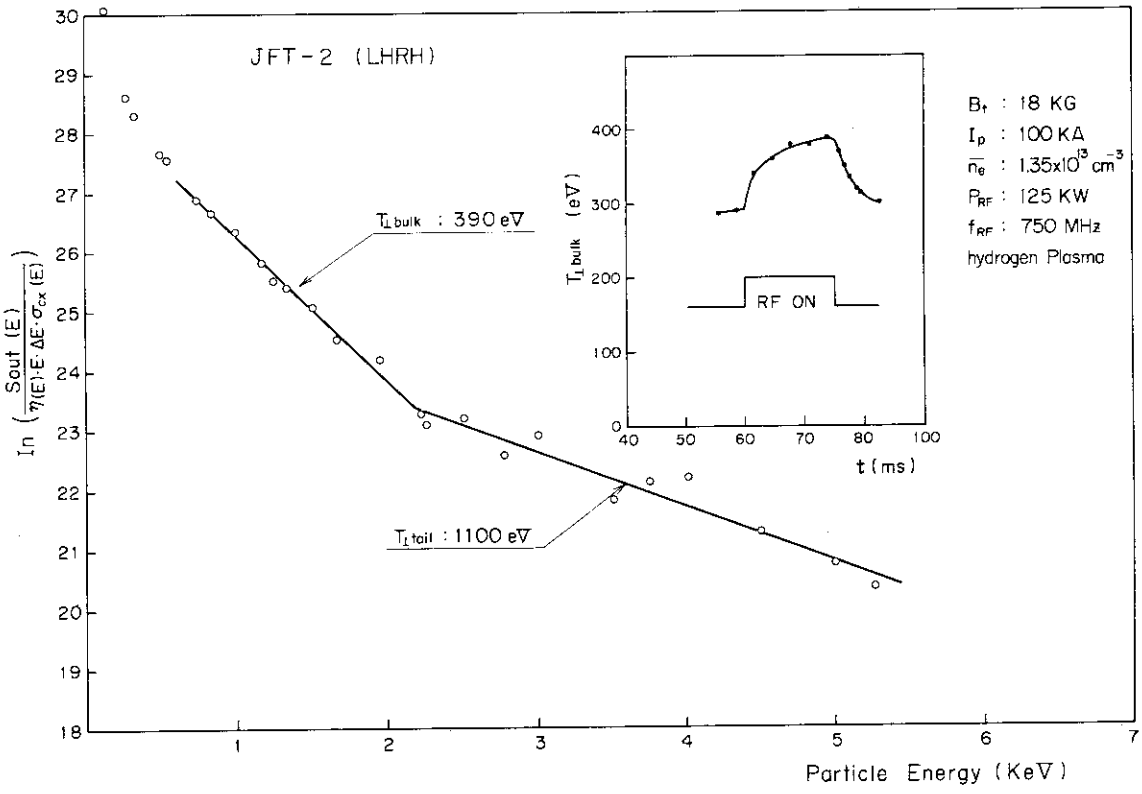

Fig. II.4-6 Measured energy spectrum of charge-exchange neutrals and the time variation of bulk ion temperature ($T_{\perp bulk}$) on the JFT-2 lower hybrid resonance heating.

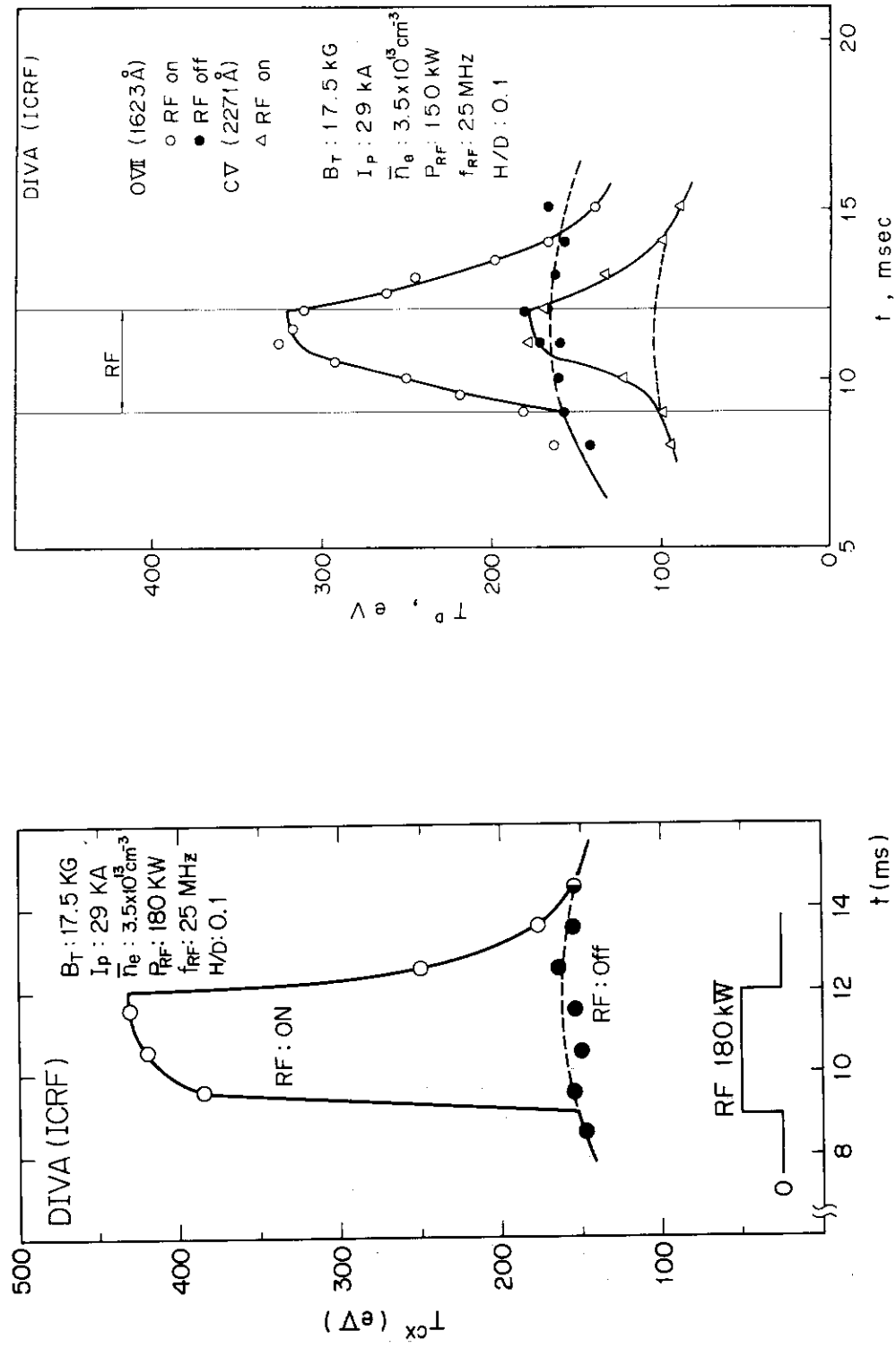

Fig. II.4-7 Time-variation of ion temperature obtained from the charge-exchange spectrum (a) on the DIVA and from Doppler broadenings of impurity lines (b) on the DIVA ion cyclotron resonance heating.

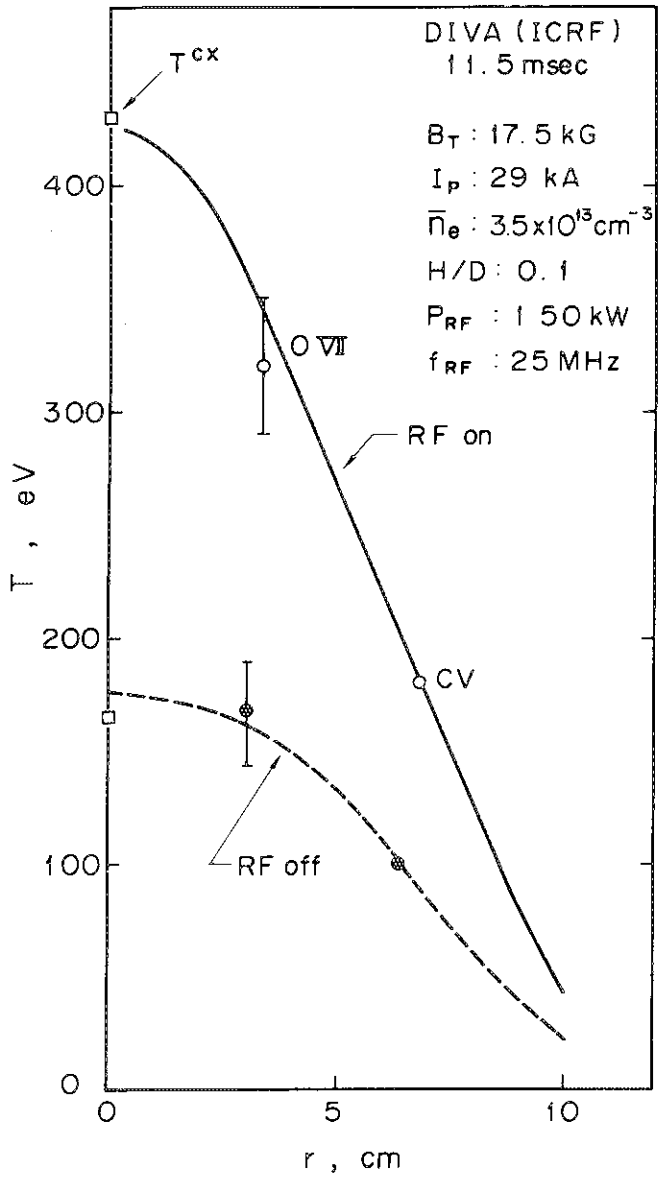

Fig. II.4-8 Radial distributions of ion temperature with and without the ICRF wave in DIVA.

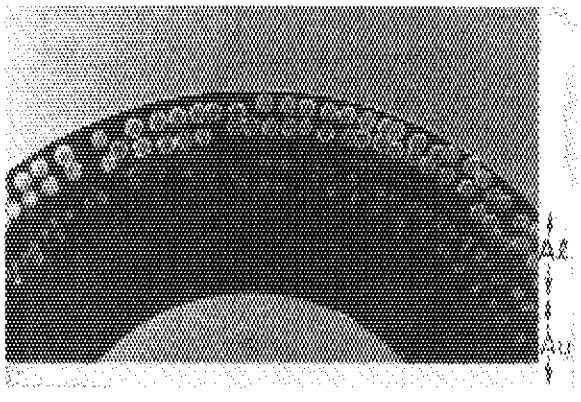

Fig. II.4-9 Photograph of a metal-absorbed pyrex plate after the irradiation of 2 or 1 mm laser beam.

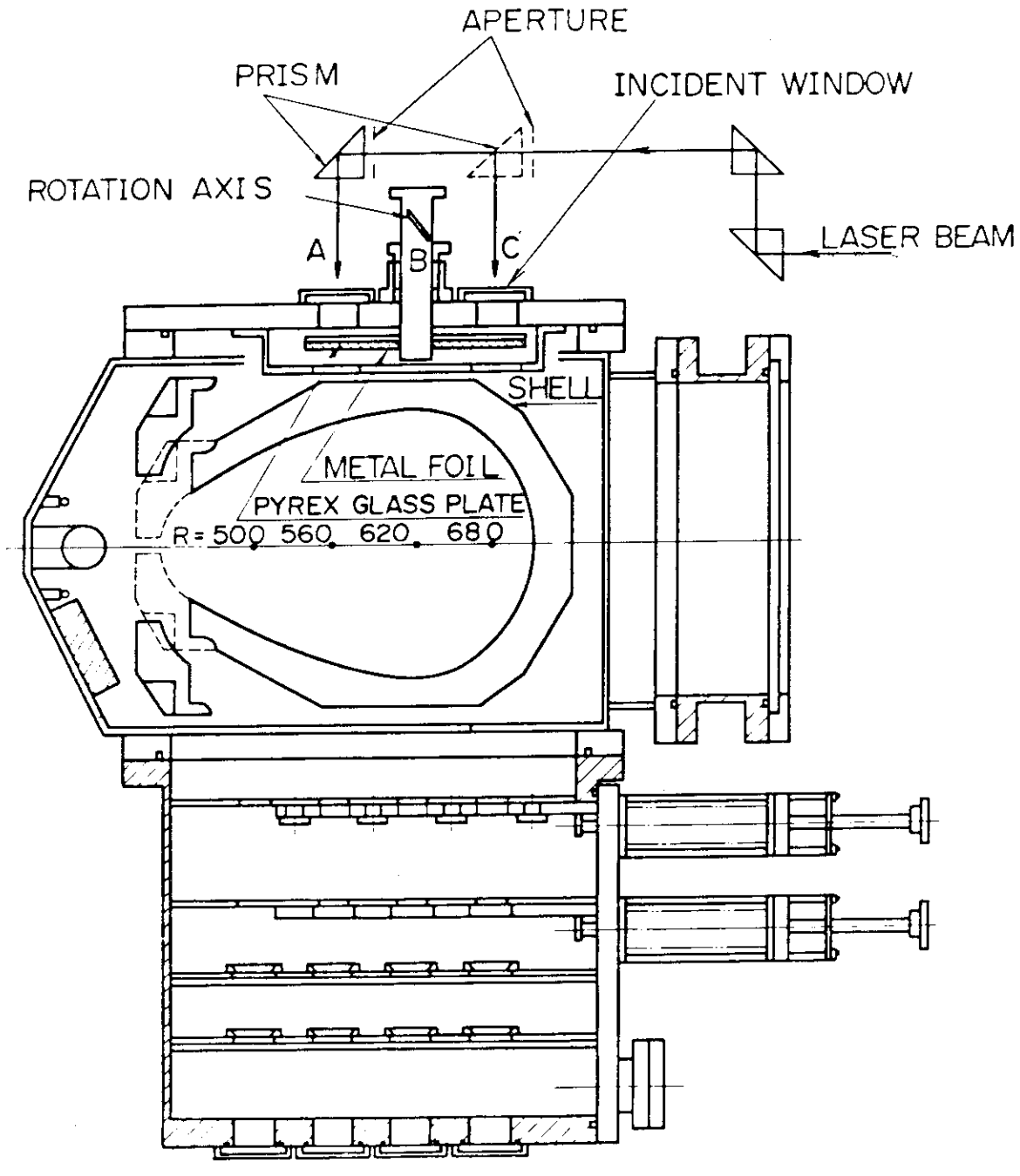

Fig. II.4-10 Blow-off arrangement used in DIVA.

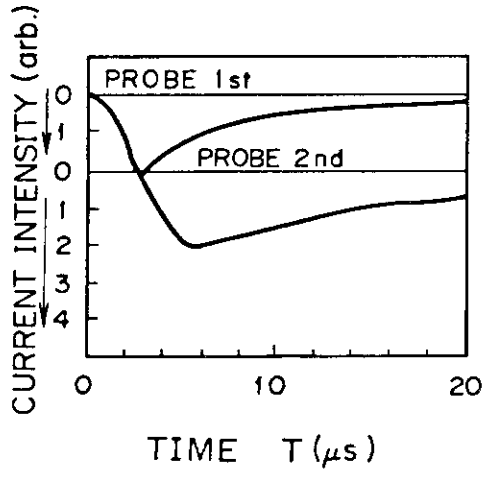

Fig. II.4-11 Ion saturation currents of aluminium ionized gas measured with two double probes.

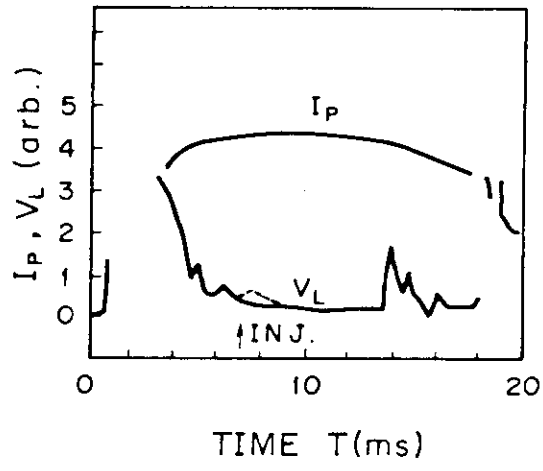

Fig.II.4-12 Loop voltage with the aluminium metal injection (dotted line) and without injection (solid line). The plasma current I_p did not change for with and without injection.

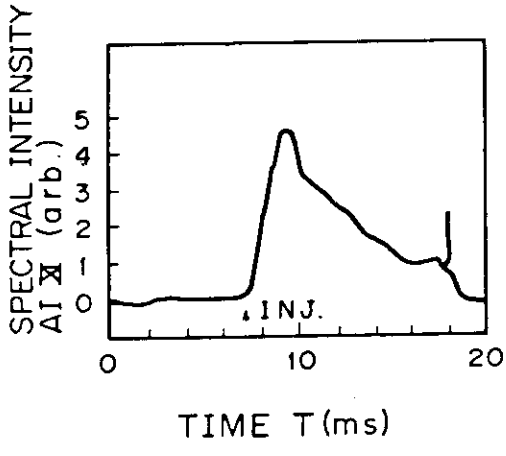

Fig. II.4-13 Time-evolution of the AlXI 550 Å line.

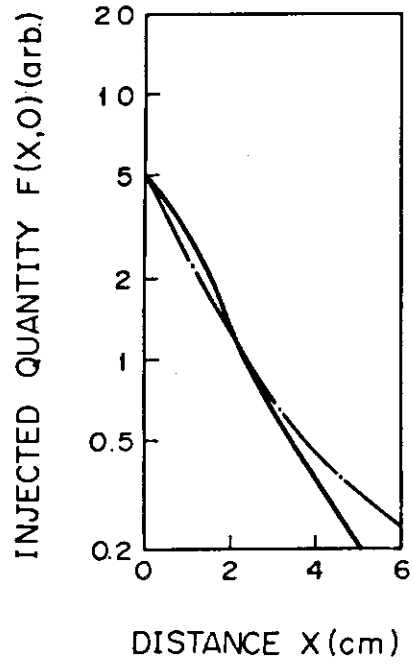

Fig.II.4-14 Amount of injected aluminium measured on the condition of r=0 and t=∞ (solid line: observed value, dot-dash line: theoretical value).

5. Design Study of JFT-2M

5.1 Introduction

Major concern in designing a new machine is to start the experiments on a high beta tokamak in Japan as soon as possible. Therefore, it is assumed that both hard and soft wares established in JFT-2 and JFT-2a/DIVA are transferred to JFT-2M. Another crucial viewpoint is a balanced consideration of physical benefits and the limit imposed by prudent engineering criteria, that is, the desire for simplicity and flexibility may be given considerable weight in keeping utility of medium size high beta tokamak among future research on nuclear fusion.

Taking into account the two factors mentioned above and the objectives of this program are;

(1) to investigate the physical and technical problems on noncircular high beta tokamak as a complementary part of D shape program in Doublet-III,

(2) to make experimental study of optimized supplementary heating including profile control and current sustain by RF heating and to study the first wall material in the reactor level thermal load,

(3) to investigate some of items important in reactor engineering, that is, fueling, long pulse operation and so on.

We have made a choice on the minimum machine size and plasma parameters for reference. The results are shown in Table II.5-1 and II.5-2. The values in the parentheses are the maximum values after upgrading the power supplies in phase II.

In addition, JFT-2M will be operated for numerous technology and instrumentation developments which directly support the JT-60 research program.

The bird's eye view of JFT-2M is shown in Fig. II.5-1.

5.2 Plasma equilibria

Noncircular plasma was chosen because it offers the best possibility for maximizing plasma beta. A value of noncircularity b/a = 1.7 was taken a representative of reference designs.

The relation between the vertical field and the n-index which is necessary to produce a noncircular plasma in JFT-2M is calculated by a B_V-n code and is shown in Fig. II.5-2. In real case of tokamak design, the n-index varies as a function of radial position. Therefore, the n-index

necessary to produce noncircular cross section is rather smaller than that shown in Fig. II.5-2 especially in low beta equilibria.

A typical example of D shaped plasma equilibria with high beta value (beta poloidal of 2.5) calculated by SPHEX code is shown in Fig. II.5-3, where the poloidal coil arrangement is also shown. In JFT-2M, equilibrium is accomplished mainly by the poloidal coil outside of the toroidal coil. The small poloidal coils installed inside of the toroidal coil have a role of converting the fast time responce necessary for control of plasma position and shape to slow one, and this slow change of the poloidal field can be compensated by the poloidal coil outside of the toroidal coil. By this control system, we can get simple composition of the tokamak poloidal coil system with minimum power supply (below 20 MW for JFT-2M poloidal coil power supply).

In order to realize flux swing stable in equilibrium and cheap in fabrication we adopt an iron core of 2 vs. By this flux swing, the plasma current of 400 kA, 0.5 sec flat top is obtained in phase I. In upgraded phase II, an air core of 5 vs can be installed instead of the 2 vs iron core. By this air core, the plasma current of 400 kA, 30 sec flat top or 1 MA, 0.5 sec flat top will be obtainable. Thereby, the effect of iron core on noncircular plasma equilibrium is investigated by a computer code (TRIM). As a result, it is concluded that the primary winding set on the top and bottom of the central iron yoke have the iron core locally saturated and then some parts of iron core becomes like an air-gaps effectively. The leakage flux produced by this local saturation gives serious effects on plasma shape. Therefore, the estimation on the primary winding distributed along the central iron yoke is necessary. The result of calculation shows that this particular winding is free from local iron core saturation and reduce well the effect of iron core on the plasma shaping as shown in Fig. II.5-4.

5.3 Component design

1) Toroidal coil

The cross sectional view of the main part of JFT-2M is shown in Fig. II.5-5. There are 16 D-shaped toroidal field coils of copper conductor surrounding the vacuum vessel. The D-shaped toroidal coil consists of a straight section and two circular sections, and the maximum tensile stress of the copper is about 11.6 kg/mm^2 in 4.5 T case, which is

rather conservative stress. For simplicity for fabrication the cross section of the toroidal coil is uniform. The electromagnetic parameters of toroidal coils are summarized in Table II.5-3. The toroidal ripples of the magnetic field are 0.15 % at the plasma center and about 1 % at the outer edge and are low enough for the expected plasma parameters. The error field is 0.68 G at the plasma center and the maximum error field is about 7.2 G and both are negligibly small. The thermal analysis is also carried out and the maximum temperature rise is 51 °C for 1.5 T and 92 °C for 4.5 T and 1 shot for each 5 minutes is possible in the maximum rating.

2) Vacuum vessel

The design of the vacuum vessel is based on the former design of JT-4. The vacuum vessel is composed of two plate sections and two bellows section, and they are bakable up to 250 °C. On the plate sections made of 20 mm thick SUS 316L plate many large ports for heating and diagnostic are mounted by metal O ring vacuum seals. This thick plate section is expected to work as a shell for MHD plasma instability. The four sections are joined by welding the lips. The maximum electromagnetic forces produced by so called saddle current are about 14 kG/cm^2 and about 9 kG/cm^2 at the bellows and held by the flange of the plate section. The vacuum vessel is evacuated up to a base pressure of below 10^{-8} torr. The main pumps are a cryogenic panel of 15 °K and a turbomolecular pump and the effective pumping speed at the vessel aperture is about 2200 l/s (N_2).

The most important problem in vacuum vessel design is to reduce the width of the bellows section and to simplify its structure. The cross-sectional view of the revised bellows section is shown in Fig. II.5-6.

3) Poloidal coil system

As described in the foregoing paragraph, the design of the poloidal coil system is made keeping in mind to simplify coil composition and also to reduce the electrical power supply. The equilibrium field system is composed of six kinds of coil functions as shown in Fig. II.5-3, i.e., S1 is mainly for equilibrium plasma position control, S2 mainly for elliptic shaping of the plasma column, S3 for triangular shaping, V1 and V2 are auxiliary control function of S1 and S2 respectively, and Q1 for magnetic limiter shaping of the plasma column. The maximum currents of

each coil are +275 kA/S1, S3, 200 kA/S2, 75 kA/V1, 50 kA/V2 and 175 kA/Q1 for the 450 kA discharge in phase I. A variety of plasma cross section is realized only by changing the current form of five power supplies. Each turn of the poloidal field coils is made of water cooled rectangular hollow conductor with its average current density of about 15 A/mm^2. The increase of poloidal coil temperature by joule loss is expected to be smaller than 5 °C for a duration of 1 second. The maximum hoop stress due to the electromagnetic force is approximately 1 kg/mm^2 and the maximum surface stress at the connection parts is 3 kg/mm^2. These values are sufficiently small. The total poloidal power supply is less than 20 MW. In phase II, these will be increased about five times of above mentioned values for the 1 MA discharge. Five sets of the equilibrium field coils are connected to the thyristors controlled by programmed, feed forward and feedback current control system.

The main issue of poloidal coil system design is to assess the necessity of the coil (Q2) placed at the inner side of torus (see Fig. II.5-3) in relation to estimation of the poloidal magnetic limiter or simple poloidal divertor. As for this, the detailed examination is now of being continued with some alternative concepts on edge cooling of the plasma.

4) Neutral beam injection system

Supplementary heating by neutral beam injection of net 4 MW and RF waves (ICRF and/or LHH) of 1∿2 MW will be applied to get a plasma beta value of about 3∿5 % in phase I. The NBI system is composed of four stands and the rating of each unit is as follows; acceleration energy of 40 kV, ion beam current of 60 A (30 A ion source ×2), beam divergence of 1.2 degree, pulse width of 5-300 ms, beam efficiency of 40-50 % and pumping speed of the cryogenic system of 5×10^5 ℓ/s. The neutral beams are injected approximately parallel to the toroidal magnetic field through the window of 20 cm × 40 cm. The combination of two co-injectors and two counter-injectors, or three co-injectors and one counter-injector is possible. The floor plan in the JFT-2 building is shown in Fig. II.5-7.

Table II.5-1 JFT-2M main parameters

Major Radius	1.25 m
Minor Cross Section Half Width	
Vertical (b)	0.5 m
Horizontal (a)	0.3 m
Ellipticity (b/a)	1-1.7
Toroidal Field	1.5 T (4.5T, 1S or 1.5T, 30S)
Maximum Plasma Current	0.4 MA (1.2MA, 1S or 0.4MA, 30S)
Heating Power NBI	4 MW (6 MW)
RF (ICH and/or LH)	1-2 MW

Table II.5-2 Expected plasma parameters

Further Heating	--	4 (6)	MW
Electron Density n	4 (12)	4 (12)	$\times 10^{13} cm^{-3}$
Electron Temperature	0.6 (1.8)	3 (5)	keV
Ion Temperature	0.6 (1.8)	3 (5)	keV
Confinement Time τ	0.03(0.09)	0.03(0.09)	S
$n\tau$	0.1 (1)	0.1 (1)	$\times 10^{13} cm^{-3} S$
Poloidal Beta	0.5	2.5	
Toroidal Beta	1	3-5	%

Table II.5-3 Toroidal field coil parameters

Toroidal Field (R=1.25m)	1.5 T	(4.5 T)
Ampere Turns	9.37 MAT	(28.1 MAT)
Number of Coils	16	
Turns per Coil	48	
Length of a Turn	5.57 m	
Average Current Density	18.2 A/mm^2	(54.6 A/mm^2)
Maximum Temperature	51 °C	(92 °C)
Resistance	121.5 m	(138.8 m)
Inductance	0.26	
Time Constant	2.1 S	(1.87 S)
Flattop Current	12.2 kA	(36.6 kA)
Flattop Voltage	1482 V	(4446 V)
Flattop Power	18.1 MW	(162.7 MW)
Voltage Between Turns	1.92 V	(5.8 V)
Flattop	0.5 S	(3S/4.5T, 30S/1.5T)
Equivalent Square Wave Width	4.1 S	

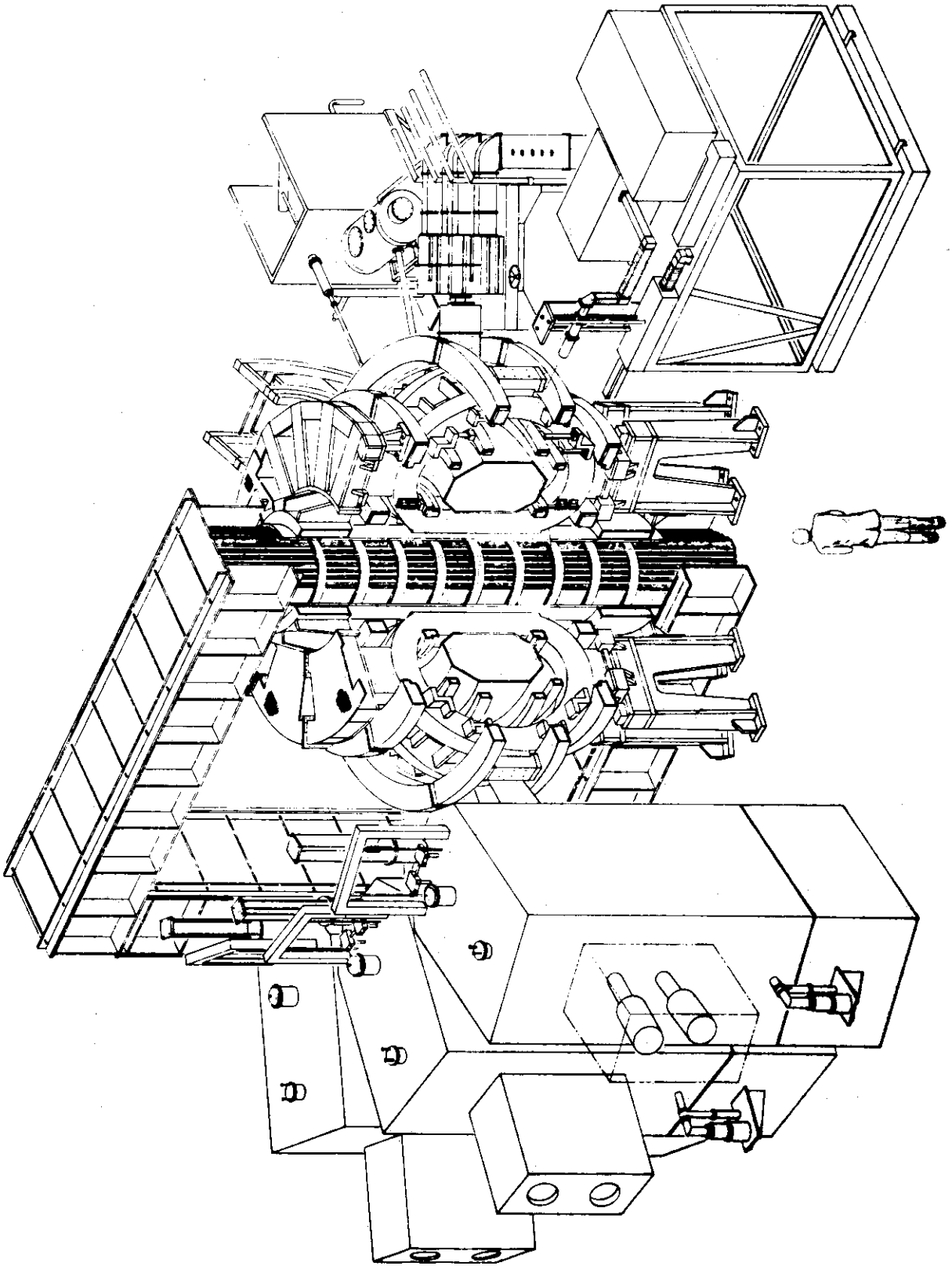

Fig. II.5-1 Bird's eye view of JFT-2M

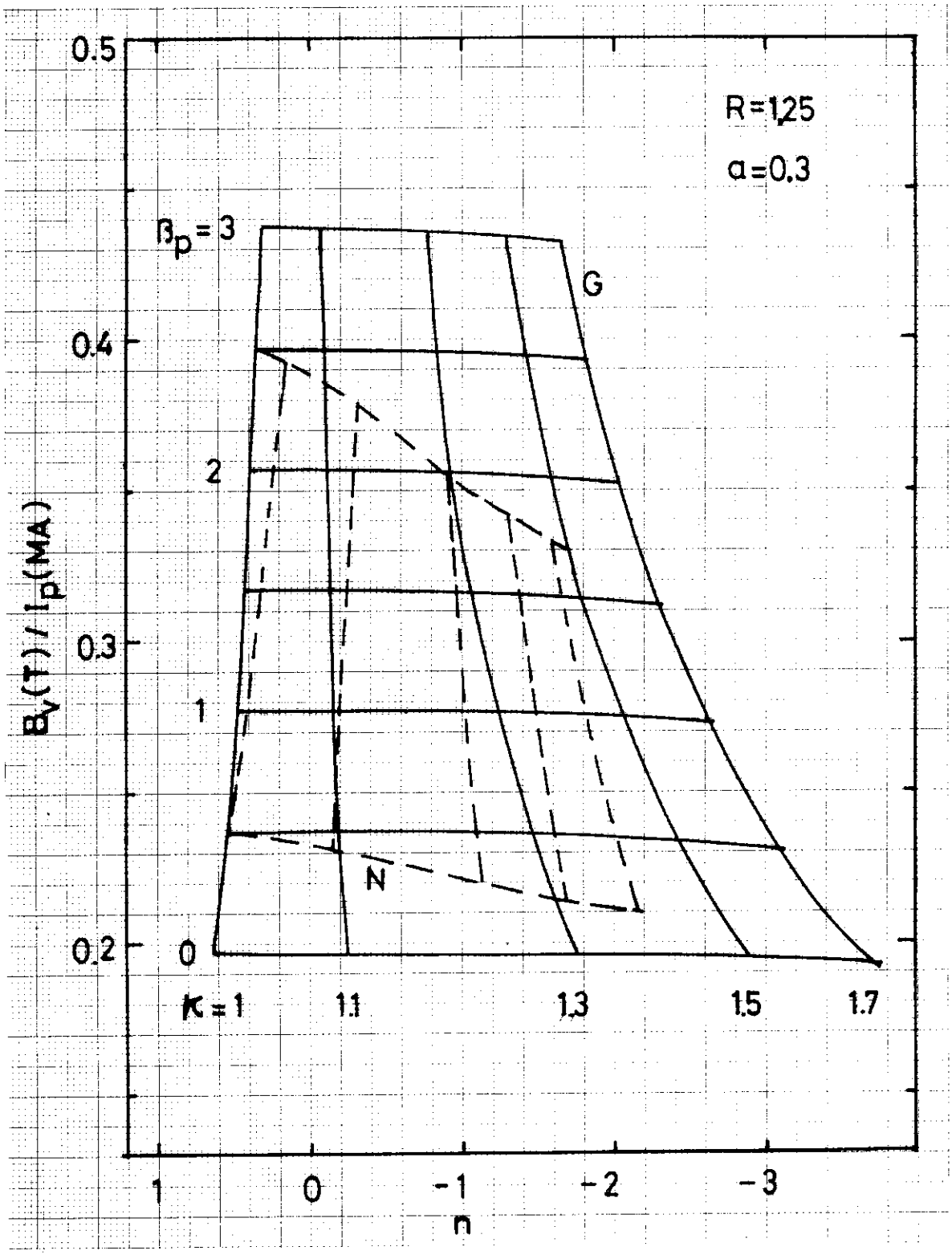

Fig. II.5-2 B_V-n diagram of JFT-2M

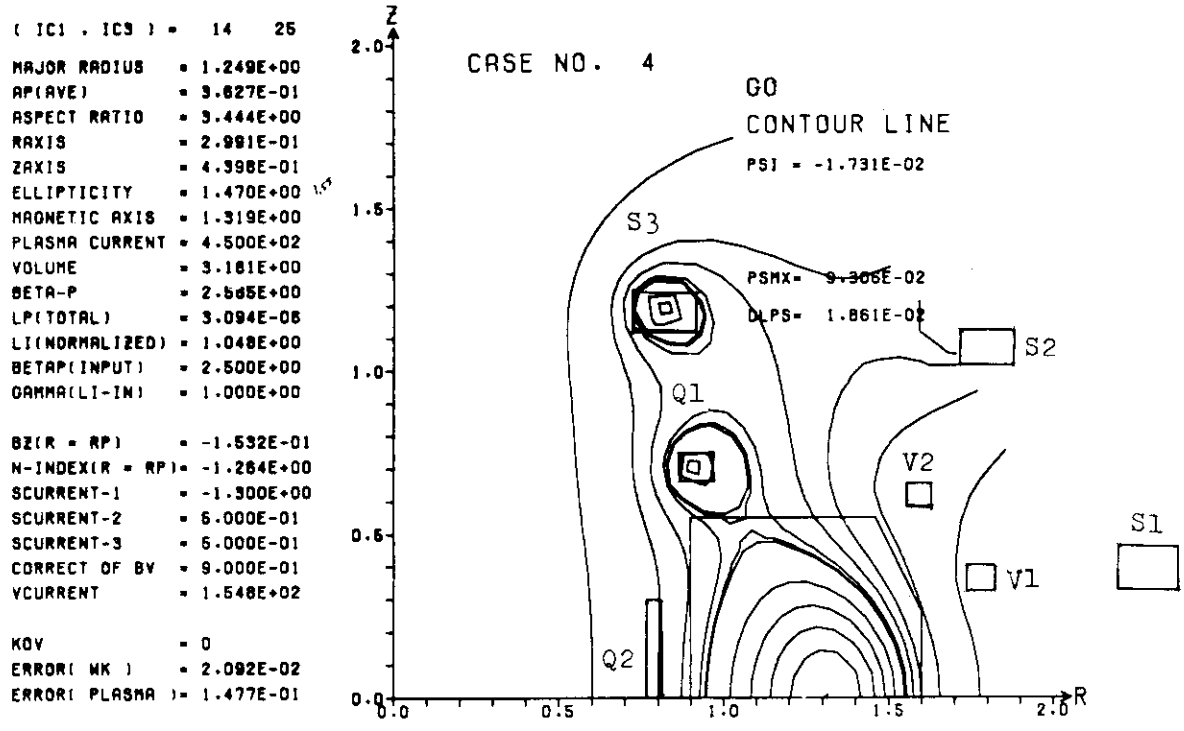

Fig. II.5-3 Plasma equilibrium configuration of JFT-2M (β_p=2.5)

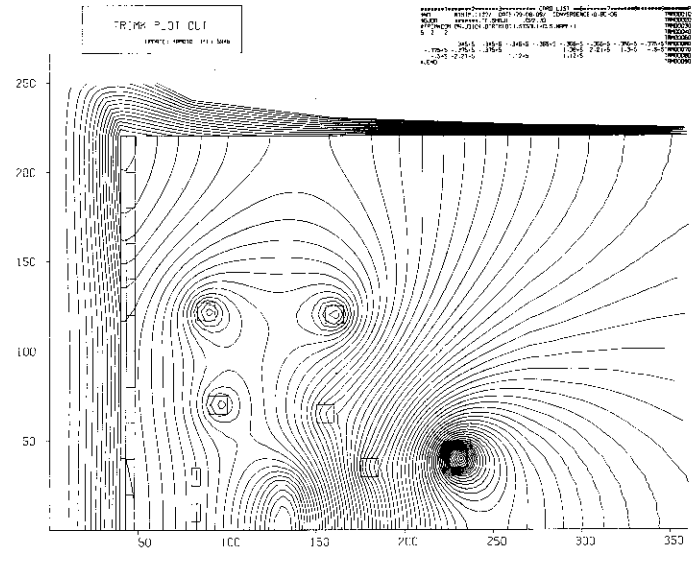

Fig. II.5-4 Iron core effects of JFT-2M

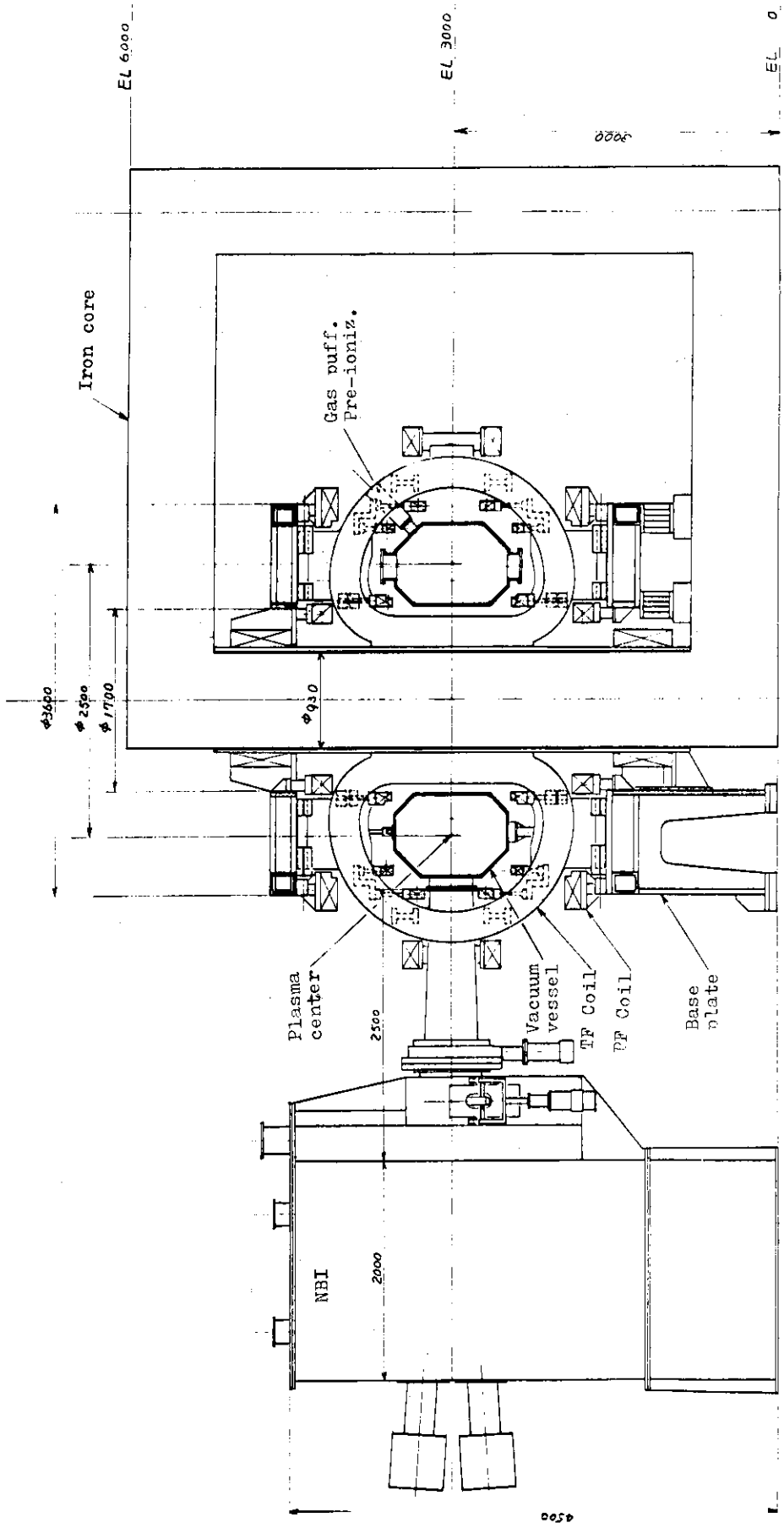

Fig. II.5-5 Cross section of JFT-2M machine

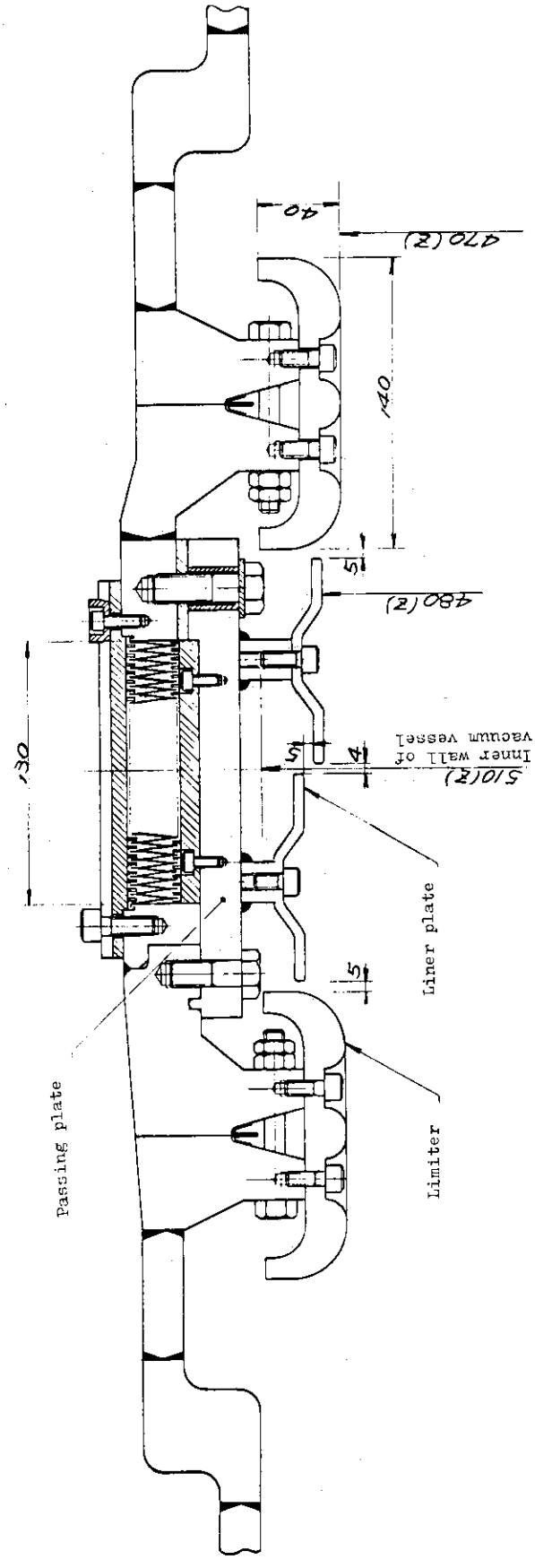

Fig. II.5-6 Cross section of bellows section

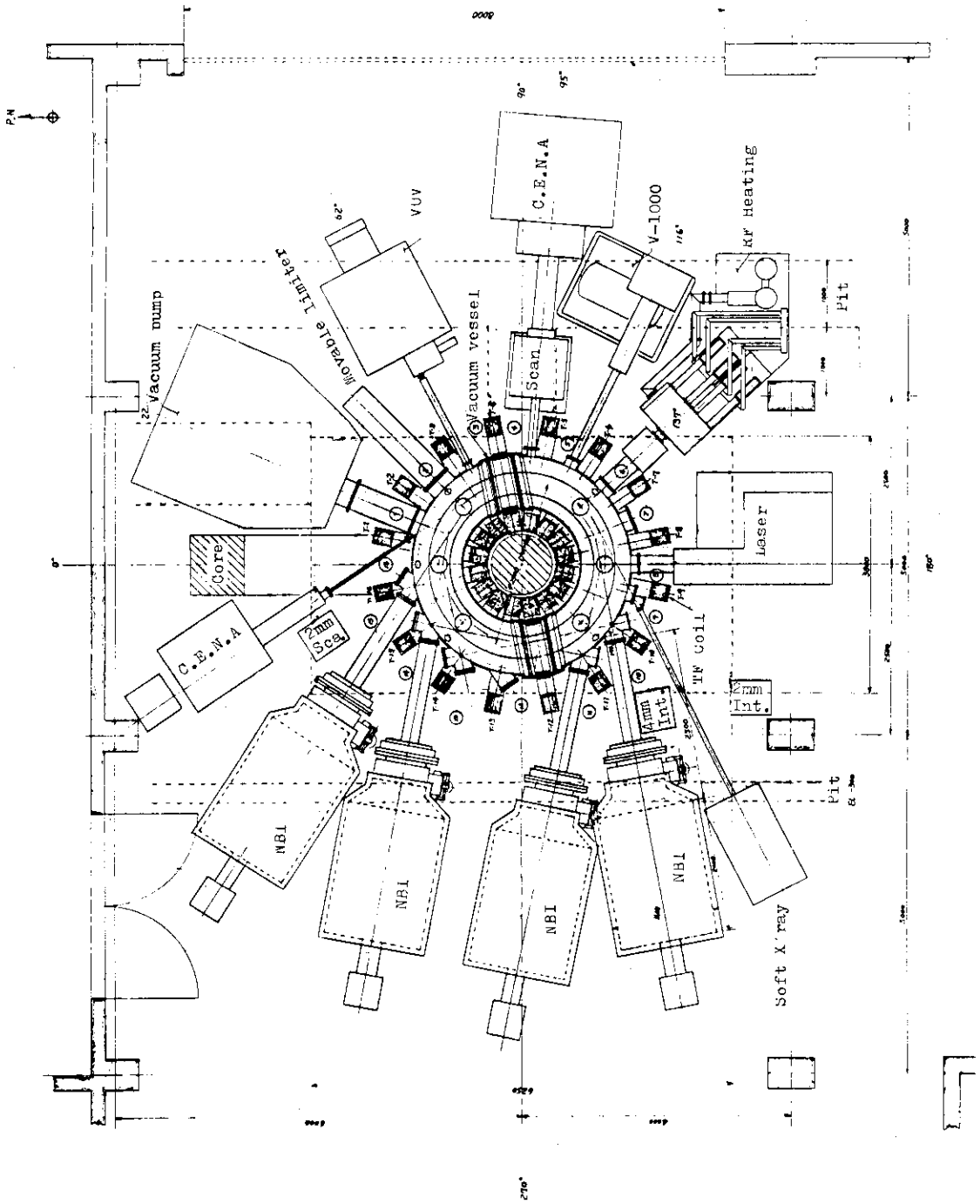

Fig. II.5-7 Floor plan in the JFT-2 building

III. OPERATION AND MAINTENANCE

1. Introduction

Facility Operation and Engineering Section is engaged in operation and maintenance of JFT-2 and JFT-2a/DIVA tokamaks and a flywheel motor-generator, and development of auxiliary equipments and instruments.

Modification of JFT-2 was started in December 1978 and is to end in July 1979. In the modified version of JFT-2 the aluminum shell will be removed to extend the plasma radius from 25 to 28 cm and to increase the port size and number. The vacuum seal of chamber and ports will be made using a metal seal to be bakable at 350 and 200 °C, respectively.

Operation of JFT-2, JFT-2a and the motor-generator was made on schedule without any major trouble.

2. Operation and Maintenance

JFT-2 and JFT-2a tokamaks were operated on schedule as shown in Figs. III-1 and III-2. In JFT-2 the emphasis was placed on maintaining the pumping system, capacitor banks, the cooling water system of the toroidal field coils and the lower hybrid heating system. In JFT-2a insulation was broken in August 1978 through 15 mm teflon gap by induced voltage when the plasma current was shut off. However, this was suppressed by short circuits between halves of the vacuum chamber. ICRF heating systems (150 kW, 25 and 50 MHz) are well operated.

The flywheel motor-generator (21740 kW) alternately used by JFT-2 and JFT-2a was operated this fiscal year for 970 hours in total. Also it took four months from December 1978 for it to be overhauled after five years of operation.

3. Development of equipment and instrument

(1) The objectives of the modification of JFT-2 are; 1) a vacuum chamber is replaced to increase the port number, 12 ports for diagnostics and two tangential ports for the neutral beam injection heating, 2) the aluminum shell has been removed to extend the minor radius from 25 to 28 cm, 3) the vacuum seal is made using a metal gasket to be bakable at 350 °C and the total pumping speed at the pumping port is 1700 l/sec for N_2 gas. The final base pressure is expected to be less than 1×10^{-8} Torr.

The final design and fabrication of the system was started by Hitachi,

Ltd. in March 1979. Equipment will be started from June 1979, and the experiment from August 1979.

The power supply and control system for the vertical coils to ensure the plasma equilibrium are shown in Fig. III-3. The power supply is controlled by the direct digital control using a digital process computer and a micro-processor-controlled regulator for the 0.8 MW thyristor of double 3-phase bridge connection. The response time of the digital control loop is $\sim$3.7 ms.

(2) Operating conditions of the Taylor type discharge cleaning (TDC) were surveyed. The production rate of H_2O species in the residual gas analysis is a measure of the effectiveness of TDC. The partial pressures of H_2O are shown as a function of plasma current (electron temperature) the filling pressure (proton density), and pulse rate as shown in Fig. II.2-8(a), (b) and (c), respectively. Low temperature ($T_e \lesssim 10$ eV), high filling pressure and high repetition rate discharge is effective for removal of the oxygen from the surface of the chamber.

(3) Test of the J × B gun type pre-ionization system has been continued.

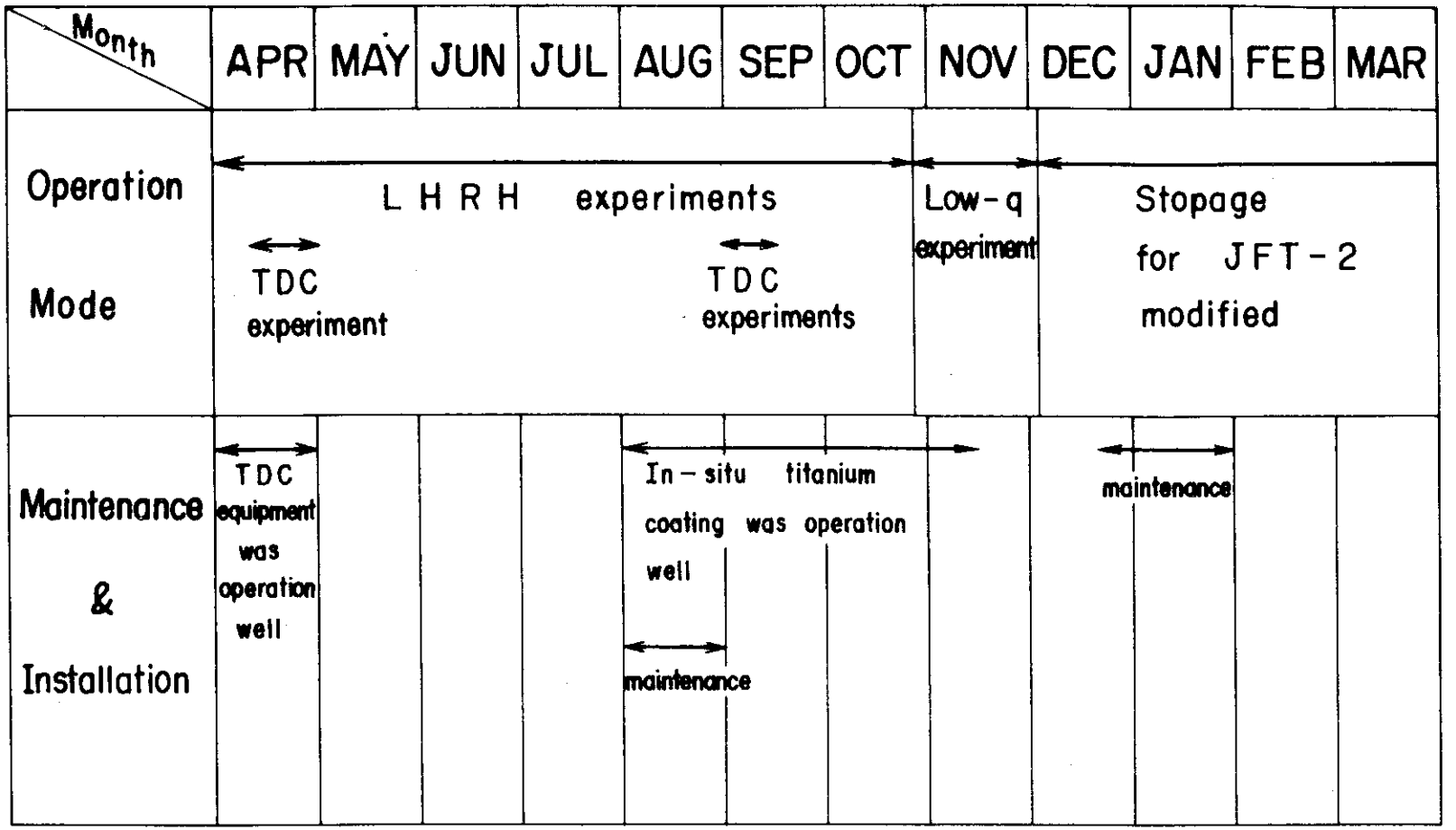

Operation of JFT-2

Fig. III-1 Operation of JFT-2

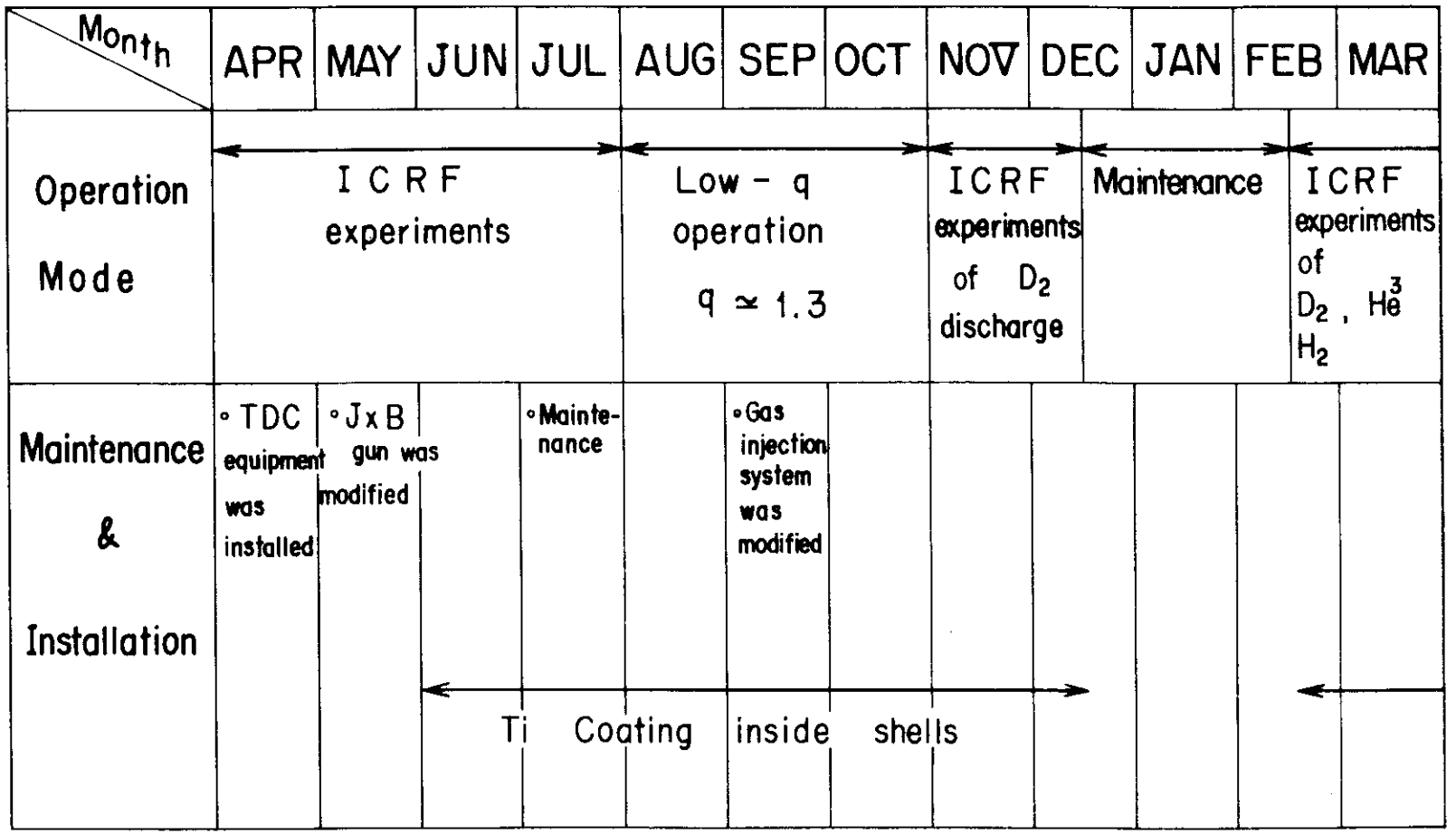

Operation of JFT - 2a (DIVA)

Fig. III-2 Operation of JFT-2a/DIVA

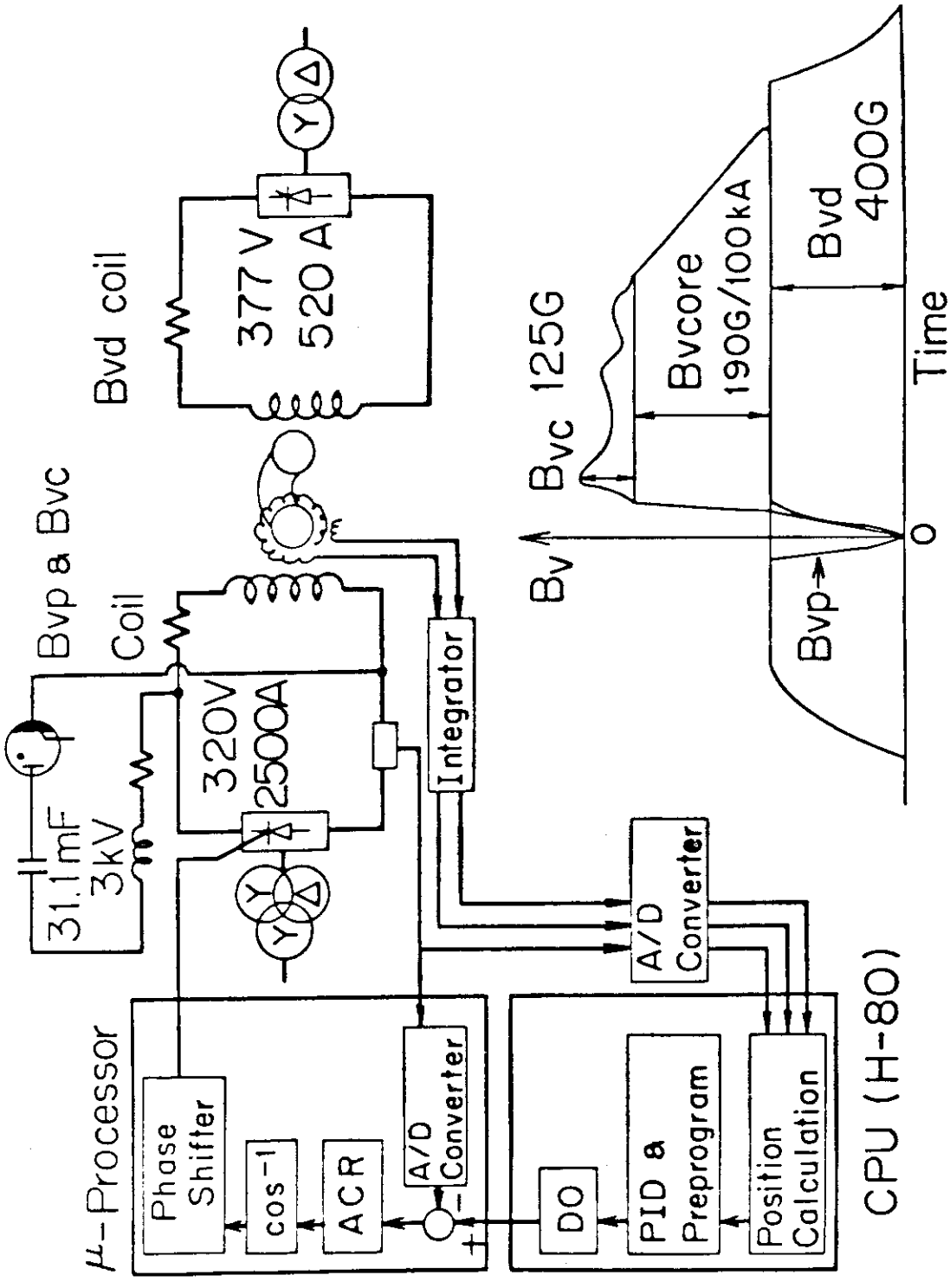

Fig. III-3 Power supply and control system for the vertical coils

IV. Development of Plasma Heating System

1. Introduction

Developments of a neutral beam injection system and a radiofrequency (RF) heating system have been continued.

In the neutral beam injection system, an ion source development and beam line studies for JT-60 injectors have been made using test stands ITS-1, ITS-2 and ITS-3. Hydrogen beams of 70 keV, 5.5 A, 0.1 sec were extracted by the two-stage ion source of 10 cm in diameter. Source plasma improvements have been made in a rectangular duoPIGatron and a bucket source, which are the full-sized models of the plasma source for JT-60 injectors. The detailed design of the prototype unit of neutral beam injectors for JT-60 was completed in March 1978. After the completion, the detailed design was evaluated. As a result, several problems were picked up which still need more elaborate design work. The final design of the prototype unit has been made and will be completed by summer of 1979.

In the RF heating, a lower hybrid heating experiment up to 200 kW has been carried out on JFT-2 tokamak, and this phase-I experiment was successfully finished in November 1978. A transmitted RF power density was increased up to 1.2 kW/cm^2 by a new coupler of stainless steel plated with copper and gettered with titanium on its inner surface. After the phase-I experiment, output power of the lower hybrid heating system for JFT-2 was increased up to 300 kW in March 1979. The conceptual design of the lower hybrid heating system for JT-60 has been made.

2. Neutral Beam Injection System

2.1 Ion source development

Neutral beam injection is one of the most powerful and effective methods for heating a tokamak plasma. For JT-60 neutral beam injectors, it is required to develop an ion source which can produce a low divergent ion beam of 35 A at 50-100 keV for 10 sec through 12 cm × 27 cm rectangular extraction grids. To obtain such high power and long pulse ion source, our efforts are concentrated particularly on studies of two-stage accelerator, on source plasma production and on development of a long life cathode.

2.1.1 Multi-megajoule pulsed ion source[1)]

Prior to the prototype rectangular ion source of JT-60 neutral beam injector, we have designed and fabricated a 75 keV, 6 A, 10 sec ion source. Figure IV.2.1-1 shows the sketch of a modified duoPIGatron plasma source with two-stage accelerator. The source plasma generator consists of hot cathode, an intermediate electrode, anode 1, anode 2 and a target cathode (or plasma grid). To perform stable arc discharge and to improve the plasma uniformity, we attached several mild steel rings to the anode 1. Figure IV.2.1-2 shows the patterns of the line of magnetic force with and without the rings. The PIG chamber (anode 2) is modified with a magnetic multipole line cusp field confinement. The ionization rate in PIG chamber usually increases with the gas pressure there. The pressure increase is obtained by controlling the gas feed both into the filament chamber and into the PIG chamber. Experimentally, we have obtained a source plasma uniformity without ±5 % over a 10 cm diameter area and the plasma density corresponds to the ion saturation current density of about 0.4 A/cm^2. However, high gas pressure in the PIG chamber will cause the difficulty in the beam extraction because of the backstream electrons enough to shorten the filament life. Then, we made a rough estimation of the backstream electron power to the filaments. It is found to be important to keep the gas pressure in the PIG chamber below several mTorr so as to obtain a quasi-DC beam in the present source.

On the other hand, the ion accelerator consists of a cylindrical hard seal ceramic insulator (ID=316 mm, OD=353 mm) and two-stage extraction/acceleration grid assembly. Each grid made of oxygen free copper has 191 holes of 4.0 mm in diameter over the central 10 cm diameter area (see Figure IV.2.1-3). The aperture pattern is split into 15 sections by 16 water lines. The aperture shape of the plasma and the gradient grid is determined to obtain good beam optics, and the aperture shape of the suppressor grid is determined to reduce the backstream electrons emanating from the surface. Figures IV.2.1-4 (a) and (b) show the computed proton beam trajectories with minimum beam divergence, and the electron trajectories from the suppressor grid, respectively. As reported elsewhere[2)], it is not difficult to keep the grid heat loading below 2 % of the total beam output. At 75 kV, 6 A, it corresponds to the heat flux of 166 W/cm^2 per unit grid plate area and 190 W/cm^2 per unit cooling area. This will be a practical value for quasi-DC beam extraction, as indicated by the reference 3).

2.1.2 Multiple-slot accelerator[4)]

By employing multiple-slot accelerator rather than multiple-circular aperture accelerator, higher geometric transparency can be obtained, which enables us to extract higher currents from a source plasma of a given radius. We have designed and tested multiple-slot accelerator which have the transparency of 64 %. The accelerator is composed of four grids forming two-stage acceleration system; the configuration is shown in Figs. IV.2.1-5 (a), (b). The plasma grid has 8 slots, each 4 mm wide 5 cm long with rounded ends, forming a square 5 cm × 5 cm array. The grid is made of copper pipes and is actively cooled by water flowing through the pipes for producing long pulse or DC-beams. The accelerator has produced beam current up to 4 A at 50-60 kV with pulse length of 20-100 msec and a duty cycle of 1/20-1/50. The beam divergence is measured by scanning calorimeter set 2.0 m apart from the accelerator. Figure IV.2.1-6 shows the typical profiles of the beam in both directions perpendicular and parallel to the slots. The beam focus in the direction parallel to the slots is extremely good, while that in the direction perpendicular to the slots is considerably worse than the beams produced by circular aperture grids. The e-folding half-width divergence is $\pm(0.7°\text{-}0.8°) \times \pm(1.5°\text{-}2.0°)$ at optimum perveance.

The heat loading of the grid is slightly less than that of the circular aperture grid due to the higher transparency. Its level is less than 1.0-1.5 % of the total beam output per each grid at optimum perveance. It is expected that such level of loading is removed easily and DC operation of the ion source is attainable. However, in practice, rapture of cooling pipes of the grid occurred frequently. They are caused by intrinsic problems of the slotted grid.

2.1.3 DuoPIGatron plasma source[5,6)]

As the high energy ion source is required for JT-60 neutral beam injectors, we have made the rectangular duoPIGatron source. To produce high-current, low divergent ion beams, it is necessary to generate a dense plasma while maintaining spatial uniformity. To make the source plasma uniform in the longitudinal direction of the rectangular grid, we have conducted experiments using the duoPIGatron source with slot-shaped nozzle snout as seen in Fig. IV.2.1-7. A typical example of the density profiles in the transverse and longitudinal directions are shown in Fig. IV.2.1-8.

X and Y denote the distance from the center of the grid in the transverse and longitudinal directions, respectively. Point cusp confinement magnets are set around the chamber walls. A comparison of density profiles is also made between two cases; when working gas is fed only into the intermediate electrode chamber, shown in the figure by NORMAL GAS FEED and when working gases are supplied into both the intermediate electrode chamber and the PIG chamber, shown by NORMAL PLUS EXTRA GAS FEED. Source plasma uniformity, especially in the longitudinal direction, is improved by operating with the proper combination of these gas feeds. Figure IV.2.1-9 shows the density profiles of the source plasma in the transverse direction with the button and point cusp confinement. The ion saturation current density reaches 0.19 A/cm^2, uniform to ±5 % over the area of 8 cm × 24 cm at an arc current of 340 A.

2.1.4 Bucket plasma source

The magnetic multiple line-cusp devices (bucket source) has produced high-density, large volume, quiescent, uniform plasma, which makes it a potential candidate for use as a plasma generator for JT-60 neutral beam injectors. The device (see Fig. IV.2.1-10) is rectangular discharge chamber (21 cm × 36 cm by 18 cm deep) with one end enclosed by a plasma grid. The chamber wall serves as an anode and is surrounded by an external systems of Co-Sm magnets (BH_{max} > 18 MG Oe) forming a line-cusp geometry. Hydrogen plasma is produced by electron emission from a hot cathode assembly (8 tungsten filaments). The plasma grid is connected to the negative terminal of the cathode filaments in order to repel the primary ionizing electrons. Density distribution at 7 mm above the plasma grid is shown in Fig. IV.2.1-11. The ±5 % uniformity contour intersects somewhere in between the B = 10 Gauss and 20 Gauss contour. Figure IV.2.1-12 shows plots of the arc voltage and ion saturation current density at a pressure of 7 mTorr. In the emission limited regime where the arc voltage exceeds about 70 volts, the arc efficiency increases. The ionization efficiency is dependent on the arc voltage and source pressure (see Fig. IV.2.1-13).

2.1.5 Hollow cathode

Hollow cathode arc discharges in hydrogen gas were experimentally studied. An impregrated tungsten emitter or an oxide-coated nickel

emitter of 1 cm in inner diameter by 2 cm long was used as the hollow cathode. When the hollow cathode was set opposite to a plain anode, discharge sustain voltage became 40 to 60 volts with the gas flow rate greater than 1 Torr·l/sec. When it was applied to a duoPIGatron ion source, the discharge voltage varied from 80 to 120 volts depending upon the gas flow rate and the source magnetic field strength. Beam extraction from the ion source was made and hydrogen ions of 3 A at 25 keV were extracted.

References

1) Y. Ohara, H. Horiike and Y. Okumura; Proc. 3rd Symp. on Ion Source and Application Technology, Tokyo, Feb. 1979 p.179-182.
2) Y. Okumura, Y. Ohara and T. Ohga; JAERI-M 7696 (1978).
3) H. Horiike, U. Kondoh, H. Morita, H. Shirakata, T. Sugawara and S. Tanaka; "Cooling of Extraction Electrode of an Ion Source in Long Pulse Operation" to be published in Rev. of Sci. Instrum.
4) Y. Okumura, H. Horiike and Y. Ohara; Proc. 3rd Symp. on Ion Source and Application Technology, Tokyo, Feb. 1979 p.111-114.
5) Y. Arakawa, M. Akiba, U. Kondoh, S. Matsuda and T. Ohga; JAERI-M 8088 (1979).
6) Y. Arakawa, M. Akiba, U. Kondoh, J. Sakuraba and H. Morita; Proc. 3rd Symp. on Ion Source and Application Technology, Tokyo, Feb. 1979 p.183-186.

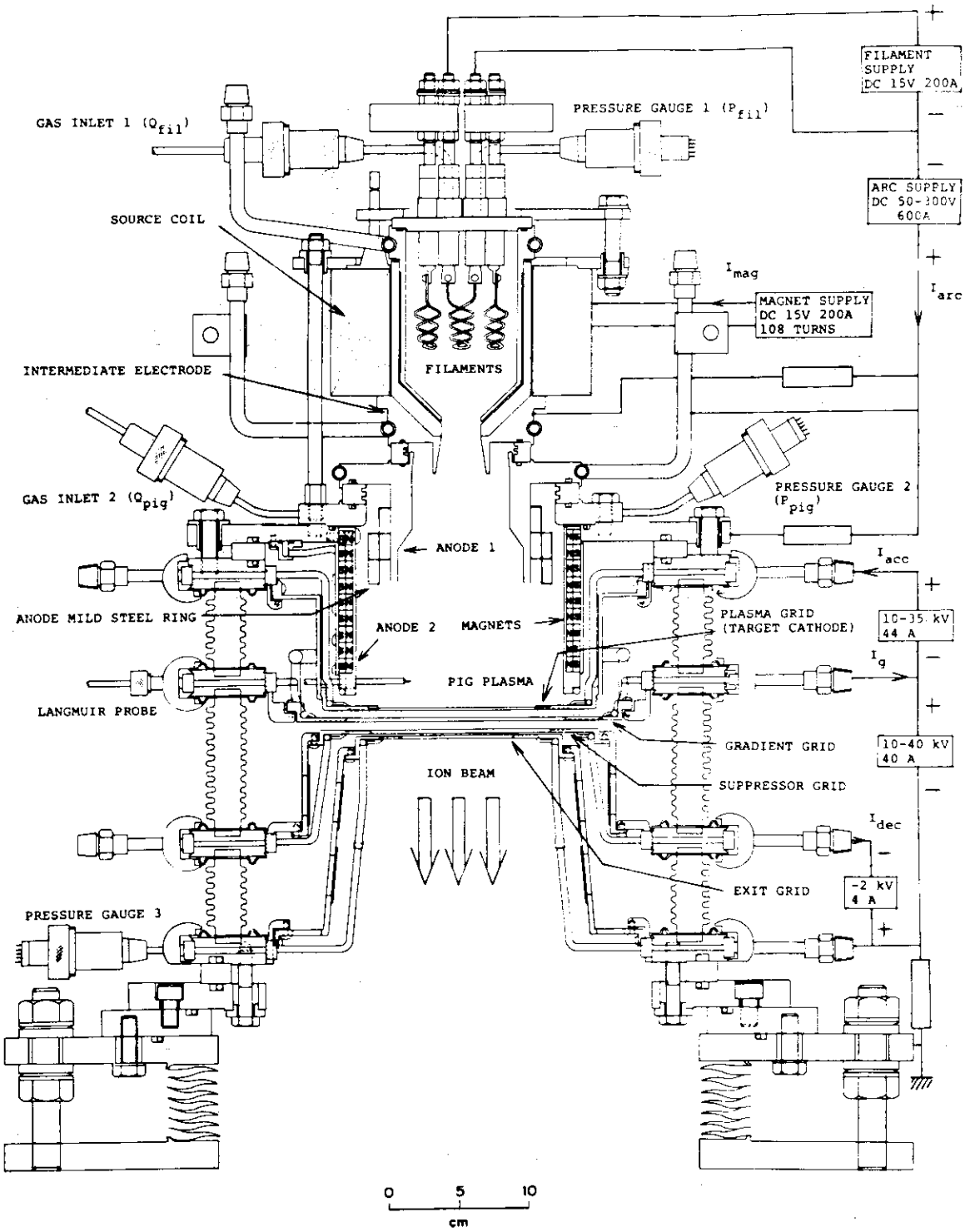

Fig. IV.2.1-1 Modified duoPIGatron ion source with two-stage accelerator.

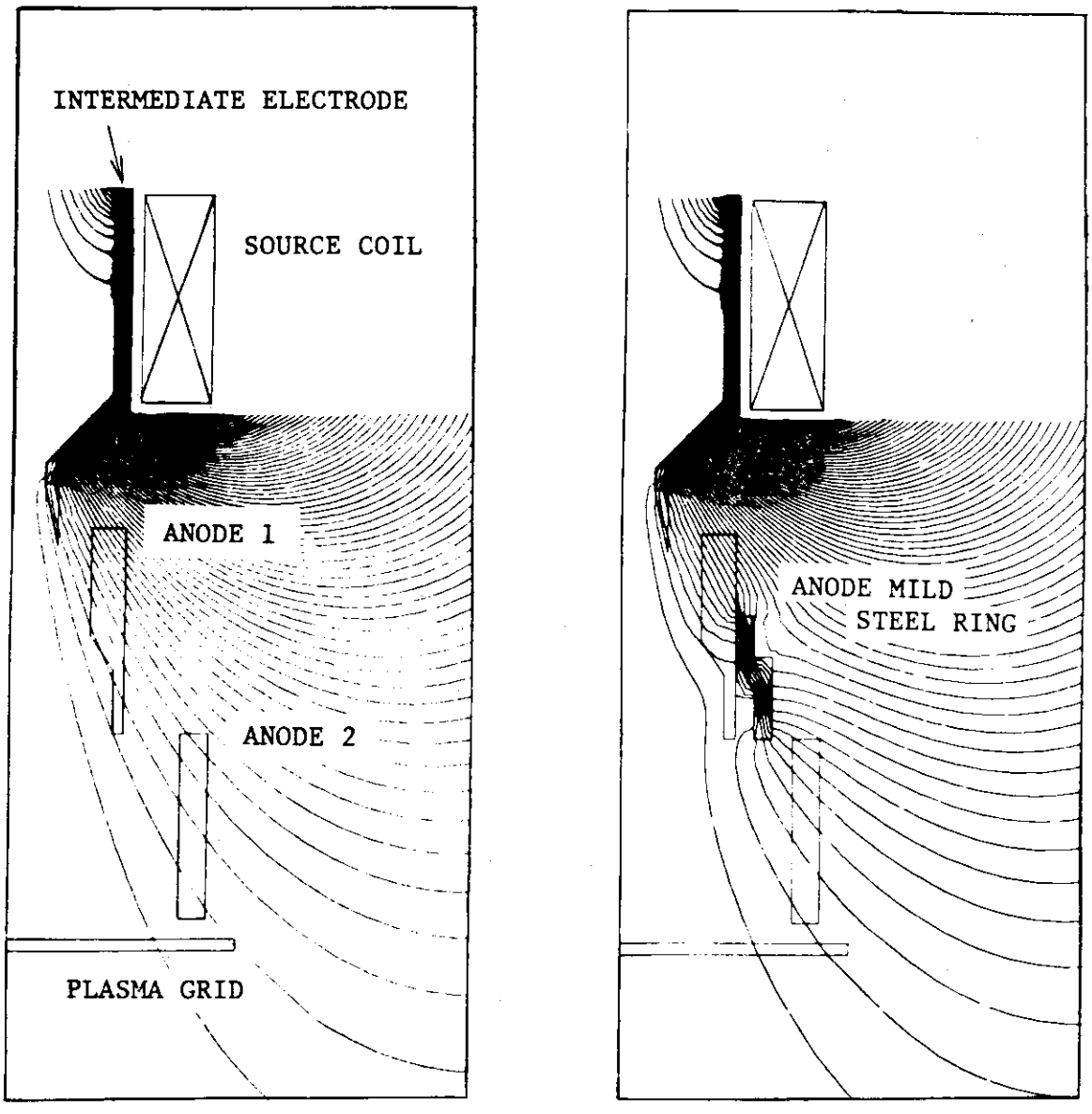

Fig. IV.2.1-2 Computed patterns of the line of magnetic force with and without anode mild steel rings.

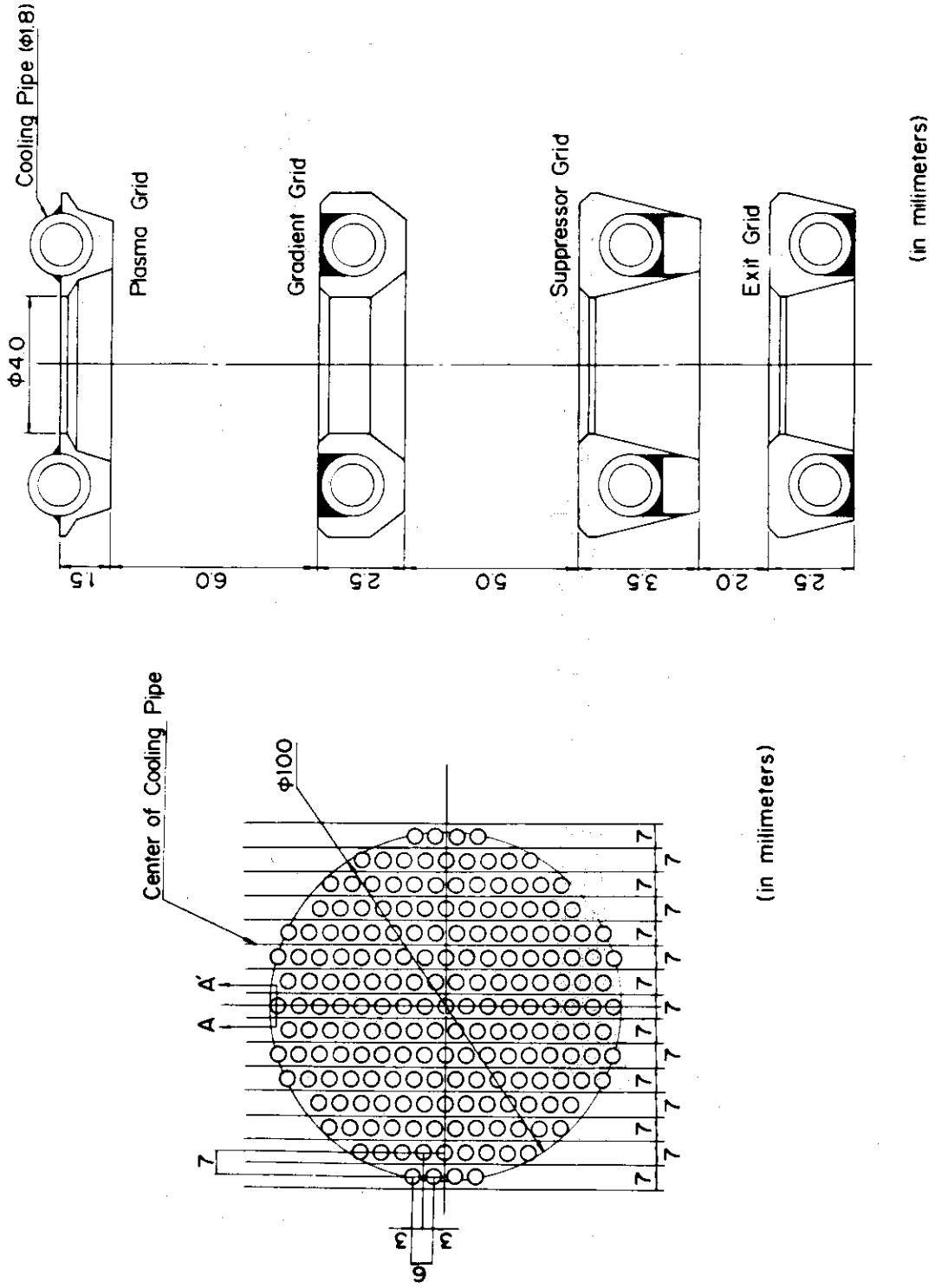

Fig. IV.2.1-3 Aperture pattern of a 10 cm diameter grid (a), and the cross sectional view of apertures in each grid (b).

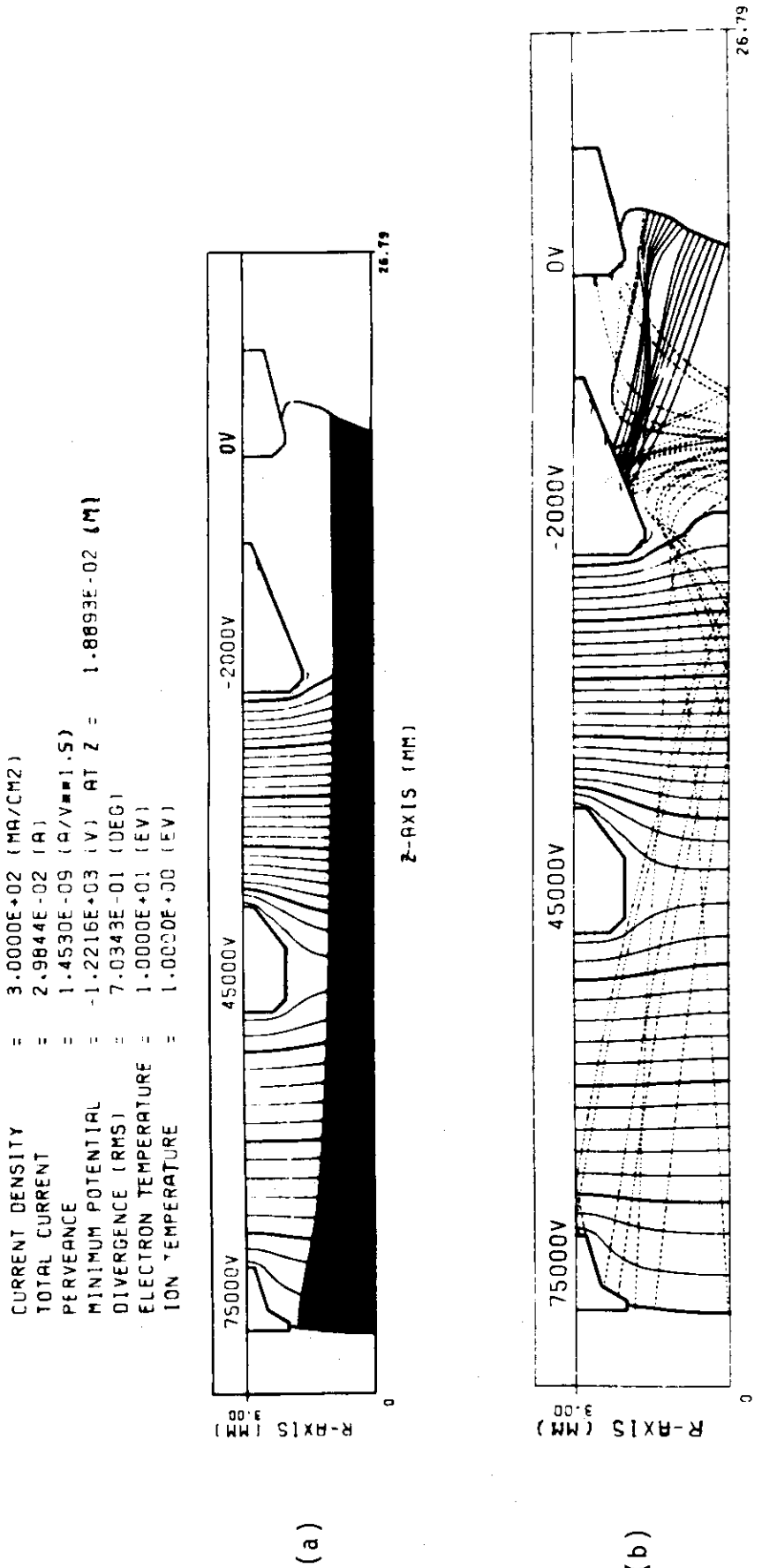

Fig. IV.2.1-4 Computed proton beam trajectories with minimum beam divergence (a), and the electron trajectories from the suppressor grid (b).

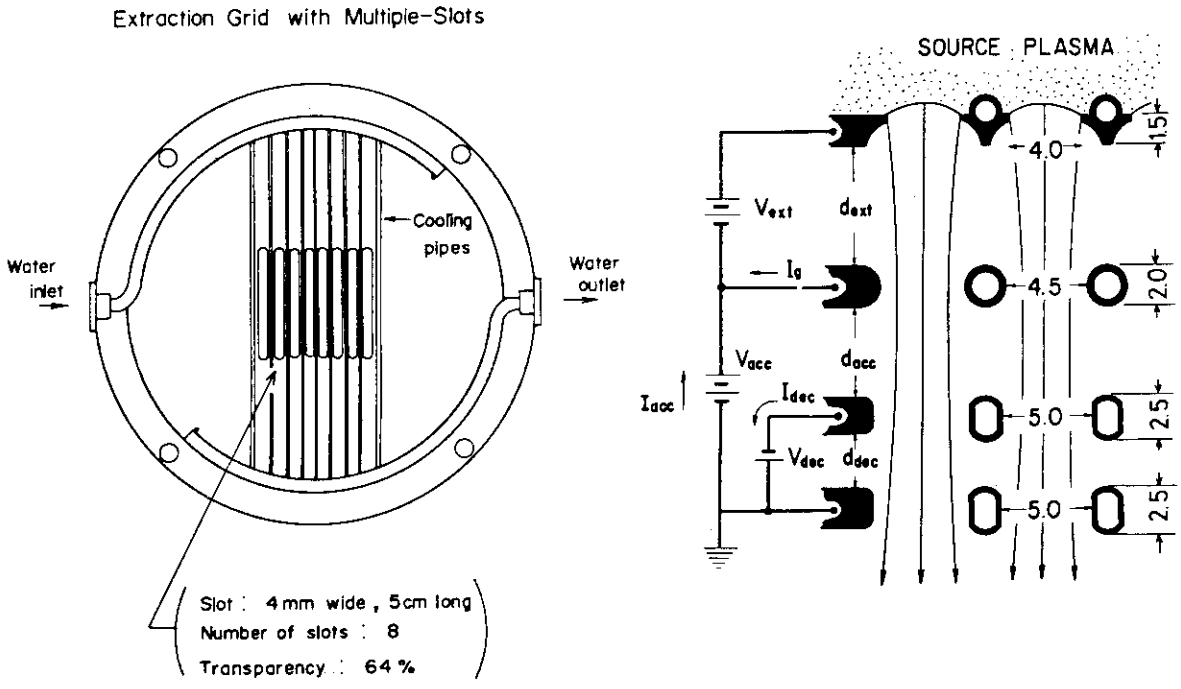

Fig. IV.2.1-5 Front view of slotted grid (a), and the cross sectional view of slots (b).

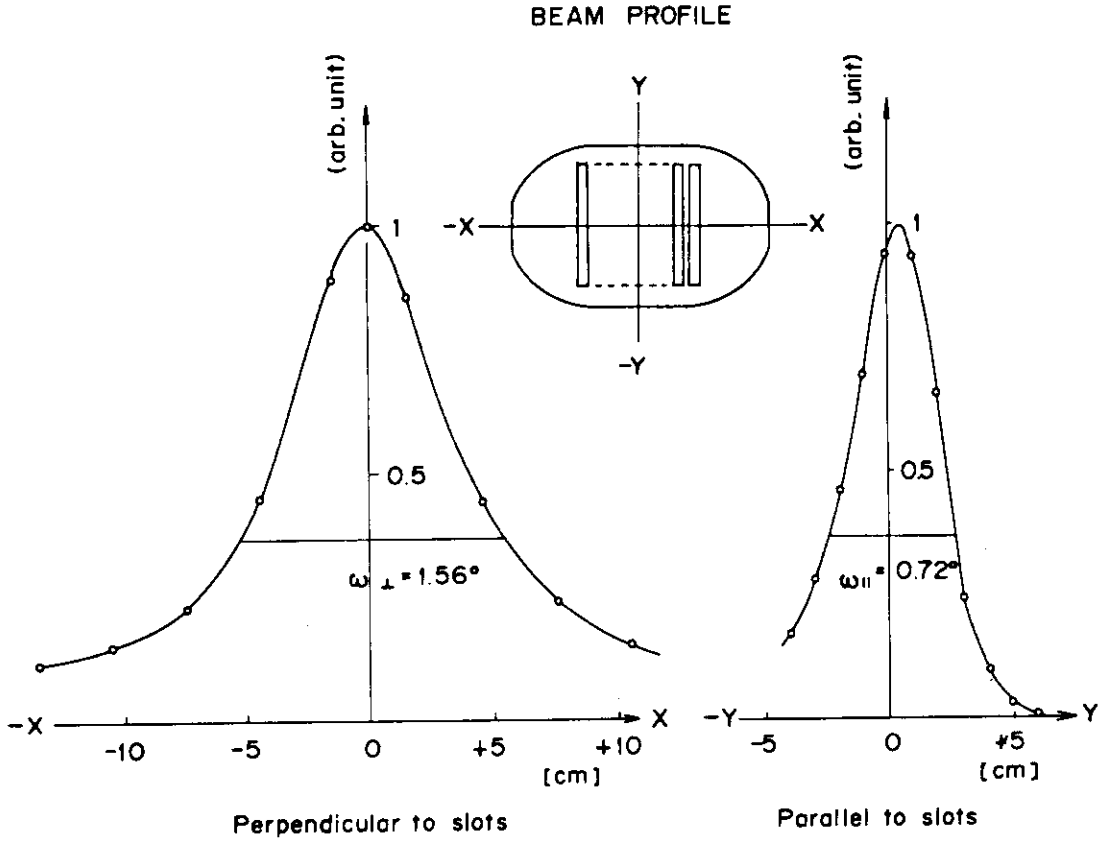

Fig. IV.2.1-6 Typical profiles of the beam in both directions perpendicular and parallel to the slots.

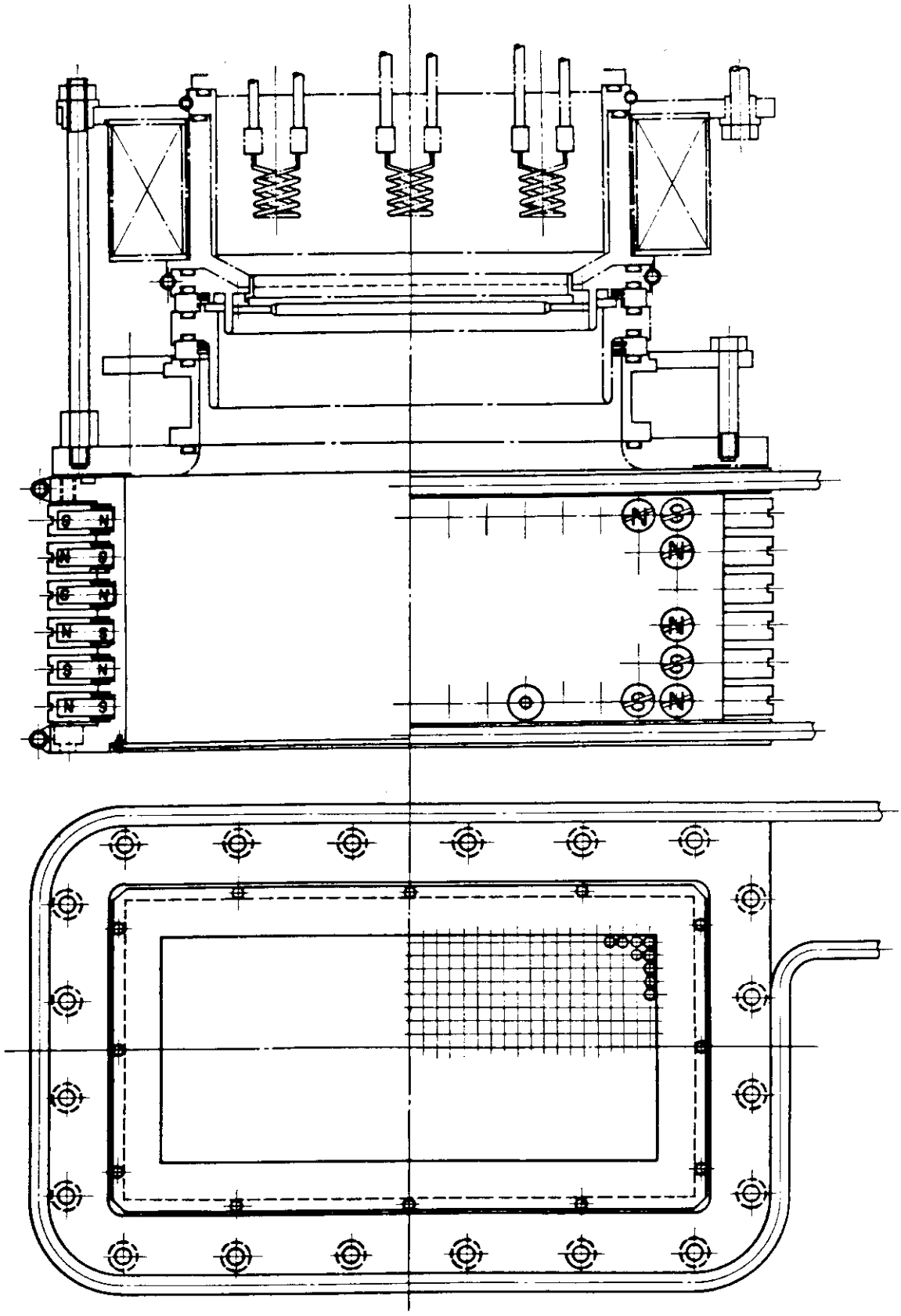

Fig. IV.2.1-7 The rectangular shaped duoPIGatron source.

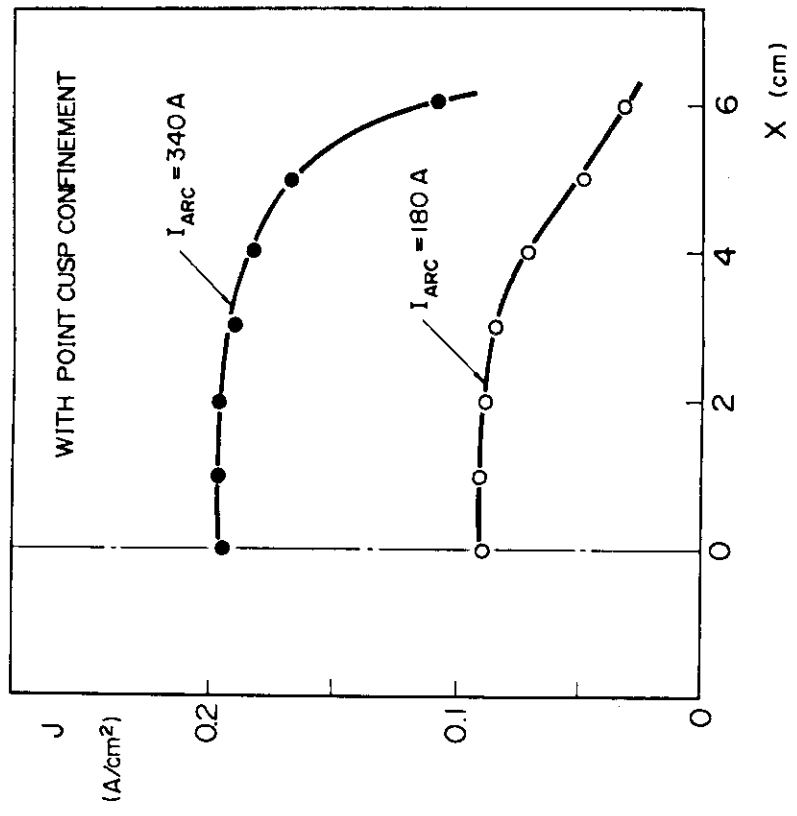

Fig. IV.2.1-9 Improved density profiles of the source plasma in the rectangular shaped duoPIGatron source.

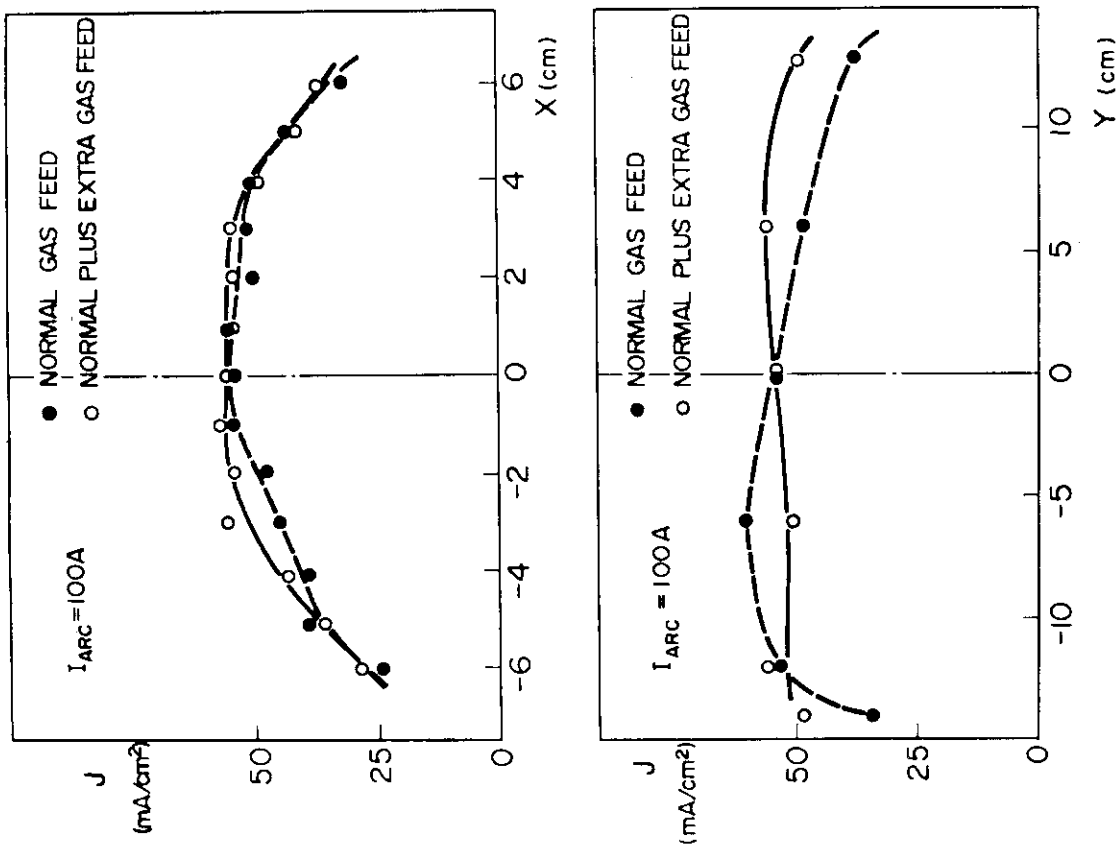

Fig. IV.2.1-8 A comparison of the density profiles with and without extra gas feed.

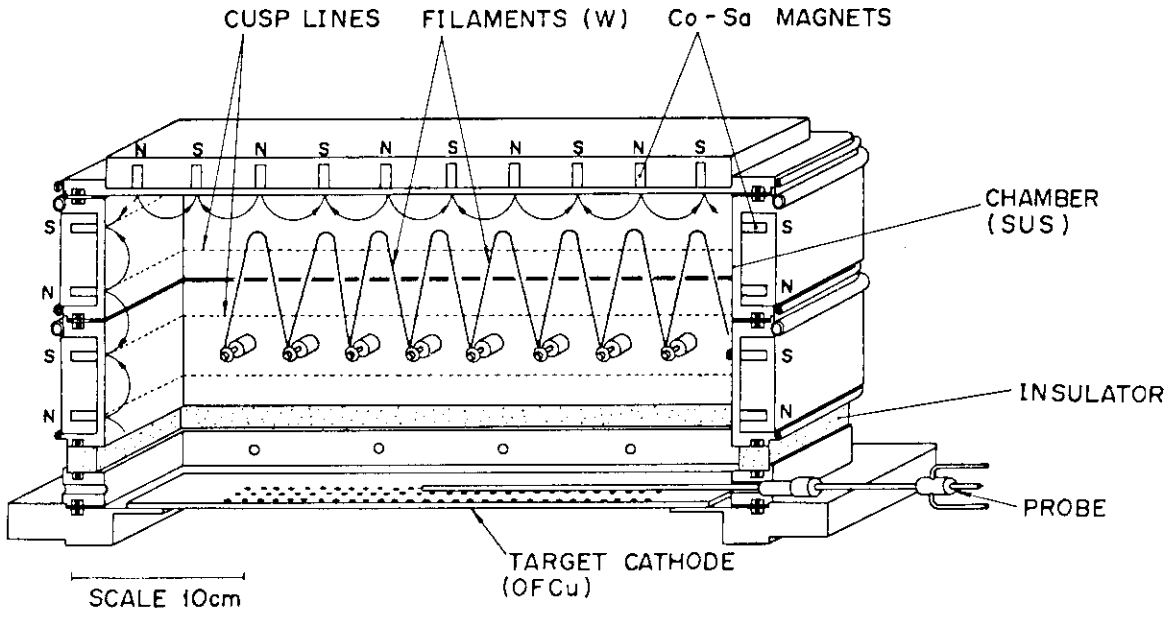

Fig. IV.2.1-10 The rectangular shaped bucket source.

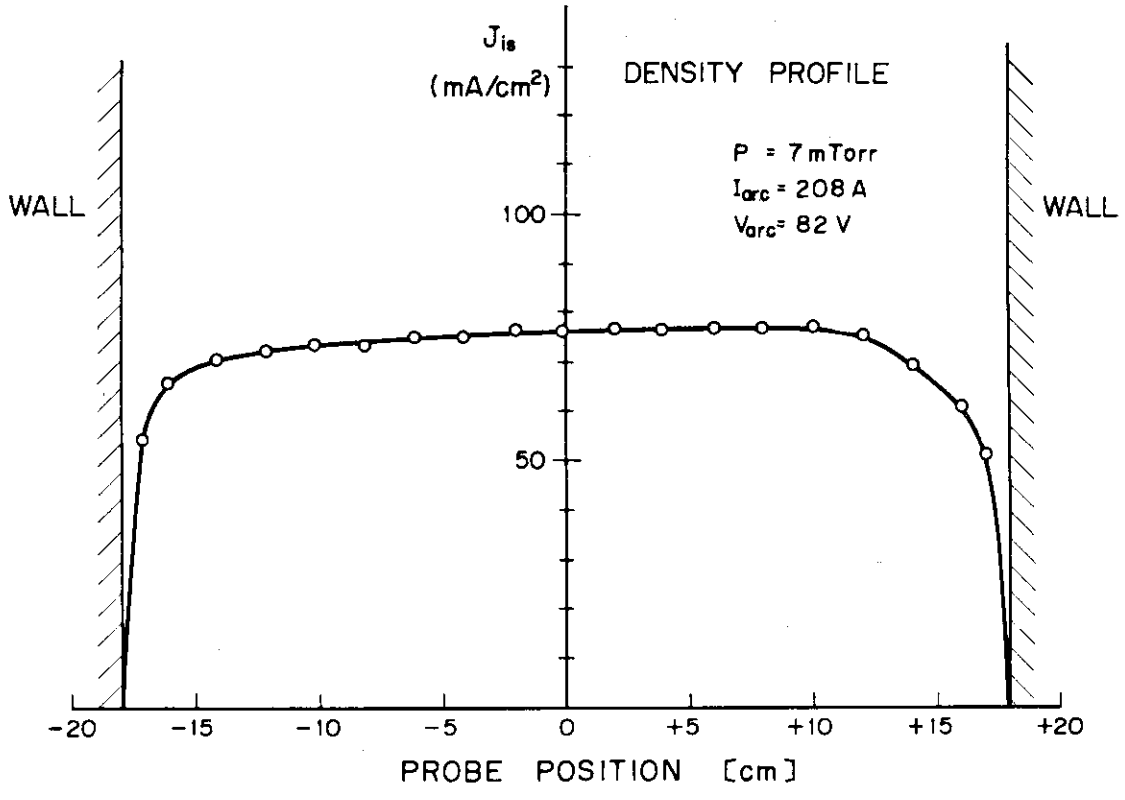

Fig. IV.2.1-11 Density profile of the source plasma in the bucket source.

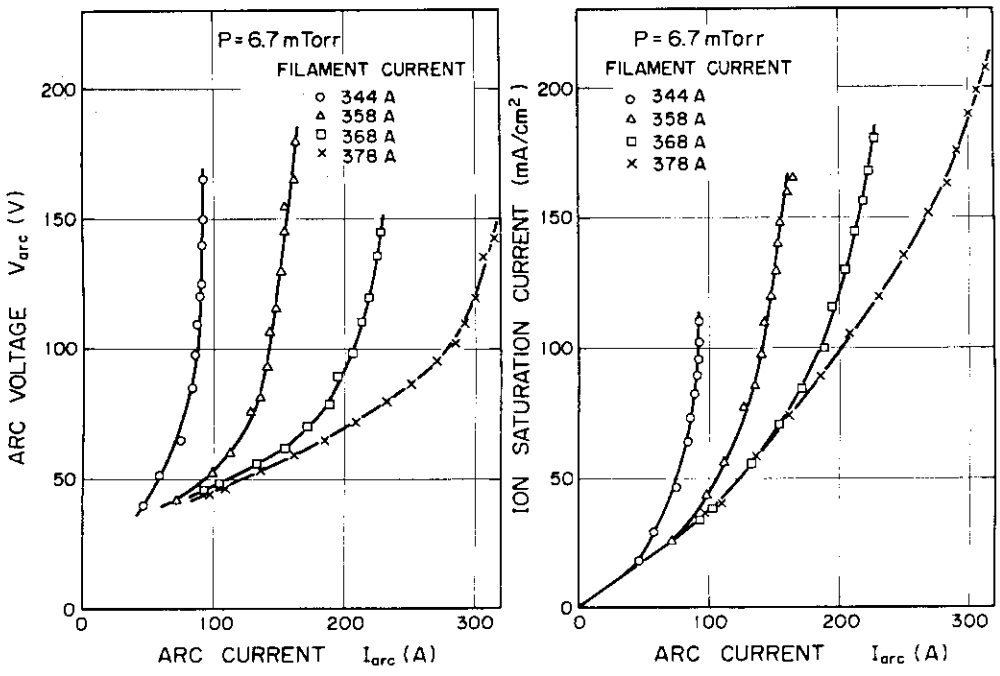

Fig. IV.2.1-12 Variations of the arc voltage and ion saturation current density with arc current.

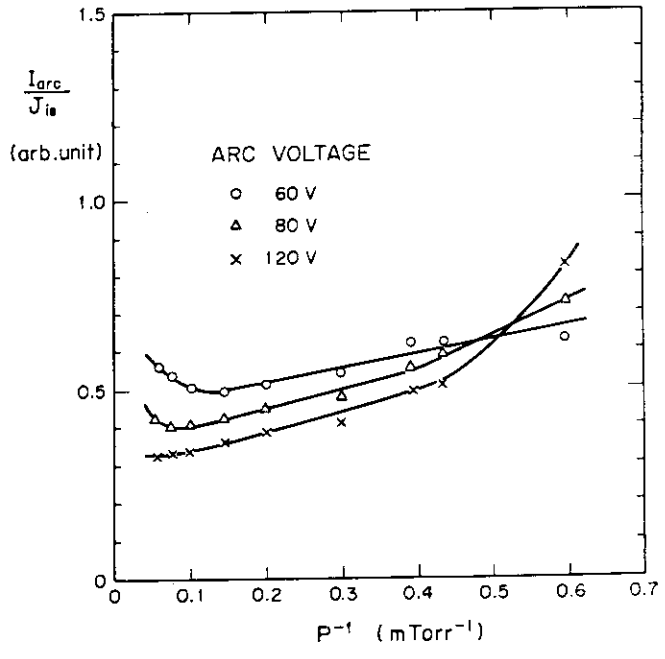

Fig. IV.2.1-13 Variations of inverse ionization efficiency with arc voltage and source pressure.

2.2 Development of the JT-60 neutral beam injection system

A design of the JT-60 neutral beam injector is under way. Following performances are required to heat the JT-60 plasma beyond 5 keV.

(1) 20 MW hydrogen atoms into the torus (at 75 kV acceleration)
(2) Number of injection port; 14
(3) Beam energy range: 30 - 100 keV
(4) Permissible cold gas influx into the torus: A value corresponding to 15 % of the fast neutral atoms amounting to 6.3 Torr·l/s.

Neutral beams are injected quasi-perpendicularly from seven pair of ports along the torus. At each pair of port an upper beamline unit is mounted on top of the lower beamline unit and beams are injected with the vertical angle of ±35.5 °. The piping and high voltage cable route has been designed mostly in the experimental building. All the necessary pipes and cables which include purified cooling water pipes, Liquid He transfer lines, Liquid N_2 transfer lines, roughing pump pipes and SF_6 gas insulated high voltage cables are fed in parallel from the underground PIG power supply room through the 1.5 m × 2.5 m wide opening in the first floor and through the scaffold to each beam line terminals.

Prior to the construction of the fourteen injector units, a prototype unit has been designed and is being ordered to the industries. After the detailed design which was made in the last annual period (1976-1977) in cooperation with four industrial groups, evaluation of the design has been made and checked. As a result, several problems have been picked up which still need more elaborate design work.

(1) Magnet and beam dump design

Although a reflecting type magnet reduces a heat flux to the beam dump very effectively, part of the ions hit the wall of the pole piece as they are being reflected. This takes place if one takes into account the beamlet divergence from each extraction aperture, and it causes intolerable heat loading on the water jacket mounted on the surface of the pole piece. On the contrary, a bending magnet doesn't make any cooling problems in the magnet itself, but the heat loading to the beam dump is extremely high and appears to be impractical.

Meantime some basic data of the burn out heat flux for the finned tube has been obtained from the beam dumping experiment using ITS-2 test

stand. This is very important from the view point of the long pulse beam extraction. Within our reasonable parameter range of the cooling water (pressure of 4-10 atm, flow speed of 3-7 m/s) burn out takes place when the cooling pipes are exposed to the heat flux exceeding the level of 0.8-1.3 kW/cm^2. Based upon these data we reconfirmed our design heat flux of 500 w/cm^2 for the beam dumping surface with a safety margin of a factor 2.

To match with the above design criteria everywhere in dumping surface, a careful design of the reflecting magnet geometry is being made including effect of the magnetic shielding materials in a stray magnetic field.

(2) Design of the cryopump against pulsive heat loading

Eddy current from the leakage magnetic field and synchrotron radiation from the torus makes the surface temperature rise considerably.

The synchrotron radiation from the torus (amounts to 6 kW/port) and the time-changing stray magnetic field impose contradictory requirements on the materials of the cryopanel. If high conductivity materials such as copper or aluminum are used, heat deposition due to eddy current caused by the stray magnetic field makes the panel temperature rise intolerably high, resulting in the deterioration of the pumping speed, while synchrotron radiation doesn't affect appreciablly. On the contrary, low conductivity materials such as stainless steel indeed reduces eddy current losses but the absorption of the synchrotron radiation becomes significant. We chose the latter design, because careful calculation taking into account of beam limiters in the drift tube which reflect some part of radiations, bellows joint which absorb some part of radiations and other geometrical effect has shown that absorption into four large cryopanels housed in the main vacuum tank is in an acceptable level. However, a small 3×10^4 l/s cryopanels in the drift pumping room is exposed to a considerable amount of radiation, for which we determined to employ a copper or aluminum coating on a stainless steel base panel.

The cryopump is of a pressure and flow controlled pool boiling type and is directly connected to the helium refrigeration system. The prototype unit also includes target chamber, power supply unit (100 kV, 80 A), purified cooling water system, and roughing pump system. The final design of the prototype unit will be completed by the summer of 1979. The total system will be accomplished by the summer of 1981.

3. Radiofrequency Heating System

3.1 Development of waveguide coupler

Open ended waveguides can be used as a wave launcher for lower hybrid RF heating. Launcher is one of the most important components of RF heating system, since it faces directly at a plasma and heating efficiency depends mostly on its design. A phased array of multi-waveguides will be used as the launcher of the RF heating system for JT-60.

A four waveguides array was tested on JFT-2. Good coupling as well as good ion heating were obtained[1,2]. The waveguide coupler used in JFT-2 is shown in Fig. IV.3.1-1. In the early stage of the experiment, the maximum power to couple to the plasma was less than 50 kW due to the breakdown near the coupler. Improvements of the ceramic window, contact of waveguides and evacuation of the vacuum waveguides could bring a transmitting power of ∿100 kW. After these improvements, multipactor discharge was likely to limit the injected power. Launcher material was changed from aluminium to stainless steel plated with copper and further coated by titanium so as to suppress the secondary electron emission. It was possible to couple the maximum power (∿200 kW) of the system, which corresponds to 1.2 kW/cm^2 in the launcher. The RF power has been increased to 300 kW at the end of FY 1978.

We are planning to input a RF power of 10 MW to plasma core in JT-60. It requires RF power density of 3.5∿4 kW/cm^2. Test of the material and design of the optimum geometrical structure for the launcher are now being conducted to achieve the above requirement. High power microwave circuits will be prepared in 1981 so as to test the launcher with intense power density.

References

1) Nagashima, T. and Fujisawa, N.: in Proceedings of the Joint Varenna-Grenoble Int. Symp. on Heating in Toroidal Plasma, Grenoble (1978).
2) Fujii, T., et al.: to be published in the proceedings of 7th Int. Conf. Plasma Physics and Controlled Nuclear Fusion Research, Innsbruk (1978).

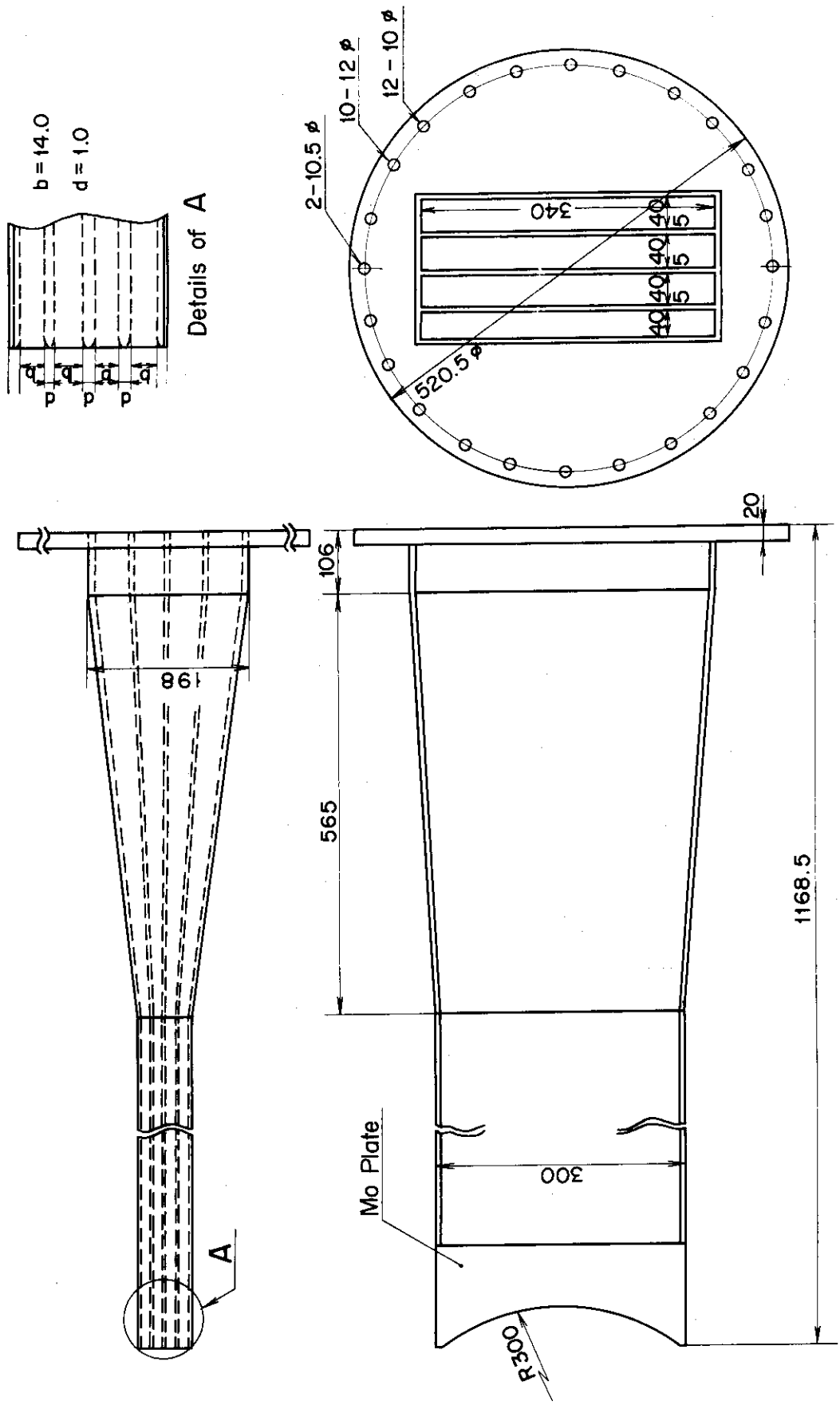

Fig. IV.3.1-1 A phased array of lower hybrid heating experiment in JFT-2.

3.2 Design study of RF heating system for JT-60

3.2.1 Outline of RF heating system for JT-60

In the JT-60 project, 10 MW-10 sec of energy deposition is planned for RF heating experiment in parallel with the 20 MW-10 sec neutral beam injection heating experiment. The design study of the RF heating system has been made with the co-operation of Nippon Electric Co., Ltd. and Tokyo Shibaura Electric Co., Ltd.

The planned RF heating system for JT-60 is shown in Fig. IV.3.2-1. Each unit of RF heating apparatus equips eight high power klystrons and other RF components, and RF power from a klystron is divided into four ways by the 3 dB couplers. Thirty-two fold ways of RF power are led to the launcher through waveguides, and RF power is launched from four RF ports into the JT-60 plasma. The launcher is replaceable without opening the JT-60 vacuum chamber, and inner space of the waveguide launcher is evacuated by the vacuum pump.

One unit of the RF amplifiers will be located on the ground floor, and the other three units on the fourth floor of RF power supply room in the JT-60 experimental building. High voltage and low voltage powers are supplied from a flywheel generator in the MG building and the central transformer substation, respectively. The central control console of the RF heating system will be located in the control building.

In the first stage (phase I), a lower hybrid heating system capable injecting of 1.25 MW during 10 sec to plasma will be constructed. Assuming the bulk heating efficiency of 30 % and transmission and insertion losses in the RF components, we will construct a RF generator of 8-10 MW. A larger RF heating system capable of delivering RF power up to 10 MW-10 sec to the plasma could be constructed in the second phase (phase II).

3.2.2 High power klystron

The absorption power P_{ab} into the JT-60 plasma is written as

$$P_{ab} = P_{dc}\eta_k\eta_c\eta_{ab}(1-\delta)$$

where P_{dc} is the d.c. input power to the klystron (beam voltage × beam current), η_k the conversion efficiency to RF power, η_c the coupling efficiency of the launcher to the plasma, η_{ab} the heating efficiency of the plasma by RF power, and δ the losses of the transmission lines and

the other circuit elements. We have obtained $\eta_c = 0.9$ and $\eta_{ab} = 0.3 \sim 0.4$ from the lower hybrid heating experiments of JFT-2. Attainable P_{dc}, η_k, and δ must be $P_{dc} = 2.4$ MW, $\eta_k \geq 0.55$ and $\delta \lesssim 0.44$ in order to obtain the required absorption power into the JT-60 plasma. Since the area where the RF heating apparatus are placed is limited and the number (4 RF ports) and area (42 cm × 65 cm each RF port) of the port is also limited, it is not practical to use RF module with smaller than 1 MW. Small modules require a large space. Therefore, we need to develop a klystron of at least 1.25 MW RF output. Such a klystron has never existed in the world, so R & D of the klystron is required. The structure of the 1.25 MW klystron from the preliminary design is shown in Fig. IV.3.2-2.

The collector as well as the magnet coil are cooled by water, and the filament by oil. Specifications of the klystron is summarized in Table IV.3.2-1. The power supply circuit delivering d.c. electric power to the filament, anode, collector, magnetic coil, and ion pump is shown in Fig. IV.3.2-3. The beam voltage is supplied by the collector power supply and the anode power supply through the rectification circuit equiping the protecting circuit to detect the over load current and over heat.

3.2.3 RF components and coupling structure

The transmission lines from the klystron to the launcher is shown in Fig. IV.3.2-4, for one unit of RF heating system. The RF power of 1.25 MW is devided into four parts using three 3dB couplers, and reaches to the launcher through the circulator and phase shifter, which must bear the load of 300 kW (or 600 kW in 100 % reflection). In the transmission lines, the rectangular waveguide or the elliptic waveguide, are used.

Lower hybrid wave energy must be coupled by means of a slow wave structure. The most practical coupler is a phased array of waveguides (grill), which has been successfully used as a coupler on the JFT-2 at JAERI, the ATC at Princeton, and the Petura at Grenoble. In the case of JT-60, the array will be 4 waveguides high by 8 waveguides wide. The side view and the top view of the coupling sections for JT-60 are shown in Fig. IV.3.2-5. The waveguide launcher is located at the angle of 40° against the meridian plane of JT-60.

The differential pumping system of the launcher is used to reduce the RF breakdown at the ceramic window and in the waveguides. The launcher

can be exchanged without disturbing the vacuum condition of JT-60 itself. The launcher is bakable at 250 °C to exhaust outgas.

Since the launcher is faced to the plasma, the direct heat damage from the plasma may taka place. Also heat is generated by the transmission loss of the electromagnetic wave. Therefore, the launcher waveguide is cooled by cold gas (nitrogen) flow.

3.2.4 Cooling system

In the RF heating system for JT-60, the cooling system is a major subsystem. Due to the high power RF output, there are many components to be cooled, such as collectors, filaments in the klystron, magnetic coils, waveguides and circulators, and so on. The heat generation in each component of the RF heating apparatus, the cooling method employed, and the flow rate of the coolant are summarized in Table IV.3.2-2. The collector is to be cooled by evaporated water.

The flow diagram of the cooling system for JT-60 is shown in Fig. IV.3.2-6. The primary water, which is produced from civil water through a water purifier and is stored in the water tank, is delivered to each part of the RF components and their recirculated through heat exchangers.

3.2.5 R & D requirements

In order to perform the program developmental works should be made on the following items.

1) Reduction of the transmission loss (δ). Since the transmission lines are very long, the line loss must be below -2.5 dB in order to satisfy the projected power into the plasma. For even this line loss of -2.5 dB, about half a RF power is lost during the transmission. The high power circulator with low losses must be developed.

2) Higher efficiencies (η_k, η_c and η_{ab}). The value of η_k will be about 0.6 at maximum for the present. The values of η_c and η_{ab} have a margin of improvement, which depends on our research in the coupling test and LHH experiments in JFT-2.

3) Safety. Since the RF heating system for JT-60 yields very high power electromagnetic waves, the RF leak must be diminished around the klystrons and waveguides. X rays from the collector must be shielded.

The following list summarizes the areas for research and development efforts. R & D on item #1 are now investigated on JFT-2 and those on item

#2 will be made in the R & D of 1 MW - 10 sec klystron, which will begin from 1980.

	Item #1	Item #2
Transmission line RF vacuum windows		*
Transmission line dc safety breaks		*
RF breakdown suppression in the transmission line	*	*
Material test for RF system components		*
RF test to determine the limit on RF power density at the plasma boundary	*	*
High power testing of RF components		*

Table IV.3.2-1 The ability of the JT-60 klystron

		Case A	Case B
ELECTRICAL			
Heater Power	W	500	300
Output Power (Saturation)	MW	1.35	1.2
Bandwidth (Instantaneous 1 dB)	MHz	9	6
Efficiency	%	50	55(57)
Power Gain	dB	39	43.4
MECHANICAL			
Input RF Coupling		Type-N	Type-N
Output RF Coupling		WR-650	WR-510
Dimension Length	mm	2700	2500
Weights			
Klystron	kg	1500	500
Magnet	kg	400	300
OPERATION			
Frequency	GHz	1.7	1.7
Rf Pulse Length Maximum	sec	10	10
Repetition Period	min	10	10
Output Power	MW	1.2	1.1-1.2
Driving Power	W	160	50(100)
Beam Voltage	kV	87	90
Beam Current	A	31	27.2
Body, Collector, Anode Voltage	kV	87	80(90)
Body Current	A	1	0.5(1)

Table IV.3.2-2 Cooling system for JT-60 RF heating apparatus

Cooling Objects	Cooling Method	Heat Generated (kcal/hour)	Flow rate (l/min.)
Filament	Oil Cooling	428	
Collector	Evaporated Water	42570	
Body	Water Cooling	1100	110
Coil for Magnet	Water Cooling	6000	10
Phase Adjuster	Water Cooling	960	1.6
Circulator	Water Cooling	2552	571
3 dB Coupler	Water Cooling	1539	2.6
Dummy Load	Water Cooling	17136	571
Launcher	Gas Cooling (Nitrogen)	4285	
Pump	Water Cooling	1700	

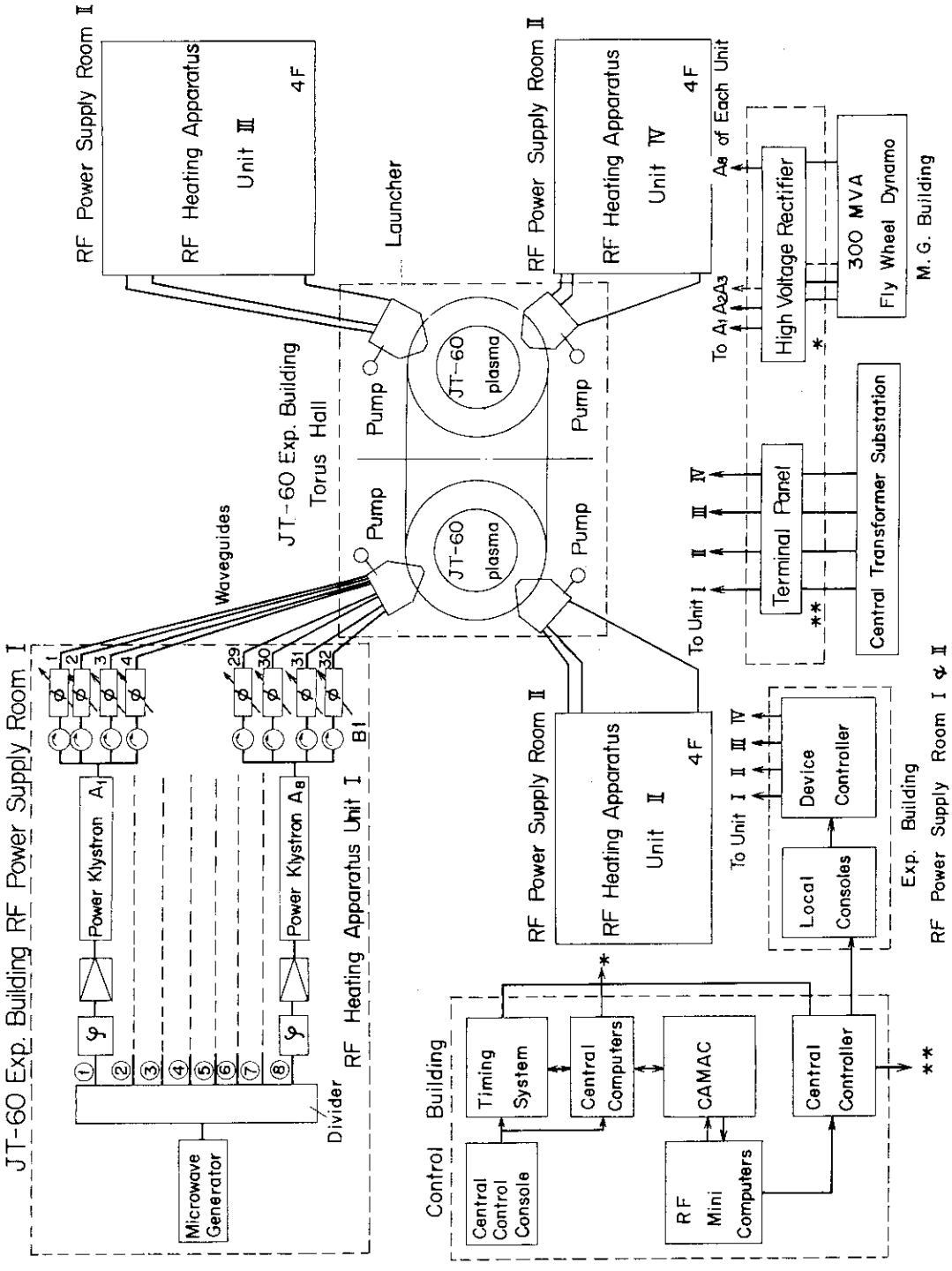

Fig. IV.3.2-1 The planned RF heating system for JT-60

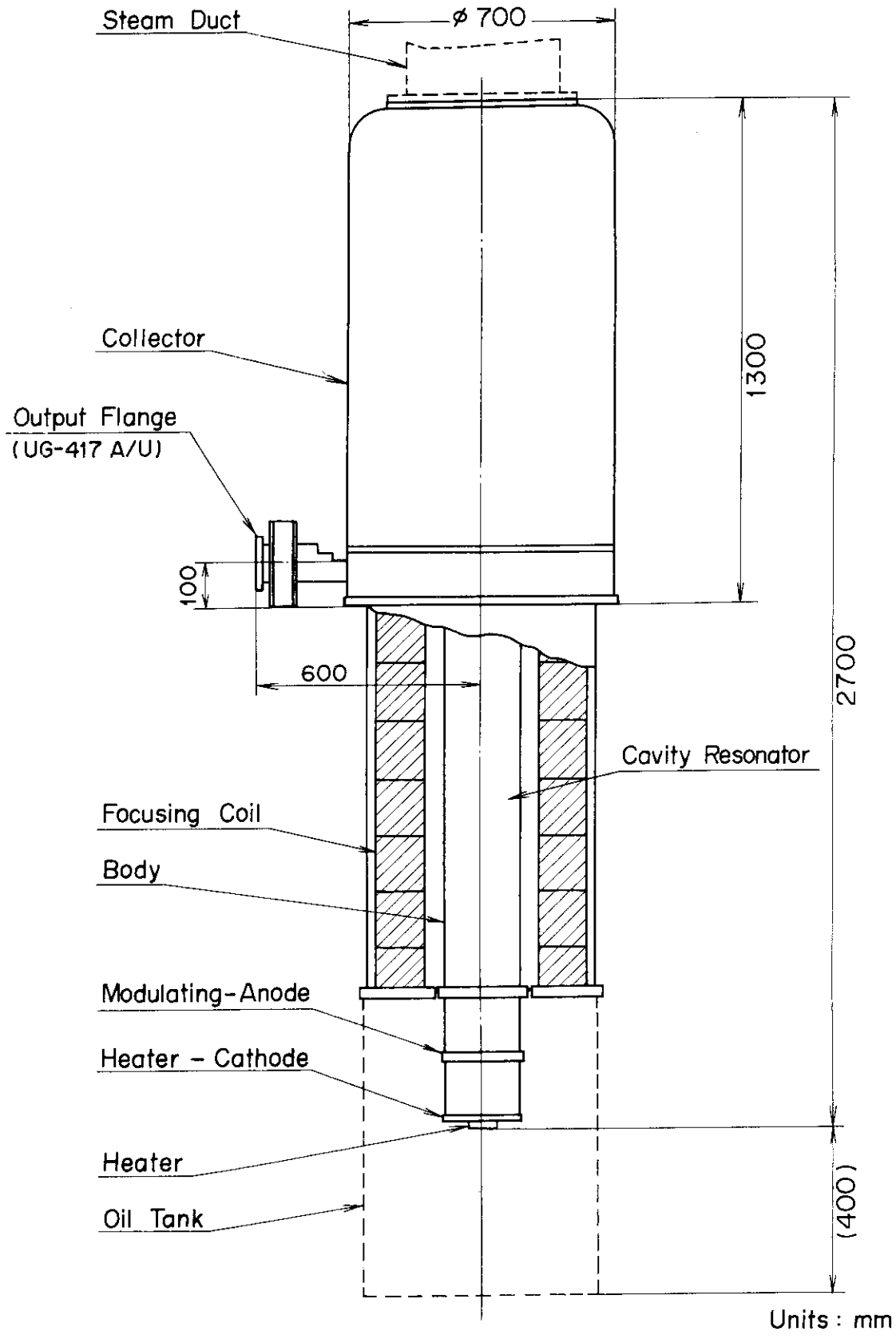

Fig. IV.3.2-2 The outline of 1.25 MW klystron.

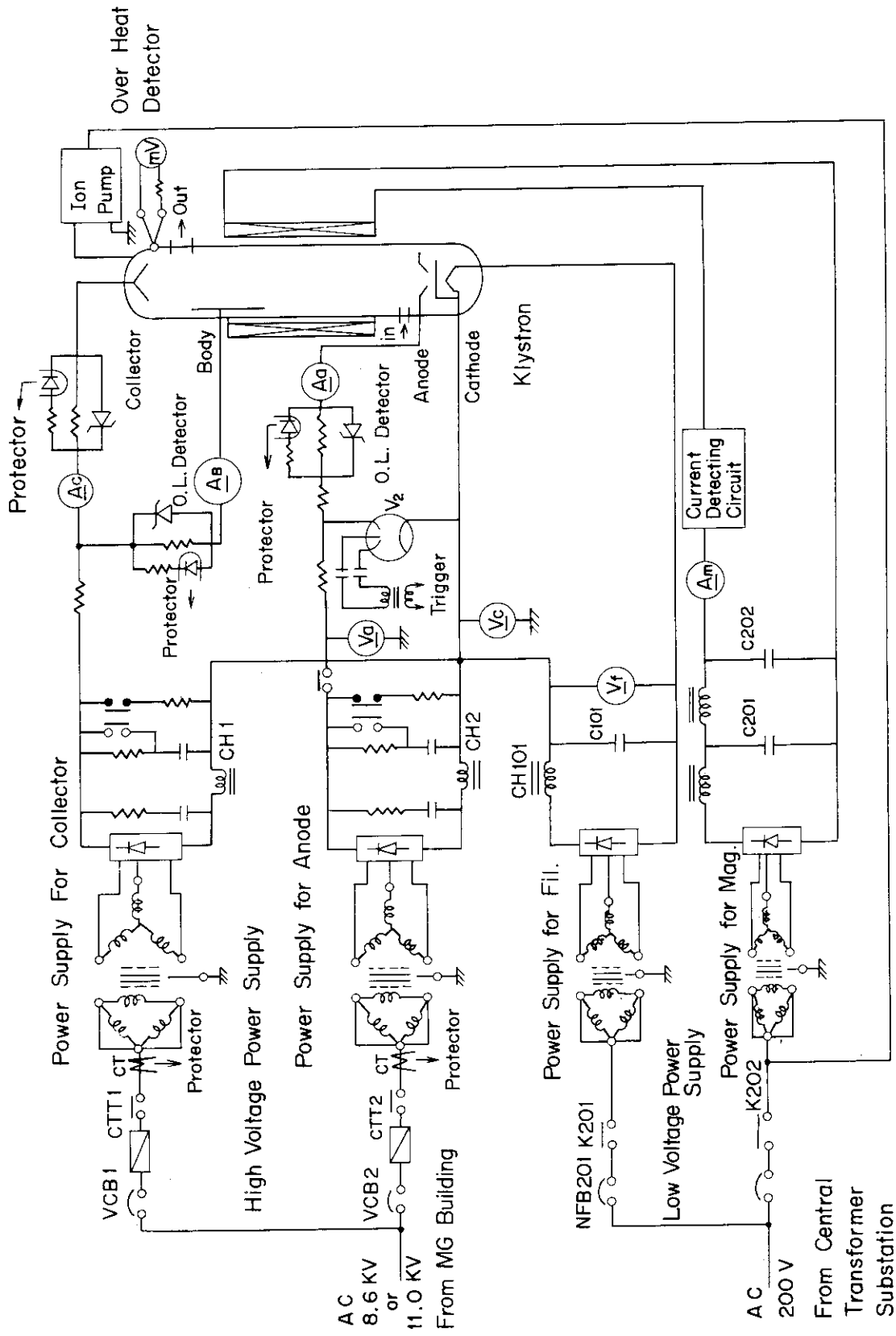

Fig. IV.3.2-3 The circuit of the power supply for JT-60 klystron

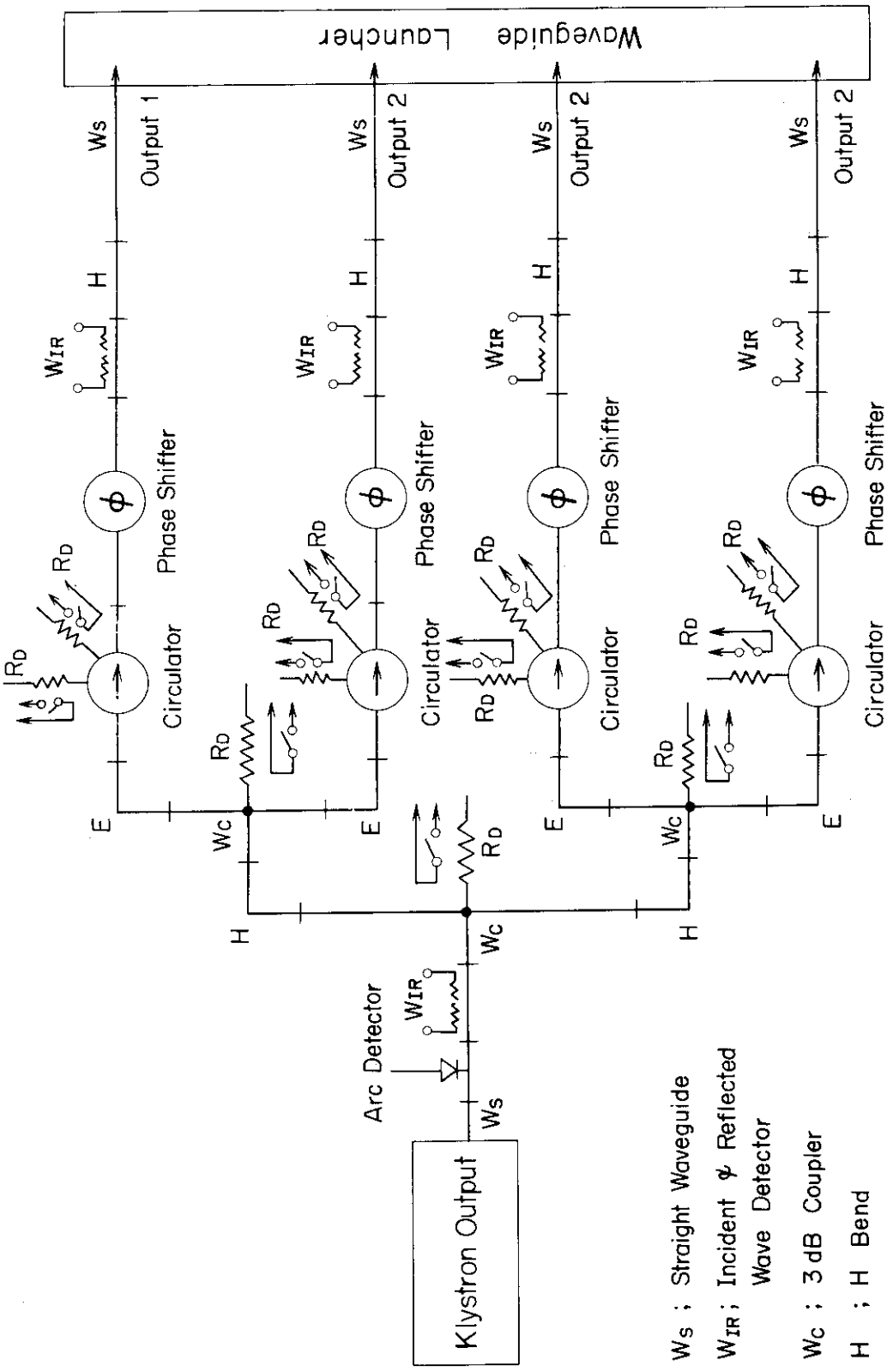

Fig. IV.3.2-4 The transmission lines from the klystron to the waveguide launcher

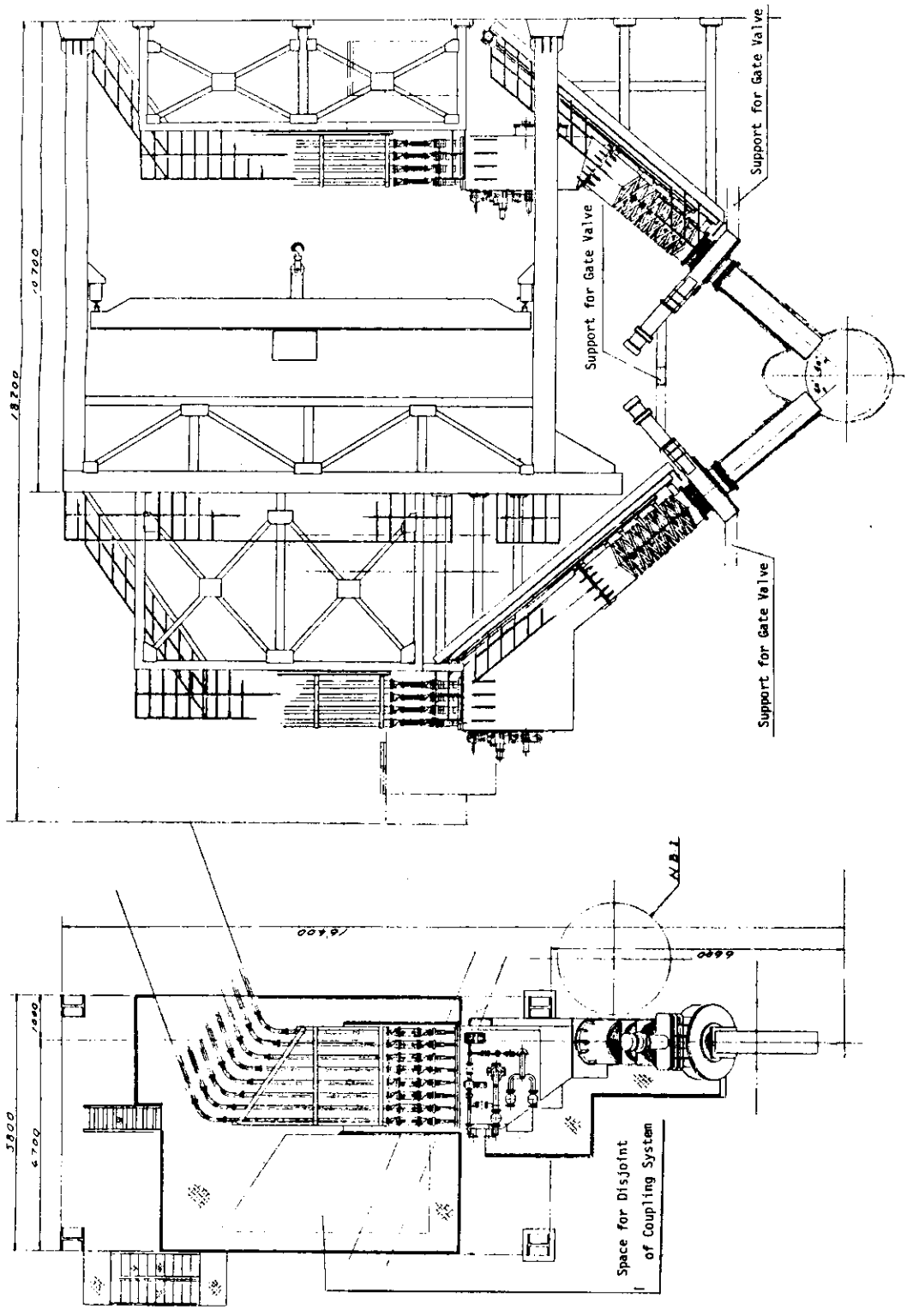

Fig. IV.3.2-5 The side view and the ground plane of the coupling system for JT-60 in the torus hall.

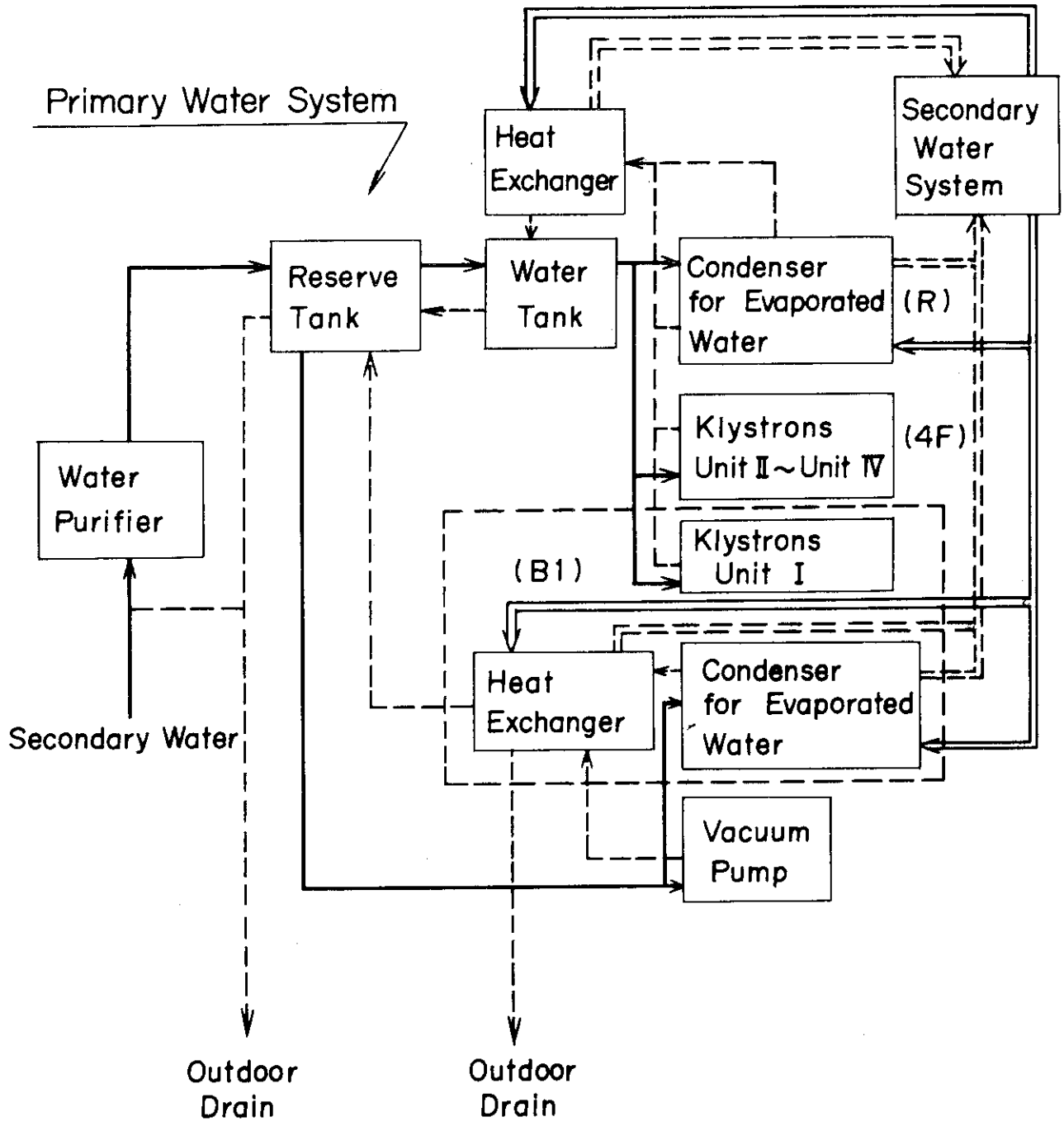

Fig. IV.3.2-6 Flow diagram of the cooling system for JT-60.

V. SURFACE SCIENCE AND VACUUM TECHNOLOGY

1. Introduction

The particle-surface interaction research program in the division of thermonuclear fusion research was started in April 1975, and has been continued in close connection with the JT-60 project and with the JFT-2 and -2a experiments.

The main objective of this program is to investigate the individual phenomena in plasma-wall interaction which can occur in today's as well as next generation tokamaks. Impurities are released from the first wall which is bombarded with energetic and/or chemically active particles leaking from a tokamak plasma through complicated processes including sputtering, particle-induced desorption, chemical reaction, evaporation, arcing, and blistering. Backscattering, trapping and reemission of the fuel particles are also of great concerns for the investigation of the recycling processes in plasma-wall systems.

In the fiscal years of 1975 and 1976, two ion accelerators, LSP and HSP, were designed and constructed[1,2] In the following year of 1977, precise measurements of the proton sputtering yield of molybdenum were made in the energy range of 0.2 - 6 keV by using LSP[3]. Measurements were also made on the dose effect on surface topography and sputtering yield of polycrystalline molybdenum by neon ion bombardment[4]. Experiments on the effect of surface roughness on various types of erosion showed that the number of sputtered particles can be effectively reduced on a honeycomb wall[5] and blister formation becomes less severe in molybdenum wall with a multigroove microstructure[6,7].

In this fiscal year of 1978, two instrumental developments have been taken place. One is the design and construction of a special scanning electron microscope which enables us to observe sample surfaces under ion bombardment[8]. This powerful instrument was connected to an exclusive beam line of HSP.

The other is the conceptual design of an ion source for refractory elements[9]. As plasma parameters of tokamaks advance and duration of a plasma discharge increases, the plasma will be most influenced by impurity influx due to self-sputtering of walls. This is because very small impurity concentrations can lead to a runaway situation if the self-sputtering yield exceeds unity. Therefore, evaluation of the self-sputtering yield of various wall materials in the energy range of 0.5 -

10 KeV (equivalent to boundary plasma temperature) is necessary as well as of the sputtering yield by light ion bombardment. This design study was performed for the construction of a potential ion source for the self-sputtering experiments. This work was done under a contract with ULVAC Corporation.

As to the sputtering experiments with low energy light ions, the work on the angular distribution of sputtered atoms by neon ion bombardment was continued and developed in this fiscal year. When technical materials are subjected to ion bombardment, the surface topography gradually changes and may influence the angular distribution of the sputtered atoms. In this year annealed and non-annealed polycrystalline molybdenum samples with respective grain sizes of ≈50 and ≈5 μm were bombarded with 0,6 and 1,5 KeV ion beams at a 45° angle of incidence[10].

Impurities in a tokamak plasma will lose energy by line and recombination radiation and bremsstrahlung. Generally speaking, the higher effective atomic number impurities will radiate greater amounts of power. Therefore, there is increasing interest in the use of low-Z materials and low-Z surface coatings for the first wall. In fact, low-Z materials and low-Z surface coatings are being laid on the table for consideration for JT-60. In this connection, we have measured the erosion rate of carbon by thermal atomic hydrogen in the surface temperature range of 100 - 900 °C because the chemical reaction of hydrogen with carbon was considered to be a serious problem. The experimental result implies that the carbon surface can be made passive to atomic hydrogen by a surface treatment[11].

The mechanism of blistering is still a controversial topic. In this fiscal year, the special scanning electron microscope was used to examine the behavior of polycrystalline molybdenum with different pre-treatments as a function of implanted helium dose. In a 1300 °C-annealed sample it has been found that the critical fluence for blister formation varies according to the crystal face of grains. In a sample pre-implanted with 100 KeV helium and subsequently annealed at 800 °C, it has also been observed that exfoliation takes precedence of blistering and that it happens in a moment[12].

In the previous year it was demonstrated experimentally that the effect of surface roughness is to inhibit the growth of blisters. In this connection, an investigation has been made on the possibilities of fabricating molybdenum microhoneycomb structures under a contract with ANELVA Corporation[13]. Pattern fabrication was accomplished by protecting

a substrate with a SiO_2 mask during reactive ion etching to permit only selected substrate areas to receive the etchant ($C\ell^+$ and $C\ell°$). A micro-honeycomb structure whose unit was 3 μm × 3 μm and 1 μm deep could be formed.

In order to control the low-Z impurities in large tokamaks, vacuum technological developments must be accompanied with the investigation of the particle-surface interaction. Studies on wall cleaning procedures including vacuum pumping, reduction of outgassing and leaks, discharge cleaning, and in-situ coatings were started in FY 1977 in cooperation with JT-60 Project Office II. In this fiscal year a more concrete form has been given to the project for developing wall cleaning and leak testing procedures in large tokamaks. The introduction of a torus pumping system with 18 K refrigerator cryopumps[14] has been put off for JT-60 because of some technological difficulties.

2. Instrumental development

2.1 Construction of special SEM for surface erosion studies[8]

The design and construction of a special scanning electron microscope has been made for the simultaneous and continuous observation of sample surfaces under ion bombardment. The system design was started in April 1977, and the finished instrument was connected to an exclusive beam line of HSP in May 1978.

The system is basically a modified scanning electron microscope and is equipped with some special parts. A solid-state detector for detecting backscattered electrons from sample surface was newly developed and installed in the SEM, which enables us to observe the backscattered electron image. In order to measure the ion fluence to sample surfaces an ion current integrator was set in the beam line. A 1200 ℓ/sec oil diffusion pump, a 400 ℓ/sec Ti-sublimation pump, a liquid nitrogen trap, and two mechanical pumps serve to evacuate the system. An operating pressure of around 10^{-8} Torr was recorded in the sample chamber. An overall view of the special scanning electron microscope is shown in Fig. V-1.

A performance test on molybdenum surface under 100 KeV helium ion bombardment showed an image resolution of 1000 Å, which is high enough for the observation and recording of surface deformation due to sputtering and blistering. Some experimental results obtained with the new instrument will be reviewed in Section 5.

2.2 Design study of metal ion source for self-sputtering experiments[9)]

The design study of a new type of metal ion source has been performed for the construction of a potential ion source for self-sputtering yield measurements. This ion source applies the principle of the magnetron. Its distinctive feature is that it has no filament but is equipped with an exclusive electron gun which can heat a massive cathode to emit thermal electrons. In conventional magnetron ion sources an electric current through the filament causes an undesirable magnetic field for the sustention of a stable arc and the lifetime of the filament is generally short. These difficulties may be solved in the new ion source.

Figure V-2 shows schematically the construction of the magnetron ion source. It consists of an anode cylinder, a cathode rod (sputter electrode), a Pierce-type electron gun, a gas inlet, an extraction electrode and two external magnet coils. The size of the cathode rod is determined from the required ion beam current and lifetime. Then the maximum electron beam power for the cathode heating is calculated by solving differential equations on thermal balance. For example, a cathode rod of molybdenum 10 mm in diameter and 9 mm long, supported by a tungsten wire 2 mm in diameter, will be heated to 2500 K by an electron beam of 250 W from the Pierce-type electron gun. A magnetic field of 500 gauss is applied to the discharge chamber perpendicularly to the direction of extracting ion beam. The argon pressure in the discharge chamber is about 1.3×10^{-3} Torr. The molybdenum rod is sputtered out by argon ion bombardment. The molybdenum atoms thus produced are ionized by electrons in the magnetron chamber. It is estimated that at 30 kV acceleration a molybdenum ion current of about 10 μA can be obtained at the target.

3. Sputtering experiments with low energy light ions[10)]

When the first wall is subjected to ion bombardment, the surface topography gradually changes and may influence the angular distribution of the sputtered atoms. Last year measurements were made on the dose effect on surface topography and sputtering yield of polycrystalline molybdenum by neon ion bombardment[4)]. The eroded surface was found to be generally covered with facets of protuberances and depressions because of different sputtering yields depending on grains.

These experiments were continued and developed in the following year of 1978. In this year annealed and non-annealed polycrystalline molybdenum samples with respective grain sizes of ≈50 and ≈5 μm were bombarded with 0.6 and 1.5 KeV neon ion beams. The angles of incidence were chosen to be 0° and 45° with respect to the surface normal. The experimental set-up is shown in Fig. V-3. The incident ion beam was mass-analyzed and defined by a 4.5 mm-diameter hole. The current density was 50 - 100 $\mu A/cm^2$ at the sample surface. During ion bombardment the pressure in the chamber was around 10^{-7} Torr and the target temperature was ambient. Angular distributions of sputtered particles were measured by depositing the particles on glass substrates which were distributed on a semi-spherical holder 76 mm in diameter. The amount of molybdenum deposited on the glass substrates was relatively measured by the micro-densitometer and then the absolute amount was determined by an atomic absorption spectrometer with a carbon rod atomizer. The agreement between the values measured by the two methods was quite good.

Figures V-4 and V-5 show the measured angular distributions of sputtered particles from an annealed and a non-annealed molybdenum samples bombarded with 0.6 KeV neon ions at a 45° angle of incidence. In conclusion, the grain size influences both the topography of eroded surface and the angular distribution of emitted particles. Many microscopic hills were formed on the bombarded surfaces in case of oblique incidence. The ratio of the lengths of the hillside to the hilltop increases with decreasing the grain size. The more forward emission and the stronger dose effect are observed as the grain size becomes smaller. The effect of the grain size can be described by the model including both the sputtering yield and the anisotropy parameters of the angular distribution dependent on the angle of incidence. The angular distribution at the normal incidence of 1.5 KeV neon ions obeys the cosine law whereas distributions at the oblique incidence show the more forward emission for the lower incident energy. The result can be understood by the depth of atomic collisions which contribute to the sputtering.

4. Interaction of atomic hydrogen with carbon[11)]

Carbon has been proposed as a candidate low-Z material for the first wall due to its high heat conductivity and low volatility at high temperatures. However, the chemical reaction of hydrogen with carbon is considered

to be a difficult problem. The bombardment of carbon with hydrogen ions and atoms is well known to produce gaseous hydrocarbons such as methane and acetylene. It has been reported that the methane production is temperature dependent and for energetic ions it has a pronounced maximum at a surface temperature of about 500 °C[15] and for thermal atoms it decreases monotonically with increasing temperature[16].

In this connection, we have measured the erosion rate of carbon by thermal atomic hydrogen in the surface temperature range of 100 - 900 °C. The experimental arrangement used is shown schematically in Fig. V-6. It consists of a gas inlet, a hydrogen atomizer, a reaction vessel, a quadrupole mass analyzer and a pumping system. In this arrangement some of the hydrogen molecules impinging on the rhenium hot filament are dissociated into atoms. The atomic hydrogen produced flows through a Teflon-coated glass tube from the atomizer into the reaction vessel because very small amount of atomic hydrogen can recombine on Teflon[17]. Thus, the pressure of atomic hydrogen in the reaction vessel could be varied from 10^{-8} to 10^{-7} Torr, which corresponded to the fluxes from 2×10^{13} to 2×10^{14} atoms/cm^2·sec. The partial pressures of atomic hydrogen, molecular hydrogen and methane were measured with the quadrupole mass analyzer. The reaction vessel was made of quartz. The carbon samples (pyrolytic graphite and nuclear grade graphite) 20 mm in diameter and 1 mm thick were heated with an infrared lamp through a quartz window and their temperatures were measured with a platinum-rhodium thermocouple. Prior to each experiment, samples were heated in high vacuum to 1000 °C for 60 min.

Figure V-7 shows a measurement of methane formation rate from pyrolytic graphite exposed to atomic hydrogen. The sample was heated up in steps of 100 degrees from 100 to 900 °C. In the initial run, a peak in the methane formation rate was observed between 500 and 600 °C (○). However, the rate decreased and the peak disappeared in the measured temperature range after the sample had been exposed to hydrogen atoms to a fluence in excess of 10^{18} atoms/cm^2 at about 500 °C (●). This experimental result implies that the graphite surface can be made passive to atomic hydrogen by a surface treatment. The time dependence of methane production rate at above 500 °C also supports the phenomenon. On the other hand, the inactive graphite surface has been found to be restored again to the

initial state when it is exposed to air. The effect of atomic hydrogen on nuclear grade graphite was also similar to that on pyrolytic graphite.

The surface passivation of carbon may be attributed to the depletion of free radicals on the surface, or to the decrease in the ratio of the production rate of methane to the rate of recombination of hydrogen on the surface. For the satisfactory explanation, however, a direct measurement of the adsorbed state on the surface will be necessary.

5. In-situ and continuous observation of molybdenum surfaces under ion bombardment[12)]

A large number of investigations deals with helium blistering over a range of materials, energies and temperatures. However, the mechanism of blistering is still a controversial topic. In FY 1978, the special scanning electron microscope which is described in Section 2.1 was used to examine the behavior of polycrystalline molybdenum as a function of implanted helium dose. Molybdenum samples with different pre-treatments were bombarded with 100 keV helium ions to fluences of about 10^{18} ions/cm^2 at ambient room temperature. The angle of incidence was 45° with respect to the surface normal.

For the first experiment, molybdenum samples, 10 mm × 10 mm and 1 mm thick, were finished with 0.3 μm alumina powder and annealed at 1300 °C for 1 hour in high vacuum. Figure V-8 is a series of scanning electron micrographs showing the developments of the surface erosion in an annealed polycrystalline molybdenum sample. The image contrast was formed with backscattered electrons. Normal blisters occur all over the surface but it has been shown that the critical fluence for blistering varies according to the crystal face of grains. Prior to the second experiment, a 1300 °C-annealed sample was pre-implanted with 100 keV helium ions to a fluence of 4.4×10^{17} ions/cm^2 and successively annealed at 800 °C for 1 hour. This was followed by the same ion bombardment at room temperature. In this case it has been found that exfoliation occurred from grain to grain and it happened in a moment (see Fig. V-9). It has been reported in the literature[18)] that small bubbles of ∿25 Å diameter are formed in the lattice at a low fluence. The transition from the blistering mode to the exfoliation mode will be explained by the ease of propagation of cracks which originate from the bubbles in the implanted layer.

When the pre-implanted sample was subjected to 1300 °C annealing a porous interconnected structure occurred in the implanted region (see Fig. V-10) and it has been considered that this porous structure allows the helium to escape to the surface. It has been also demonstrated that blistering stops at very high doses ($\sim 10^{20}$ ions/cm^2) where the surface has been eroded owing to sputtering and blistering.

References

1) Tsukakoshi, O., Narusawa, T., Mizuno, M., Sone, K., Ohtsuka, H., and Komiya, S.: JAERI-M 6331 (1975).
2) Obara, K., Ohtsuka, H., Yamada, R., Abe, T., and Sone, K.: JAERI-M 7250 (1977).
3) Ohtsuka, H., Yamada, R., Sone, K., Saidoh, M., and Abe, T.: J. Nucl. Materials 76 & 77 (1978) 188.
4) Yamada, R., Saidoh, M., Sone, K., and Ohtsuka, H.: J. Nucl. Materials 82 (1979) 155.
5) Abe, T., Obara, K., Nakamura, H., Sone, K., Ohtsuka, H., Yamada, R., Saidoh, M., and Shimizu, M.: J. Nucl. Sci. Technol. 15 (1978) 471.
6) Saidoh, M., Sone, K., Yamada, R., Ohtsuka, H., and Murakami, Y.: JAERI-M 7182 (1977).
7) Sone, K., Saidoh, M., Yamada, R., and Ohtsuka, H.: J. Nucl. Materials 76 & 77 (1978) 240.
8) Obara, K., Abe, T., and Sone, K.: JAERI-M 7797 (1978).
9) "Metal ion source for self-sputtering experiments" (1979), a report in collaboration with ULVAC Corp. (not published).
10) Yamada, R., Sone, K., Ohtsuka, H., and Saidoh, M.: J. Nucl. Materials 84 (1979) 101.
11) Abe, T., Obara, K., and Murakami, Y.: to be published in J. Nucl. Materials.
12) Saidoh, M., Sone, K., Yamada, R., and Ohtsuka, H.: JAERI-M 7997 (1978).
13) "Fabrication of microhoneycomb structure" (1979), a report in collaboration with ANELVA Corp. (not published).
14) Annual Report of the Division of Thermonuclear Fusion Research and the Division of Large Tokamak Development, for the period of April, 1977 to March, 1978, JAERI-M 8059, p.109.
15) Roth, J., Bohdansky, J., Poschenrieder, W., and Sinha, M.K.: J. Nucl. Materials 63 (1976) 222.
16) Balooch, M., and Olander, D.R.: J. Chem. Phys. 63 (1975) 4772.

17) Zitzewitz, P.W., and Ramsey, N.F.: Phys. Rev. A3 (1971) 51.

18) Mazey, D.J., Eyre, B.L., Evans, J.H., Erents, S.K., and McCracken, G.M.: J. Nucl. Materials 64 (1977) 145.

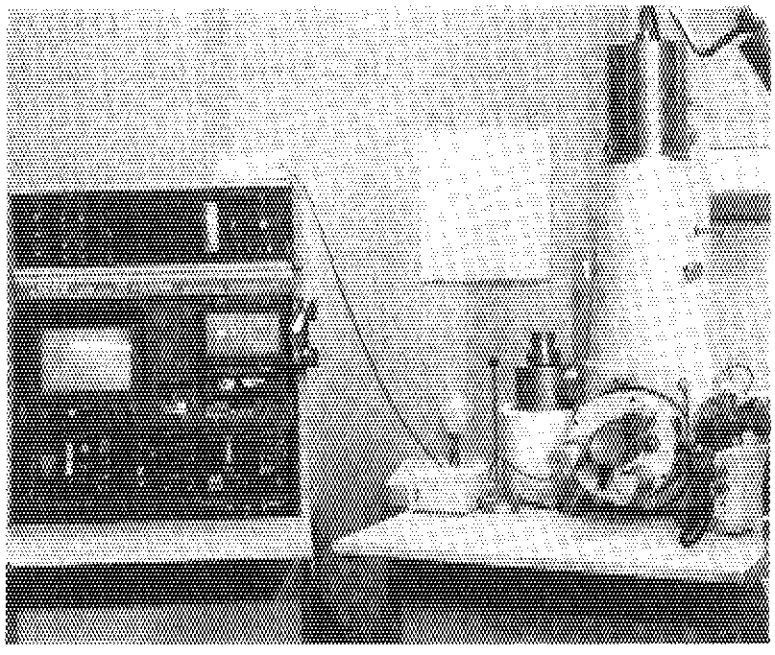

Fig. V-1 Over-all view of special scanning electron microscope for simultaneous and continuous observation of sample surfaces under ion bombardment.

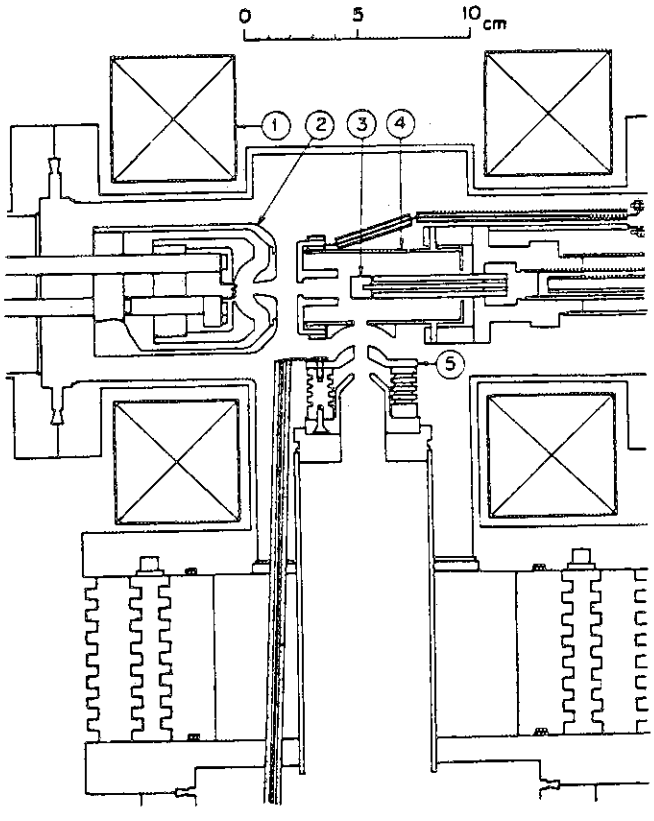

Fig. V-2 Schematic diagram of new magnetron ion source (1) magnet coils, (2) electron gun, (3) cathode rod (sputter electrode), (4) anode cylinder, and (5) extraction electrode.

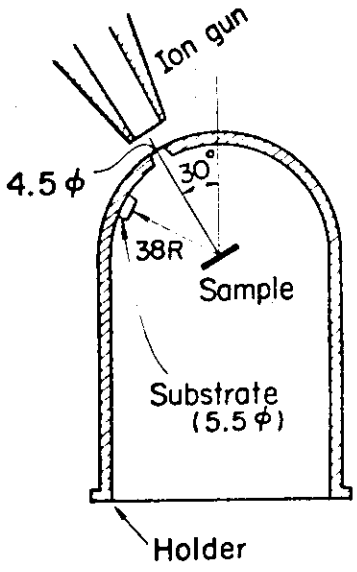

Fig. V-3 Experimental set-up for measurement of angular distribution of sputtered atoms.

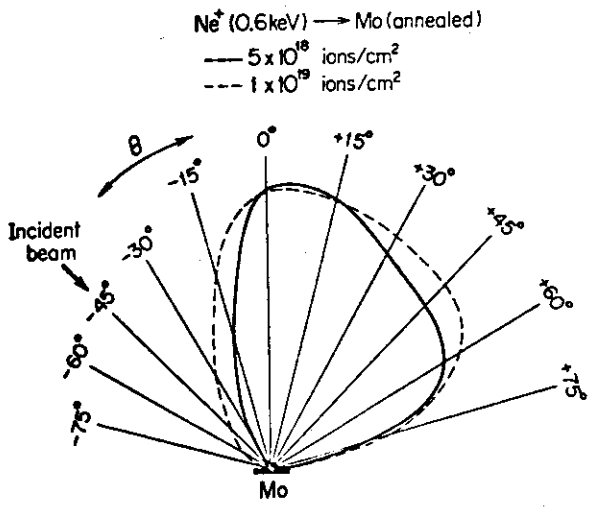

Fig.V-4 Measured angular distributions of sputtered particles from annealed molybdenum plate bombarded with 0.6 keV neon ions at 45° angle of incidence.

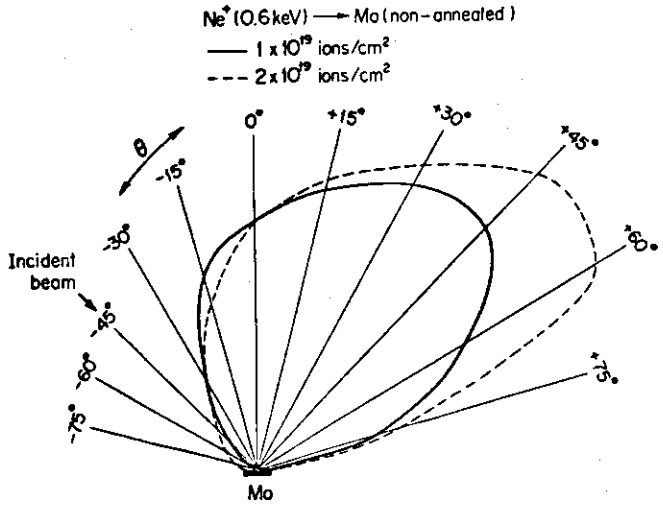

Fig.V-5 Measured angular distributions of sputtered particles from non-annealed molybdenum plate bombarded with 0.6 keV neon ions at 45° angle of incidence.

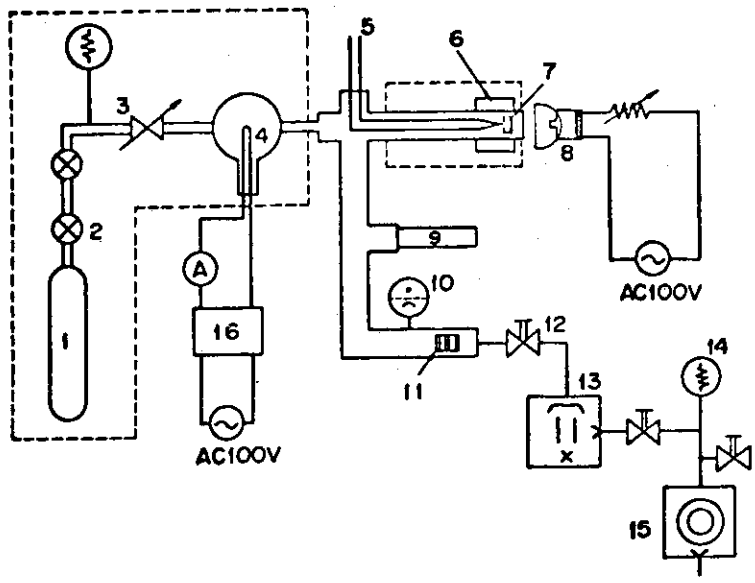

Fig. V-6 Experimental set-up for measurement of erosion rate of carbon by thermal atomic hydrogen
1 - 3 gas inlet, 4 hydrogen atomizer, 7 reaction vessel, 9 quadrupole mass analyzer, and 11 - 15 pumping system.

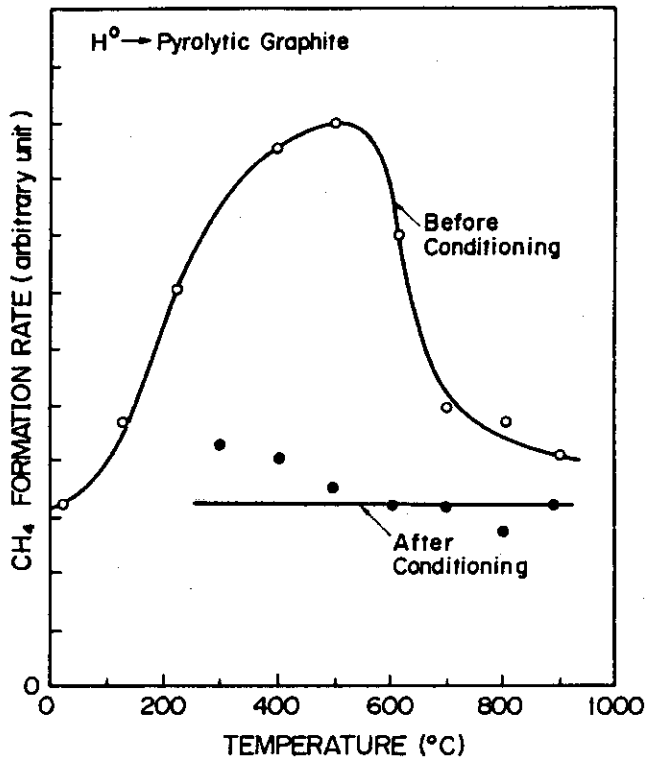

Fig.V-7 Measured methane production rate from pyrolytic graphite as a function of target temperature.

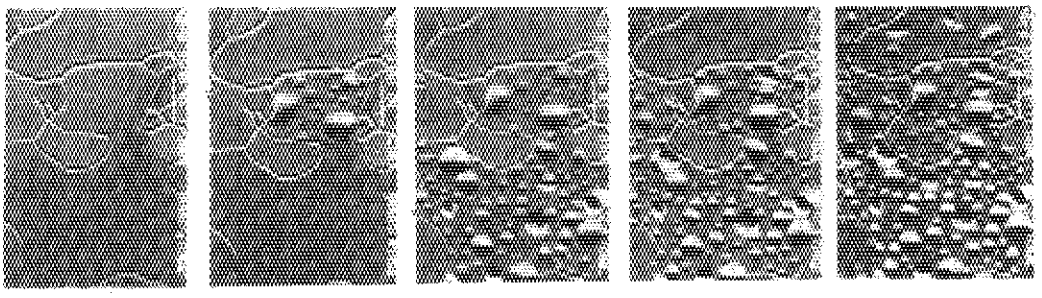

Fig. V-8 Series of scanning electron micrographs showing developments of surface erosion in polycrystalline molybdenum. Prior to bombardment sample was annealed at 1300 °C for 1 hour in high vacuum. It was bombarded with 100 keV helium ions up to a fluence of 9.0×10^{17} ions/cm^2 at ambient room temperature.

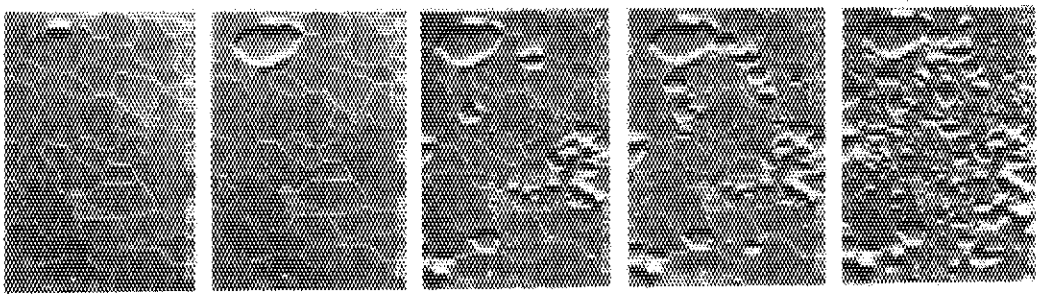

Fig. V-9 Series of scanning electron micrographs showing developments of surface erosion in polycrystalline molybdenum. Prior to bombardment sample was pre-implanted with 100 keV helium to a fluence of 4.4×10^{17} ions/cm^2 and subsequently annealed at 800°C for 1 hour. It was bombarded with 100 keV helium ions up to a fluence of 5.4×10^{17} ions/cm^2 at room temperature.

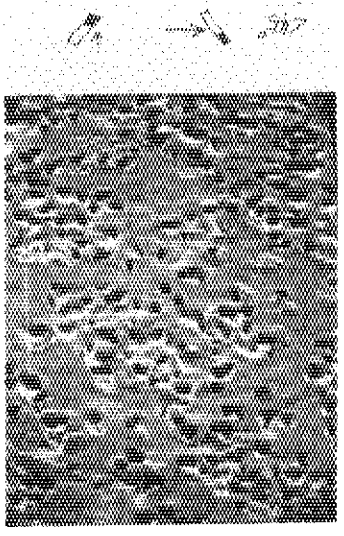

Fig.V-10 Scanning electron micrograph of eroded molybdenum surface. 100 keV-helium implanted sample was subjected to annealing at 1300°C showing porous interconnected structure.

VI. SUPERCONDUCTING MAGNET DEVELOPMENT

1. Introduction

The main objective of research and development of superconducting magnet and its system for fusion research is the construction of a superconducting tokamak machine, for example, Plasma Engineering Test Facility (PETF) after JT-60.

For this purpose, JAERI has done the following works in FY 78;

1. construction of conductor test facility,
2. improvement of the heat flux through the conductor surface to liquid helium,
3. measurements for the improvement of the critical current density of Nb-Ti conductor,
4. verification of Nb_3Sn multifilamentary conductor,
5. design and sample manufacturing of Nb_3Sn 11 T 12 kA forced cooling conductor,
6. construction of cluster test facility, including helium liquefier/refrigerator,
7. detailed design of the Japanese coil for Large Coil Task,
8. winding test of the Japanese LCT conductor.

Large Coil Task is being carried out on the basis of IEA agreement (LCT. Annex-I), which JAERI signed in April of 1978. It is emphasized that many problems concerning to the actual construction of large superconducting tokamak machine have been investigated through the detailed design of Japanese LCT coil and many verification tests.

2. Detailed design and construction of cluster test facility

Cluster test facility consists of two cluster test coils, vacuum chamber system, data acquisition system and refrigeration system.

This facility has a capability to carry out the verification test of a test module coil which is to be constructed by the design with an original idea and this test module coil has an enough size to examine with less difficulty the mechanical and thermodynamical phenomena in such a large coil as will be used in LCT[1)]. Therefore, this flexibility will make it possible to verify new ideas which will be proposed during LCT and after LCT.

Cluster test coils whose parameters are shown in Table VI.2-1 are now under construction and the test module coil is under detailed design. Figure VI.2-1 shows a bird's eye view of these coils. Supporting systems of this facility are also under construction and especially for refrigeration system, a new cryogenic system has been designed for cooldown, steady state operation and warmup of the coils. A two cycling system, separated turbine expansion and liquefaction, is employed in order to avoid contaminations and damage of turbo-expanders during long cooling operation.

The components and thermodynamical cycle of this system are shown in Fig. VI.2-2. The system consists of cold box, feed and recovery compressor, recycle compressor, liquid helium-dewar, helium purifier, gas bag, impure gas tank and pure gas cardle. Vacuum insulated cold box includes the low temperature components, heat exchangers, turbo-expanders, isolated valves and interconnecting pipe. Two turbo-expanders with static gas bearing are operated at different temperature level. Joule-Thomson valve is automatically controlled by the outlet temperature of the cold turbo-expander (turbine 2). The liquid helium dewar is of vertical design, the helium boiling loss is less than 0.6 percent a day. Swash plate driving system is applied to the compressors for the purpose of the high compression efficiency, low noise, reliability and space performance. A pair of helium purifier are provided to remove impurities from the recovery helium flow and the full helium compressor flow for initial system clean-up. The system is operated at medium pressure (about 18 atm) for the sake of high reliability during long term operation.

The helium liquefier/refrigerator can be utilized as either a liquefier or a refrigerator at 4.5 K, or a combined system of liquefier and refrigerator depending on the type of thermal load. The system may be operated with or without warm turbo-expander (turbine 1) depending on capacity requirements. The system have a capacity of 100 liters of liquid helium per hour or 220 watts of refrigeration at 4.5 K with warm turbo-expander operation. Without warm turbo-expander operation, the system have a capacity of 60 liters per hour or 200 watts of refrigeration at 4.5 K.

3. Japanese coil design for LCT

According to the basic specification for LCT, detailed design for the Japanese LCT coil has been accomplished in March 1979. During the course of this work, detailed analysis and design efforts have been made on the following items;[2,3,4,5)]

1. conductor stability, 2. electrical fields and forces, 3. structural mechanics, 4. magnet cooldown and warmup, 5. pulse field and thermal loss, 6. magnet quench and protection, 7. fabrication, 8. instrumentation, 9. quality control and 10. others.

Sections of the coil are shown in Fig. VI.3-1 and 3-2 and key parameters are summarized in Table VI.3-1.

Principal features of Japanese LCT coil design are;

1. Good stability of the magnet based upon the high heat flux through the conductor surface to liquid helium, and
2. "Edge-wise and pancake" winding of the superconducting cable.

The first feature is an important technique for the design and construction of large superconducting magnet system and the development of the second feature will contribute to reduce the pulse field loss in the tokamak toroidal field coil, which is one of the most serious problem in the design for the next tokamak machine.

Many verification tests have been carried out and the winding test of the cable did not indicate the exsistence of so many problems in edge-wise and pancake winding which has been thought to be difficult[6)].

The manufacturing of the coil will begin within a few months and is expected to be completed in mid 1981. Facilities and building for the domestic test of the Japanese coil are also under detailed design and will be prepared in 1981.

4. Conductor research and developments for LCT

Test facilities for superconducting cable have been installed. They are;

1. 8.5 T, 24 cm bore Nb-Ti superconducting magnet.
2. 13 T, 7 cm bore Nb_3Sn superconducting magnet.
3. 5.5 T, 10 ton tensile test facility.
4. 12 kA DC power supply.

The manufacturing of these facilities was a good work for the development of the superconducting coil and especially in case of 8.5 T magnet, Nb-Ti conductor is operated at the maximum field of 9.3 T[7].

Using these test facilities, measurements and verification tests have been carried out for the research and development of the large current superconducting cable. It is quite important to improve the critical current density of Nb-Ti in the high magnetic field above 7 T, however, few measurements on Japanese superconducting cables had been made in the high field region until JAERI began a systematic test of the critical current density in the field from 7 T to 13 T. A typical result of this measurement is shown in Fig. VI.4-1. This result, showing that the actual capability of Japanese manufacturers was not so good, has contributed to improve their techniques.

As for the heat flux from conductor surface to liquid helium, many efforts have been made to improve the cooling capability, because this is one of the most important basis for a stable large superconducting magnet.

In case of pool-cooling, available heat flux depends deeply on the condition of the conductor surface and many ideas and possibilities have been examined to improve the heat flux characteristics. As a result of these efforts, two methods were verified to be quite efficient; one is to roughen the surface by the mechanical grinding and the other is to coat the surface with oxidized material by the chemical treatment. Figure VI.4-2 shows the improvements of the heat flux by using mechanical and chemical treatment at the same time.

5. Nb_3Sn conductor developments

5.1 Performance of multifilamentary Nb_3Sn conductor

As a conductor to be used in 10 - 12 T high field magnets, the critical current and bending effect of multifilamentary Nb_3Sn conductor has been studied. The sample is a rectangular wire consisting of 42037 niobium filaments in a tin-bronze matrix. The filaments are arranged in 127 groups of 331 ones. Each group is surrounded by a niobium barrier and an outer matrix of OFHC. The samples are treated at the temperature of 650, 700 and 750 K from one to 300 hours.

The critical current data on these samples are plotted in Fig. VI.5-1. The highest critical current density of Nb_3Sn including niobium and bronze material are achieved by a reaction at 650 K for 200 hours. Figure VI.5-2

shows a critical current degradation as a function of bending diameter of Nb_3Sn conductor. The critical current is decreased a few percent by a bending diameter of 150 mm.

5.2 Forced cooled Nb_3Sn large current conductor

In order to study a conductor to be used in the next machine after JT-60, a forced cooled Nb_3Sn large current conductor has been developed. The conductor is designed with the operated current of 12 kA at 11 T and the average current density is 20 A/mm^2.[8] The helium cooling channel is designed for the flow rate of 8 g/sec and the pressure drop is 3 atoms per 200 m.

Figure VI.5-3 shows a cross sectional view of the conductor. The arrangement has been designed to satisfy the mechanical requirement and to obtain an enough cooling perimeter and low pulsed field loss for the coil of the next machine with the stored energy of 1 - 10 GJ. Figure VI.5-4 shows the normalized critical current as a function of tensile strain measured at 4 and 5 T for seven-strand cable conductor manufactured by the tin-dip process before assembling. It is found that no degradation of critical current happens under the condition of 1 % strain.

References

1) Ando, T., Yoshida, K., Shimamoto, S., and Yasukouchi, K.: Cluster Test Facility for Superconducting Tokamak Toroidal System Development. Proc. Appl. Superconductivity, 1978.
2) Detailed design report of Japanese coil for Large Coil Task in collaboration with Furukawa, Hitachi, Hitachi Cable, Mitsubishi, Sumitomo, Toshiba Co. (unpublished)
3) Shimamoto, et al.: Design and analysis reports on LCT coil design. (unpublished)
4) Nishi, M., Ando, T., Yoshida, K., and Shimamoto, S.: Measurement of Heat Transfer Characteristics and Stability Analysis of Large Superconductor, JAERI-M 8134 (1978).
5) Hosoda, Y., and Shimamoto, S.: Eddy Current Loss Analysis for the Helium Vessel of IEA-LCT Coil, JAERI-M 8204 (1978).
6) Verification Test Report on the winding of LCT Conductor in collaboration with Mitsubishi Electric Co. (unpublished)

7) Shimamoto, S., Ando, T., Nishi, M., and Yoshida, K.: A 8.5 T - 24 cm Bore Nb-Ti Magnet for Short Sample Test on Tokamak Superconductor. Cryogenics 19 (1979).

8) Report on a forced cooling Nb_3Sn Large Current Conductor in collaboration with Toshiba Ltd. (unpublished)

Table VI.2-1 Main parameters of cluster test coil

Coil Type	Pool Boiling Circular Coil 1.5 m dia.	
S.C. Material	NbTi	
Rated Current	2145	A
Averaged Current Density	30	A/mm^2
Maximum Field	7.0	T
Number of Turns	1560	turns
Stored Energy	8.96	MJ
Stability	Fully Stabilized	
Heat Flux	0.29	W/cm^2
Structural Material	304L Stainless Steel	

Table VI.3-1 Main design parameters of Japanese LCT coil.

Coil Type	Pool Boiling, 4.5 mh × 3.6 mW Edge-wise and Pancake Winding		
S.C. Material	NbTi		
Critical Current Density	6×10^8	A/mm^2 (8 T)	
Rated Cable Current	10220	A	
Averaged Current Density	26.56	A/mm^2	
Maximum Field	8.1	T	#1.
Number of Turns	658	turns	
Stored Energy	110.1	MJ	
Number of Conductor Grading	2	Grades	
Stabilizer	OFHC Copper, 10-20 % Hard with rough surface		
Heat Flux	0.8	W/cm^2	
Stability	Stable against half-turn Normal		
Structural Material	304 LN Stainless Steel		
Maximum Stress on Conductor	12.5	kg/mm^2	#1.
Maximum Stress on Structure	16.2	kg/mm^2	#1.
Allowable Stress on Conductor	22.7	kg/mm^2	
Allowable Stress on Structure	25.3	kg/mm^2	

#1. Normal Test Condition.

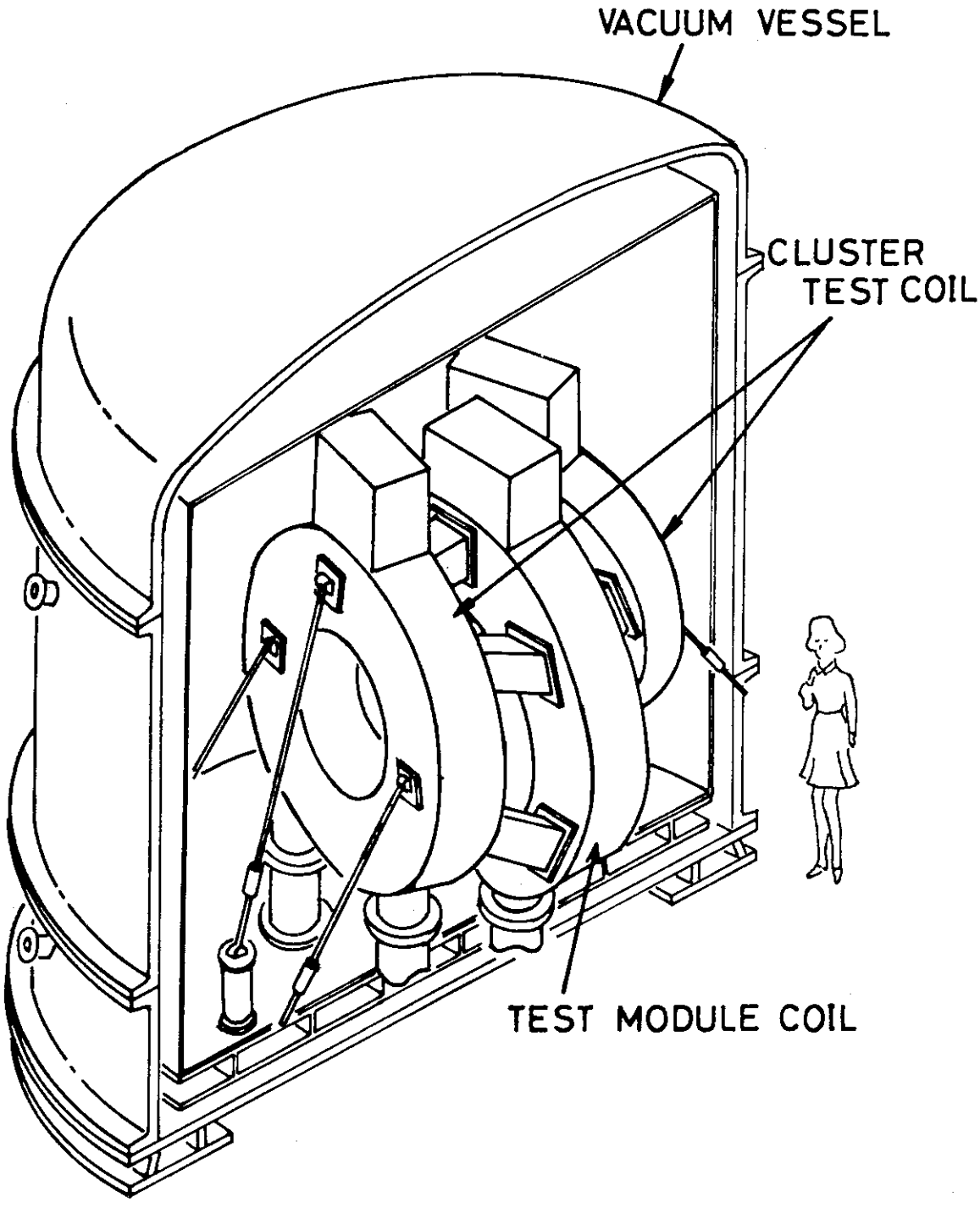

Fig. VI.2-1 Bird's eye view of cluster test facility.

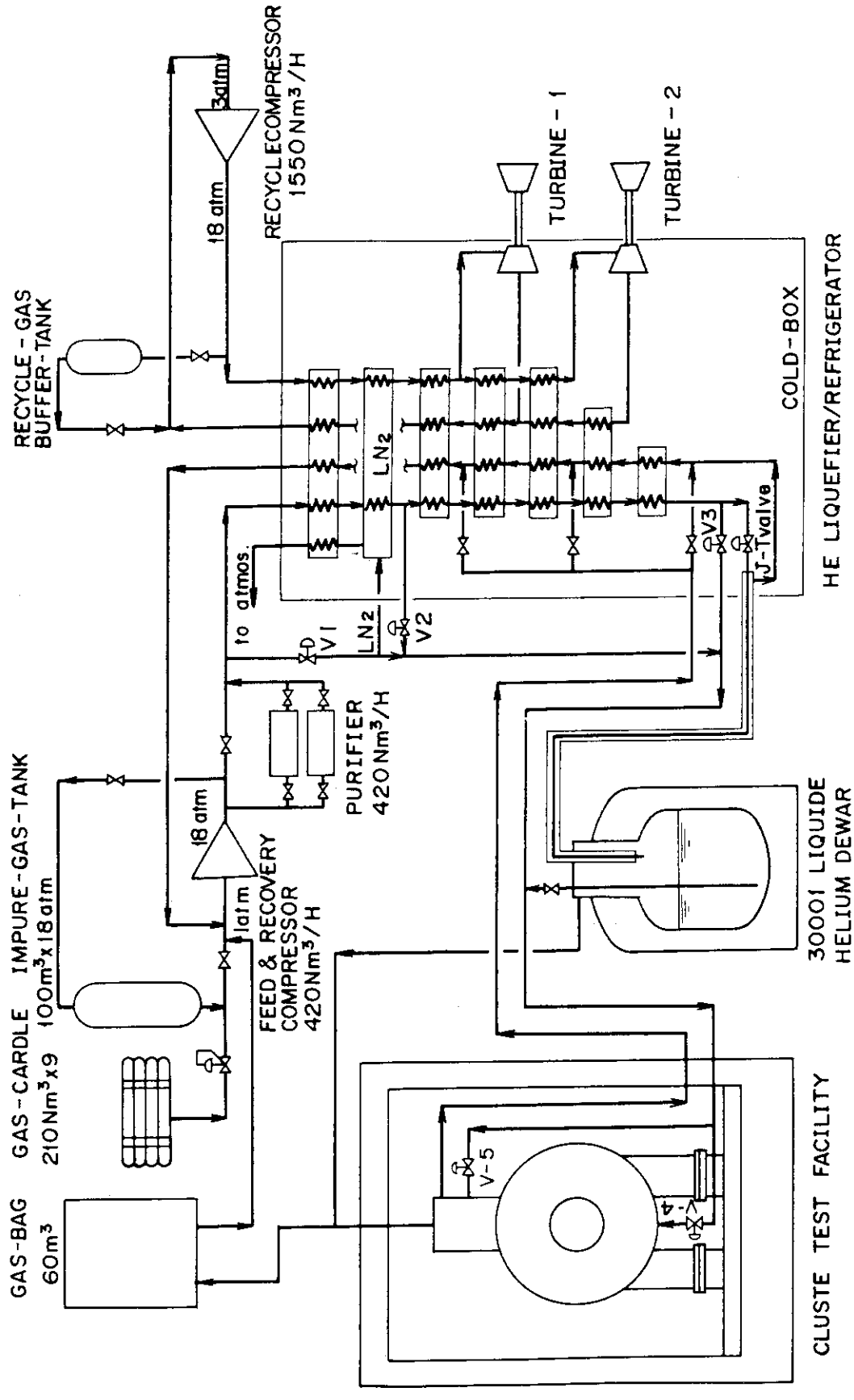

Fig. VI.2-2 Helium liquefier/refrigerator flow diagram.

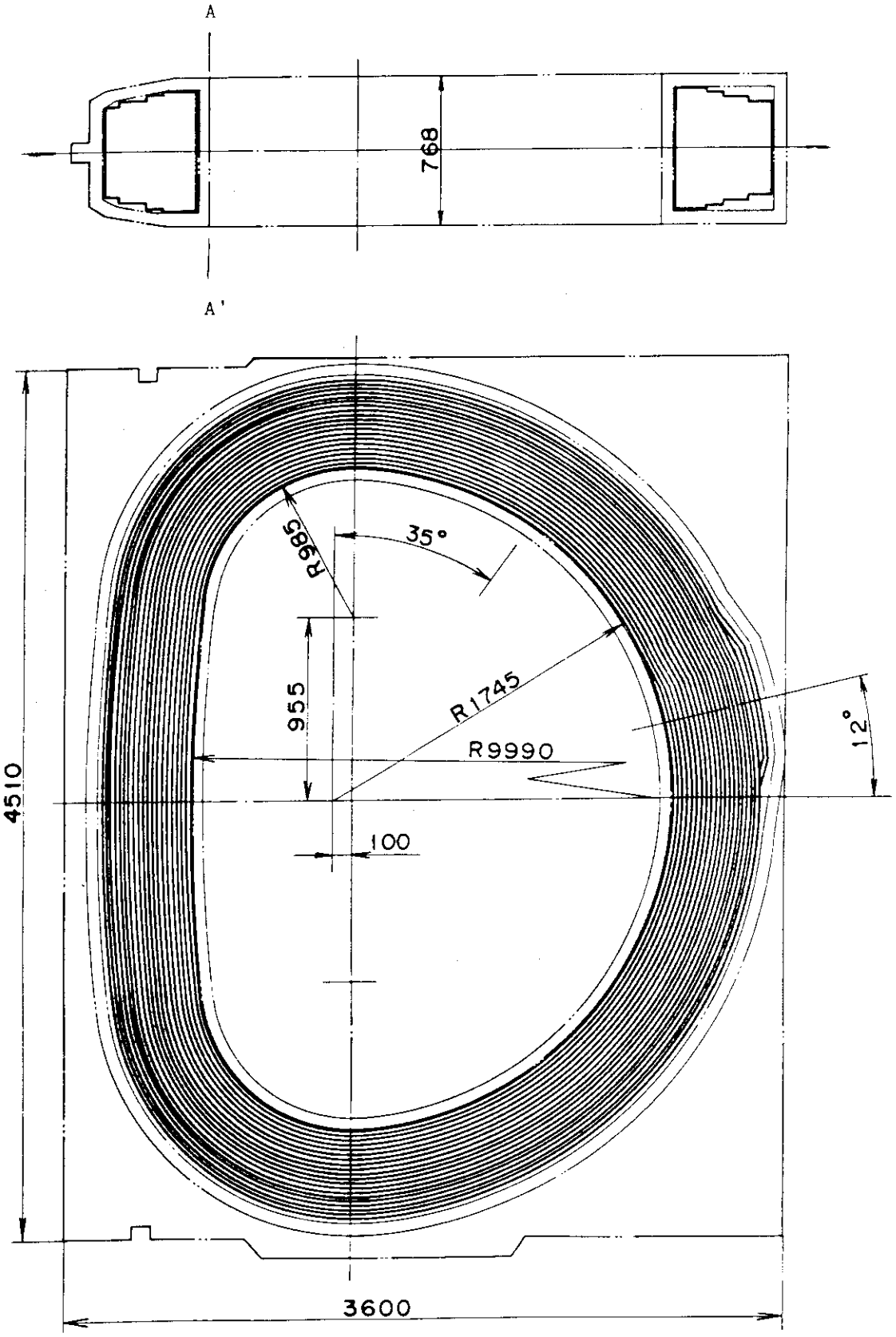

Fig. VI.3-1 Vertical cross section of Japanese LCT coil.

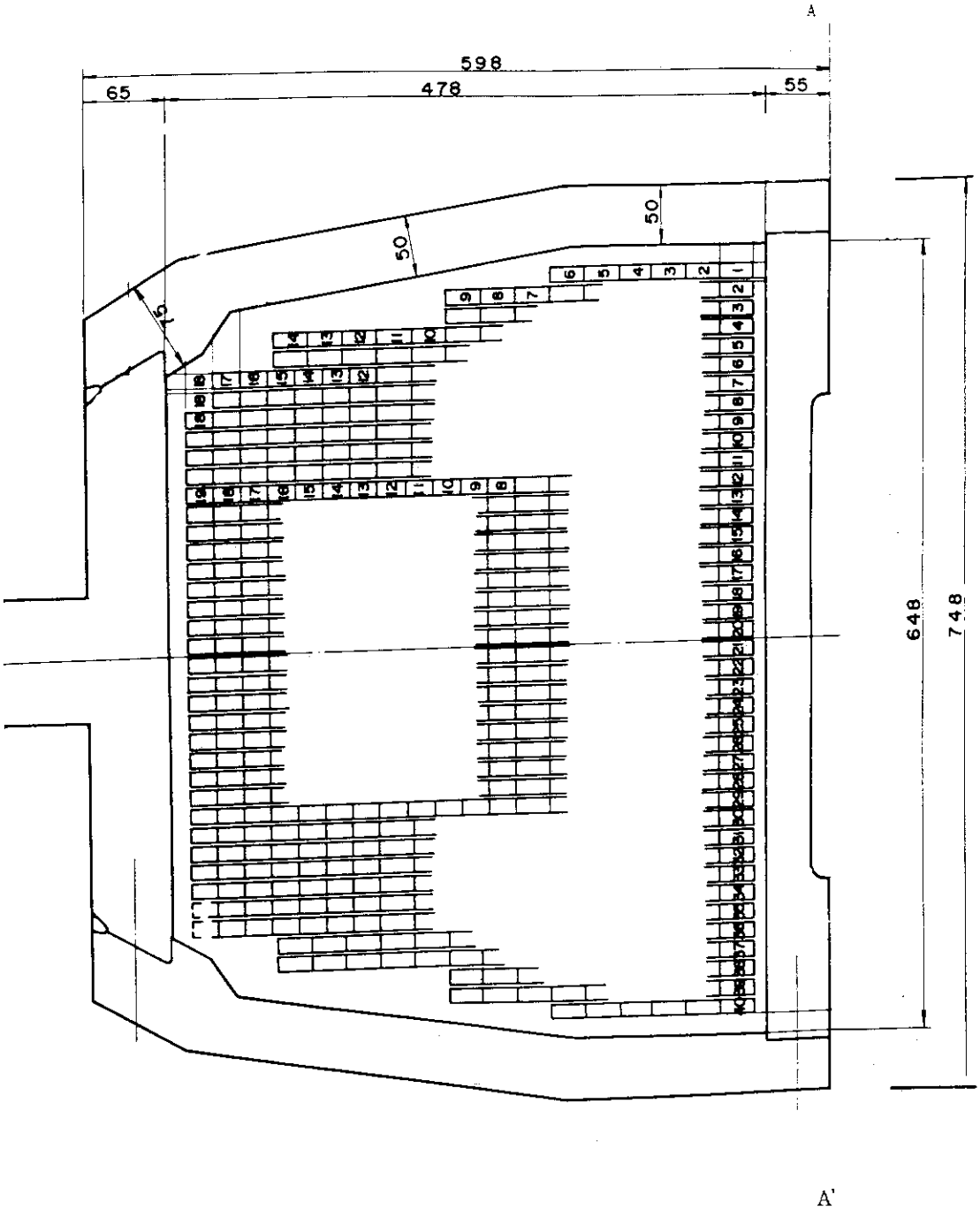

Fig. VI.3-2 Horizontal cross section along A-A'.

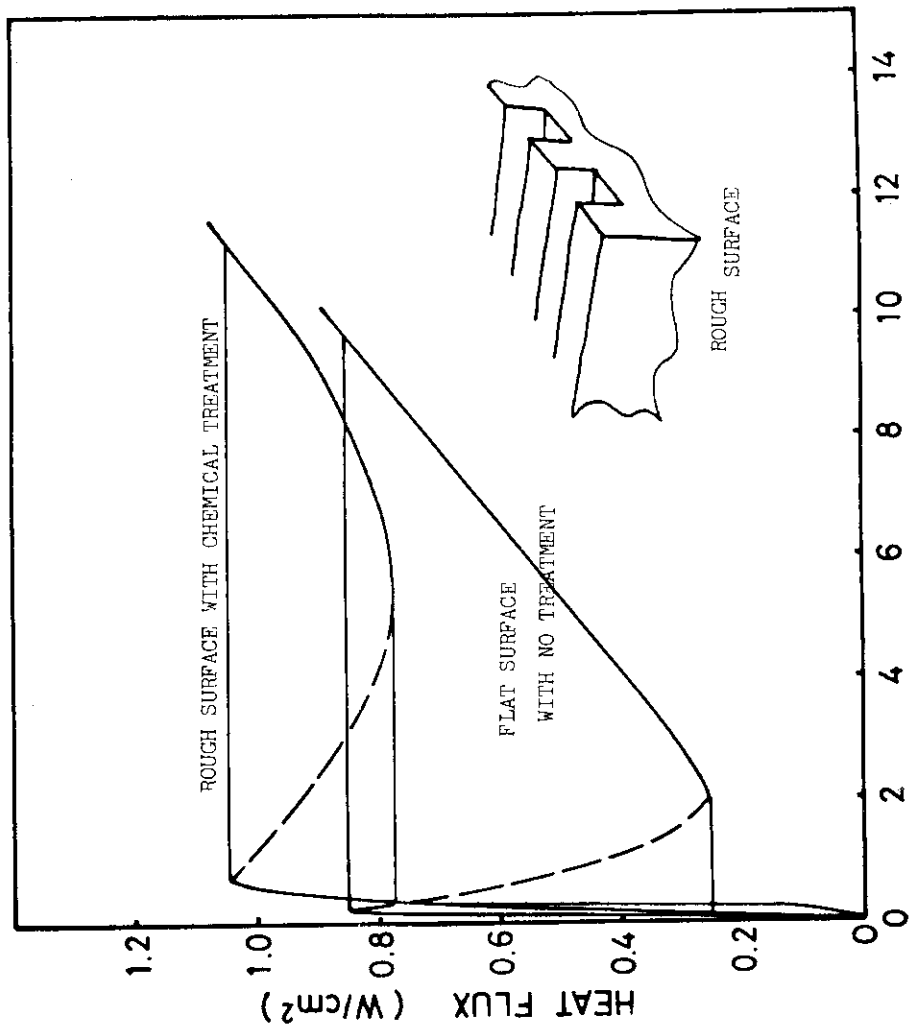

Fig. VI.4-2 Improvement of heat flux by surface treatment.

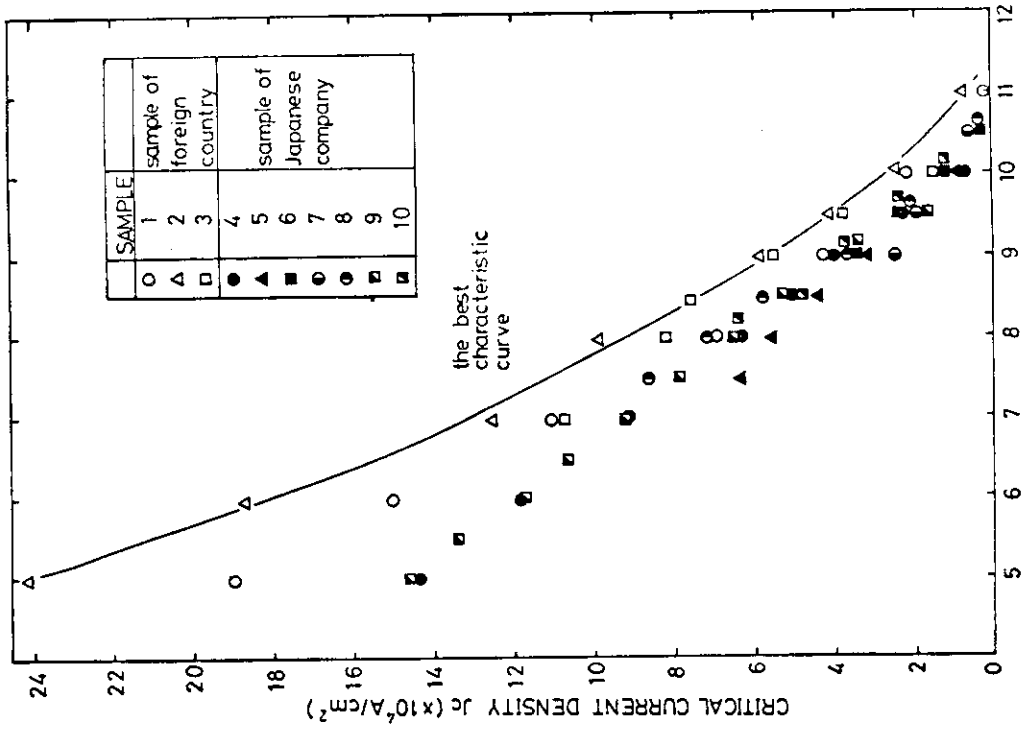

Fig. VI.4-1 A result of Jc-H measurement.

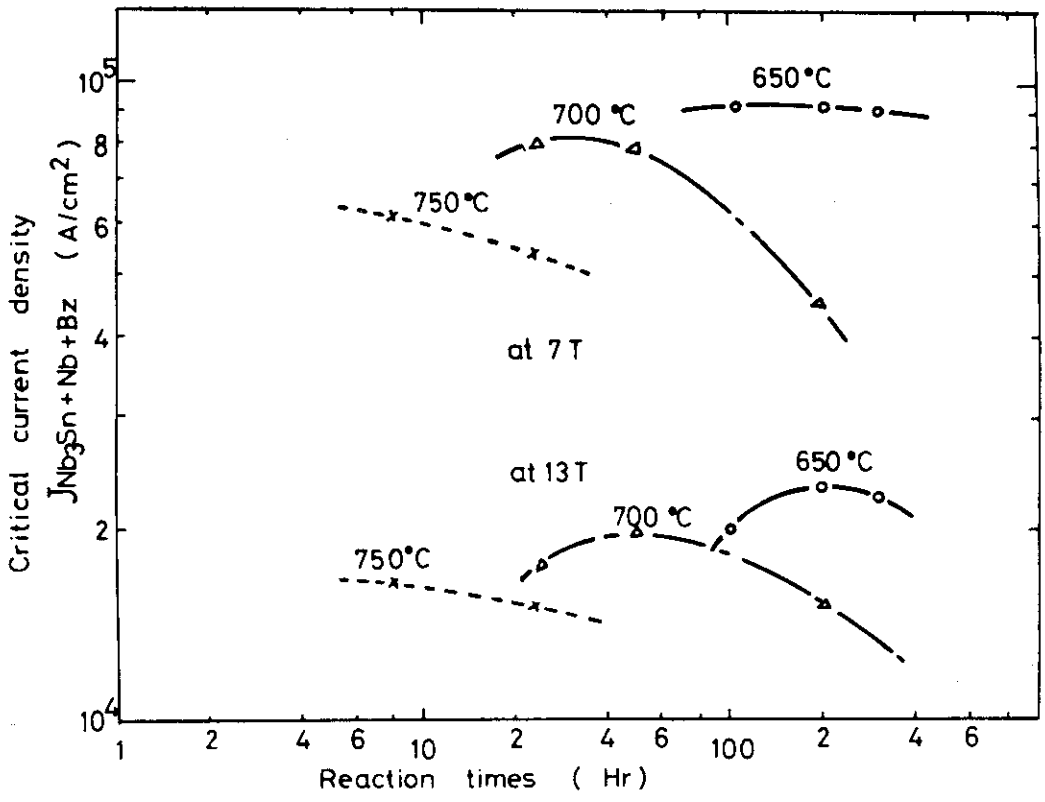

Fig. VI.5-1 Critical current density of Nb_3Sn by thermal-treatment at various reaction time and temperature.

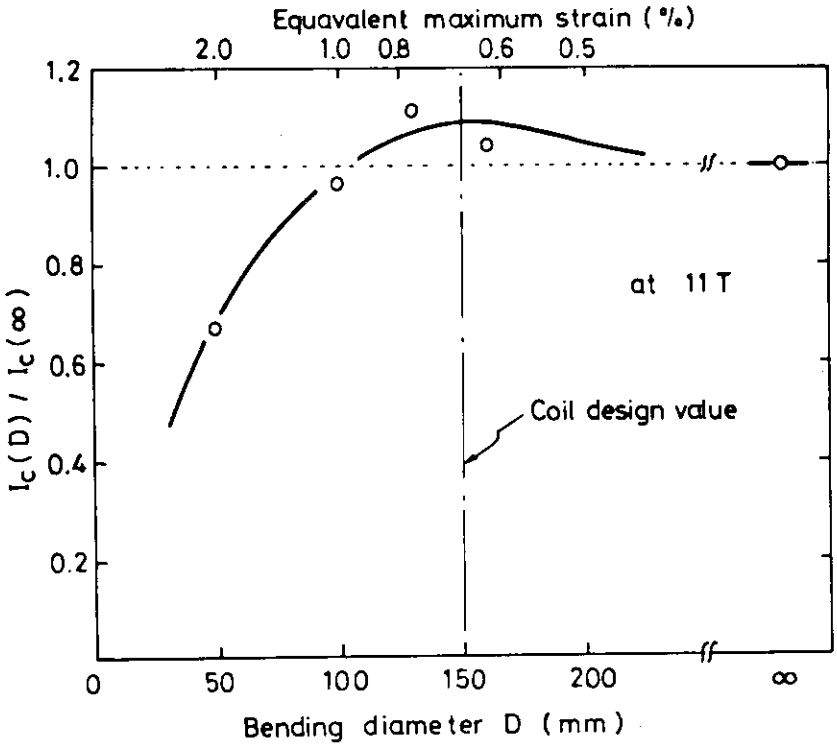

Fig. VI.5-2 Effect of bending diameter on critical current density of Nb_3Sn multi-filamentary conductor.

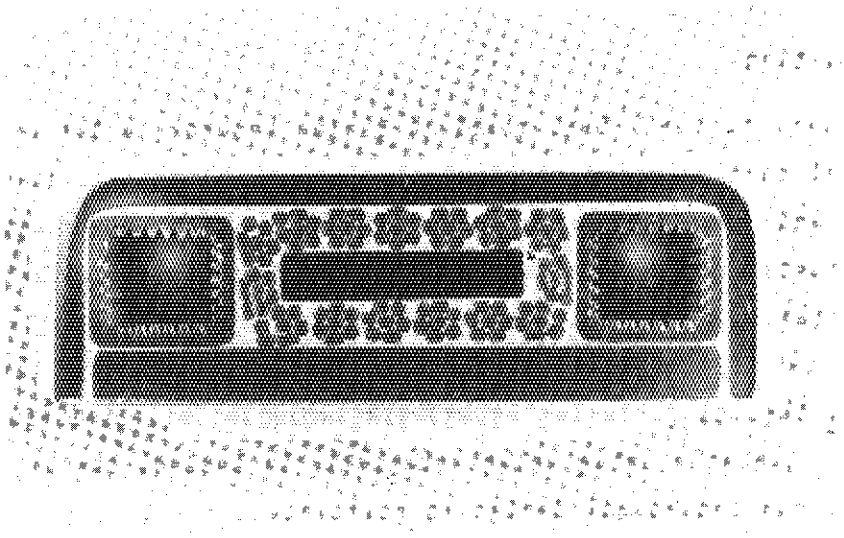

Fig. VI.5-3 Cross section of 12 kA 11 T Nb_3Sn conductor.

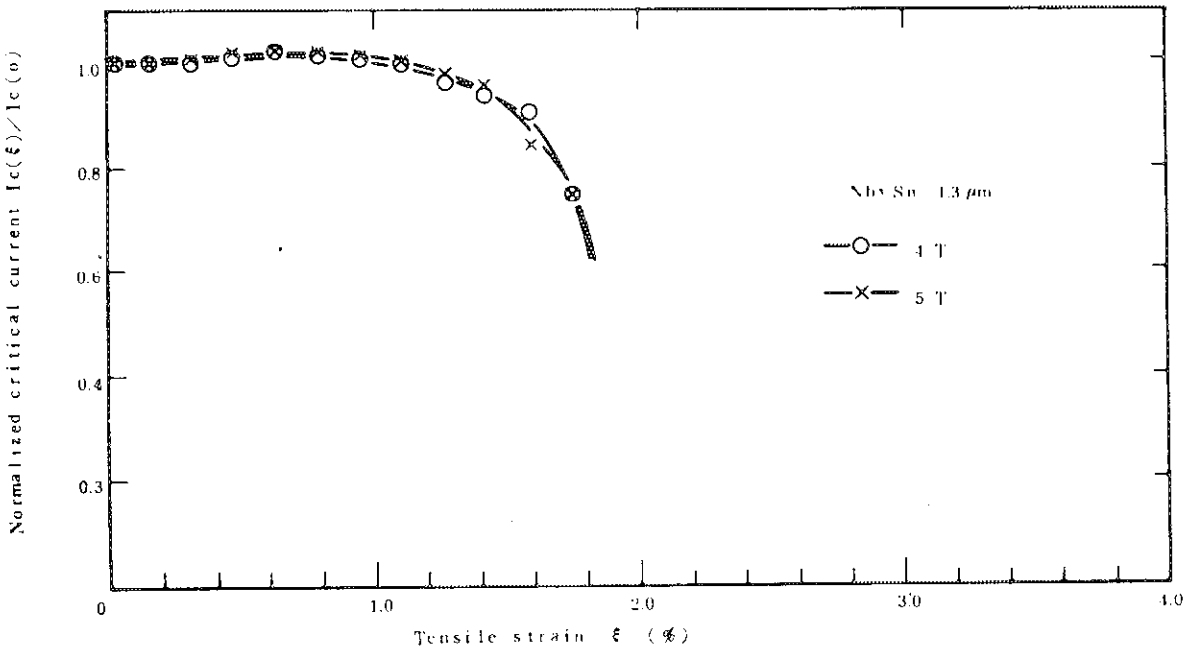

Fig. VI.5-4 Effect of tensile strain on critical current.

VII. TRITIUM

1. Introduction

To demonstrate D-T fuel cycle of fusion reactor, a lot of works, such as fuel recirculation, tritium production, blanket technology, waste treatment, and etc., have to be accomplished. At the beginning of this study, we investigated the subjects of two categories; one is process technology relevant to fuel recirculation and tritium production and another is a design of tritium handling facility at 10^4 Ci level. In the former, thermal diffusion experiment using H_2-He system and permeation of H_2 and D_2 gas with Pd-Ag alloy membrane, is tested, and in the latter, preliminary and conceptual design is performed.

2. Tritium process technology

2.1 Isotope separation system

Table VII.2.1-1 summarizes the characteristics of the typical tritium separation methods and their applications.

Cryogenic distillation method, which has been demonstrated as a tritium removal facility from D_2O coolant at ILL in France, is expected to be the useful process for the production of large amount of tritium and the separation of tritium in fusion reactor circulation system (plasma effluent, blanket coolant). Main subjects to be established are the criteria of design and operation of distillation column, cooling system and isotopic equilibrator.

Thermal diffusion method, which has been developed as one of the useful tritium production technologies in France and USA, is expected to be the optimum technology for tritium production. The advantages of the method are small inventory, leak tightness and handling ease in batch operation.

Chemical exchange method is a useful technology for enrichment of tritiated water such as D_2O moderator and tritium waste solution as well as water distillation method. In order to be practicable use, hydrohobic catalyst should be developed for the improvement of exchange column efficiency as well as pre-treatment of waste solution.

Water distillation method is simple and safe technology for tritium enrichment even though small separation factor. Selection of packing

materials is the key subject of design and operation of the distillation column.

Preliminary experimental work of the thermal diffusion method was carried out using H_2-He mixture by glass and steel columns. Figure VII.2.1-1 illustrates an experimental equipment, which installs the hot tube fabricated Inconel-600 selected because of its stability under high temperature (800 °C) and hydrogen atmosphere. Figure VII.2.1-2 shows the separation performances obtained under different geometrical conditions at constant temperature (600 °C). It is found that the column length, clearance between hot tube and cold one and operating pressure as well as the operating temperature are important parameters in optimum design of column.

2.2 Purification system

Crude tritium gas extracted from irradiated target materials and plasma effluent gas contain such impurities as He, N_2, CO, NH_3, water-vapor and hydrocarbons. These substances should be removed beforehand isotope separation. Metal getters (U, $LaNi_5$, Zr-Al, Ti) and palladium-silver alloy membrane are the useful materials for the purification system. In order to establish the methods, purification characteristics should be examined under different operating conditions (gas velocity, impurities content, temperature).

We began to study the permeability of hydrogen isotopes gas through Pd-Ag alloy membrane. Figure VII.2.2-1 shows a typical result obtained with commercial membrane (75Pd-25Ag). The permeation rates of H_2 and D_2 gas increase linearly with the increase of operating pressure, $[P_h^{1/2} - P_1^{1/2}]$, (P_1 = 1 kg/cm^2) under wide temperature range. Following equations were obtained by Arrehnius plot of the experimental results.

$$R_{H_2} = 6.360 \times 10^{-6} A (P_h^{1/2} - P_1^{1/2})(1/t)\exp(-617.24/T)$$

$$R_{D_2} = 4.361 \times 10^{-6} A (P_h^{1/2} - P_1^{1/2})(1/t)\exp(-695.70/T)$$

R_{H_2}	: permeation rate of H_2 gas	(mol/min)
R_{D_2}	: permeation rate of D_2 gas	(mol/min)
A	: surface area of membrane	(cm^2)
P_h	: feed gas pressure	(psia)
P_1	: permeated gas pressure	(psia)
T	: operating temperature	(°K)
t	: thickness of membrane	(cm)

3. Conceptual design study of TRITIUM research laboratory

To provide tritium technology stepwisely, preliminary and conceptual design study is performed as a initial approach, on overall tritium system components necessitated to fusion reactor development at the handling level of 5 g per year.

The principal requirements for this design are

1) to assure the excellence of safe handling
2) to obtain technological data for each component of tritium systems
3) to evaluate preliminarily tritium release from the facility
4) to estimate maintenance and operation requirements.

For the assurance of safe handling we emphasized to take into consideration physical and chemical properties of tritium as well as the radioactivity. Main characteristics of this design are:

1) to adopt multiple barrier containment system
2) to make clear zoning division (cold, semi-hot and hot) and decide the proper ventilating air flow direction
3) to select of materials and components compatible with tritium
4) to make tritium accountable safely
5) to maintain tritium concentration in control and uncontrolled area of this laboratory less than guide line level.

In this design radiation exposure has to be fulfilled less than 0.01 mrem/y at the site of populational area, tritium concentration of the stack exhaust less than 2×10^{-7} μCi/cm^3, tritium concentration of the controlled area less than 0.01 $(MPC)_a^{48}$/y or 0.1 $(MPC)_a^{48}$/w, and radiation exposure of uncontrolled area less than 30 mrem/w.

The principal objectives of the tritium research laboratory are as follows:

1) to develop tritium test production system using neutron irradiated lithium aluminium alloy
2) to develop tritium process technology, principally isotope separation and related system
3) to develop blanket technology such as compatibility of Li_2O with metals, the damage effect of neutron irradiation of Li_2O
4) to develop safe handling technology, that is,
   i) tritium containment and removal system for enclosures and its atmosphere such as cell and its air, glovebox and its atmosphere and jacket of piping and equipment, and sweep gas

ii) emergency clean up system
iii) waste treatment system such as concentration of tritiated water and solidification
iv) storage
v) monitoring
vi) accountability
vii) the other systems such as waste disposal, development of protection materials for tritium handling, and so on.

The building which will be built near by fission reactors, is two story with partial basement, approximately 4000 m^2 of floor area, reinforced concrete structure to withstand the design base earthquake, and its inside surfaces is coated with epoxy resin. The layout of the facility is decided taking into consideration firstly safe operation in tritium handling and secondly rational transfer of radioactive materials such as neutron irradiated target and capsules, containers for tritium loaded getters and wastes. Figure VII.3-1 shows a main conceptual flow of radioactive materials and containment schemes. The individual room located in this laboratory is classified to each zone clearly according to the handling level and treating what sorts of radioactivity. Ventilation air will be supplied from supporting machine room by passing service area in hot zone and the direction of air stream is maintained from service area to each room where the enclosure is located. The supporting machine room will be supplied filtrated and drinkable water, and is equipped electric facility which is double ended 6.6 kV substation and other utilities such as cooling water, liquid nitrogen, several kinds of inert gas and etc. A 30 m high stack is installed for dispersal of the exhausted air.

Several typical apparatus will be equipped in this building is briefly outlined as follows:

(1) Cell and Cask

Cells will be constructed for tritium test production, blanket engineering and waste storage. Production cells consist of two cells, that is, loading and decapsulation cell and tritium extraction cell. The latter is provided for tritium extraction from neutron irradiated lithium aluminum alloy and fixation of crude tritium gas with getter. Blanket engineering cells consist of three cells. One cell is used for

loading, cutting and polishing of neutron irradiated blanket materials such as Li_2O, lithium contained ceramics. The others are used to observe metallurgical structure and to measure dimension changes caused by neutron irradiation. Waste storage cell will be constructed for temporary storage of solid waste.

Cell will be made of steel and the thickness of wall of operation side for gamma ray shielding is 43 cm in production cells and 27 cm in blanket engineering cells. Each cell is sealed with stainless steel lining of 4 mm thick, and equipped manipulator, periscope, windows and other several accessaries for convenience of operation. The irradiated samples are introduced by using specially designed loading apparatus.

Ventilating air of cells is introduced to cell air purification system.

Casks will be made for the purpose of transportation of irradiated target (for production, and for blanket engineering) and waste. These casks are designed to meet B(M) class criteria which is obliged safety analysis test such as drop impact and fire check.

(2) Gloveboxes

Twelve gas tight gloveboxes arranged in the glovebox rooms, will be installed for purification of crude tritium gas extracted from neutron irradiated lithium aluminum alloy in tritium test production, for isotope separation by thermal diffusion and by cryogenic distillation in tritium process technology and for some of metallurgical experiments in blanket engineering. The other three gloveboxes will be installed for decontamination, tritium storage and waste treatment.

The glovebox is mainly made of stainless steel and equipped with various accessaries such as glove port covers, penetrated service tubing, pass box and double jacketted tubing for tritium gas transfer.

The atmosphere of the gloveboxes is treated with tritium removal systems.

(3) Tritium Removal Systems

Tritium will be found in atmosphere of enclosures by permeation and by leakage from tritium loaded experimental apparatus, and tritium concentration is reduced to safety level by the operation of tritium removal system. Four systems are to be provided to detritiate cell air, glovebox helium, glovebox argon and air tight room air, respectively.

Cell Air Purification System (CAPS)

Tritium concentration in cell air will be effectively reduced to safety level by the use of CAPS normally operated in once through mode or off-normally circulation mode. The CAPS consists of a prefilter, a blower, a preheater, a catalytic reactor, an after cooler, molecular sieve dryers and control systems. The capacity of CAPS is 1200 m^3/hr.

Tritium Removal From Glovebox Atmosphere

The atmosphere of the glovebox will be helium or argon which is continuously circulated to helium gas purification system (HGPS) or argon gas purification system (AGPS). In HGPS detritiation is performed by catalytic oxidation at 200 °C with the addition of small amount of oxygen and following molecular sieve adsorption of tritiated water and cryogenic adsorption with liquid nitrogen for purifying oxygen and residual tritiated water. In AGPS the same detritiation system will be adopted as HGPS except cryogenic adsorption where the use of oxygen getter is considered. Each capacity of the tritium removal from glovebox atmosphere is 270 m^3/hr.

The Other Processing System

Tritium processing for various effluent gas from vacuum exhaust of experimental apparatus, purge gas originated to maintain cell air and glovebox atmosphere to the pressure which is slightly less than that of the air tight room, and vent gas of liquid waste tank, will be carried out by effluent gas treatment system (EGTS). EGTS is operated ordinarily in once through mode and consists of compressors, pressurized holding tank, a buffer tank, a blower, a preheater, catalytic oxidizers with hydrogen swamping apparatus. If the tritium concentration at the outlet of final molecular sieve dryer is over the level which can be exhausted, circulation mode is available.

Emergency air clean up system (EACS), will be provided to protect working area and environment from the off-normal and accidental release of the tritium in the event of primary and secondary containment failure. If such a release occurs the affected room will be rapidly isolated from the remainder of the building and the EACS will be operated and the air is recirculated to remove tritium.

(4) Waste Treatment and Storage System

Liquid waste will be stored in sealed tanks according to their concentrations. Liquid of the concentration less than 3 μCi/cc is

collected as low level waste which will be diluted to permissible concentration at 3×10^{-3} μCi/cc, and sent to drainage. The middle level liquid waste where the tritium concentration is between 3 and 300 μCi/cc will be stored and used to develop enrichment technology by water distillation method. The highest level liquid waste, the concentration higher than 300 μCi/cc will be temporarily stored in a tank and successively solidified in a way of multiple barrier containment method. The high level waste is primarily treated with cement and adsorber mixture, packed secondly with asphalt and finally with concrete and steel container. Solid waste is stored in the temporary storing facilities of which the capacity is 40 drums for γ-ray emitting waste and 306 drums for the tritium waste.

Tritium sources used in this building will be stored in a double jacketted cartridge filled with metallic getter (such as a uranium, Zr-Al alloy) and placed in a glovebox of helium atmosphere. Each cartridge has an ability of 10 g storage.

(5) Radiation Control System and Central Control System

Exhaust gas in main ventilation ducts and stack are continuously monitored by γ-ray compensated type high efficiency tritium monitors and by dust monitors. Double alarm system will be provided to find out off-normal or accidental signals with high reliability. Rooms and laboratory monitors will be equipped to evaluate integrated dose caused by tritium leak and to detect spatial γ-ray and radioactive dust. If radiation dose rate is greater than the control level, alarm will be announciated to protect working personnel from exposure. Each tritium removal system is controlled by the signals of process monitors. Handfoot monitors are arranged in changing area to keep out of the enlargement of radioactive contamination to cold area. Several portable monitors and liquid scintillation spectrometer are placed to find contamination in hot and semihot area.

Master control systems will be provided for smooth control of the operation of tritium removal systems and displays of each operation signal of experimental apparatus and process systems.

In this facility we are hoping to develop various essential technologies for tritium handling required for the next systems where much larger amount of tritium will be handled and more directly related technology for fusion device will be developed.

Table VII.2.1-1 Typical Methods of Tritium Separation

Method	Cryogenic distillation	Thermal diffusion	Chemical exchange	Water distillation
Object	Tritium separation (Isotope separation)		Tritiated water enrichment (Waste processing)	
Inventory	Large	Small	Medium	Medium
Through-put	Large	Small-Medium	Large	Large
Operation	Continuous	Batch	Continuous	Continuous
Operating conditions	∿20 °K ∿1 atm	∿1300 °K ∿1 atm	30° - 300 °C ∿1 atm	∿70 °C <1 atm
Equipment	Column Cooling system (Small-Simple)	Column Heating system (Medium-Simple)	Column Electrolysis cell (Large-Simple)	Column (Large-Simple)
Tritium leak	Small	Small	Small	Small
Safety	High	High	High	High
Applicability				
• Small amount production	C	A	C	C
• Large amount production	A	A	C	C
• Reactor circulation system	A	B	C	C
• Waste processing	C	C	A	A

A : very good, B : good, C : not good

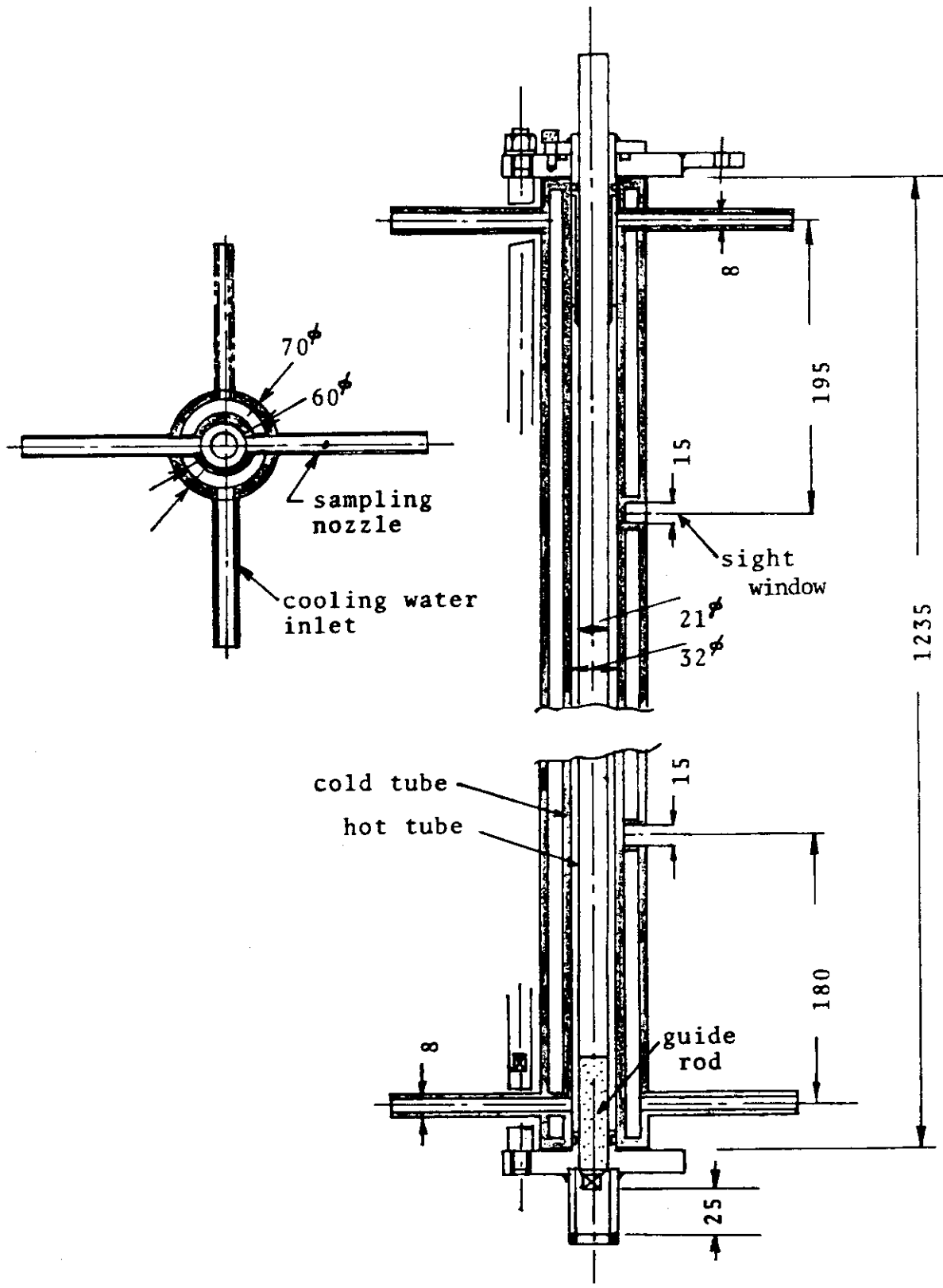

Fig. VII.2.1-1 Schematics of an experimental column (effective length of hot tube : 1 m)

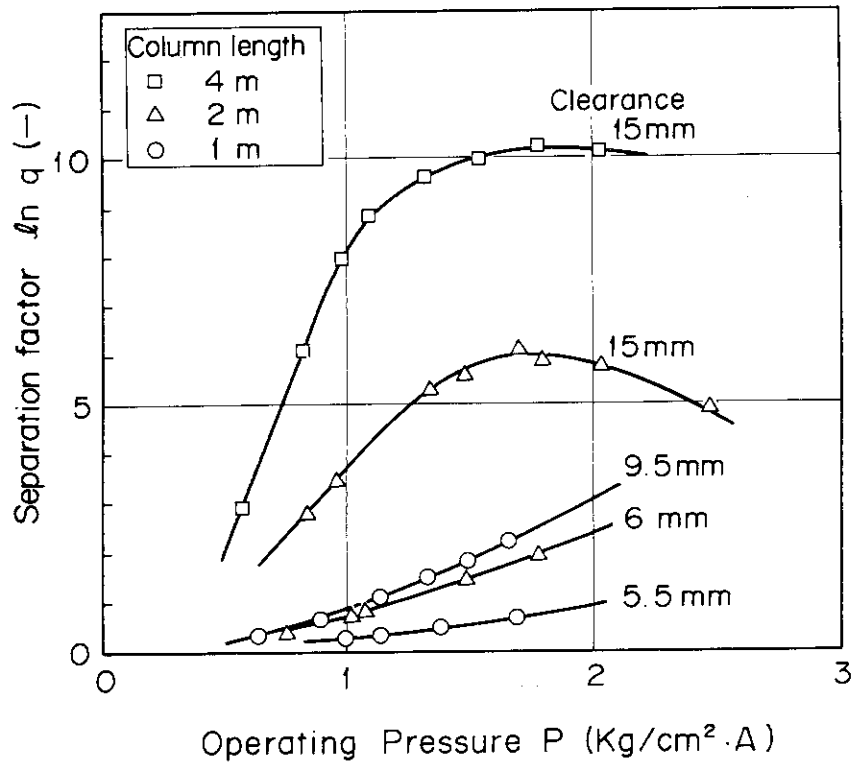

Fig. VII.2.1-2

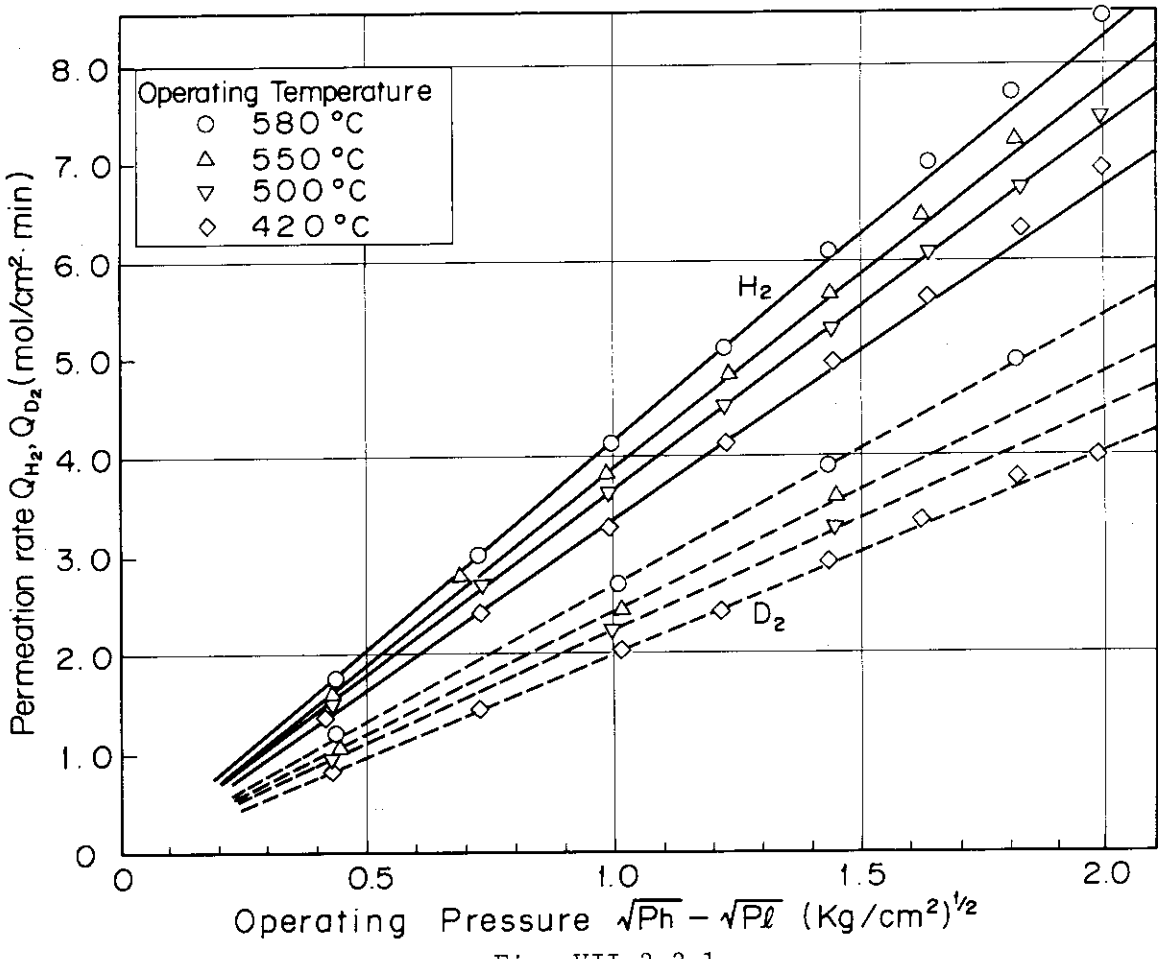

Fig. VII.2.2-1

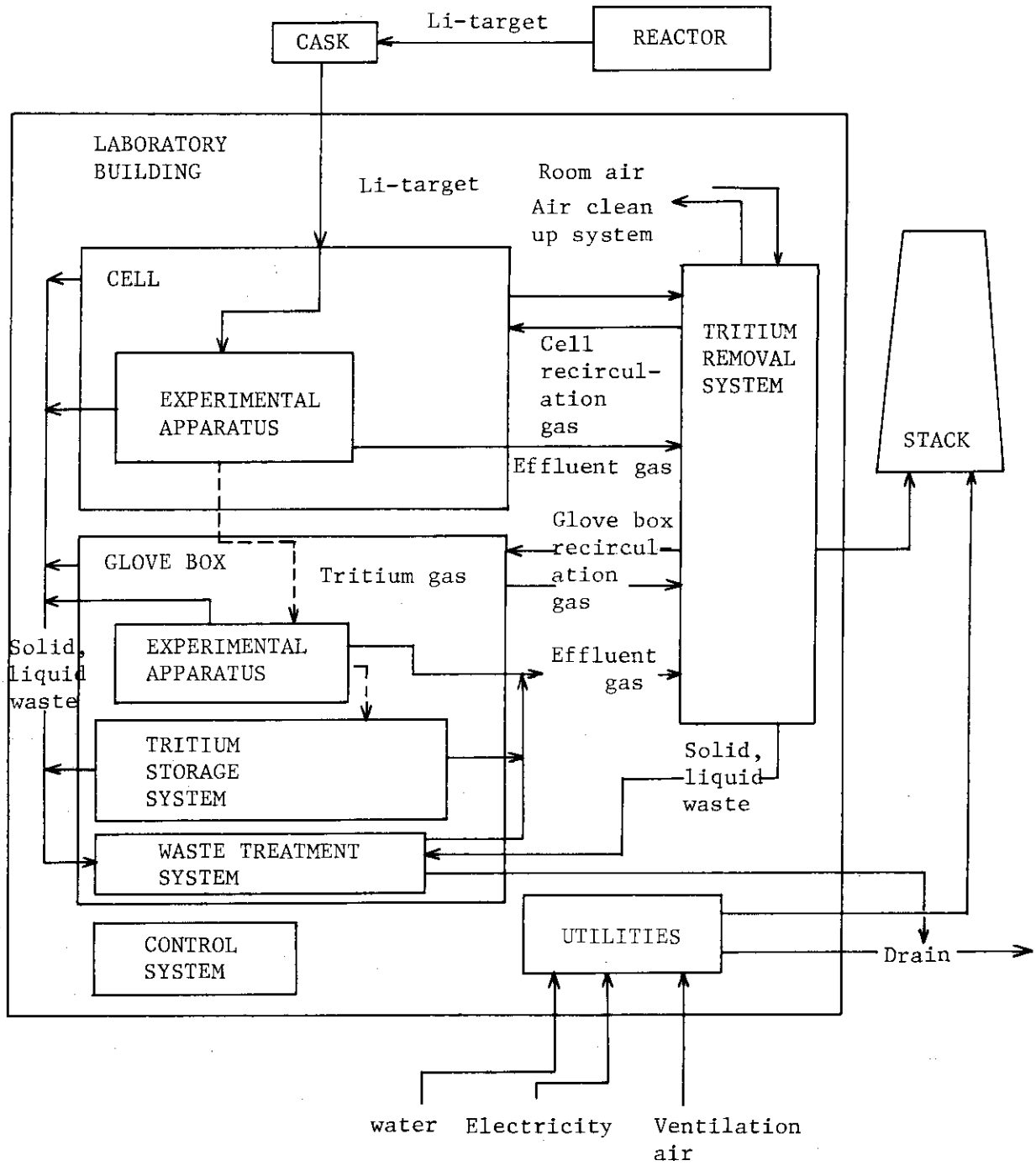

Fig. VII.3-1 Schematic diagram of Tritium Research Laboratory

VIII. REACTOR DESIGN STUDY

1. Preliminary design of JAERI Experimental Fusion Reactor (JXFR)

1.1 General

The first preliminary design of a tokamak experimental fusion reactor to be built in near future started in April 1975 and finished in March 1977. The design report has been completed and published as JAERI-M 7300 (Sept. 1977). It was also presented at the IAEA Technical Committee and Workshop on Fusion Reactor Design (1977, Madison). This design covered the overall reactor system including plasma characteristics, reactor structure, blanket neutronics, shielding, superconducting magnets, neutral beam injector, electric power system, fuel (D and T) circulating system, reactor cooling and tritium recovery systems and maintenance scheme. By this design many problems to be overcome have been identified.

The second preliminary design with special emphasis placed on developing realistic and credible solutions to the design problems started in April 1977 and finished in March 1979. Then an overall evaluation of the design will be carried out for another year. The main design parameters are summarized in Table VIII.1-1.

1.2 Plasma

The power balance of the JXFR plasma was reanalysed to mitigate the previous toroidal field of 6 T on the basis of the results obtained from MHD equilibrium calculations. The constraints imposed are to keep the previous power level (∿100 MW) and injection power (∿30 MW). The impurity considered is carbon which is the surface material of the first wall and the estimated concentration is 3 %. The toroidal field was reduced to 5.5 T by enhancing the toroidal beta to 2.5 %.

1.3 Neutronics

1.3.1 Sensitivity analysis of blanket and shield neutronics calculation

Uncertainties of neutronics calculation in the first preliminary design of Japan Experimental Fusion Reactor (JXFR) have been evaluated by sensitivity analysis based on linear perturbation theory. Uncertainties were estimated of the (n,p) reaction rates of ^{58}Ni and ^{54}Fe in outer

superconducting magnet (SCM), the displacement rate in the stabilizer (Cu) in inner SCM, and the tritium breeding ratio in outer blanket. The (n,p) reaction and the Cu displacement are most sensitive to the cross section of Fe, a major constituent of the blanket structure, and the tritium breeding ratio is so to the cross sections of ^{7}Li and ^{16}O in Li_2O. The calculation of induced activity and radiation damage in SCM is equivalent to solving the deep penetration problem; cross section perturbation has large influence on the results of this problem. Taking into account the uncertainty of the cross section data, the uncertainties of (n,p) reaction and Cu displacement rate are found to be 60 ∿ 80 %.

1.4 Reactor structure

The following items are studied in this design: (1) mechanical stress due to internal pressure in a blanket vessel with a rectangular cross section and the effect of neighboring blanket vessels, (2) change of temperature distribution in a blanket vessel and effect of flow control, (3) high temperature (500 °C) and effect of thermal cycles on the first wall of the blanket vessel, (4) change of the first wall temperature during plasma burst and effect of protection wall, (5) integrity of a blanket module and integrity of a shield structure.

1.4.1 Stress analysis of blanket vessel

The blanket consists of about 2,300 blanket vessels made of Type 316 stainless steel with a rectangular cross section having round corners. Each blanket vessel is a double-walled thin-shell structure and is cooled by helium gas at 10 kgf/cm^2 (0.98 MPa). Inlet and outlet temperatures are 300 °C and 500 °C, respectively. Large deformation and stress arise due to internal pressure for such a structure. In order to reduce the deformation and stress, the blanket structure is so designed that the neighboring vessels are mutually supporting.

The stress analysis of the blanket vessel with a three-dimensional finite element method and the feasibility of the blanket structure is performed.

1.4.2 Design study of blanket structure

A design study of a blanket structure for JAERI Experimental Fusion

Reactor (JXFR) has been carried out.

The study covers the fabrication and testing of a blanket structure (blanket cells, blanket rings, piping system and blanket modules), assembly and disassembly of a blanket module and monitoring and testing technique.

From the results of this design study, many problems on the design and fabrication of a blanket structure have become clear. Research and development items, which will be required in future, in the design and fabrication have been studied.

1.5 Superconducting magnets

Design studies of the superconducting magnets for the JXFR have been carried out. Performed were toroidal field magnet design, poloidal field magnet design, refrigeration system design, magnet safety analysis and magnet assembling and disassembling system design.

The maximum toroidal field in a coil is 11.0 T providing 5.5 T at the plasma center. The magnetomotive force is 185.6 T. Two alternative designs were done. Copper stabilized Nb_3Sn conductors are used in both designs. Conductors are wound in slots of stainless steel disc supports in one design, while conductors reinforced with stainless steel are wound in pancake in the other. Pool boiling method is used in cooling of conductors in both designs.

Two different designs were also performed for the poloidal magnet. Nb_3Sn conductors enclosed in Ti-alloy sheath are used in one design. Ti-alloy sheath serves as a helium container and conductors are cooled by forced flow of supercritical helium at 7 atm, 4.6 K. In the other, NbTi superconductors are wound in pancake and coils are cooled by pool boiling in FRP containers.

1.6 Plasma heating systems

Further refinement of design of the neutral beam heating system was done. Especially effect of ions and electrons produced in the acceleration space of the ion source and beam orbits in the direct converter was analyzed extensively. It was found that heating of the arc chamber by back-streaming electrons is a limiting factor of current density in the ion source. In order to reduce this effect pumps are installed between the ion source and the neutralizing cell in the new

design. Current density and beam cross-section of the ion source are restricted by beam divergence in the in-line direct converter. Erosion of collector plates of the converter by sputtering is also a serious problem.

Utilization of RF heating instead of neutral beam heating was investigated. It is assumed that the plasma is heated by electron Landau damping near the lower hybrid frequency. RF power is coupled with the plasma by four units of multi-waveguide phased array launchers. A launcher to feed 8 MW power through a 90 cm × 60 cm port was designed. It was shown that RF heating is also a promising method of heating in a tokamak reactor when good power absorption of the plasma is demonstrated.

1.7 Design study of shielding vessel

Design study of the shielding vessel for a Tokamak experimental fusion reactor has been carried out. Performed here are structural design, thermal design, assembling and disassembling system design and safety analyses.

Shielding vessel is a toroidal tubular structure and is situated between blanket and toroidal magnet. For assembling and disassembling, the shielding vessel is divided into 8 sectors along the toroidal axis. At the central part of each sector, 1.3 × 5.0 m port is located for the NBI and evacuation.

Shielding vessel consists of vacuum vessel, heavy concrete structure, lead layer and legs. Bellows and SUS 304L plate are fixed on the heavy concrete structure as the vacuum vessel. SUS or high manganese steel plate structure are filled with heavy concrete, water layer and B_4C powder in a heavy concrete structure. Two layered 25 mm thick lead blocks are fixed on the outer surface of the heavy concrete structure as a lead layer.

The shielding vessel is cooled by water and maximum temperature gradient within heavy concrete is calculated as 2.2 °C/cm. Primary stress of the SUS structure and fundamental mode of characteristic frequency of the shielding vessel sector are calculated as 4.1 kg/mm^2 and 16.7 Hz, respectively.

1.8 Instrumentation and control systems

The preliminary design of instrumentation and control systems is made for JAERI Experimental Fusion Reactor (JXFR).

The items for plasma control are power control, plasma position and shaping control. The items of instrumentations are studied for the plasma control items mentioned above. The characteristics, functions and structures required for instrumentation and control systems are studied. Technological problems and R & D items for these instrumentation and control systems are pointed out through these design studies.

1.9 Remote handling equipments

Design studies have been made of repair and maintenance system for a Tokamak experimental fusion reactor.

Studied are the overhaul system (including redesign of the rotating carriage), survey of the remote handling techniques (in nuclear power plants and reprocessing plants), overhaul operations and remote handling equipments, conceptual designs of the remote handling equipments (overhead crane manipulator and vehicle-mounted manipulator), the overhaul system (conceptual designs of GAC·ANL-TNS and JXFR) and cost data.

The purpose was to indicate problems and research/development areas in the repair and maintenance system.

2. Design studies for INTOR-J

A design study of INTOR has been carried out in order to evaluate the validity of the guiding design parameters and also to demonstrate the feasibility of installing the tritium breeding blanket.

The engineering issues were evaluated of the two concepts proposed for impurity control and ash exhaust, namely, a concept with poloidal divertors and a non-divertor concept. As a result of a preliminary study, the following findings have been obtained.

1) Some of the INTOR guiding parameters enforce severe conditions to the engineering design, but a concept satisfying the parameters is shown to be feasible. In that sense, the guiding parameters may be considered appropriate.

2) Tritium breeding blanket (Helium cooled Li_2O blanket) with the breeding ratio greater than 0.5 is shown to be feasible in the case without divertor. The ratio of 0.4 is possible for the case with divertors.

The vertical cross sectional view of the reactor with divertors is shown in Fig. VIII.2-1.

3. Design related studies

3.1 Development of a code system for calculation of exposure dose rates around a fusion device

A code system THIDA has been developed for calculation of the exposure dose rates around a fusion device. It consists of the following: one- and two-dimensional discrete ordinate transport codes; induced activity calculation code; activation chain, activation cross section, radionuclide gamma-ray energy/intensity and gamma-ray group constant files; and gamma-ray flux to exposure dose rate conversion coefficients.

Table VIII.1-1 Main design parameters of JXFR (2nd preliminary design)

Power	
Fusion power (MW)	125
Thermal power (MW)	140
Electrical power (MW), Gross	-
Net	-
Net thermal efficiency	-
Wall loading (MW/m^2)	0.3
Operation mode	
Operation period (s)	180
Burn time (Flat top) (s)	100
Duty factor	0.6
Plant availability	0.5
Load factor	0.3
Reactor dimensions	
Major radius (m)	6.75
Plasma radius (m)	1.5
First wall radius (m)	1.75
Plasma volume (m^3)	300
Plasma	
Mean temperature (keV)	7
Mean ion density (10^{14} cm^{-3})	1.1
Mean electron density (10^{14} cm^{-3})	1.4
Effective charge	1.9
Confinement time (s)	7.2
Injection power (MW)	26
Toroidal field (T)	5.5
Safety factor	2.5
Poloidal beta	2.2
Toroidal beta	0.025
Plasma current (MA)	4.4
Blanket structure	
Blanket module/Reactor	8
Blanket cells/Blanket module	284
Injection and evacuation hole/Blanket module	1
Nominal max. 1-st wall temp.(°C)	500
Materials	
Structural material	316SS
Blanket fertile material	Li_2O
Reflector materials	Stainless steel & W
Neutronics	
Neutron current at 1-st wall ($n\ cm^{-2}s^{-1}$)	9.5×10^{12}
Neutron wall loading ($MW\ m^{-2}$)	0.2
First wall displacement damage rate ($dpa\ y^{-1}$)	0.8
Max. helium production rate in 1-st wall ($appm\ y^{-1}$)	9.4
Max. hydrogen production rate in 1-st wall ($appm\ y^{-1}$)	29
Tritium breeding ratio	0.9
Nuclear heating per DT neutron ($MeV\ n^{-1}$)	16.1
Total induced activity at one hour after shutdown (Ci) (after one year operation)	9.1×10^7
Toroidal field magnet	
Number of coils	16
Bore, width/height (m)	7/11
Magnetomotive force (MAT)	186
Max. field strength (T)	11
Stored energy (GJ)	50
SCM material	Nb_3Sn
Neutral beam injector	
Number of ion sources	24
Deuterium beam energy (keV)	200
Injection power (MW)	32
Power efficiency	0.3
Cooling system	
Number of loops	4
Coolant, pressure ($kg\ cm^{-2}$)	He,10
Inlet/outlet temp. (°C)	300/500
Flow rate (kg/s)	180
Secondary system	He
Third system	Air cooler
Tritium inventory (kg)	
Fuel recirculating system	0.3
Tritium recovery system including blanket	0.1
Total inventory including storage	0.5

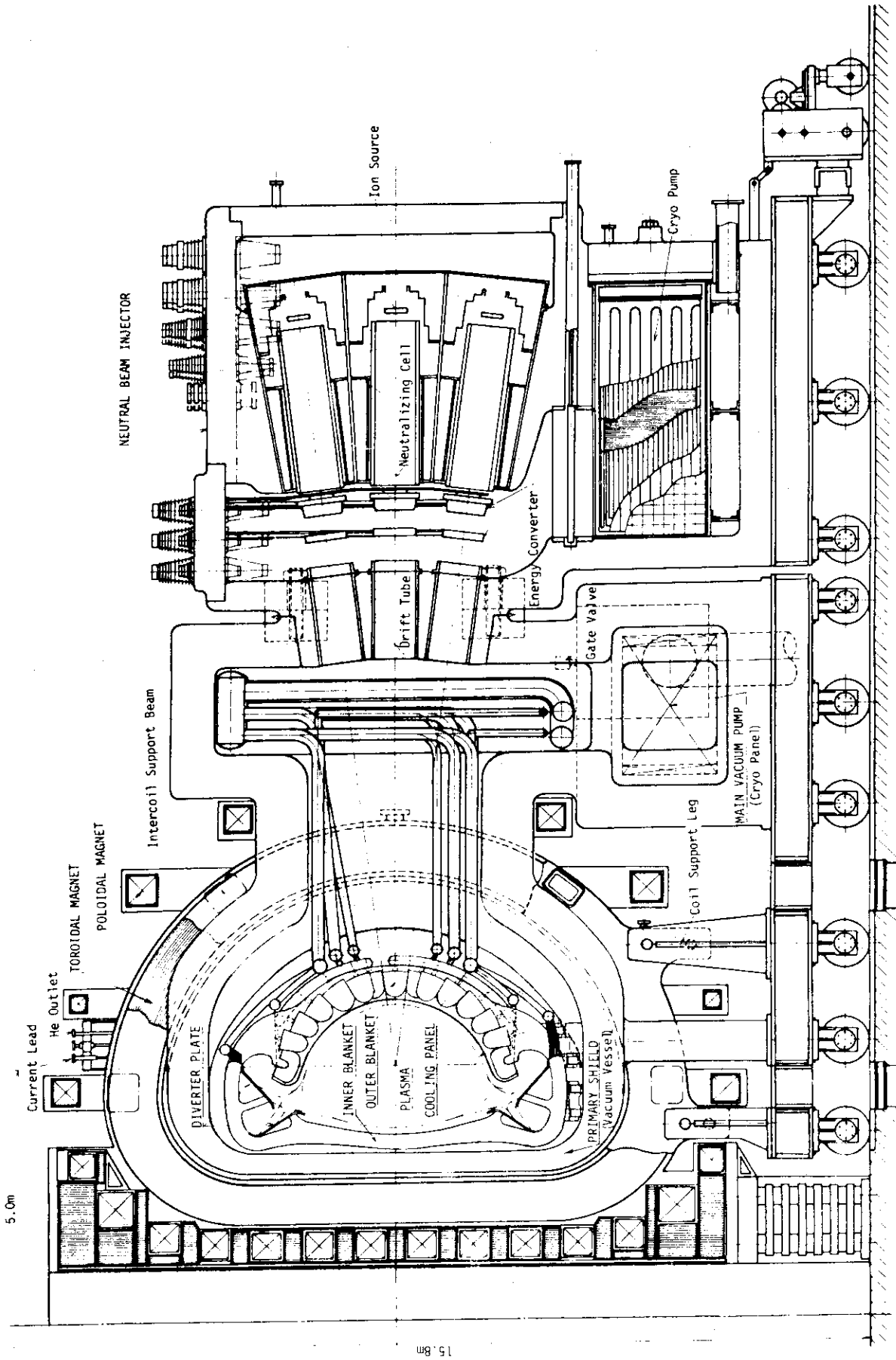

Fig. VIII.2-1 Vertical view of INTOR-J (with divertor)

IX. DEVELOPMENT OF LARGE TOKAMAK - - - JT-60

1. Introduction

Construction of JT-60 was started by placing an order for the Tokamak machine in April 1978, following a ten-month contract negotiaion with Hitachi, Ltd., the preferred among the bidders. Upon completion of re-examination design of the power supplies and control system, the next item, the poloidal field coil power supply was ordered to Toshiba Corporation in early 1979. It is scheduled that the toroidal field coil power supply and the control system will be ordered in 1979. The completion of JT-60 is expected in 1983.

Design work are continued on other parts of JT-60 — the cooling system, emergency power supply, power station, and others. The design of diagnostic equipments is also continued. The design of experimental and control buildings are completed, and the design of power supplies building is continued. The construction of the experimental and power supplies buildings will begin in the next fiscal year 1979-80. The development of heating systems of JT-60 is described elsewhere in the report.

2. Outline of the progress of JT-60

For JT-60 Project, the fiscal year of 1978 is characterized as the starting year of construction of JT-60. On April 17, JAERI made a contract about manufacture of the tokamak machine of JT-60 with Hitachi, Ltd. The contract covers toroidal field coils, a vacuum vessel, poloidal field coils, primary cooling system, vacuum system, baking power supply, movable limiters and supporting structure.

Coil winding of the initial three toroidal field coils were accomplished in this year. Fabrication of these coils were performed with better accuracy than the R & D stage. Especially the finish of junction of winding has been much improved. The vacuum vessel was thoroughly reevaluated following the changed specifications about plasma disruption time constant and about additional diagnostic ports. Material procurements were initiated for the vacuum vessel, poloidal field coils and supporting structure.

Specifications of power supply systems and control systems have been almost settled. The power supply system for the poloidal field coil was ordered to Toshiba Electric Co., Ltd. on March 31, 1978. In the next year, the power supply system for the toroidal field coils and the control system

will follow it.

JT-60 Technical Steering Committee, organized in the previous year by specialists from outside of JT-60 Project to review technical reliability of JT-60, presented the primary report about the reliability of the tokamak machine in June, 1978. Its comments were reflected on design and fabrication of JT-60. The Committee presented the second report in March, 1979, mainly on the vacuum system, the control system and function of safety protection.

Although there is no legal requirement for safety analysis for JT-60 at the national level, JAERI's Advisary Committee on Nuclear Installation Safety made intensively safety evaluation of JT-60. At this analysis, emphases were put on environmental effect by JT-60 construction including noise, radiation etc. The Committee submitted the report to approve the safety of JT-60 on September 13, 1978.

In parallel with this, Atomic Energy Council of Ibaraki Prefecture discussed on environmental effect by JAERI's fusion program at the anticipated site in Naka-machi, which is apart from Tokai Research Establishment of JAERI to westward by about eight kilometers.

Design of Experimental Building and Control Building were finished and design of Power Supply building is now under way. The modified layout of buildings of the new site is shown in Fig. IX.2-1.

JT-60 is scheduled to be accomplished in December, 1983 as shown in Fig. IX.2-2. The critical path of the time schedule is along with construction of Experimental Building and assembly of the tokamak machine. The site procurement was left over to the next fiscal year and its delay is the main obstacle against schedule keeping.

On June 1, 1978, Fusion Research and Development Center was established to generalize the fusion research and development activities at Tokai Research Establishment. In Division of Large Tokamak Development, Large Tokamak Administration Section and JT-60 Program Office were established to reinforce project management. The former deals with affairs about contracts concerning JT-60 and general management affairs and the latter deals with planning and coordination of JT-60 Project. The most recent organization for fusion activities at JAERI is shown in Fig. IX.2-3. JT-60 Program Office covers also the future programs of the next generation machine and JT-4 program.

Thus, the year of 1978 is a memorial year of beginning of JT-60 construction.

Reference

JT-60 Program Office, Project Management of JT-60 (Fiscal Year of 1978), JAERI-memo 8281 (June, 1979), (in Japanese).

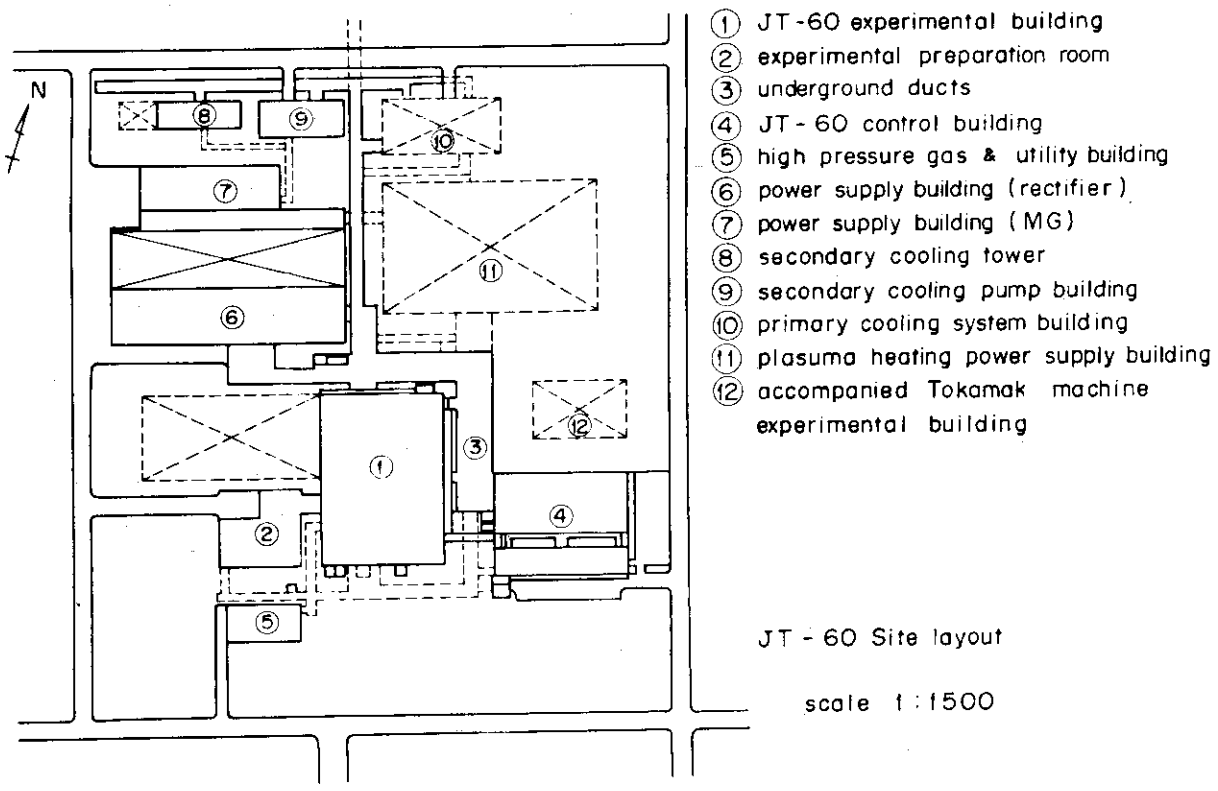

Fig. IX.2-1 Layout of JT-60 site

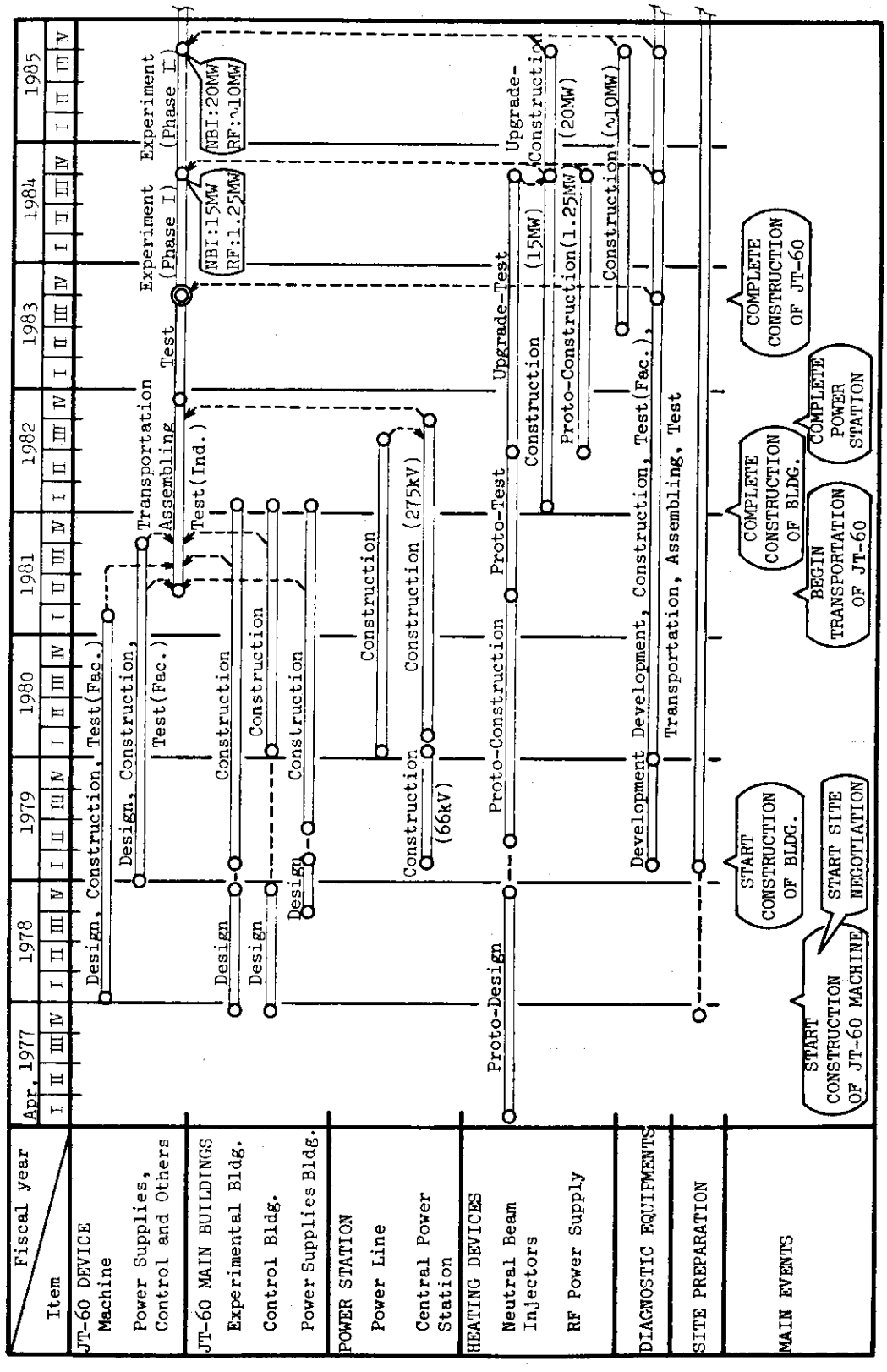

Fig. IX.2-2 JT-60 time schedule

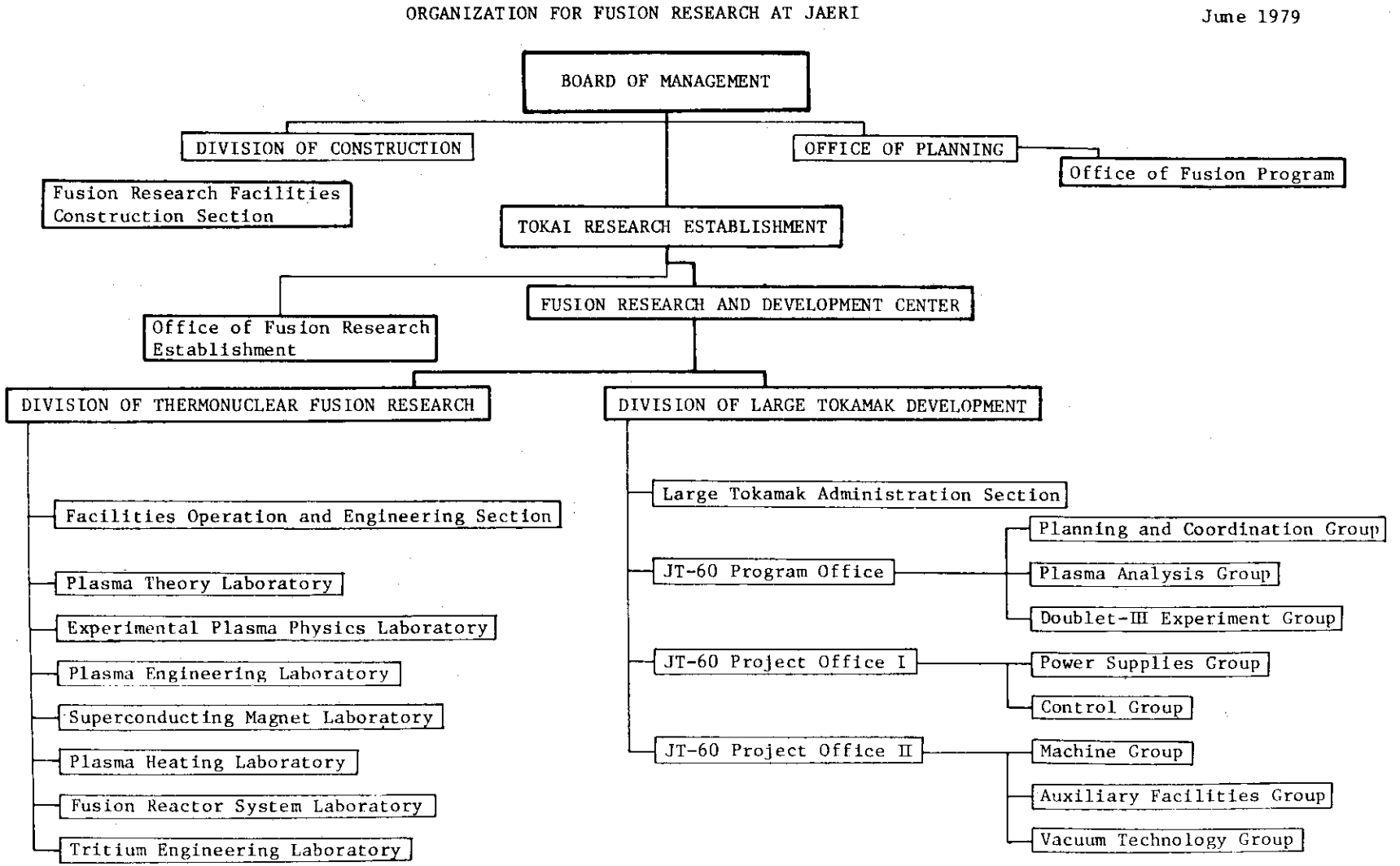

Fig. IX.2-3 Organization for fusion research at JAERI

3. Outline of machine

3.1 Major activities

3.1.1 Major activities

The contract was completed on April 17, 1978 with Hitachi, Ltd. for construction of the machine and its auxiliary systems.

By the end of this fiscal year construction design was already completed for the toroidal field coils and has been advanced for a vacuum vessel, poloidal field coils, support structures, a primary cooling system, a machine control system, and their layout in the experimental building. Furthermore, fabrication of the toroidal field coils, which was regarded as a critical path in the construction of JT-60, was already started and winding of the third coil was completed.

Reviews were made on the experimental program of JT-60 and the results from currently operating devices. Necessity was recognized to increase its experimental and operational flexibility. Therefore, several changes of the specifications were proposed, especially in connection with the design of the vacuum vessel. Much effort has been made in reexamination of the design of the machine to satisfy the proposed specification changes in the latter half of fiscal 1978.

Seismic analysis of JT-60 was carried out with an analytical method newly developed for a large, complex structure such as JT-60 machine and some additional design changes were proposed.

Reviewed and discussed were also the methods of the leak detection of the vacuum vessel and the surface treatment of the first wall by JT-60 Technical Steering Committee and its sub-committee.

The design of JT-60 machine was also reviewed and the structural integrities of the main components, a vacuum vessel, toroidal field coils, poloidal field coils were evaluated by ISES 81 subcommittee led by Prof. Udoguchi. And in this committee proposed were the design criteria to evaluate the structural integrity of each component from the points of structural analysis and fracture mechanics.

The sensors for machine monitoring necessary for operating the machine such as temperature, strain, displacement and so on were studied by ISES 82 sub-committee and reliability and technical problems of the sensors were made clear.

Measurements of flashover voltage were performed under intense ^{60}Co

γ-ray irradiation in order to examine creeping discharge characteristics of the connecting part of the poloidal field coils when exposed to hard X-rays produced on runaway discharges. Fruitful results obtained in this experiment are shown in 3.3.1.

3.1.2 Changes of specifications

Several changes of the specifications were proposed through re-examinations of the recent experimental results from currently operating devices and the experimental program of JT-60.

The changed specifications are the following.

(1) Change of time constant of plasma disruption

Since the design condition that the plasma current of 2,7 MA decreases to zero in at least 50 msec may be too optimistic judging from the available experimental results, it was changed from 50 msec (guaranteed) to 50 msec (guaranteed) and 1 msec (target).

Eddy currents induced in the vacuum vessel were calculated and mechanical integrity of the vacuum vessel was examined in case of plasma disruption with time constant of 1 msec. And it was found that the maximum stress intensity is slightly less than the allowable one.

(2) Prolongation of operation period of Taylor discharge cleaning

JT-60 has two operation modes of discharge cleaning; one with high plasma current and longer duration time and the other with low plasma current and shorter duration time. Recent results from existing devices, especially JFT-2, JFT-2a, and PLT, showed the effectiveness of the latter discharge cleaning-Taylor discharge cleaning. Therefore, operation mode of discharge cleaning with plasma current of about 80 kA and current duration time of about 25 msec was included into the design conditions.

But continuous operation with these conditions causes excessive temperature rise of the bellows of the vacuum vessel and operation period is limited to shorter than half an hour. Therefore, design effort was made to increase allowable operation period and the temperature rise was found to be allowable for operation period less than 200 hrs at an elevated temperature.

(3) Enlargement of NBI ports

To make the most of the machine, an increase of the capability of additional heating power from 20 MW to 40 MW was proposed. Therefore, the

NBI ports were enlarged to make it possible to upgrade the additional heating power in future.

This provides an access for four ion sources per port in stead of two in the present design.

(4) Additions of diagnostic ports

Reviewed was the diagnostic plan of JT-60 and several proposals were made of the addition of the following diagnostic ports. That is IN_4 ports for active diagnosis by neutral particle, IN_5 ports for diagnosis of plasma in a burial chamber of the magnetic limiter, U_7 ports for conventional electromagnetic diagnostics, S_4 ports for diagnosis of the center of the plasma column, T ports for diagnosis in the toroidal direction and C ports for coating the NBI ports.

To install the above ports, some of the existing ones were eliminated.

(5) Installation of a pair of adjustable movable limiters

A pair of adjustable movable limiters is to be installed in the vicinity of the sub-magnetic limiter coils to provide protection of the fixed limiter neighboring the sub-magnetic limiter coils, to control the plasma diameter and to research the limiter materials.

They are each mounted to an actuator which is operated by an electric motor and the limiter heads are easily remountable with the vacuum vessel kept in ultra high vacuum.

3.2 Present design

3.2.1 Design conditions

JT-60 machine is composed of a vacuum vessel, toroidal field coils, poloidal field coils, support structures, a primary cooling system, a machine control system, fast movable limiters, a vacuum pumping system, a plasma monitor system, a gas supply system and a preionization system. The latter four systems are discussed in Section 5 and 6.

The design conditions for each operation mode are summarized in Table IX.3-1. Main design conditions are as follows.

(a) Total number of full power pulses does not exceed 5×10^4. In addition to the full power operation, 1.5×10^5 shots of 50 % rated operation are taken into account in the design life time. (b) The number of such pulses that the plasma is not generated in the build-up phase is 5 %

of total pulses. (c) The number of abnormal plasma disruption with time constant of at least 50 msec is 20 % of total pulses, and furthermore that with time constant shorter than 50 msec (at least 1 msec) is 10^3. (d) The total exposure, the maximum exposure intensity per shot and the maximum energy of X-rays due to runaway electrons are 2×10^8 R, 10^5 R and 10 MeV, respectively. (e) The negative spike of plasma induces the one-turn voltage of 3 kV with the pulse length of 100-400 μsec. (f) The maximum acceleration of the earthquake does not exceed 0.2 G at the base of the machine.

3.2.2 Vacuum vessel

(1) Vacuum vessel

The design of the vacuum vessel was almost completed. The specifications are summarized in Table IX.3-2. And the cross sectional view of the vacuum vessel is shown in Fig. IX.3-1.

Much effort was made in stress analysis[1] of the vacuum vessel to decide the thicknesses of the rigid ring and the bellows in the former half of this F.Y. From geometrical interference with the support structures of the poloidal field coils, reinforcement ribs of the rigid ring were taken away, and instead of it, the thickness of the rigid ring was changed from 40 mm to 65 mm in order to increase the rigidity of the vacuum vessel.

Stress of the bellows induced by thermal expansion of the rigid ring increases, but that by the outer pressure such as vacuum pressure, saddle-like eddy current decreases with increase in the thickness of the bellows. Therefore, the thickness and height of the bellows were also changed from 2.0 mm and 80 mm to 2.5 mm and 70 mm in order to decrease the stress by the outer pressure.

Dash-pots were also taken away because they were found to be not so effective in suppressing the stress from static analysis and the space they occupy is fairly valuable for plasma diagnostics. But alternates are now under consideration, for they seem necessary to suppress the dynamic behavior.

Decrease of the thickness of the bellows in its fabrication process was examined by comparing the thickness of the bellows fabricated by trial in R & D and that measured before fabrication. And it was found to be less than 0.17 mm, which hardly affects the stress intensity of the bellows.

Much effort was concentrated in design reexamination following the

changes of the specifications. Geometrical arrangements and interferences were examined for enlargement of NBI ports and additions of plasma diagnostic ports with energetic effort.

Thermal analysis of the vacuum vessel was carried out to estimate how long Taylor discharge cleaning can be continued, and it was made clear that the temperature rise of the bellows of the vacuum vessel is allowable for operation period shorter than 200 hrs at an elevated temperature.

Stress analysis of the vacuum vessel carried out in case of plasma disruption with time constant of 1 msec showed that the maximum stress intensity is slightly below the allowable one.

Allowable He leak rate of the vacuum vessel of 5×10^{-7} torr·ℓ/sec is required to satisfy the ultimate pressure of 1×10^{-8} torr, as shown in Table IX.3-2. And in order to perform the allowable He leak rate examined were the leak detection methods for each component in the factory, before assembling and after assembling at the site. They were reviewed and discussed by JT-60 Technical Steering Committee and its lower sub-committee organized by specialists and authorities in vacuum physics and technology. And some fruitful comments were obtained.

The specifications required for the gate valves for ports are baking temperature of 300 °C, He leak rate of the valve of less than 1×10^{-8} torr·ℓ/sec (target) and 1×10^{-7} torr·ℓ/sec (guaranteed), guarangeed life of 2×10^{3}, diameter larger than that of the port to which the gate valve is attached and the gate seal material of all metal. Three candidates were selected to provide for the verification tests planned in the following F.Y.

The design of the thermal control system of the vacuum vessel was also examined. Combined system was almost closed with electric heater for heating and with N_2 gas and water for cooling. Now reliability is being examined of such components as a valve, blower and so on.

(2) First wall

In this F.Y. the design of the first wall was examined in consideration of the plasma-machine interaction, especially thermal and stress analysis in case of plasma disruption with time constant of 1 msec.

Molybdenum liners are attached to the rigid ring as shown in Fig. IX.3-1. The thickness, typical width and length of the liner are 0.5 cm, 8 cm and 40 cm, respectively. But the detailed dimensions are not decided. The heat load to the liner of 10 MW × 10 sec, equivalent to 10 W/cm^2 causes the

maximum temperature rise of 75 °C. The maximum stress due to electromagnetic force in case of plasma disruption with time constant of 1 msec is greater than the yield stress of Mo. Therefore, slits parallel to the toroidal field are provided to reduce the eddy current. But the slit width is required to be less than 2 mm to protect the bellows of the vacuum vessel against heat flux from plasma through the slits. The recrystallization of the Mo liner under the direct bombardment of unattenuated neutral beams in case of plasma disruption are negligibly small even after 10^4 shots when the delay time of the NBI interlock system is below 0.5 sec[2].

Seventeen toroidal fixed limiters with an elliptical cross section are installed projecting 2 cm from the liner surface. The heat load to the fixed limiter of 10 MW × 10 sec, equivalent to 680 W/cm^2 if concentrated on only three, causes temperature rise of 1200 °C, so the maximum surface temperature is expected to exceed 2000 °C in the hot liner experiment. To decrease the edge concentration of the heat load, the limiter edges are rounded off. In case of plasma disruption with time constant of 1 msec the stress of the fixed limiter overhanging the bellows is also greater than the yield stress of Mo, and design effort was made in reducing it.

Magnetic limiter plates are positioned on the outer side of the vacuum vessel. The heat load to the magnetic limiter plate of 5 MW × 5 sec, equivalent to 100 W/cm^2 with swinging a separatrix line over the length of 10 cm causes the maximum temperature rise of 120 °C. The stress due to electromagnetic force in case of plasma disruption with time constant of 1 msec is under consideration.

3.2.3 Toroidal field coils

The toroidal field (TF) coil system consits of 18 TF coil blocks, as shown in Fig. IX.3-2. Eighteen coil blocks equally located at a major radius of 3.32 m maintain the field ripple to about 0.3 % in the plasma region. The detailed specifications are listed in Table IX.3-3.

Fabrication design was already completed in the early stage of this F.Y. The width of the TF coil was reduced from 840 mm to 696 mm to improve an accessibility to the vacuum vessel. And minor changes were made of the thickness of the support structure to increase its rigidity.

Fabrication of TF coil was also started and was advanced without any trouble. Winding of third coil was completed at the end of this F.Y. Strict inspections were carried out in each process to obtain the required

performance and to assure high reliability. Especially, great care was devoted to the coil dimension and geometry, which cause error field[3] and consequently have an important effect on plasma confinement. So far, satisfactory results were obtained with dimension deviation less than 3 mm.

Further reexamination of the design was carried out from the point of fracture mechanics and back data are now being collected on tensile strength, distribution of cracks, crack propagation rate, fatigue property, etc., to provide statistical fracture analysis.

3.2.4 Poloidal field coils

The poloidal field coils (PF coils) are composed of ohmic heating coils (OH coils shown in Fig. IX.3-3), vertical field coils (V coils), quadrupole field coils (Q coils), horizontal field coils (H coils) and magnetic limiter coils (M coils). The first four coils are located in the space between the vacuum vessel and the toroidal field coils and the last inside the vacuum vessel. The specifications of PF coils are shown in Table IX.3-4.

The cross-sections and arrangement of the PF coils were examined considering not only the required field conditions but accessibility of the diagnostic ports to the vacuum vessel and trade-off between the mechanical safety margins of PF coils and their support structures. As the connection structure of PF coils necessary for assembly/disassembly, metallurgical joint was selected instead of the mechanical one because of its superiority of the mechanical strength. The support structures of the PF coils are to be supported with support rods extended only from the lower support structure to decrease their stress caused by tortion of the upper support structure due to electromagnetic forces of toroidal field coils.

The M coils are encased in the cases consisting of rigid rings and bellows, which are to be made of Inconel 625. The design of the bellows of M coils cases was examined to withstand the plasma disruption with time constant of 1 msec and confirmed as the following dimensions; pitch, thickness and number of revolution per bellows assembly are 6 mm, 0.9 mm and 80, respectively.

3.2.5 Support structures

Support structures consist of upper and lower support structures, a central column, support columns of a vacuum vessel and trusses connecting

the upper support structure with the wall of the building. They must have enough strength to endure the weight of about 5000 tons, several kinds of electromagnetic forces, earthquakes and so on.

Basic design was examined and almost fixed except the central column. Upper and lower support structures are separated into 8 parts to reduce the eddy current.

Seismic analysis of JT-60 made it clear that the support columns of the vacuum vessel do not have enough mechanical strength against earthquakes, which causes an excessive displacement of the vacuum vessel. Therefore, design of the support columns of the vacuum vessel was changed by connecting the adjacent support columns each other so that their strength should increase.

3.2.6 Primary cooling system

Primary cooling system is designed to fulfill following two functions; one is to remove the waste heat from field coils and plasma influx energy from a vacuum vessel within 600 seconds interval between pulses, and the other to cool down the vacuum vessel in the baking operation mode.

The primary cooling system is divided into two separate subsystems, the field coils cooling subsystem and vacuum vessel cooling subsystem. Each subsystem consists of circulating system and heat exchangers.

The main requirements for the primary cooling system are summarized in Table IX.3-5. In this F.Y. clarified were the rough requirements necessary for the design of the building such as the geometrical arrangements of the components of the primary cooling system. Total flow rate for field coils cooling subsystem was changed from 2500 m^3/hr to 2000 m^3/hr in company with the progress of the design of the toroidal field coils.

Detailed design is now in progress.

3.2.7 Movable limiters

Fabrication design of fast movable limiters was not started yet. However, details on design and fabrication techniques were established in the engineering development carried out in F.Y. 1977. So, fabrication of them is not regarded as a critical path on the course of construction of JT-60.

Examined were only rough requirements necessary for the design of the building and geometrical interference with the diagnostic instruments.

3.2.8 General layout and building

Experimental building, which is 93 × 64 meters in length and width and 40 meters in height, consists of a torus hall, an assembly hall, a storage hall, a loading area, diagnostic areas, RF power supply area and so on. It is connected with the power supply building, control building by main undergound ducts. Detailed drawings of the experimental building are shown in Figs. IX.3-4 and IX.3-5.

Test areas for neutral beam injector and fast movable limiter were separated from torus hall in order to make it possible to test them during operation. Wiring, piping and arrangement of the machine components in the experimental building were arranged with energetic efforts.

3.2.9 Machine control system

Machine control system consists of two subsystems named "machine control system I" and "machine control system II" under the central controller named "ZENKEI". The former is composed of a primary cooling system, a thermal control system of the vacuum vessel and the magnetic limiter plate, a vacuum pumping system, gate valves and sensors for machine monitoring, and provides total machine control. The latter is composed of a fast movable limiter, a gas supply system and a preionization system, and provides discharge control.

As micro-computerized CAMAC system was introduced for interface between ZENKEI and machine control system, the design of the machine control system was examined in the latter half of this F.Y.

The following functions are required for the machine control system. (1) Micro-computerized CAMAC system must be introduced for the interface between ZENKEI and machine control system. (2) Machine control system must be able to transfer informations and operate the installations remotely following the instructions from ZENKEI. (3) The safety and protection system must be made of hard-wired circuitaries.

3.3 Related studies

3.3.1 Flashover characteristics of poloidal field coils under γ-ray irradiation[4)]

Measurements of flashover voltage (FOV) and other parameters which characterize the creeping discharge were performed under intense ^{60}Co γ-rays

irradiation in order to examine creeping discharge characteristics of the connecting part of the poloidal field coils when exposed to hard X-rays produced on runaway discharges. Alternating current voltage (50 Hz) was applied to model coils.

Figure IX.3-6 shows the FOV characteristics of the model coils at the exposure rates of 1×10^6 R/h and at 0 R/h. "t" in the figure indicates the insulation thickness. As shown in this figure, FOV at an exposure rate of 1×10^6 R/h is almost the same or slightly higher than that under non-irradiation; at this exposure rate, the coil insulation is not affected.

FOVs of sphere gap and along cylindrical bar samples were measured under the same irradiation. The value decreased for the sphere gap.

FOV results at extremely high exposure rate of X-rays for these samples were also obtained.

3.3.2 Prevention measures for adhesion of bolts in ultra-high vacuum and at elevated temperature

In JT-60 Molybdenum first walls (liners, fixed limiters and magnetic limiter plates), which are to be attached to the vacuum vessel made of Inconel 625 by supports and bolts, are designed to be demountable in case of a fatal damage or wall material experiments. But after baking at 500 °C or hot liner experiment at 400 °C, adhesion between these bolts and the vacuum vessel seems to be inevitable. Therefore, the experimental sturdies were performed about the protection measures for adhesion between bolts and the vacuum vessel.

In this experiment, bolts made of SS 304 and Inconel 625 were selected as the test materials. The bolts coated with MoS_2 by inorganic bond, MoS_2 by sputtering and TiN by ARE and uncoated ones were tightened by the nuts made of Inconel 625 simulating the vacuum vessel with a torque of 30 kg·cm, and then heated for 140 hr at the temperature of 650 °C and under the pressure of 10^{-7} torr. After heating measured were the torques to loosen the nuts.

The results showed that it was impossible to loosen the nuts from the uncoated bolts due to adhesion and the torques to loosen the nuts from the coated bolts made of SS 304 and Inconel 625 were 19 kg·m and 7 kg·m, respectively. Therefore, it is clear that coating is effective in suppressing adhesion to some extent.

3.3.3 Seismic analysis of the JT-60 machine[5,6)]

Seismic analysis of the JT-60 machine was carried out to confirm its integrity in earthquakes with an analysis method newly developed for JT-60.

Block diagram of the analysis method is shown in Fig. IX.3-7. For analysis, machine model comprises "simple model" of respective components constituting the machine. Each simple model is based on the engineering criterion that it should have as similar dynamic characteristics to those of a "detailed model", which is faithful to the real component structures and further as few nodal points as possible. So, analysis of the machine model gives information of not only overall behavior but also local vibration of each component with few nodal points. The analysis method is thus useful especially for a large complex structure such as JT-60.

The results showed that JT-60 has the first natural frequency of 4.5 Hz and distinguished horizontal and vertical vibration mode of the vacuum vessel. The bellows of the vacuum vessel are deformed forcedly due to the displacement of the adjacent rigid rings, which exerts a large stress up to about 24 kg/mm^2 on the bellows under the worst matching in vibration phase and amplitude of the rigid rings. Therefore, the need is indicated for design change of the support structure of the vacuum vessel should be made, such as increase in rigidity of support arms.

References

1) Takatsu, H., Shimizu, M., Yamamoto, M., and Ohta, M.: JAERI-M 8017 (1978).
2) Nakamura, H., and Kuriyama, M.: JAERI-M 8359 (1979).
3) Nishio, S., Ohkubo, M., Kawasaki, K., Ando, T., and Miki, N.: JAERI-M 7846 (1978).
4) Ando, T., Tanaka, R., Hirao, T., Tamura, N., Ohkubo, M., Iijima, T., Ieda, M., Nagao, M., Aki, F., Sato, T., Goto, K., and Watanabe, T.: JAERI-M 8360 (1979).
5) Takatsu, H., Shimizu, M., Okumura, M., and Kawakami, M.: JAERI-M 8155 (1978).
6) Takatsu, H., Shimizu, M., Okumura, M., and Kawakami, M.: JAERI-M 8350 (1979).

Table IX.3-1 Operation modes and design conditions.

Operation mode	Full power	50% rated	Discharge cleaning with longer duration	Discharge cleaning with shorter duration
Plasma current	2.7 MA	1.35 MA	∿ 0.8 MA	∿ 80 kA
Toroidal field	45 kG	22.5 kG	∿ 10 kG	∿ 10 kG
Poloidal field coils	100 %	50 %	∿ 30 %	∿ 10 %
Plasma current duration	5 sec	-	∿ 1 sec	∿ 25 msec
Interval between shots	10 min	-	∿ 2 min	∿ 0.3 sec
Total shots	5×10^4	1.5×10^5	10^5	-

Table IX.3-2 Specifications of a vacuum vessel and first walls.

Vacuum vessel	
Structure	U-shaped bellows and rigid rings
Cross section	Ref. Fig.IX.3-1
Material	Inconel 625
Thickness	
Rigid ring	65 mm
Bellows	2.5 mm
Magnetic permeability	<1.02
Electric resistance	>1.3 mΩ
Allowable He leak rate	$<5\times10^{-7}$ torr·ℓ/sec
Expected outgassing rate	$<1\times10^{-11}$ torr·ℓ/sec·cm^2
Expected ultimate pressure	$<10^{-8}$ torr
Baking temperature	
Vacuum vessel	500°C
Ports	250°C
Vacuum seal	
Vacuum vessel	Welding
Ports	Metal seal
Earthquake proof	0.2 G
First walls	
Materials	Molybdenum
Cross sections	Ref. Fig.IX.3-1
Thickness	
Liner	5 mm
Fixed limiter	40 mm
Collective plate	20 mm
Baking temperature	200 ∿ 500°C
Expected outgassing rate	$<10^{-11}$ torr·ℓ/sec·cm^2
Earthquake proof	0.2 G

Table IX.3-3 Specifications of TF coils.

Number of coil	18	
Coil current	52.1	kA
Total turn	1296	turns
Coil major radius	3.32	m
Coil inside radius	1.94	m
Coil outside radius	2.86	m
Field at plasma center	45	kG
Maximum field in coil	98	kG
I^2R	390	MW
$LI^2/2$	2.85	GJ
Equivalent square wave pulse length	38	sec
Total energy consumption per pulse	8.66	GJ
Coil inductance L	2.1	H
Coil resistance R	84	mΩ
Coil time constant L/R	25	sec
Maximum current density	26.8	A/mm^2
Forcing voltage	7.5	kV
Flat top voltage	4.4	kV

Table IX.3-4 Specifications of PF coils.

Type of PF coils		OH	V	Q	H	M
Ampere turn	MAT	±5.5	±1.8	±0.5	±0.13	±0.75
Total turns		60	64	40	12	16
Max. current	kA	91.7	57.3	25.0	20.0	94.4
I^2R	MW	40.4	39.7	11.1	1.9	30.3
$LI^2/2$	MJ	35.3	18.7	1.1	0.1	4.1
Time constant	sec	2.4	0.8	0.3	0.4	0.4
Equivalent square wave pulse length	sec	7.3	5.8	6.8	7.0	5.6
Ground voltage	kV	<30	<25	<10	<5	<5
Turn to turn voltage	kV	<1.5	<1.5	<1.5	<1.5	<1.5

Table IX.3-5 Specifications of primary cooling system.

		Field coil system	Vacuum vessel system
Total removal energy	MW	18.4	0.9
Total water flow rate	m^3/hr	2000	130
Maximum system pressure	kg/cm^3G	16	12
Number of pump		4	2
Number of heat exchanger		5	1
Max. outlet temperature from heat exchanger	°C	42	
Resistivity of coolant	Ω-cm	10^5	
pH of coolant		5 ∿ 9	

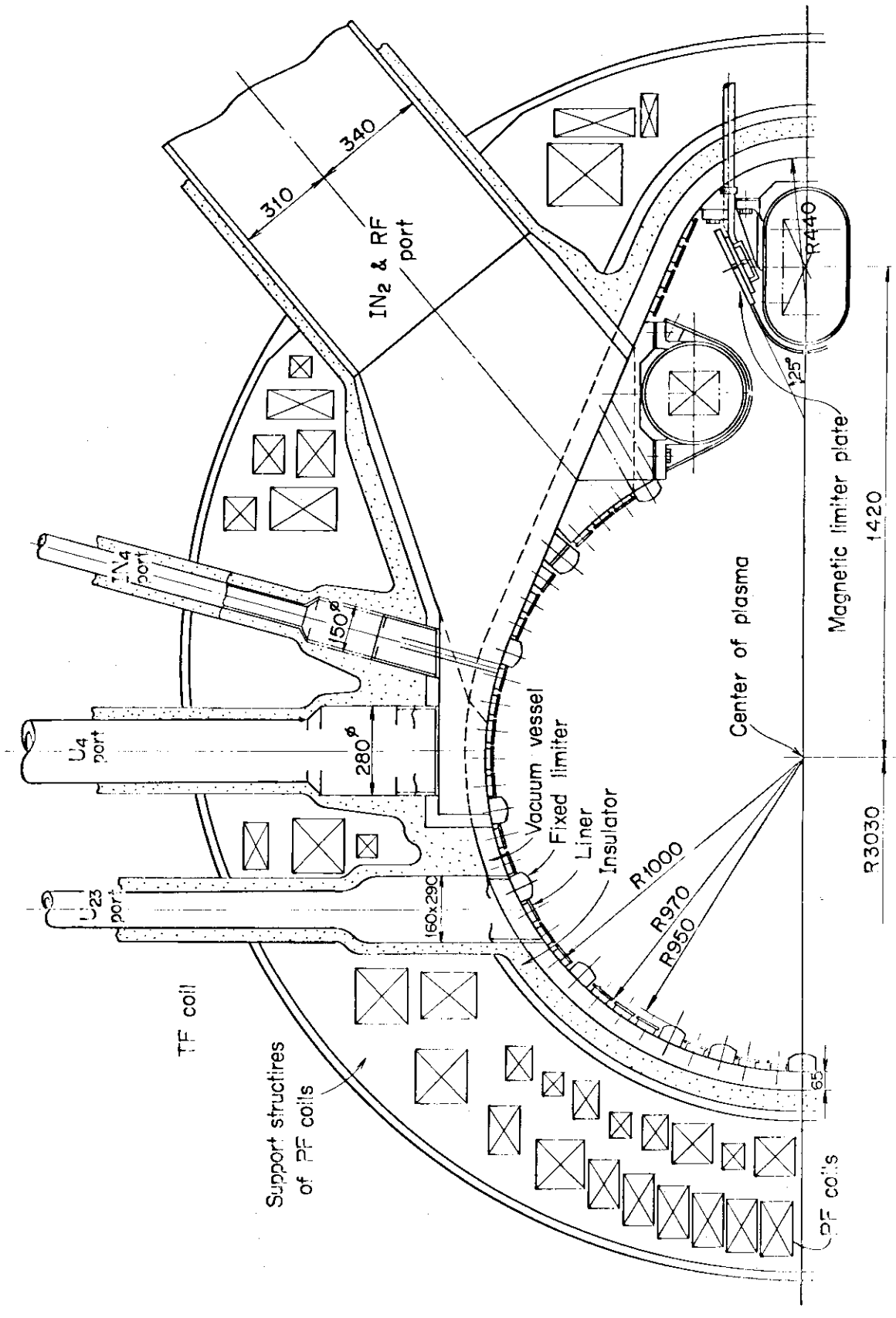

Fig. IX.3-1 Cross sectional view of a vacuum vessel.

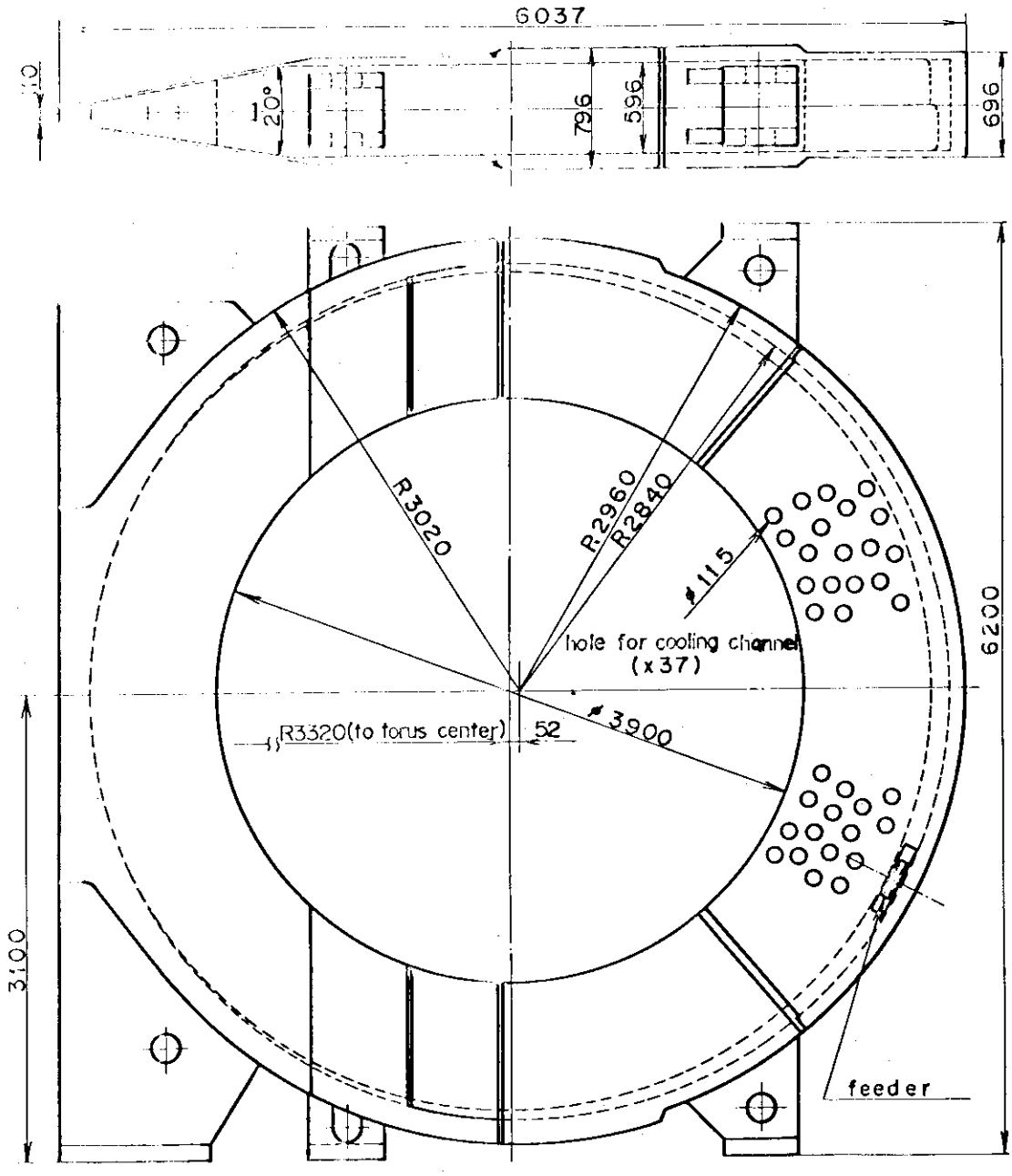

Fig. IX.3-2 TF coil block.

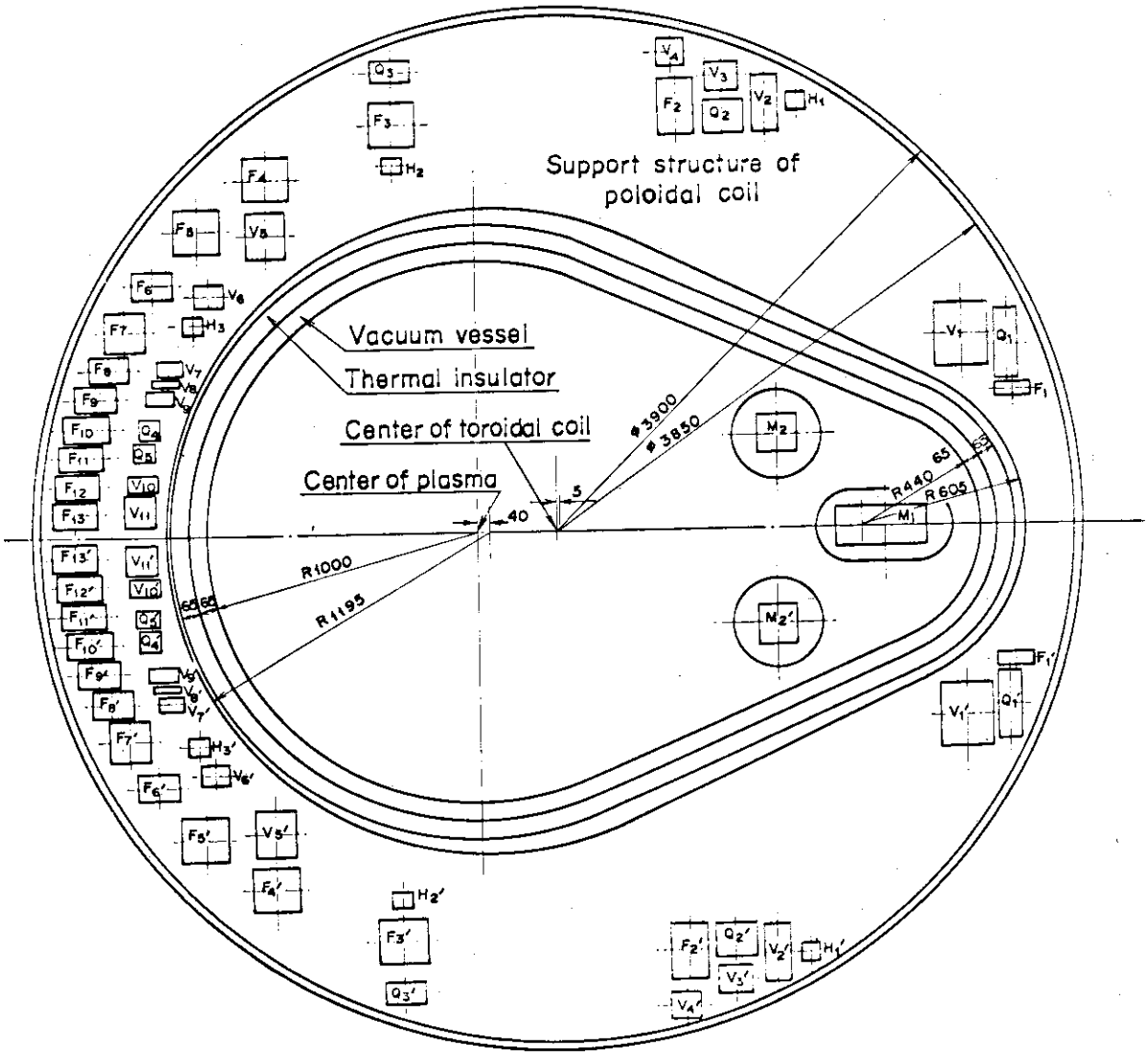

Fig. IX.3-3 Arrangement of PF coils.

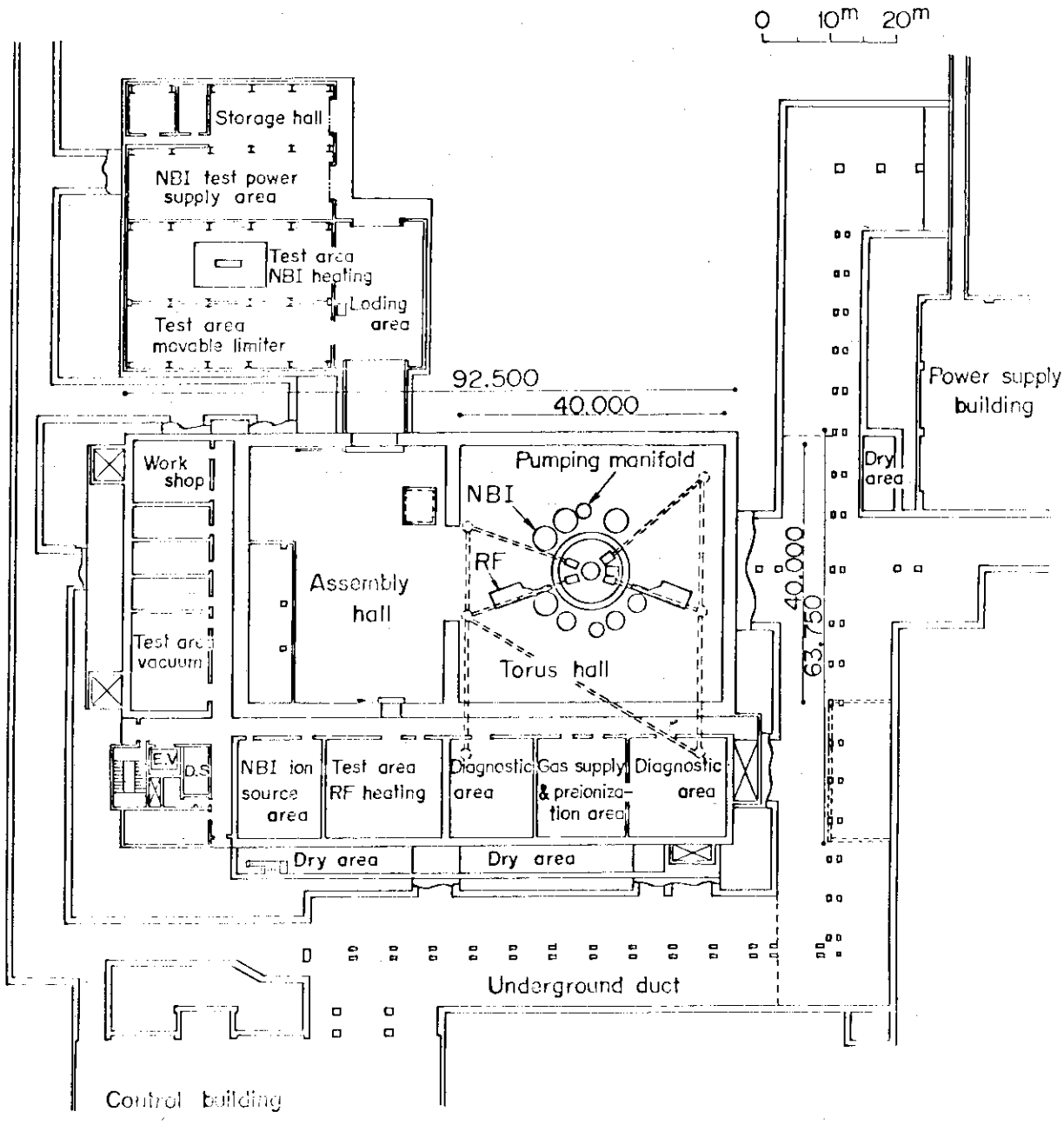

Fig. IX.3-4 Layout in experimental building --- top view.

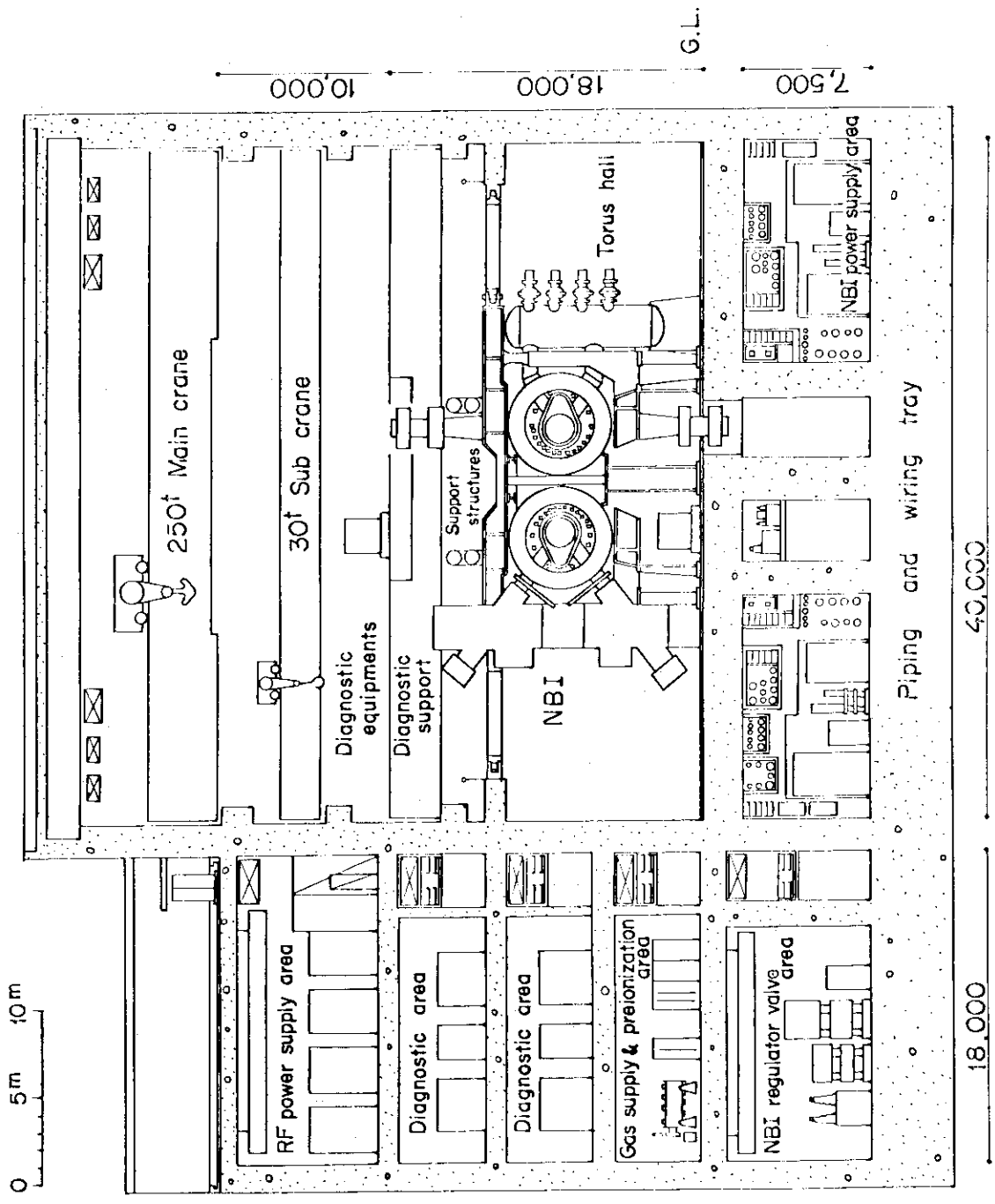

Fig. IX.3-5 Layout in experimental building --- cross sectional view.

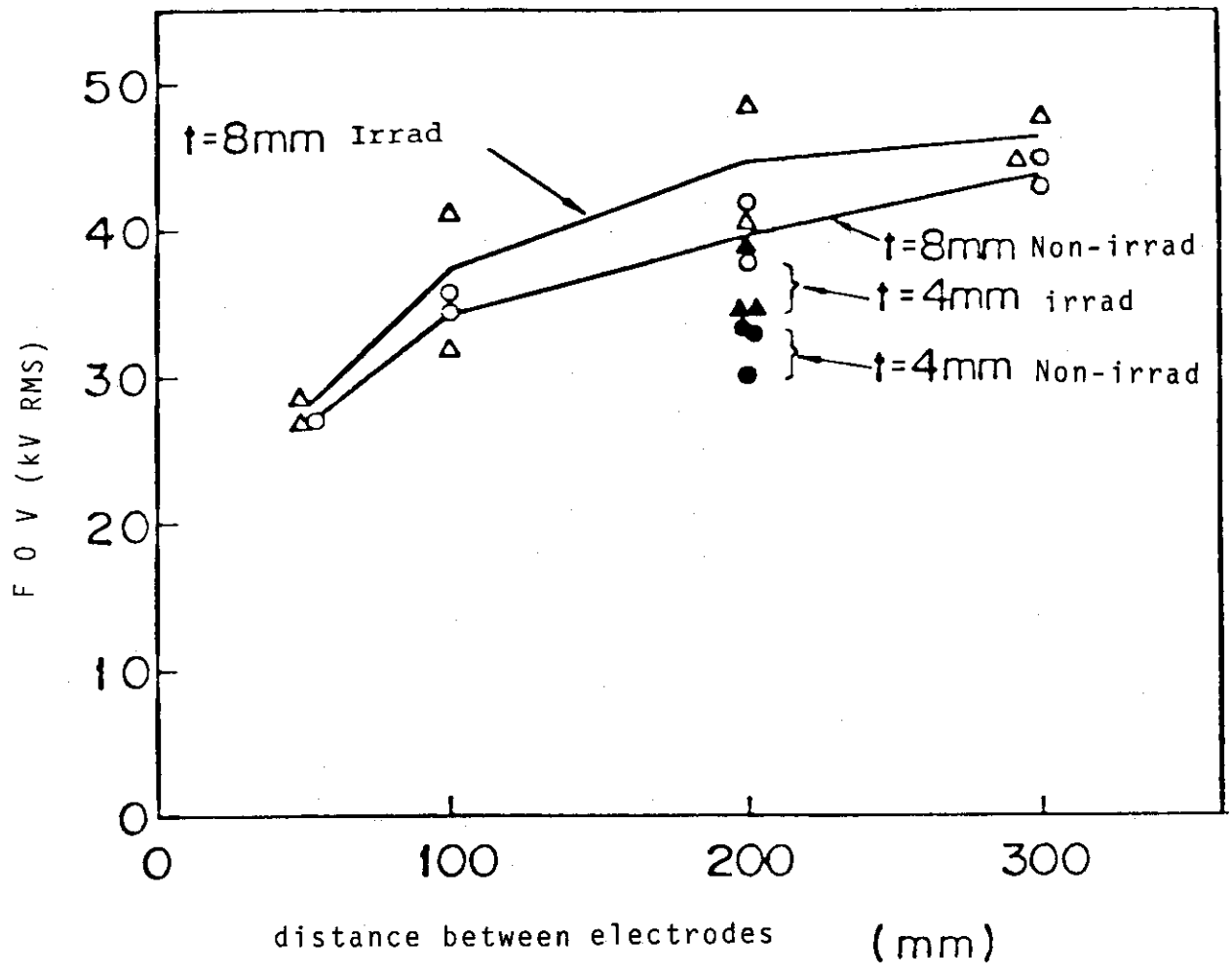

Fig. IX.3-6 FOV characteristics of model coils at exposure rates of 1×10^{6} R/h and 0 R/h.

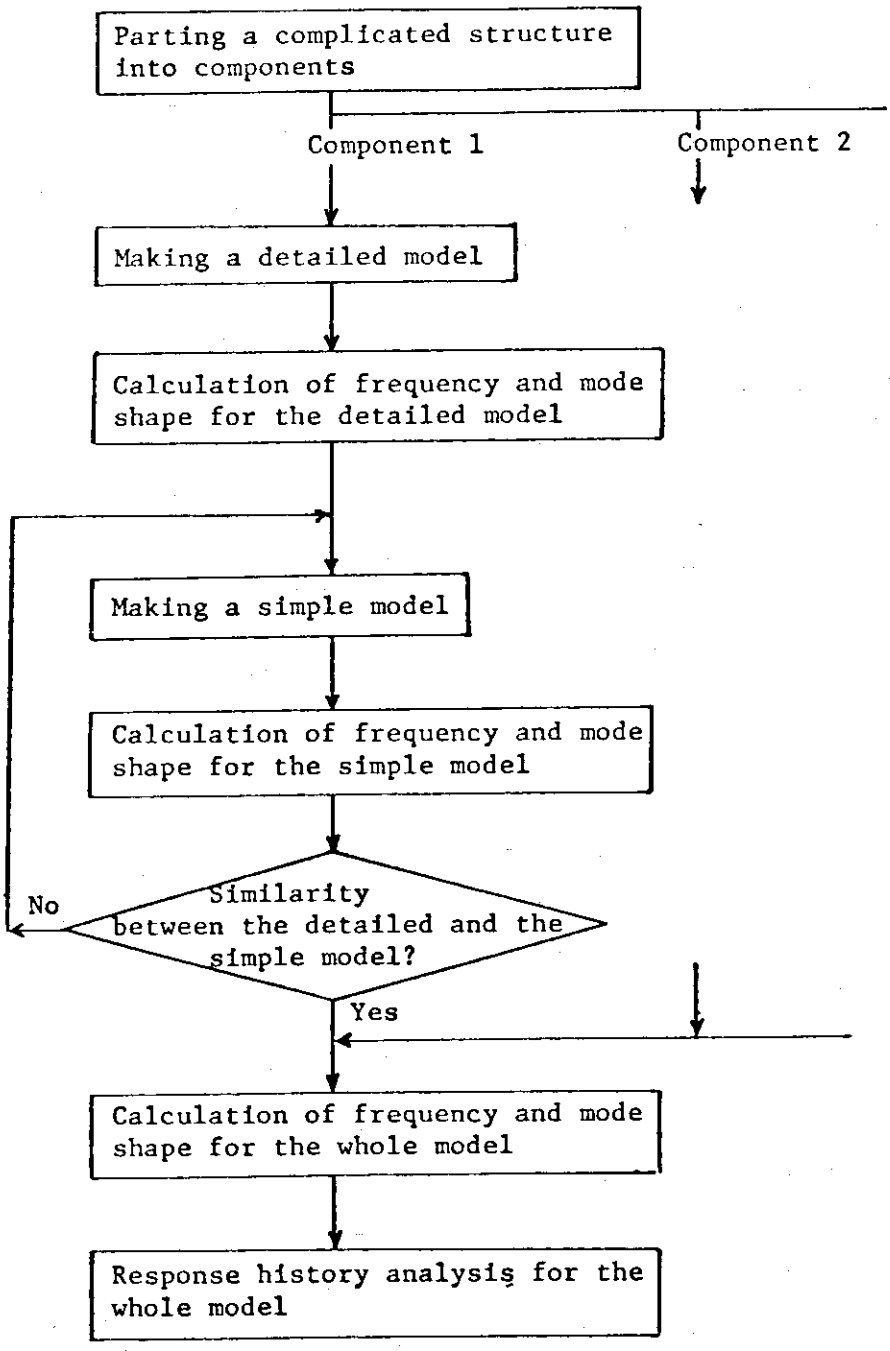

Fig. IX.3-7 Block diagram for seismic analysis of JT-60.

4. Status of power supplies

4.1 Major activities

During the first half of the period (April to September 1978), major efforts were concentrated on the reexamination of the preconstruction (detailed) design of the JT-60 power supply system to finalize its ordering specifications. A contract was given to industries in February 1978 to carry out the reexamination design and the work was completed in September as scheduled.

The major areas covered by the reexamination design are:

1) More detailed design of the vertical type motor generators for both the toroidal and the poloidal field power supplies. This is motivated particularly by the slight modification in the design of the toroidal field coils and the detailed evaluation of the required power and the operation performance of the poloidal field power supply.

2) Design improvements to reduce the interferences with the utility power network.

3) Modifications of the OH and the equilibrium field circuits to improve their performance during the plasma current build-up time, and the re-examination of thyristor converter systems design.

4) Design improvements of some components of the OH circuit such as the inductive energy storage coil, the resistors, the vacuum circuit breakers and some mechanical switches.

5) Modifications and improvements of the control system of the power supplies; to reexamine and specify its functions to be shared as a sub-controller of the JT-60 central controller.

6) Reevaluation of cost of the power supply system and design modifications for reducing the cost of some of the major components.

7) Perfection of the ordering specifications of the entire power supply system.

The final choice of some of the design alternatives was also made during the course of the above-mentioned work. Design-related studies, for example, analyses of volt-second consumption of the OH circuit and transient phenomena arising in the poloidal field coils and the vacuum chamber associated with fast behavior of plasmas, etc. were made in parallel with the design reexamination.

The design and the related studies of the grounding system of the entire JT-60 system were made for the purpose of making provision for safety and protection of the system. The grounding system is also required to reduce interferences among power lines and signal circuits and electromagnetic and/or electrostatic disturbances to noise-sensitive devices such as diagnostic instruments, computers and control equipments.

On the basis of the work made in the first half of the period, the ordering specifications of the poloidal field power supply were completed in the middle of October. The contract to construct a part of the poloidal field power supply was concluded with the Toshiba Corporation at the end of March 1979. By this contract, the motor generator, the OH field power supply and their appurtenances were entered into the stage of manufacture.

4.2 Present design

4.2.1 Toroidal field power supply

The JT-60 toroidal field power supply system provides a large electric power to the toroidal field coils and the maximum toroidal field of 45 kG is generated at the center of the plsma chamber for 5 seconds.

This system consists of two lines, namely;

1) utility power line
   the line which feeds the electric power directly from the utility power network

2) MG line
   the line which feeds the electric power generated by a motor-generator-flywheel set

The circuit is shown in Fig. IX.4.2.1-1.

As a result of the design modification of the toroidal field coils, new toroidal field coil parameters were settled as follows;

resistance　R = 79.16 mΩ at 42 °C
inductance　L = 1.90 H

The load pattern of both lines is shown in Fig. IX.4.2.1-2. The peak load of the power system becomes 325 MW and the total energy is 8.5 GJ (current rise time: 30 sec.). The power and energy of both lines are as follows;

	Power	Energy
Utility power line	160 MW	4.75 GJ
MG line	215 MW	3.75 GJ

The detailed design of the toroidal field power supply was completed and the specifications of each component were reexamined. The serious engineering problems such as the design of the thrust-bearing of the MG-flywheel set, the flywheel material strength, the high speed rotor vibrations, reduction of the interferences with the utility power net work were studied in the reexamination design. By this design study, solutions or countermeasures were found to make secure the overall design of the toroidal field power supply.

The design of electrical energy recovery system and thyristor starter of the MG is under investigation.

4.2.2 Poloidal field power supply

(1) The poloidal field system of JT-60

The poloidal field system comprises AC and DC parts. The former consists of an AC generator, AC interrupters and transformers, and the latter consists of DC circuit breakers, an inductive energy storage coil, DC switchgears and six thyristor converters. Each of the six thyristor converters independently energizes the respective poloidal field coils. The electric power is supplied to these converters through a common bus from the poloidal field AC generator. The generator must be controlled so that its output voltage is kept constant during the operation and each coil voltage is controlled by respective thyristor converters to meet various plasma behaviour.

The overall AC power required from the generator is 500 MVA and the energy requirement for one-cycle operation is 1.3 GJ which is delivered from the generator with the rotating speed variation of 600 RPM to 420 RPM. A schematic diagram of the JT-60 poloidal field power supply system is shown in Fig. IX.4.2.2-1, the main characteristics of the major components are summarized in Table IX.4.2.2-1.

The poloidal field coils and hence their power supplies are closely related to plasma behaviour, so detailed circuit analyses including plasma characteristics are necessary for determining the operational performance and the ratings of components. Mutual couplings among the poloidal coils should also be taken into account to analyze the circuit behaviour.

(2) The ohmic heating circuit

The circuit design of the OH circuit system has been made using vacuum circuit breakers. The basic feature of JT-60 OH circuit system is to make a multi-stage build-up of plasma current using a set of inductive energy storage (IES) coil.

We have investigated the OH circuit based on this idea taking into account of the energy and interruption capacity to build-up the plasma.

On the basis of this consideration, we selected two stage build-up by IES coils to simplify the OH circuit and increase the operational reliability. Two arrangements of the OH circuit have been considered as shown in Fig. IX.4.2.2-2, hereafter called A and B type. The circuit analyses have been done, and it is found that both A and B are feasible for JT-60 two stage build-up, but type B has some merits such as the flexibility of experiment during the plasma current build-up phase, the removal of the polar conversion switch and the reduction of energy dispersion in R_1 and R_2 in Fig. IX.4.2.2-2.

The series connection of R_1 and PSF1 will give us a flexibility of OH coil voltage which, without this, is determined solely by the time constant of R_1 and L_{oh}. The B type circuit therefore has a possibility of plasma current control even in the build-up phase.

In the flat-top phase, there is the possibility that the voltage ripples will disturb the plasma measurement, especially the one-turn loop voltage measurement. The OH converters have been designed to reduce them by using the multi-pulsed operation of converter up to 24 pulse. This is found to be insufficient, because the ripples on the one-turn voltage at the vacuum vessel are calculated as high as 1 volt. The B type OH circuit has a low-pass filter composed of R_1 and L_s, and is expected to serve satisfactorily to attenuate the voltage ripples.

Figure IX.4.2.2-3 shows the B type OH circuit excluding the charging circuits of commutation condensers. The OH coil and L_s store the magnetic energy to obtain the rapid rise of plasma current. Their maximum store energy are 35 MJ, respectively. Inductances and resistances of L_s, R_1 and R_2 are variable in steps. During the premagnetization, PSF1 and PSF2 energize L_{oh} and L_s. To maintain the plasma current or to build-up it further, PSF2 is mainly used. Both PSF1 and PSF2 which can deliver the maximum voltage of 2500 V are controlled to be circulating current mode or by-passing mode depending on the experimental requirements.

(3) The vertical field power supply

The current in the vertical field coil must be controlled by a power supply which is intended to ensure the proportionality of vertical field to the plasma current particularly in the build-up phase, and to keep the plasma at desired place in the flat-top phase.

For the fast excitation of the vertical field during the current build-up time, we have studied the following four methods for the vertical field power supply for JT-60:

(1) Connection of the vertical field coil in parallel with the OH coil;
(2) Inductive energy storage method like as in the OH circuit;
(3) Full thyristor converter;
(4) Diode rectifier and thyristor converter.

Our design has been fixed on the method (4), which was selected taking account of the controllability, the operational flexibility and the cost. Power factor improvement at the AC line is also expected for this method.

The modified circuit is shown in Fig. IX.4.2.2-4 where the mechanical switch VP2 is previously selected off or on in the following two cases, the fast rise mode and the magnetic limiter mode, respectively.

* Fast rise mode

Switch VP2 is open, and the vertical field power supply must deliver voltages of up to 10 kV for the fast rise mode. The series connection of PSVF1 and PSVF2 can cover this voltage range of zero to 10 kV, where PSVF1 is composed of diode rectifiers which can deliver no-load voltage of 5 kV and PSVF2 is also 5 kV thyristor converters. Figure IX.4.2.2-5 shows the available voltage range of the vertical field power supply for both cases of VP_1 on and off. As the plasma current reaches to its flat-top, the PSVF1 voltage is switched off by VP1. The control of the vertical field at the flat-top is made by PSVF2 which can deliver voltages of ±5 kV.

* Magnetic limiter mode

For the magnetic limiter mode experiment, the switch VP_1 is open and VP_2 is closed. The magnetic limiter field leaks in the center of the vacuum vessel as error vertical field. This vertical field must be compensated at the beginning of plasma formation as low as possible. This can be made by controlling the vertical field coil current around -15 % of its full current. So whenever the magnetic limiter is operated, the vertical field power supply has to drive a bi-directional current in the coil. The plasma radius will be smaller than that of the fast rise at the early

phase of build-up due to the effect of the magnetic limiter. Since the expected time-rate of plasma rise is smaller, the maximum voltage of 5 kV will be sufficient for the positional control of the plasma during the build-up time. The parallel connection of PSVF2 and PSVR, both of ±5 kV thyristor converters, can cover the current from -15 % to 85 % by operating the circulating current control mode. It is also possible by controlling the cross current between two thyristor converters, to increase the current in the vertical field coil from negative to positive with no "dead time" at current zero.

(4) The quadrupole field, the horizontal field and the magnetic limiter coil power supplies

The quadrupole field power supply and the horizontal field power supply are designed as bi-directional thyristor converters so that the current in the coils can be varied in their direction during discharges. Figure IX.4.2.2-6 shows a schematic diagram of the quadrupole field, the horizontal field and the magnetic limiter coil power supplies. The magnetic limiter power supply controls the coil current to be constant during the operation. In some cases, however, the current in the magnetic limiter coil will be modulated within the range of ±15 % of its full current by slowly changing its voltage to prevent the concentration of heat deposition on the limiter plates. The schemes of operations are shown in Fig. IX.4.2.2-7.

(5) Power supply for discharge cleaning

The effectiveness of the discharge cleaning by weak plasma current has been demonstrated on Alcator, PLT, ISX-A and also JFT-2. This low-powered discharge cleaning is believed to have an effect to remove oxygen more effectively than high power discharges. In this discharge, a short pulse and a high repetition discharge rate are essential, but the plasma current is not so important.

In JT-60, the existance of welded vacuum vessel with low resistance will prevent the pulsive electric field from penetrating into the plasma region. The repetition rate and the magnitude of the voltage will be limited by the Joule input of the induced currents on the vessel. The OH circuit of JT-60 is capable of offering two methods for low-powered discharge cleaning either by means of a condenser discharge or by a short

pulsed operation of the thyristor converter PSF1.

* Condenser discharge

The OH circuit has two large condenser banks of 100 μF which are used in the commutation circuit of vacuum circuit breakers. By the change of circuitry of this condenser banks, discharges with the voltages of up to 25 kV across the OH coil and the repetition rate of up to 1/4 sec can be obtained. The plasma current will be lower than 100 kA.

* Short pulsed operation of PSFC

The pulsed operation of PSFC with 30 ms- 2000 V will produce a plasma open-circuit voltage of 30 V. The pulse shape of this voltage is optimized for low-powered discharge cleaning of high repetition rate between 1 to 20 per second. Of course, it will be limited by the endurable heat loss on the vacuum vessel. The plasma current will be about 30 kA.

4.2.3 Ground fault analysis in the JT-60 grounding system

Simulation calculations of transient potential distributions resulting from current surges rushing at a given position of ground mats and fault analyses assuming possible ground faults at the d.c. circuits, etc. were made to confirm the effectiveness of the JT-60 grounding system. Figure IX.4.2.3-1 shows a simulation model of ground fault analysis. A typical result of calculation is shown in Fig. IX.4.2.3-2 where simultaneous ground faults of the d.c. feeders of the toroidal field and the OH field power supplies are assumed.

4.3 Related studies

4.3.1 Volt-second consumption of the JT-60 OH circuit

The estimation of the necessary volt-second to build-up the plasma current to 2.7 MA and to maintain it for 5 seconds were made for various plasma conditions. Here the coupling of the OH coils with other coils was neglected. This is severe side estimation considering that the aid of the fluxes from the vertical field coil is neglected. The plasma resistance is assumed to be a time dependent function, but the variation of plasma inductance is neglected.

The following equation is valid for the plasma circuit,

$$M_{ohp}\,\dot{I}_{oh} = -(L_p\,\dot{I}_p + R_p\,I_p) \ .$$

An exact estimation of the flux swing can be obtained by integrating both sides of the above equation.

$$\Delta\Psi = |M_{ohp}\ \Delta I_{oh}| = L_p\ I_p + \int_0^{t_f} R_p\ I_p\ dt\ ,$$

where L_p is the internal and external inductance of the plasma at time $t = t_f$. The current I_p rises in the build-up phase as $I_p = I_{pmax}\ t/\tau$, where I_{pmax} is the peak value of the plasma current, while τ defines the build-up time. For the plasma resistance, we assume the following time dependence with parameter nx;

$$R_p = R_{pin}\ EXP(-\ln(R_{pin}/R_{pfin}) \times (t/\tau)^{nx}),$$

where R_{pin} is the plasma resistance at $t = 0$, R_{pfin} is that at the full current and nx is the index which defines the time evolution of the plasma resistance; in case of $nx = 1$, the plasma shows skin current distribution and $nx = 0.3$ shows the typical evolution which is obtained from the calculation of the zero dimensional plasma code developed at JAERI. The volt-sec consumption calculated for various plasma conditions is summarized in Table IX.4.3.1-1.

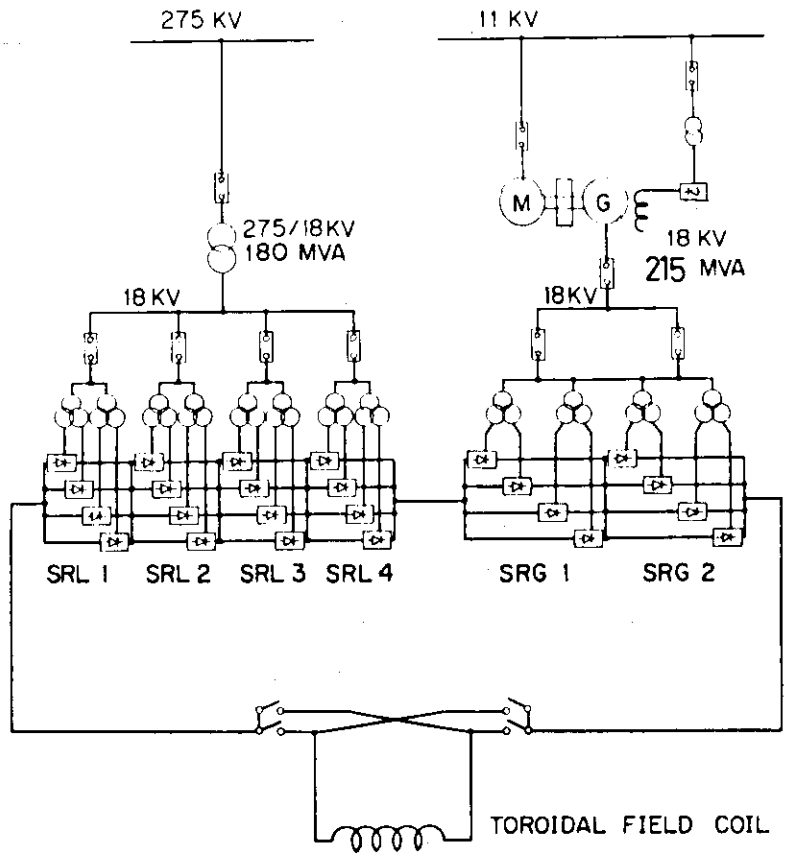

Fig. IX.4.2.1-1 Simplified circuit diagram of the JT-60 toroidal field power supply

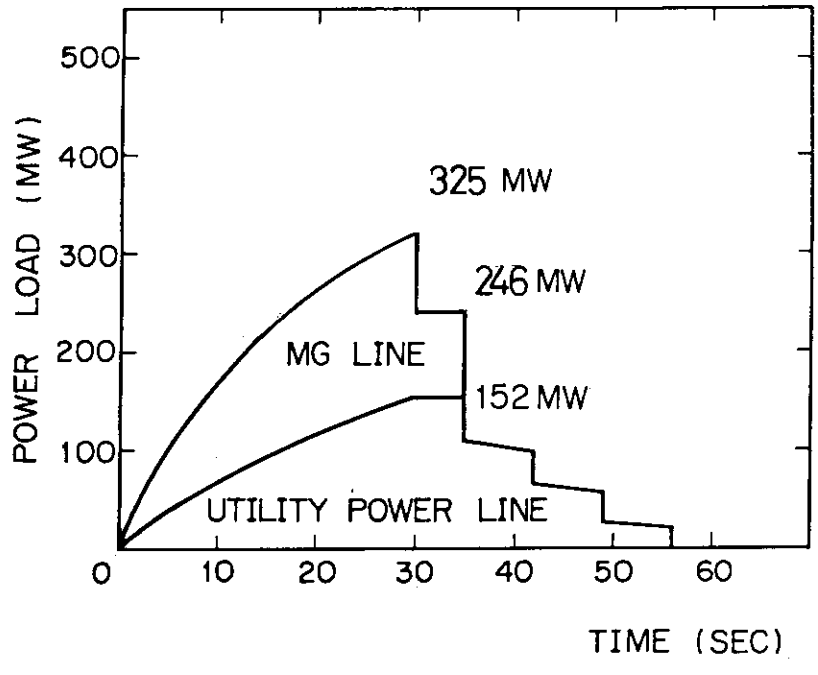

Fig. IX.4.2.1-2 Load pattern of the toroidal field power supply

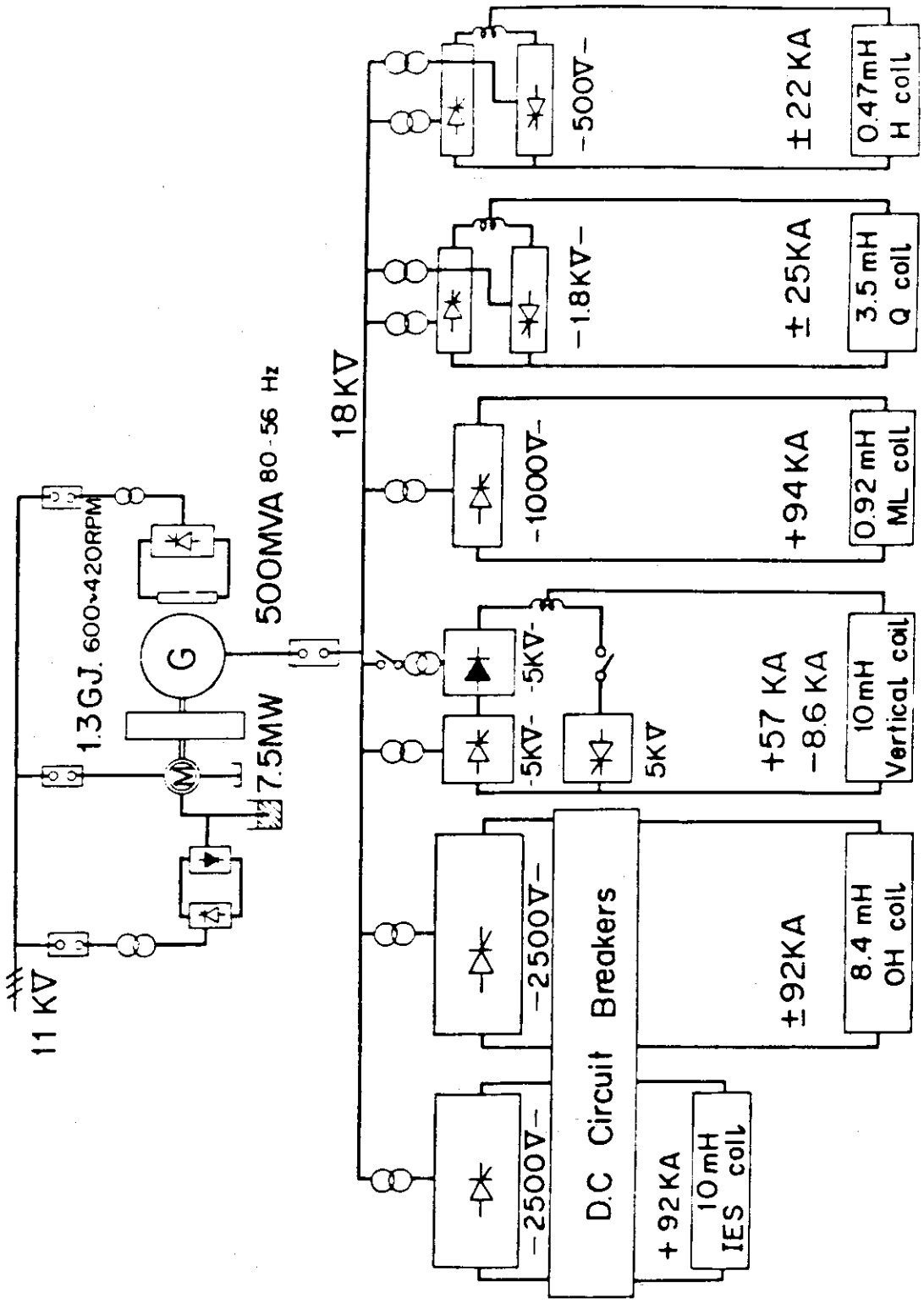

Fig. IX.4.2.2-1 Schematic diagram of the JT-60 poloidal field power supply system

Table IX.4.2.2-1 Specifications of main components

Generator	Vertical shaft salient pole type		1	set
	Pole		16	poles
	Capacity		500	MVA
	Voltage		18	kV
	Current		16	kA
	Frequency		79.2 - 56	Hz
	Xd,Xq		1.84, 1.18	p.u
	Xd"		0.24	p.u
	Power factor		more than 0.45	
	Flywheel effect		5500	ton-m^2
	Revolution		600 - 420	RPM
	Energy yield		1.3	GJ
Induction motor	Wound rotor three-phase induction motor		1	set
	Pole		10	poles
	Capacity		7.5	MW
	Voltage		11	kV
	Revolution		600	RPM
	Speed-up time (From 0 to 600 RPM)		20	Min.
	Control		Stationary scherbius system and water rheostat	
D.C Circuit Breaker	Vacuum circuit breaker		2	sets
	Voltage		25/15	kV
	Current		92	kA
	Commutation capacitor		1.0	mF
	di/dt,dv/dt		450A/μs, (mean) 120A/μs(at zero) 300V/μs	
I.E.S. Coil	Reactor of iron core with air gaps		3	sets
	Inductance		1.4/2.9/5.7	mH
	Connection		Series	
	Total inductance		8	mH
	Peak current		92	kA
	Resistance		7.5	mΩ
	R.M.S. current	92kA	2.9	sec
	Rated voltage		15	kV
Time constant controller	Resistance		0.032 - 1.0	Ω
	Variable		9n 16 steps	
	Maximum energy dissipation		78	MJ
	Rated energy dissipation		50	MJ
	Allowable temperature rise		70	°C
Thyristor convertor	OH coil and IES coil	PSF1	SCR 24 pulse	92kA-2500V
		PSF2	SCR 24 pulse	92kA-2500V
	Vertical field coil	PSVF1	SR 24 pulse	57.3kA-5kV
		PSVF2	SCR 24 pulse*	57.3kA-5kV
		PSVR	SCR 24 pulse*	8.6kA-5kV
	Quadru-pole field coil	PSQ	SCR 12 pulse*	±25kA-1800V
	Horizontal field coil	PSH	SCR 12 pulse*	±22kA-500V
	Magnetic limiter coil	PSM	SCR 12 pulse	94kA-1000V
			* bi-polar	

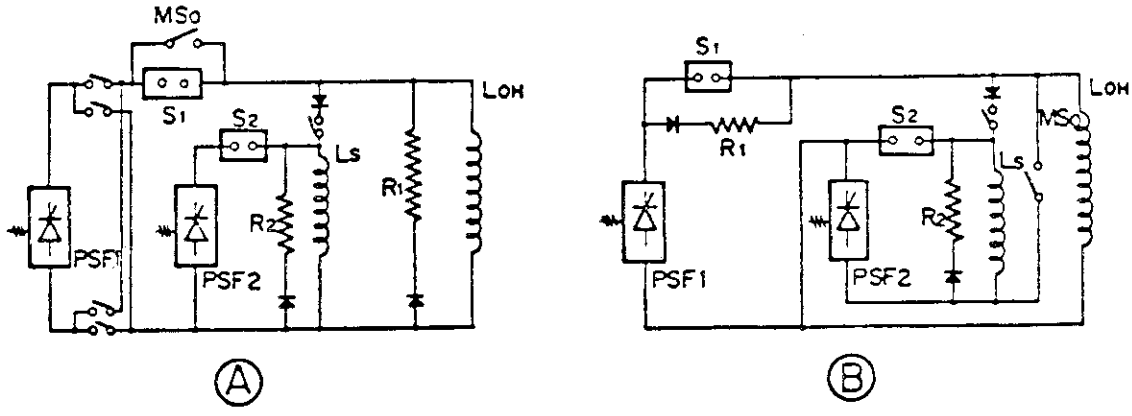

Fig. IX.4.2.2-2 Two arrangements of two stage build-up OH circuit

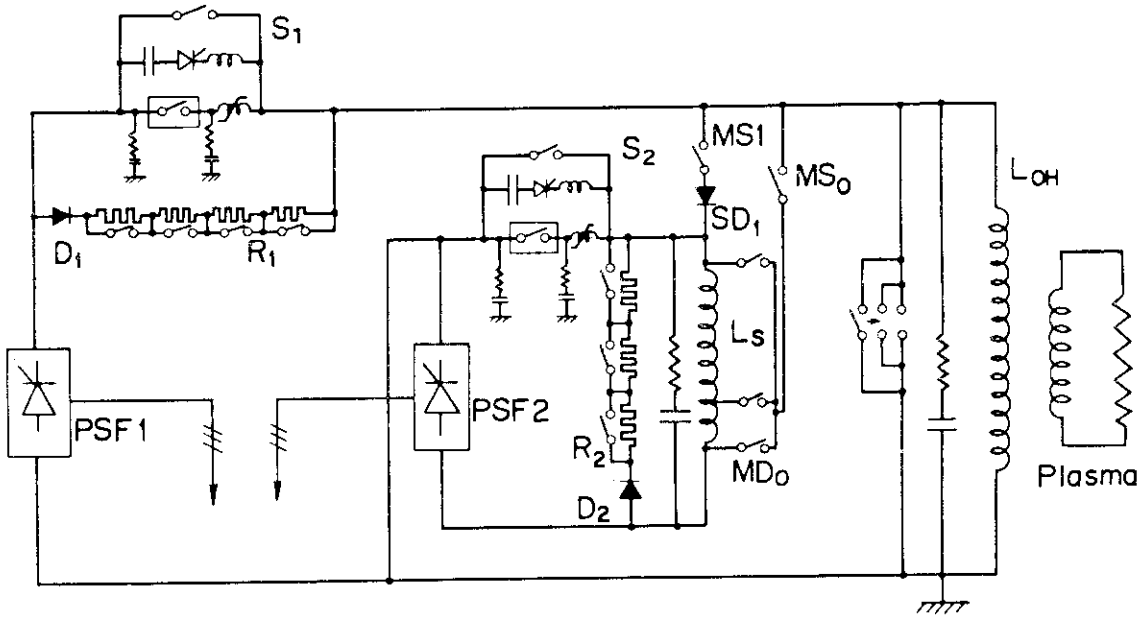

Fig. IX.4.2.2-3 JT-60 OH circuit

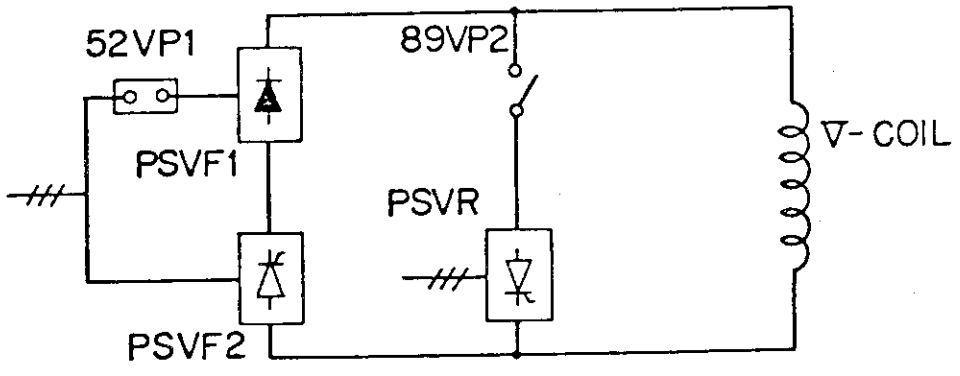

Fig. IX.4.2.2-4 Modified circuit for vertical power supply

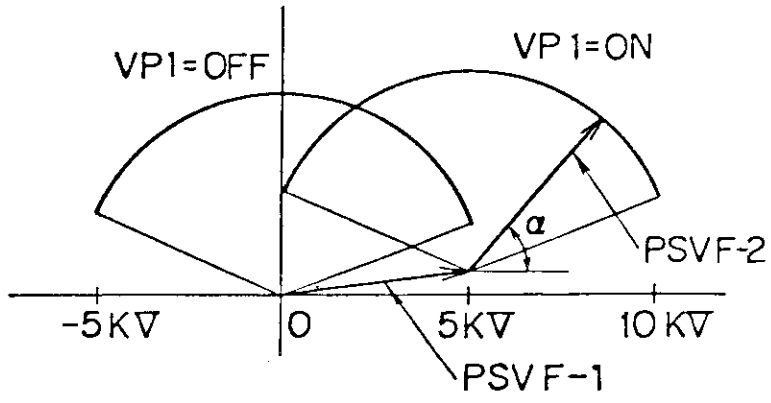

VOLTAGES DELIVERED FROM VERTICAL FIELD POWER SUPPLY WHERE 52VP1 IS CLOSED(RIGHT) OR OPEN(LEFT)

Fig. IX.4.2.2-5 Available voltage region of the vertical field power supply (α is the firing delay angle)

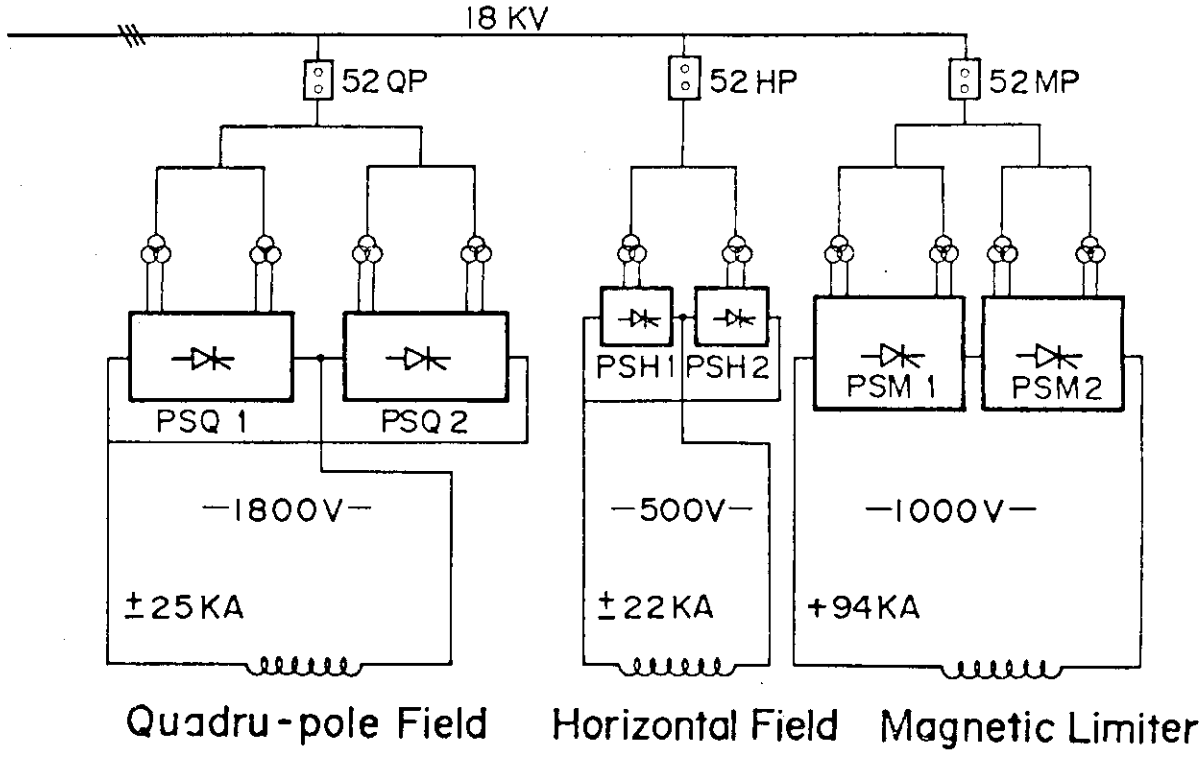

Fig. IX.4.2.2-6 Schematic diagrams of Q. field, H. field and M.L. coil power supply

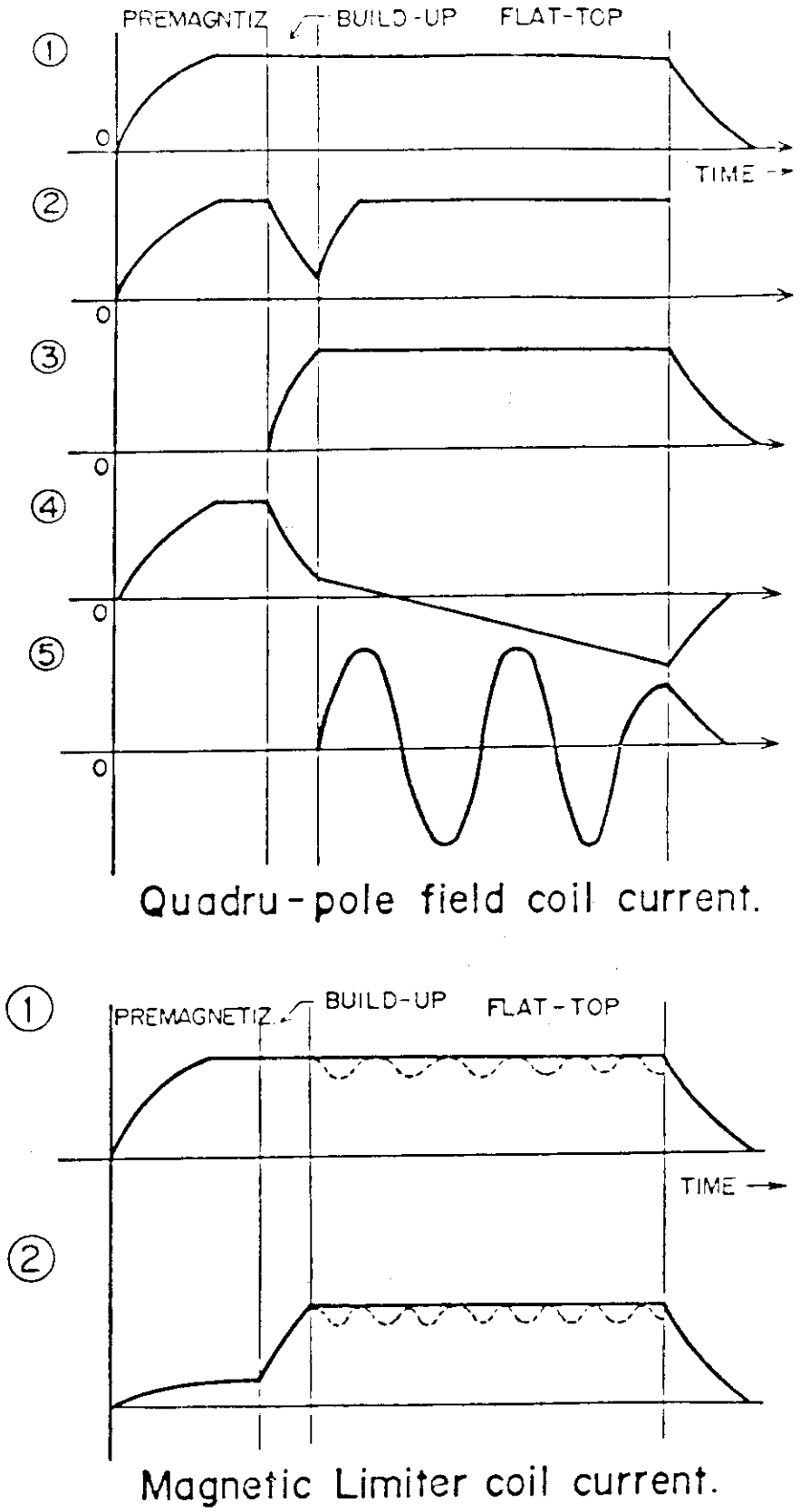

Fig. IX.4.2.2-7 Operation modes of the quadrupole field and magnetic limiter system power supplies

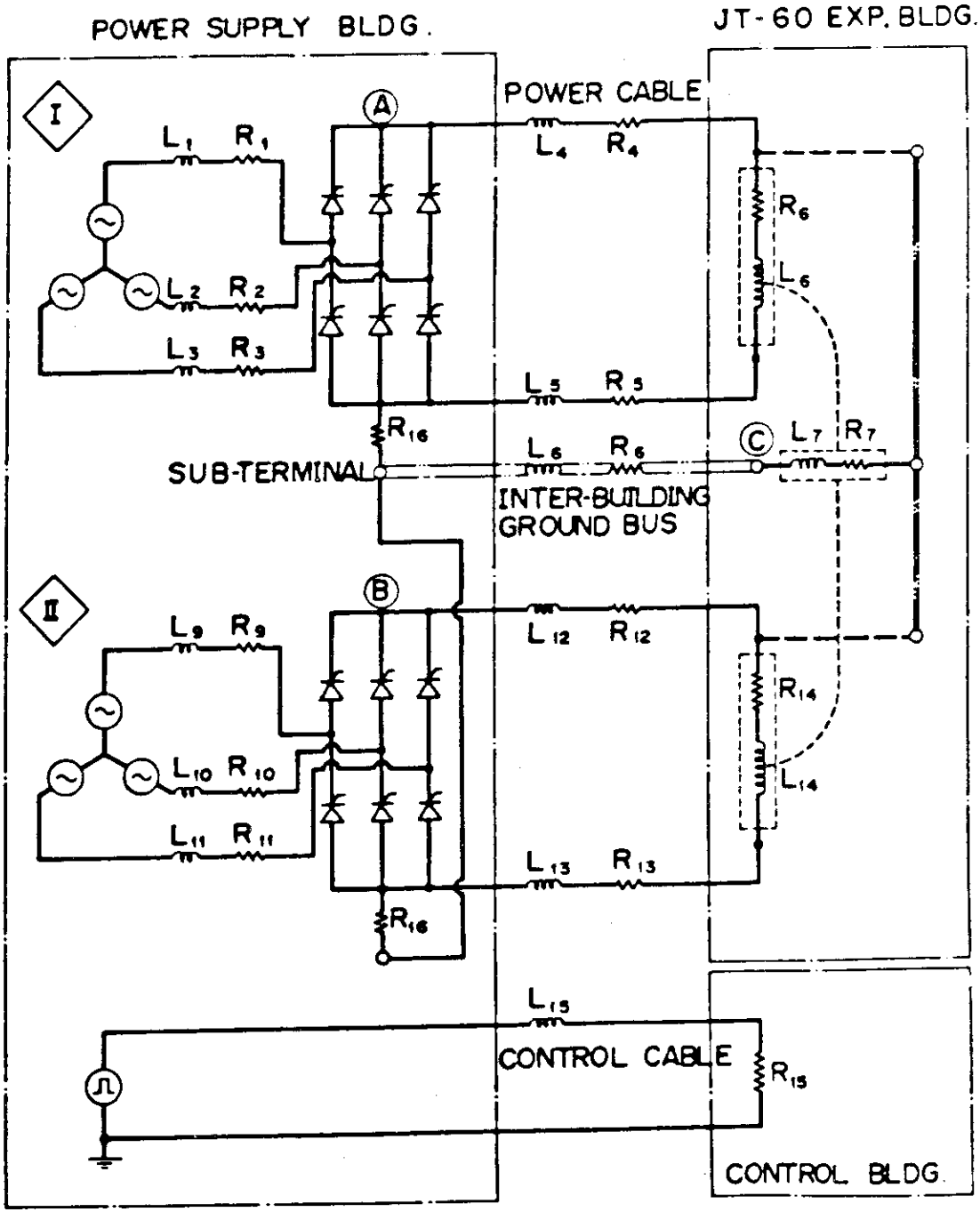

Fig. IX.4.2.3-1 Simulation model of ground fault analysis

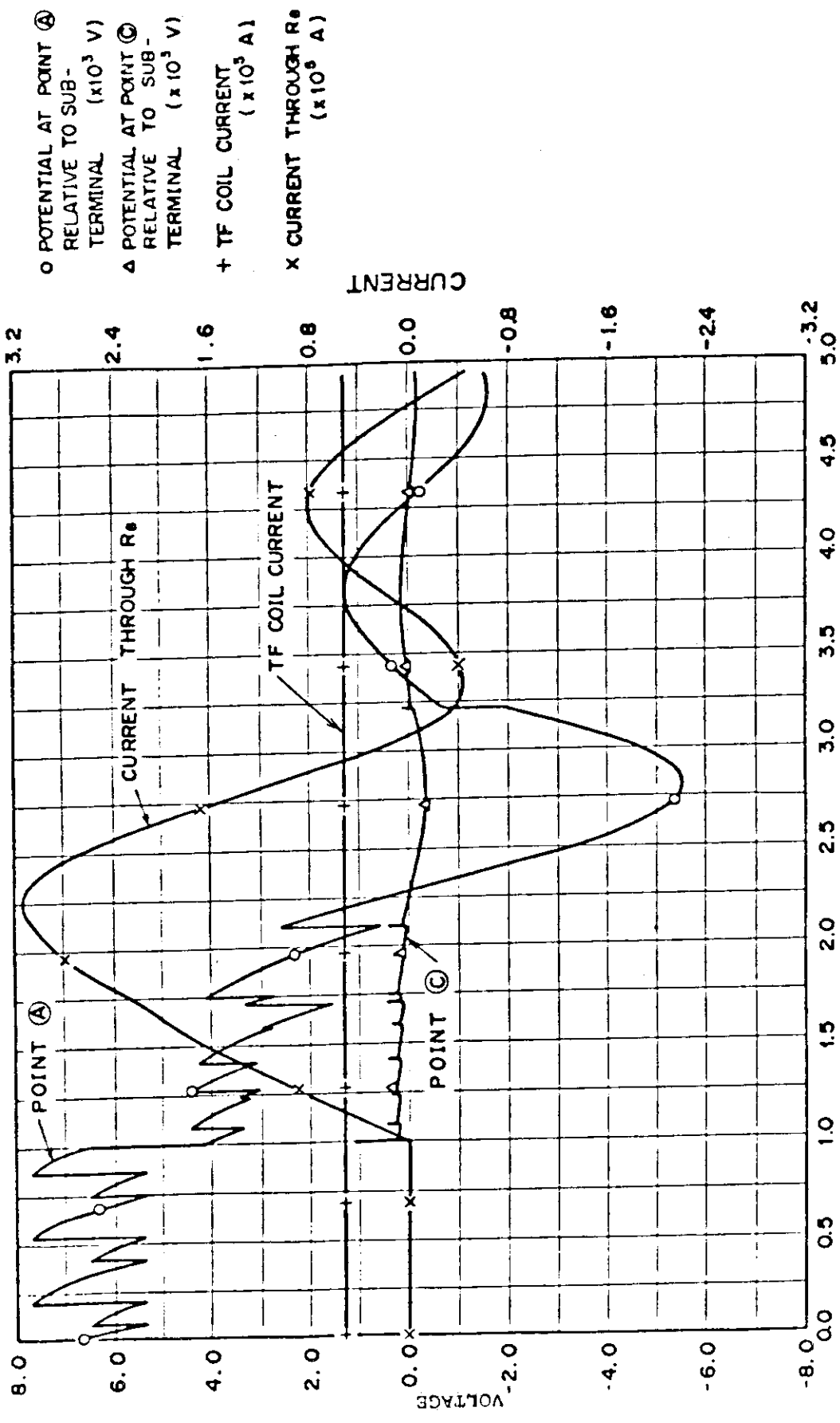

Fig. IX.4.2.3-2 Example of voltage and current waveforms in case of ground fault

Table IX.4.3.1-1 Volt-sec consumptions under various plasma characteristics

CASE	1	2	3	4	5	6	7	Units
Initial temperature	10	10	10	10	10	10	10	eV
Initial Z_{eff}	2.5	2.5	2.5	2.5	1.25	2.5	2.5	
Initial resistance	1.0	1.0	1.0	1.0	0.5	1.0	2.0	mΩ
Build-up time	0.1	0.1	0.2	0.1	0.1	0.1	0.1	sec
End of the build-up								
Plasma current	2.7	2.7	2.7	2.7	2.1	2.7	2.7	MA
Parameter Nx*	0.3	0.3	0.3	0.3	1.0	1.0	1.0	
Temperature	1.0	2.0	1.5	1.0	1.0	1.0	1.0	keV
Z_{eff}	5.0	1.0	5.0	5.0	1.0	5.0	5.0	
Correction of neoclass	o	o	o	x	o	o	o	
Resistance	2.8	0.2	2.0	1.0	0.5	2.8	2.8	μΩ
Consumption of $\int R_p I_p dt$ for the B.U.	1.1	0.17	1.72	0.5	1.7	7.8	12.5	Volt-sec
Flat-top								
Flat-top time	5.0	5.0	5.0	5. 0	5.0	0.3	0	sec
Temperature	2.0	2.0	4.0	2.0	2.0	2.0	-	keV
Z_{eff}	5.0	1.0	5.0	5.0	1.0	5.0	-	
Correction of neoclass.	x	x	o	x	o	o	-	
Resistance	0.33	0.06	0.32	0.33	0.18	1.0	-	μΩ
Consuption of $\int R_p I_p dt$ for the F.T	4.5	0.8	4.4	4.5	2.4	0.8	-	Volt-sec
Consumption of $L_p I_p$	15.39	15.39	15.39	15.39	12.0	15.39	-	Volt-sec
Total volt-sec**	20.99	16.39	21.5	20.39	16.1	24.0	-	Volt-sec

* Nx=1.0 Skin profile
Nx=0.3 Typical plasma evolution

** JT-60 OH coil can deliver 24 Volt-sec

5. Design of control and diagnostic system

5.1 Major activities of control and diagnostic systems

The study and evaluation of the detailed design of control system has been performed and completed. Carrying out the work, the function and the operating boundary of each control equipment such as ZENKEI, plasma control, machine operation control, power supply control, etc. were classified and evaluated. The expected purpose was achieved, considering to coordinate these functions and boundaries.

According to the obtained results, the referencing specification plan of ZENKEI control equipments was prepared for the ordering of the system to the industry which are expected in the next year.

And for the diagnostic systems, the design reexamination is continued for whole diagnostic system and the technical specifications have been studied through the year. Several developmental items were extracted in each diagnostic method. We have started to develop or to test some principal components of diagnostic apparatus under contract with some manufacturers.

5.2 Status of control and diagnostic systems

The control system of JT-60 has a hierarchical structure of central and sub-controllers as shown in Fig. IX.5.2-1, the sub-controllers control their own objective devices and equipments; i.e., secondary cooling system, poloidal coil power supply, etc., while the central controller controls the sub-controllers. The sub-controllers will be purchased from the same vendors that supply the objective devices and equipments themselves. The hierarchical structure enables to operate the devices and equipments independently from others during commissioning, maintenance and fault finding.

In general, it is necessary from the viewpoint of maintenance and software development to reduce the number of computer types as small as possible. Only two types of computers are to be used in our control system. The first type is a mini-computer in the central controller, and the second is a 16-bit micro-computer used in the sub-controllers. The latter is housed in a CAMAC module as an auxiliary controller. However, the plasma data processing system may probably have the third type, either a general-purpose computer or a midi-computer.

The central controller itself has a hierarchy of three levels as

shown in Fig. IX.5.2-1. The highest level functions throughout the operation of JT-60, while the lower levels function mainly during discharges.

Devices and equipments used in discharges can be divided into two groups. Those in the first group are applied only open loop program control; they are toroidal magnetic field power supply, preionization system, movable limiter, magnetic limiter and auxiliary heating systems. Those in the second group are feedback-controllable; they are gas feed system, and power supplies of air-core transformer, vertical magnetic field, horizontal magnetic field and quadrupole magnetic fields. The first group is controlled mainly by the program control computer in the second level, while the second group is controlled also by the feedback control computer in the third level.

Figure IX.5.2-1 shows block diagram of control of the feedback controllable devices. Note that we can superpose the program control on the feedback control of these devices. Figure IX.5.2-3 shows the construction to realize the block diagram. Thyristors to feed current to the poloidal field coils are fired directly by the micro-computers housed in auxiliary controllers in the corresponding CAMAC crates.

Some diagnostic devices are dedicated to the control system; they include magnetic probes for plasma position and shape detection, Rogowski coil, one-turn voltage coil, interferometry, etc. Any other devices are also possibly used for control purpose. Control of these devices is time shared; during discharges by the control computers and during intervals between discharges by the data processing computers.

Safety and protection of JT-60 are assured by hard-wired system independent of the computers. However, effort is also made to forecast and prevent the abnormal events by the computers; in other words, the control system is designed so that the hard-wired system is the last gate for abnormal events and most of them are prevented before they can actually occur. Concretely, on-line simulation of operations is carried out before each discharge to check and validate its conditions. Once abnormal events have actually occurred, the computer analyses their causes and indicates them to operators together with advisory actions, using fault tree analysis technique. The control system is equipped with the timing system which transmits a sequence of timing pulses for the precise timing of events for discharges.

JT-60 has three buildings; they are experimental building, control building and power supply building, respectively. Most of CAMAC crates are scattered in the experimental and power supply buildings. The feedback control computer is deposited in the power supply building because its major objects are power supplies. Only the central controller and control consoles exist in the control building. This deposition of controllers enables to carry out fast controls locally at their necessitated sites so that the data transmission between the control building and the other buildings are slow enough to introduce signal multiplexing and bit serial techniques; whereby we can use fiber-optic transmission economically.

The fiber-optic transmission has two advantages: First, it is possible to isolate vulnerable integrated electronic circuit from damaging inputs. Second, it cannot be influenced by the time variation of electromagnetic field, and it cannot radiate noise signals itself, either. In the CAMAC configuration, the U-port adapters will be used which have conversion ability between optical and electrical signals.

5.3 Present design of plasma control

5.3.1 Modeling[1)]

The first necessary step in the control strategy is to adopt a model. The behavior of a plasma is described by a set of nonlinear, distributed-parametered and time-dependent differential equations. The explicit control method is given by the modern control theory for linear system. The practical viewpoint of control further prefers a lumped-parametered and time-invariant model.

First we introduce a method to describe the plasma-coil system by a set of circuit equations in order to bring in the lumped-parameter approximation[2)]. The circuit equation is a straight description of a tokamak, because it is nothing but a transformer with the secondary circuit of a plasma. Some tokamak components such as a vacuum vessel, which carry eddy currents and have the shell effect, make distributed parameter circuits. The toroidal current I_n on such a tokamak component n is approximated by Fourier series: $I_n = \Sigma_k I_{nk} \cos\omega k$, where ω is the poloidal angle. In the following, I_{nk}, is labelled by a single subscript and is deemed to be independent one another.

We now express the currents in the plasma channel and the tokamak components by the following circuit equations: for the plasma current

$$\sum_m \frac{d}{dt} M_{pm} I_p + \eta_p I_p = 0, \tag{1}$$

and for the current on the component m

$$\sum_{n \neq p} M_{mn} \frac{dI_n}{dt} + \eta_m I_m + \frac{d}{dt}(M_{mp} I_p) = V_m \ , \tag{2}$$

where η denotes resistance and V_m is the applied voltage on the coil. In the case that the component is a passive element such as a vacuum vessel, $V_m = 0$. Inductances in the above equations are derived from the magnetic flux functions by the equation $M_{mn} I_m I_n = \int_m \psi_n i_m d\ell_m$. Generally a mutual inductance between a component and a plasma is a function of β_p, ℓ_i, r_p (minor radius) and R_p (major radius). Especially, we have $M_{pp} = L_p = \mu_0 R_p \{\ell n(8R_p/r_p) + \ell_i/2 - 2\}$.

Two more basic equations are those for energy balance and particle balance; they are conceptually given by

$$\frac{dN}{dt} = -\frac{N}{\tau_p} + S_f, \tag{3}$$

$$\frac{d(kNT)}{dt} = -\frac{kNT}{\tau_E} + P_{in} \ , \tag{4}$$

where S_f is particle input due to gas feed[7]. We linearize eqs. (1)-(4) in the time range where time variations are small enough to approximate $d(xy)/dt = x_0 dy/dt + y_0 dx/dt$. We reduce some variables such as R_p, β_p, η_p, P_{in}, Λ, etc. using the well known relations: $\beta_p = 8kNT/(\mu_0 R_p I_p^2)$, $\eta_p \propto T^{-3/2}$, $P_{in} = \eta_p I_p^2$, $\Lambda = \beta_p + \ell_i/2 - 1$, $\mu_0 I_p^2 \{\ell n(8R_p/r_p) + \Lambda - 1/2\} + 4\pi R_p I_p B_v = 0$ (equation of motion), etc.

We thus have the following equation for state vector $x' = (I_1 \ldots\ldots I_m\ N\ T)$ and control input vector $u' = (V_1 \ldots\ldots V_n\ S_f)$: $D\dot{x} = Ex + Fu$. If D is regular, we can effect D^{-1} on its both sides to obtain the so-called state equation of linear dynamical system:

$$\dot{x} = Ax + Bu. \tag{5}$$

At the flat-top stage of the plasma current we can approximate A and B matrices time invariant. At the current rising stage, this approximation does not hold. We can, however, divide the current rising stage into several intervals and deem the matrices time invariant in each interval.

5.3.2 Program control

The ultimate purpose of the program control must be to specify all control inputs when plasma parameters are given. We, however, have little experience to challenge this purpose. Instead, we consider the following problem: when some control inputs are given by operators, how to adjust the rest control inputs by computers. We call the devices whose inputs are specified by operators "prior devices" and the others "posterior devices". The posterior devices are thyristors of air-core transformer power supply, other poloidal power supplies and gas feed system. The prior devices are vacuum circuit breakers of air-core transformer power supply and other open-loop controllable devices. The control system is made in such a way that the control inputs of the posterior devices can be programmed more flexibly than those of the prior devices.

We rewrite eq. (5) into the form

$$\dot{x} = Ax + B_1u_1 + B_2u_2. \tag{6}$$

The term B_2u_2 expresses the prior setting. We can deem this term as known disturbances against u_1 and obtain the trajectory of u_1 and x under the restriction of an appropriate co-function:

$$J = \langle e(T),\ Fe(t)\rangle + \int_t^T [\langle e,\ Qe\rangle + \langle u_1,\ Ru_1\rangle]dt\ , \tag{7}$$

where $e = x_{id} - x$, x_{id} is ideal state vector and matrices, F, $Q \geq 0$ and $R > 0$ are specified according to the control purpose. The necessary calculations for the program control are carried out during the interval between two seccessive discharges.

5.3.3 Feedback control

In general, we cannot expect the application of the programmed input $u_1 = u_{10}$ leads to the computed results $x = x_0$ because of approximations introduced, modeling errors, errors in the assumptions of initial conditions, etc. It then follows that errors themselves may contribute to deviate the true state x from the nominal one x_0 so that small initial deviation may get larger and larger as time goes on. The feecback control thus becomes necessary; i.e. the control correction $\delta u = u - u_0$ should be calculated based on the state perturbation vector $\delta x = x - x_0$.

We bear in mind two steps for the feedback control. In the first step,

single loops are controlled separately; plasma current, horizontal plasma position, vertical plasma position, ellipticity of plasma cross section and plasma density are controlled by air-core transformer coil power supply, vertical magnetic field coil power supply, horizontal magnetic field power supply, quadrupole magnetic field coil power supply and gas feed system, respectively. Variables x, y, u, etc. in Fig. IX.5.2-2 are scalar values. The feedback control computer in Fig. IX.5.2-3 is used only to calculate plasma positions and ellipticity from magnetic probe signals. Connections for this first step are shown by dashed lines in Fig. IX.5.2-3. This first step bases on the classical PID control theory, which has been proved to be effective in several tokamaks.

Difficulty in such a multiple-single-loop feedback system may arise from interactive effects; for example, the action of the feedback loop for the plasma current affects the action of the loop for the horizontal plasma position. This interaction is normally such that the stability margins of system operation are reduced, and it is desired to design the multiple-loop system in such a way to avoid the interactive effects which are prejudicial to system stability.

The second step will be tried to overcome these difficulties. Multivariable control algorithm based on the modern control theory is implemented in the feedback control computer. Dashed lines for the first step are replaced by the dotted lines is Fig. IX.5.2-3, so that five clusters of CAMAC crates work under the order of the feedback control computer. Variables in Fig. IX.5.2-2 become vector values. Plasma parameters such a temperature, current distributor, etc. are introduced in the cost function of the feedback control in this second step.

References

1) Ogata, A.,and Ninomiya, H.: Jpn. J. Appl. Phys. 18 (1979) 825.
2) Suzuki, Y., Ninomiya, H., Ogata, A., Aikawa, H., and Kameari, A.: J. Appl. Phys. 16 (1977) 2237.
3) Ogata, A., and Tazima, T.: Jpn. J. Appl. Phys. 17 (1978) 753.

5.4 Present design of diagnostic systems

5.4.1 Interferometric and scattering measurements

Interferometric diagnostic system is composed of millimeter and submillimeter wave interferometers in order to measure the line averaged electron density. The former is designed for the measurement of peripheral and magnetic limiter region of the plasma and the latter for the central region. This interferometric system is not responsible for the sufficient spatial resolution, because of the limitation of the port access, but the time resolution can be obtained upto some μ-sec.

For the millimeter wave interferometer, the phase modulation characteristic by a varactor diode of the intermediate frequency stage is preliminary obtained (Fig. IX.5.4.1-1), and the minimum detectable fringe is to be less than $\pi/10$ rad.

Because of the difficulty to ensure U_1 port access, it is necessary to insert waveguides and reflector horns from U_{23} port to the position of U_1 port major radius.

Submillimeter interferometer for the measurement of the central electron density is designed according to the following view points,

(1) bending effect of probing beam propagating in the plasma
(2) subtracting the contribution of mechanical vibration of vacuum vessel from the density signal
(3) optical mixing system for the interferometer which has the vibration free characteristic to fit the wave fronts of the reference and the probe wave
(4) stability of the output frequency and power of submillimeter laser oscillator
(5) vacuum sealing window and laser beam guiding optics
(6) detector characteristics and data processing considering the feedback to the plasma control, etc..

Specifications to Thomson scattering apparatus had been studied in details. Preliminarily developmental items are as follows.

[A] The Intensified Charge Coupled Device (ICCD), which is one of the two dimensional photodetectors was tested in following fundamental specifications.

(1) noise level

In cooling mode, the minimum detectable charge could be obtained at 2000 electrons.

(2) coupling optics

The fiber coupling between Image Intensifier (II) and CCD was tested. The coupling efficiency and MTF value could not be obtained expected values. The fiber coupling should be reformed to other coupling configuration.

(3) gating

The gating operation could be realized under the switching time lower than 50 μ-sec and the gating ratio greater than 34 dB.

[B] Some optical characteristics were tested for low-loss glass fiber, middle-loss glass fiber and plastic fiber. The testing results are as follows.

(1) usable length restricted by fiber transparency

low-loss glass fiber	more than 100 m	(400 - 1200 nm)
middle-loss glass fiber	several meters	(500 - 1200 nm)
plastic fiber	less than 1 m	(500 - 900 nm)

(2) N A value

Testing values were in good agreement with theoretical values.

(3) pulse distortion

Testing results of 20 nsec light pulse were shown that the distortion effect was negligibly small. It is concluded that the low-loss glass fiber is the best optical transmission line of JT-60 scattering apparatus.

5.4.2 Spectroscopic measurement

Spectroscopic measuring systems are planned to obtain informations of neutral atoms and low-Z and high-Z impurities the JT-60 plasma. The spectroscopic systems are classified as follows:

(1) The visual spectroscopic systems used to diagnose the plasma of Te < 100 eV, i.e., peripheral and the magnetic limiter region.

(2) The vacuum ultra-violet (VUV) spectroscopic systems used to diagnose the plasma of 100 eV < Te < 1 keV.

(3) The extreme ultra-violet (XUV) spectroscopic systems used to diagnose the plasma of Te > 1 keV in the central hot-core region.

(4) The far infrared measurement systems for cyclotron radiation detection to diagnose Te profile.

In the JT-60 machine, which is designed to establish the control of the reactor grade hydrogen plasma with the long duration (10 sec) NBI and RF heating systems, it is required that whole diagnostic systems should serve as sensors for the plasma control. It means spatial distribution of the intensities of the spectral lines in the visible, VUV, and XUV range should be measured during a single discharge. Development of two-dimensional detector and holographic gratings with flat focal plane are needed to satisfy such requirements.

The fabrication and the feasibility test for such elements of the optical systems will be completed in 1979 FY.

5.4.3 X-ray and particle measurements

Detailed design work on some important problems which were shown in the previous conceptual design has been done in this fiscal year.

(A) X-ray and neutron measurements

Some electronic circuits have been investigated for the pulse measurements at high counting rates (∿100 MHz repetition).

Two types of preamplifiers, a charge sensitive type and a current type, were investigated. The former is not suitable for the high counting rate pulse measurement because of its long fall time (∿5 μs), the latter is suitable because of its good response for the short collection time of charges in the detector.

A main amplifier, LeCroy Model 133B, was tested on the following items, such as double pulse resolution and noise.

A discriminator, LeCroy Model 623, was tested on the following items; such as output pulse wave form, pair-pulse resolution and transient time between input pulse and output pulse.

It was found that the total system composed of the above devices can be used for the pulse measurement at a mean counting rate up to 10^7 cps.

(B) High energy neutral particle detectors

Silicon surface-barrier detectors (SSD) were investigated for detecting high energy neutral particles. One of the various types of trial SSD's (see Fig. IX.5.4.3-1) has a good performance. Hydrogen atoms H_1^0 with energies of 10 ∿ 13 keV can be measured with this types of SSD's cooled to -130 °C by liquid N_2. The energy loss due to the Au coating layer (20 μg/cm^2) and the dead layer can be considered to be about 3.5 keV. This energy loss and the noise determine the lowest detectable energy.

The energy spectrum for 14 keV H_1^0 is shown in Fig. IX.5.4.3-2. The energy resolution is about 4.0 keV FWHM in the energy region of 12 ∿ 30 keV.

As X-rays are also emitted from plasma, it is important to separate neutral signals from X-ray ones. The separation of signals by use of the pulse shape difference is not suitable for this purpose because of the high noise level. It is necessary to examine the other methods for the separation.

5.4.4 Plasma monitors

Up to the present time, various types of electromagnetic probes such as pick-up coils, one turn loops, Rogowski coils, diamagnetic loops, and floating electrodes, are planned to be equipped in and around the vacuum vessel of JT-60. We consider three usages for the pick-up coils; one for the feedback sensors of plasma position and shape, another for the measurement of MHD oscillations, and the other for the measurement of eddy current induced in the vacuum vessel. Pick-up coils for the feedback control are composed of two types of sensors; one is for measuring poloidal flux tangential to the plasma cross section, the other for measuring poloidal flux normal to the plasma cross section. They are located around a plasma with every 60° on the poloidal circle. Pick-up coils for MHD oscillations are located around a plasma with every 15° on the poloidal circle in the several toroidal sections. Pick-up coils for eddy current are located along the edge of the thick part of the vacuum vessel both in and out of the vacuum vessel, based on the eddy current mode analysis. Other ordinary probes (one turn loops and Rogowski coils) are also equipped in and out of the vacuum vessel. Floating electrodes are prepared for the measurement of charged particle flux coming limiters, liners and magnetic limiter plates, which are designed to be electrically floated from neighbouring other limiters, liners, or magnetic limiter plates. Thermocouples are used for the measurement of the temperature of limiters, liners and magnetic limiter plates. All the probes located in the vacuum vessel are designed to bear up against the backing temperature of the vacuum vessel of 500 °C. Other monitoring apparatus such as visible TV, and X-ray TV etc. are also planned to be equipped with JT-60.

5.4.5 Data processing system

The system will have a two level structure of large- or mini-computers will be housed in the auxiliary controller modules of CAMAC crates. They control the diagnostic devices and gather data from them during a shot. Only the micro-computers have active functions during a shot, while the upper level computers function during the interval between two successive shots.

The data amount to be gathered is estimated and summarized in Table IX.5.4.5-1. The sampling period is uniformly 1/100 of the confinement time, which is supposed to be 0.1 sec at the minimum. Apparently, this sampling period is too long to study fine phenomena, for example, to study the structure of oscillations. One problem is that the shorter sampling period requires the more memory capacity.

Our solution is to equip transient recorder module with fine time resolution which is triggered only when the fine phenomena really occur to save the memory capacity. The transient recorder has to equip the post trigger capability. In order to synchronize various diagnostics, the trigger pulse has to be fed from a common source. It is necessary to separate the input channels into fast and slow ones also from the viewpoint of filtering, because the time constant of the input filter has to depend on the sampling period to avoid the alias effect. It is assumed that one transient recorder with capacity of 5 kW is dedicated to each post-triggerable channels at the data amount estimation. Table 5.4.5-1. Data amount (in kW unit) to be gathered in the data processing system. Dependence on the experiment is also given, i.e.,

A: in any experiments,
B: depends scramble for ports,
C: auxiliary diagnostics,
D: D_2 experiments,
H: further heating experiments,
M: magnetic limiter experiments,
X: usage is not clear yet.

5.5 Related studies

5.5.1 Eddy current analysis

The error field due to eddy currents induced in the toroidal field

coil modifies the original magnetic field distribution and affects the plasma equilibrium especially in the current build-up phase. This modification of original magnetic distribution also affects the estimation of the capacity of power supply.

The estimation of eddy currents induced in the structures of JT-60 is usually made by three numerical methods: i.e., the finite element circuit method[1], the three dimensional finite element method[2] and the method using the tokamak circuit conception[3]. However, in the case of the toroidal field coil, the estimation of the eddy current effect has been made by 1/25 model experiment in JT-60 because the evaluation of this effect by the numerical method is very difficult. The model has two components: the toroidal field coil and the poloidal field coils. One of the experimental results is as follows, the vertical field in the plasma region is decreased about 0.06 Wb/m from the original value at the end of the current build-up phase.

References

1) Kameari, A., and Suzuki, Y.: Proc. 7th Symp. Engng. Problems Fusion Research (Oak Ridge, 1977) vol.2, 1386

2) Ninomiya, H., Ogata, A., Tanabe, Y., Sawada, Y., Yamamoto, K., and Yamaguichi, M.: Proc. 10th Symp. Fusion Technology

3) Ninomiya, H., and Suzuki, Y.: JAERI-M 7710 (1978)

Table IX.5.4.5-1

	NORMAL COLLECTION								POST TRIGGER COLLECTION		
	A	B	C	D	H	M	DH	X	A	H	DH
1. Microwave and FTR	1350		15						80		
2. Thomson scattering	42		.2								
3. Spectroscopy	3105				600				3105		
4. X-ray measurement	330	60							330		
5. Neutron measurement	25						10				
6. Neutral particle measurement	75			60	150		150			150	150
7. Boundary plasma measurement	70					26		80			
8. Electromagnetic measurement	285								285		
Total	5285	60	15.2	60	750	26	160	80	3800	150	150

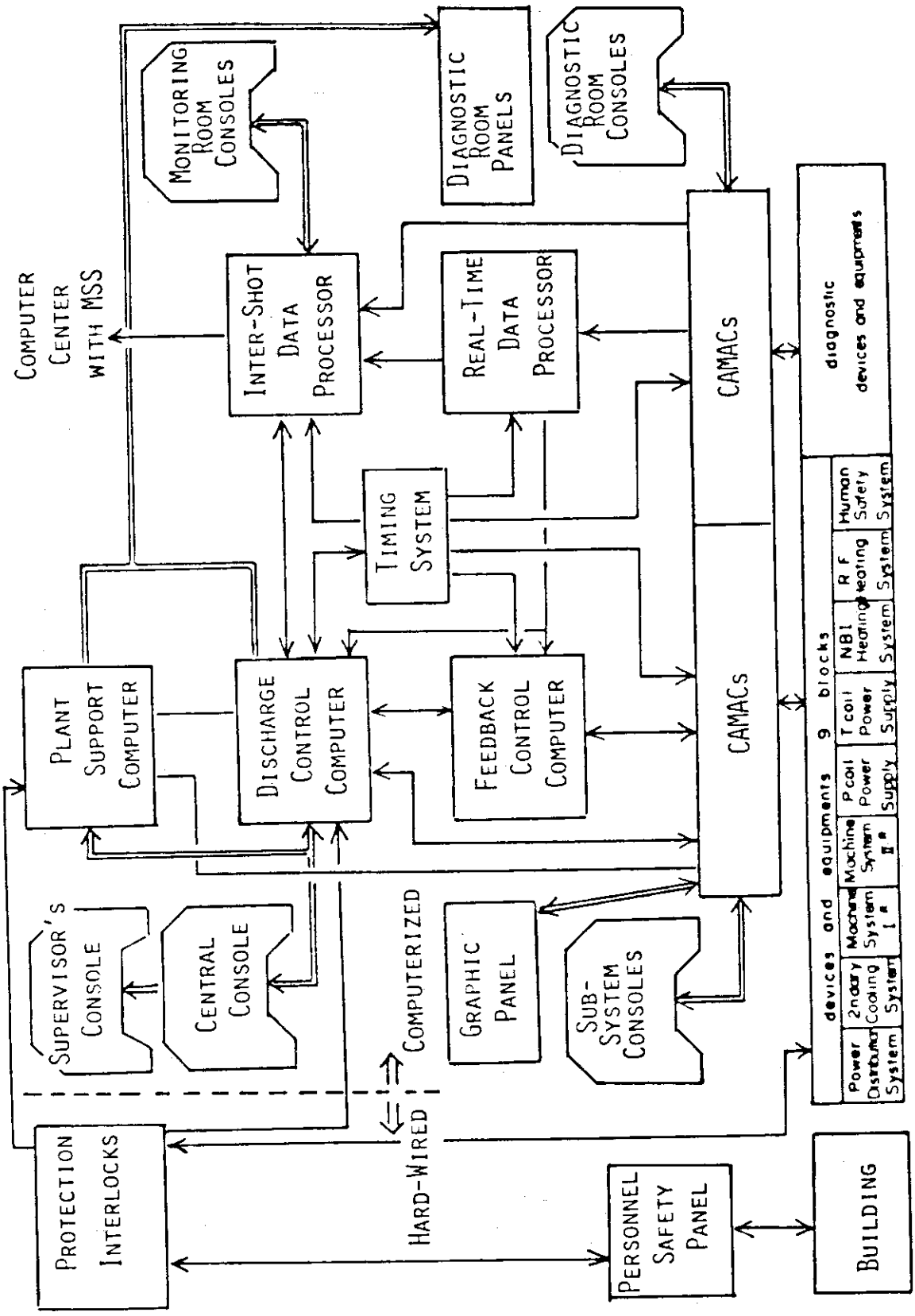

Fig. IX.5.2-1 Structure of JT-60 control system.

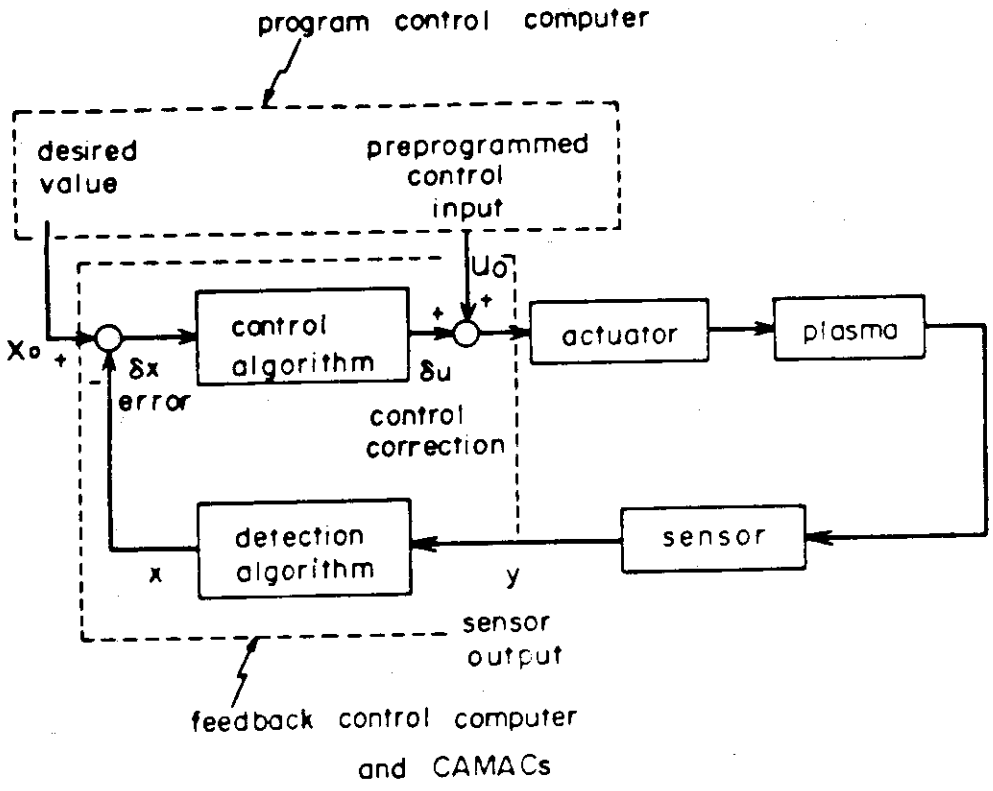

Fig. IX.5.2-2 Block diagram of plasma control

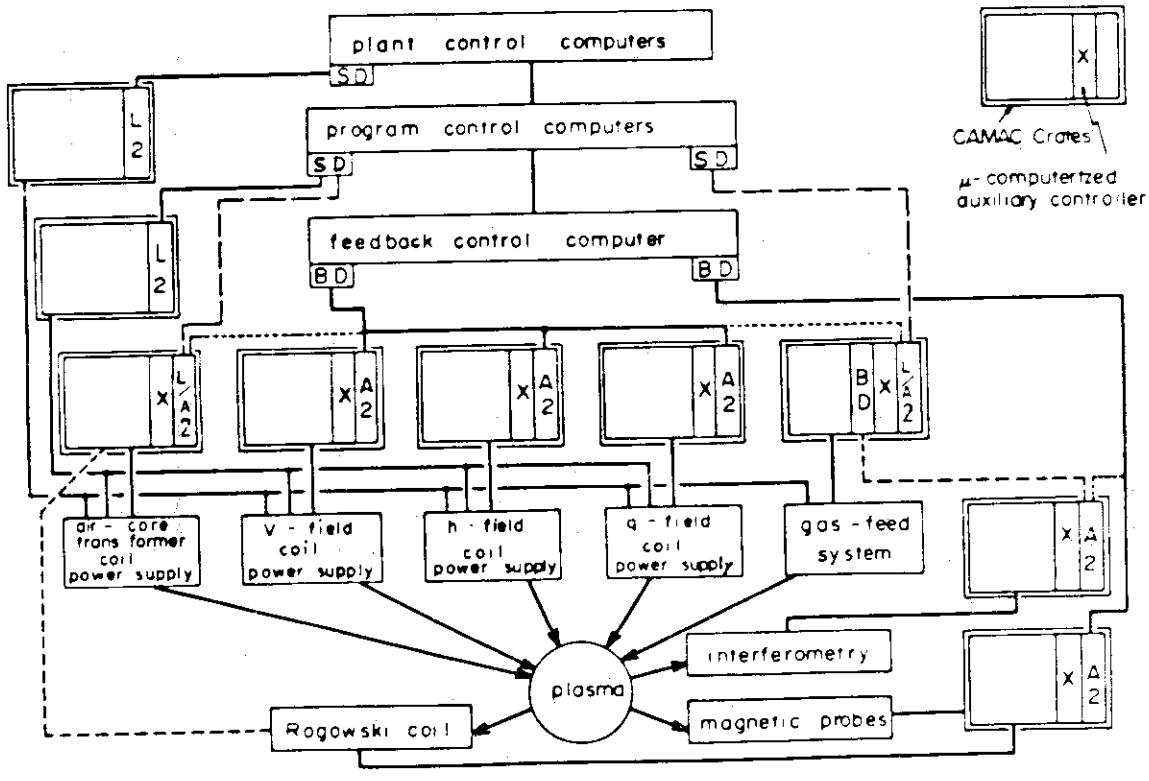

Fig. IX.5.2-3 System construction for plasma control

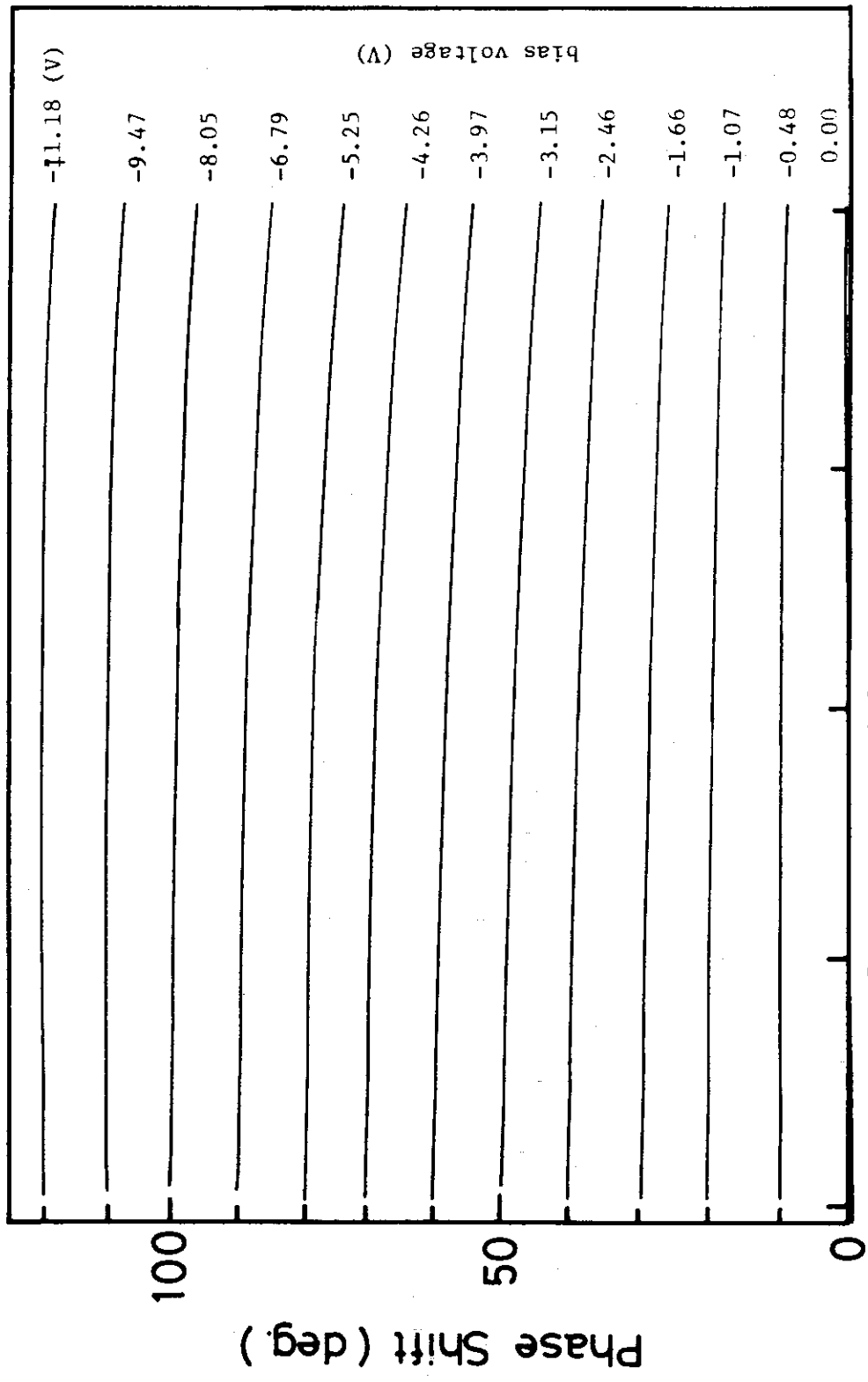

Fig. IX.5.4.1-1 Phase modulation characteristics of varactor diode

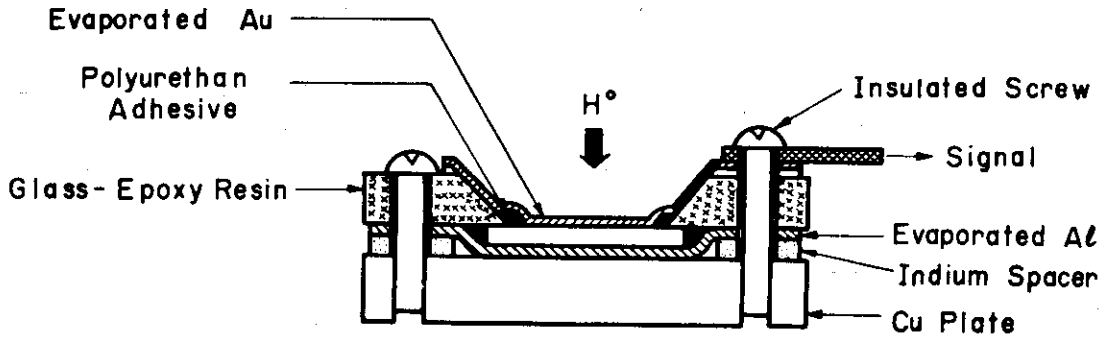

Fig. IX.5.4.3-1 Construction of a trial SSD

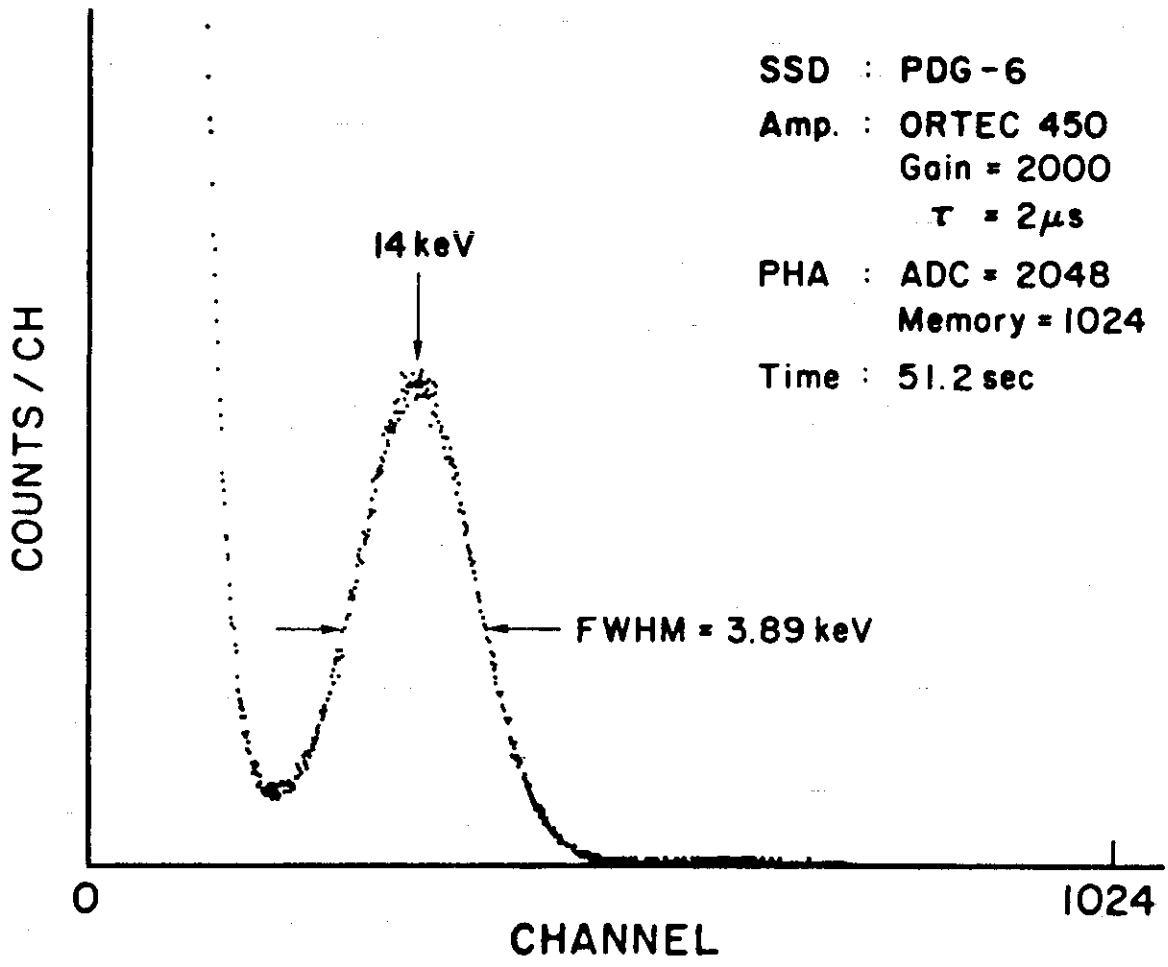

Fig. IX.5.4.3-2 Spectrum of 14 keV H_1^0 beam

6. Design of auxiliary systems

6.1 Review of auxiliary system design

In the fiscal year 1975-8 the design of vacuum pumping system, secondary cooling system, and power distribution system were made by industry as part of the detailed design of JT-60. The design studies of gas supply and preionization systems were also made. During the past year the design was reexamined and some modifications were incorporated into the design.

6.1.1 Vacuum pumping system

The vacuum pumping system of JT-60 is to provide ultrahigh vacuum in the vacuum vessel and help produce clean surfaces at the first wall (limiters and liners). It also should have a pumping capability large enough to evaluate the vacuum vessel in an interval between discharges.

The system consists of the following major subsystems:

Pump subsystem (main pumps, roughing pumps, and maintenance pumps),
Compressor subsystem,
Cooling subsystem,
Liquid nitrogen supply subsystem,
Nitrogen gas inlet subsystem, and
Control and measurement subsystems.

The main pumps are turbomolecular pumps and have a net total pumping speed of 13,000 ℓ/sec (N_2). The vacuum pumping system consists of two identical sets each connected to a pumping port of vacuum vessel.

6.1.2 Secondary cooling system

The secondary cooling system is to remove and dissipate heat generated in each system of JT-60 transferred through its heat exchanger. Major components of the system are a cooling tower, water pumps and pipes, and water processing units.

The design was made under the following conditions; maximum wet thermometer temperature 26.5 °C, maximum temperature of supply water 30 °C, and maximum allowable water supply 150 m^3/hr. Some of the characteristic values of the system is summarized below:

Total circulation of water	9,400 m^3/hr
Inlet temperature at exchanger	31 °C
Outlet temperature at exchanger	39 °C
Cycle number	4
Total water supply	130 m^3/hr
Average heat removed	5.6×10^7 kcal/hr

6.1.3 Power distribution system

The power distribution system receives electric power from the central power station and distributes the power directly to the toroidal and the poloidal field coil power supply and through power distribution subsystems to the vacuum pumping, secondary cooling, and other systems and to the buildings. The distributed power is as follows:

1. Toroidal field coil power supply:
   - to motor-generator 25 MVA
   - to the coil directly 180 MVA
2. Poloidal field coil power supply:
   - to motor-generator 20 MVA
3. Supplementary heating power supply:
   - to motor-generator 25 MVA
4. Operation distirbution subsystem: 20 MVA
5. Building distribution subsystem: 15 MVA

6.1.4 Gas feed system

The gas supply system is organized by four subsystems which consist of main feed system, auxiliary one and two kinds of impurity feed systems. The gases (H_2, D_2, He, Ne, O_2 and Ar) fed to the vacuum vessel are controlled by FMV (Fast Magnetic Valve) and PEV (Piezoelectric Valve). It is summarized in Table IX.6.1.4-1.

6.1.5 Preionization system

The system aims at producing a weakly-ionized plasma before a discharge. Proposed two types of preionization method are an electron gun and a J×B plasma gun, respectively.

Specifications of these systems are summarized as follows:

1. An electron gun

Filaments current		45 A
Emission current		0.5 A

2. A J×B plasma gun

Power supply	capacitor	100 μF
	charge voltage	10 kV max.

Table IX.6.1.4-1 Gas injection system of JT-60

Feed line	Functions	Valve***	Injection duration sec	Injection rate Torr.ℓ/sec	Max. supply amount by one shot Torr.ℓ	
Main Feed Line (H_2 only)	quick initial gas filling	FMV-H	0.01	*6-60	300	Supply amount is controlled by back pressure.
	slow initial gas filling	PEV-H PEV-L	free	0.5-1,800	**300	It is used to discharge cleaning and Oxidation - Deoxidation porcess.
	density control	PEV-H PEV-L	maximum 10	0.5-1,800	700	It is controlled by plasma density feedback.
	plasma termination	PEV-H	0.1-0.5	0.5-1,800	350	It is controlled by preprograming.
Auxiliary Feed Line (O_2, He, Ne, Ar, etc.)	slow initial gas filling	PEV-H PEV-L	free	0.5-1,800	**300	Same to Main Feed Line.
	density control	PEV-H PEV-L	maximum 10	0.5-1,800	700	Same to Main Feed Line.
	plasma termination	PEV-H	0.1-0.5	0.5-1,800	350	Same to Main Feed Line.
	quick impurity injection	FMV-L	0.01	*0.7-7	7	Same to Impurity Feed Line -I.
	slow impurity injection	PEV-L	0.01-10	0.5-10	50	Same to impurity Feed Line -I.
Impurity Feed Line -I (He, Ne, Ar, etc.)	quick impurity injection	FMV-L	0.01	*0.7-7	7	Supply amount is controlled by back pressure.
	slow impurity injection	PEV-L	0.01-10	0.5-10	50	It is controlled by preprogramming.
Impurity Feed Line -II (He, Ne, Ar, etc.)	quick impurity injection	FMV-L	0.01	*0.7-7	7	Same to Impurity Feed Line -I.
	slow impurity injection	PEV-L	0.01-10	0.5-10	50	Same to Impurity Feed Line -I.

* Injection vate is Torr.ℓ/10 msec.
** Supply duration is 50 sec before examination discharge.
*** Function of values are explain in detail in Attachment.

7. Studies on plasma physics relevant to JT-60 program

7.1 One-dimensional transport simulation

In order to study space-time evolution of plasma parameters in additional heating phase, we have carried out one-dimensional transport simulation. We assume a cylindrical plasma and employ following MHD equations neglecting the effect of impurities.

1) Equations

$$\frac{\partial n}{\partial t} = \frac{1\partial}{r\partial r} r(D \frac{\partial n}{\partial r}) + \alpha_i n n_0 - \beta n^2 + s_{nb}$$

$$\frac{3\partial}{2\partial t} nkT_e = \frac{1\partial}{r\partial r} rn(\chi_e \frac{\partial}{\partial r} kT_e - \frac{5}{2} v_p kT_e) + v_p \frac{\partial}{\partial r} nkT_e - \frac{3}{2} n \frac{k(T_e-T_i)}{\tau_{eq}}$$

$$- P_{br} - P_{cy} + \eta j_z^2 + (p_{nb})_e$$

$$\frac{3\partial}{2\partial r} nkT_i = \frac{1\partial}{r\partial r} rn(\chi_i \frac{\partial}{\partial r} kT_i - \frac{5}{2} v_p kT_i) + v_p \frac{\partial}{\partial r} nkT_i + \frac{3}{2} n \frac{k(T_e-T_i)}{\tau_{eq}}$$

$$- \frac{3}{2} \alpha_c n n_0 k(T_i-T_0) + (p_{nb})_i$$

$$\frac{\partial}{\partial t} j_z = \frac{1\partial}{\mu_0 r\partial r} r(\frac{\partial}{\partial r} \eta j_z)$$

2) Transport coefficients

Empirical coefficients for electron thermal conductivity χ_e, ion thermal conductivity χ_i, and diffusion D are employed:

$\chi_e = 5\times10^{19}/n$ (m^2/s), $\chi_i = 3(\chi_i)_{neoclassical}$, and $D = \chi_e/10$ (m^2/s)

Other transport coefficients such as electrical resistivity η and equipartition time τ_{eq} are assumed (neo)classical.

3) Boundary conditions

Boundary conditions are $\frac{\partial}{\partial r}$ (n, T_e, T_i, j_z) = 0 at r = 0(axis), and at $r = r_p$ (surface) n, T_e, and T_i are given a certain values such as $4\times10^{18}/m^3$, 50 eV, 50 eV, respectively, and $\int j_z ds = I_p$.

4) Neutrals

The density of neutral hydrogen particles at each time is given by a steady-state equation considering ionization and charge-exchange

processes, since these processes occur rapidly enough compared with other processes of the plasma such as the diffusion and the thermal conduction. Here the neutrals are assumed to be mono-energetic and a cylindrical model is used. The boundary value of first-generation neutrals with a temperature of 50 eV is determined considering the recycling ratio of hydrogen particles. Here we assume the recycling ratio is unity or 0.6.

5) NBI

The particle source term by neutral beam injection s_{nb} is described as

$$s_{nb}(r) = \sigma(r)n(r) \oint \frac{d\theta}{2\pi} \oint \frac{d\psi}{2\pi} \left(\frac{R}{R_o}\right) \left(\frac{I_{nb}(\xi,\eta)}{e}\right) \exp\{-\int \sigma(r')n(r')ds\}$$

neglecting the excursion of ion drift orbits from the magnetic surfaces. And the respective energy source terms of electron and ion by neutral beam injection are given as

$$(p_{nb}(r))_e = \frac{2m_e s_{nb}}{m_i} \nu_e kT_e \int_0^{\tau_t} \left(\frac{E_{nb}}{T_e}\right) \exp\left(-\frac{t}{\tau_c}\right) dt,$$

$$(p_{nb}(r))_i = \left[\frac{3(\pi)^{1/2}}{4} \left(\frac{m_i}{m_e}\right)^{1/2}\right] \left(\frac{2m_e s_{nb}}{m_i}\right) \nu_e kT_e \int_0^{\tau_t} \left(\frac{T_e}{E_{nb}}\right)^{1/2} \exp\left(-\frac{t}{\tau_c}\right) dt$$

6) Computed results

We calculate a case of perpendicular injection with energy of 75 keV and power of 20 MW. Then we consider that injection energy is composed of three energy components ratio of E_{75keV}: $E_{75/2keV}$: $E_{75/3keV}$ = 6 : 3 : 1. Computed results are as follows.

(1) From the empirical scaling law of averaged density $\bar{n}_e$, an attainable one in JT-60 would be 2×10^{19} m^{-3} in joule-heated plasma. The initial value of $\bar{n}_e$ is chosen to be 2×10^{19} m^{-3}. After joule heating of one sec, an averaged ion temperature $\bar{T}_i$ and an energy confinement time τ_E become up to $\sim$1 keV and 0.2 sec, respectively.

(2) NBI starts at 1 sec and $\bar{T}_i$ reaches a maximum of 5 $\sim$ 7 keV at 1.6 sec. After 1.6 sec, $\bar{T}_i$ gradually decreases as shown in Fig. IX.7.1-1. The decrease of $\bar{T}_i$ is directly related to the energy losses due to neoclassical ion heat transport and ion-electron relaxation which increase with the density. Note that the total energy of ion continues to increase.

(3) $\bar{n}\tau_E - \bar{T}_i$ diagram is shown in Fig. IX.7.1-2. In the case of the recycling ratio of unity, we can attain our target regime at $\bar{T}_i$ = 5 keV. In the other case of the ratio of 0.6, however, we cannot reach the regime. This is because the used empirical transport coefficients are very sensitive to the density and its distribution. Figures IX.7.1-3 and IX.7.1-4 show the distributions of ion temperature and density for the different recycling ratios. The distributions of ion temperature are almost same in both cases. But, the shape of the density distribution is broad for the recycling ratio of unity and becomes narrower with time for the ratio of 0.6. This is because the particle source from NBI concentrates near the plasma center when the density of plasma outer region is low due to the recycling ratio smaller than unity. In order to attain our target regime, the higher density should be better, unless neutral beams cause a plasma surface heating.

(4) Figure IX.7.1-5 shows the gross power balance of the plasma in NBI heating phase. It follows that the energy loss due to electrons is the most dominant. This indicates that the improvement of the electron energy confinement is the most important in future large tokamaks.

We show optimistic results as above expecting powerful impurity control by the magnetic limiter but in the case of significant impurity contamination, results will be different. These are now under investigation.

7.2 Studies of neutral beam injection heating

(1) One of serious problems associated with neutral beam injection heating of a large tokamak is the surface trapping of the injected beams. A quasi-perpendicular injection permits sufficient penetration of the beams. On the other hand, the quasi-perpendicular injection causes an increase in ripple loss of fast ions as well as impurity influx from the wall and the limiter hitted by the loss particles.

We have developed a computer code using Monte-Carlo techniques which treats the fast ion behavior in a non-axisymmetric field. This code has been used to analyse the ripple loss of fast ions in a large tokamak. Fast ion losses due to charge exchange reactions and the finite size banana orbits were also evaluated by this code simultaneously. The loss rates of the fast ions and the impurity influx sputtered by the escaping

particles have been studied with respect to the magnitude of the toroidal ripple and the injection conditions which are appropriate to JT-60, JAERI large tokamak under construction.

The ripple-associate loss particles are categolized in two groups. The first is the loss particles escaping from the plasma by the ripple-trapped drift motion, and the fraction of these particles is denoted by Γ_{rp}. The second is the loss particles escaping from the plasma by taking the banana orbit motion, which probably comes from the ripple-enhanced banana drift and the detrapping from the ripple wells near the plasma periphery. The fraction of particles belonging to the later group is given by Γ'_{ob}.

The fractions of these ripple-associated loss particles are shown in Fig. IX.7.2-1 as a function of the initial fast ion pitch angle on the mid-plane θ_0, where the birth point of the fast ions is set at r = 0.9a. It is noticeable that Γ'_{ob} is much larger than Γ_{rp} except the case of small θ_0. The injection geometry of JT-60 predicts $\theta_0 \sim 16°$ at r = 0.9a and thereby the ripple-associated loss of fast ions can be reduced to a sufficiently small amount. However, the ripple-associated loss particles are concentrated on a toroidal limiter of JT-60, and hence the heat load of the limiter and the impurity influx from it becomes serious for NBI heating of high density plasmas.

(2) To investigate the effect of neutral beam injection (NBI) heating, it is necessary to take the slow down process into consideration when the injection time, fast ion slow down time and energy confinement time are comparable. A computer code of a simple zero dimensional plasma coupled with fast ions was developed. Radiation loss by impurities, loss of neutral beam and fast ions are also considered in this code. Fast ion energy distribution is calculated and the power transferred to bulk ions and electrons at every moment after the initiation of neutral beam injection is obtained. This code was checked with the results of PLT high power NBI heating experiments and then applied to JT-60 case. Resultant $\bar{T}_i - \bar{n}\tau_E$ diagram is shown in Fig. IX.7.2-2. As shown in the figure, control of recycle ratio is important to further heat the JT-60 plasma up to the target region.

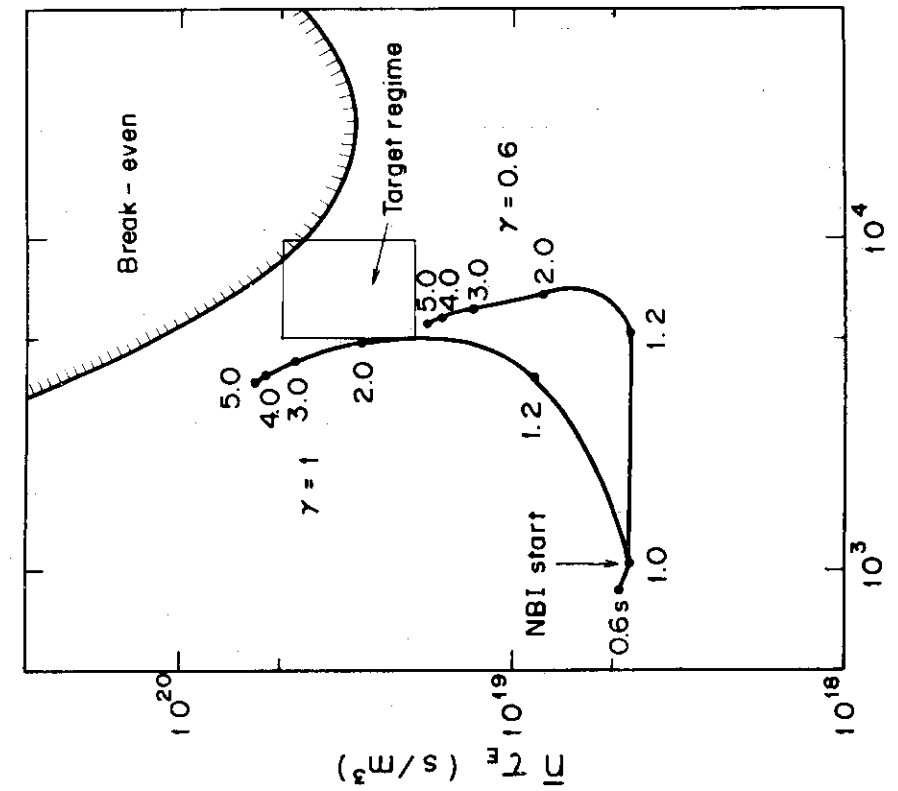

Fig. IX.7.1-2 $\bar{n}\tau_E - \bar{T}_i$ diagram of JT-60.

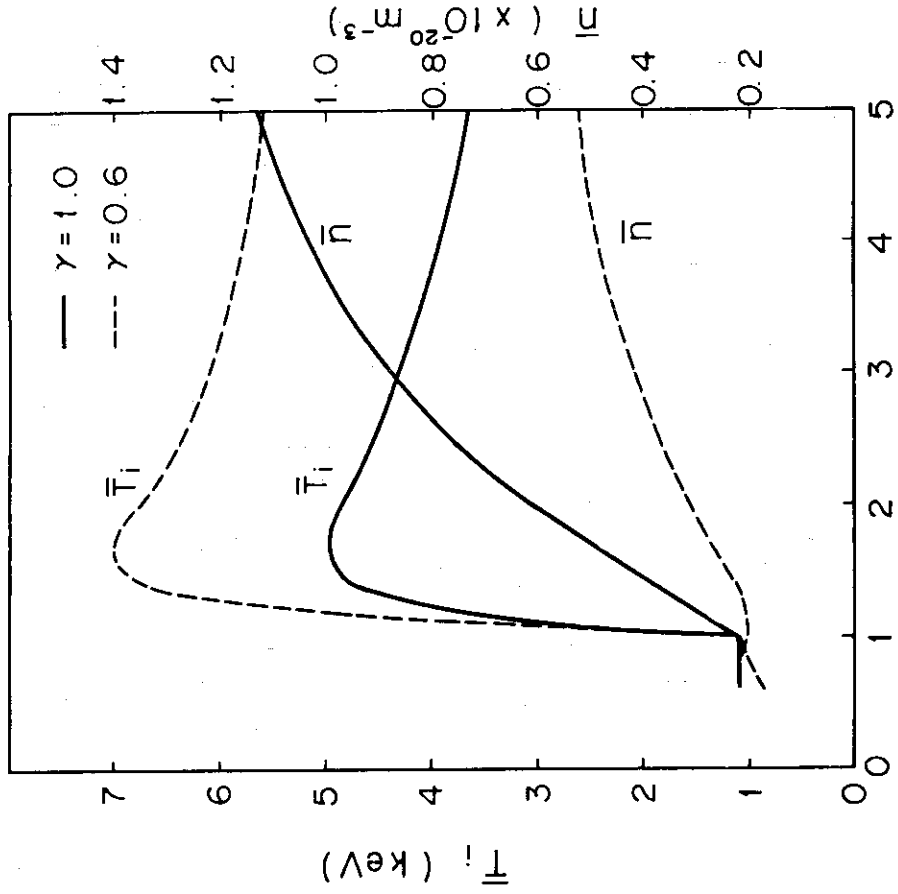

Fig. IX.7.1-1 Time evolutions of averaged ion temperature and averaged ion density for respective recycle ratio γ=0.6 and 1.0.

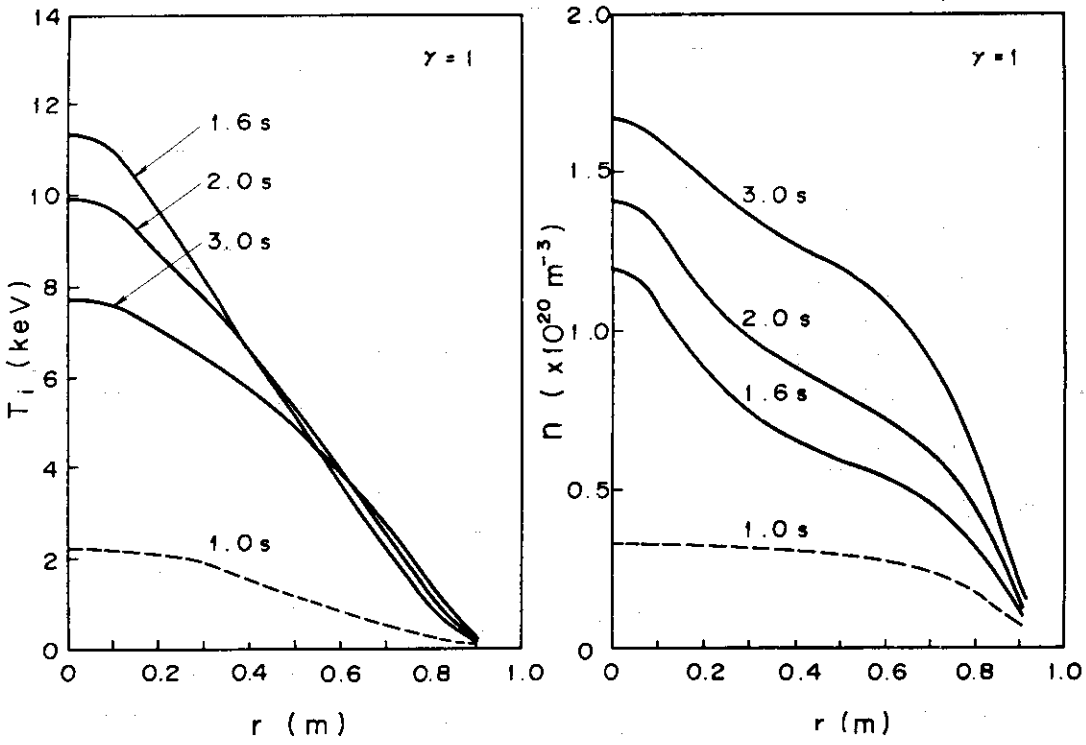

Fig. IX.7.1-3 Radial distributions of ion temperature and ion debsity for a recycle ratio of γ=1.0 in NBI heating phase.

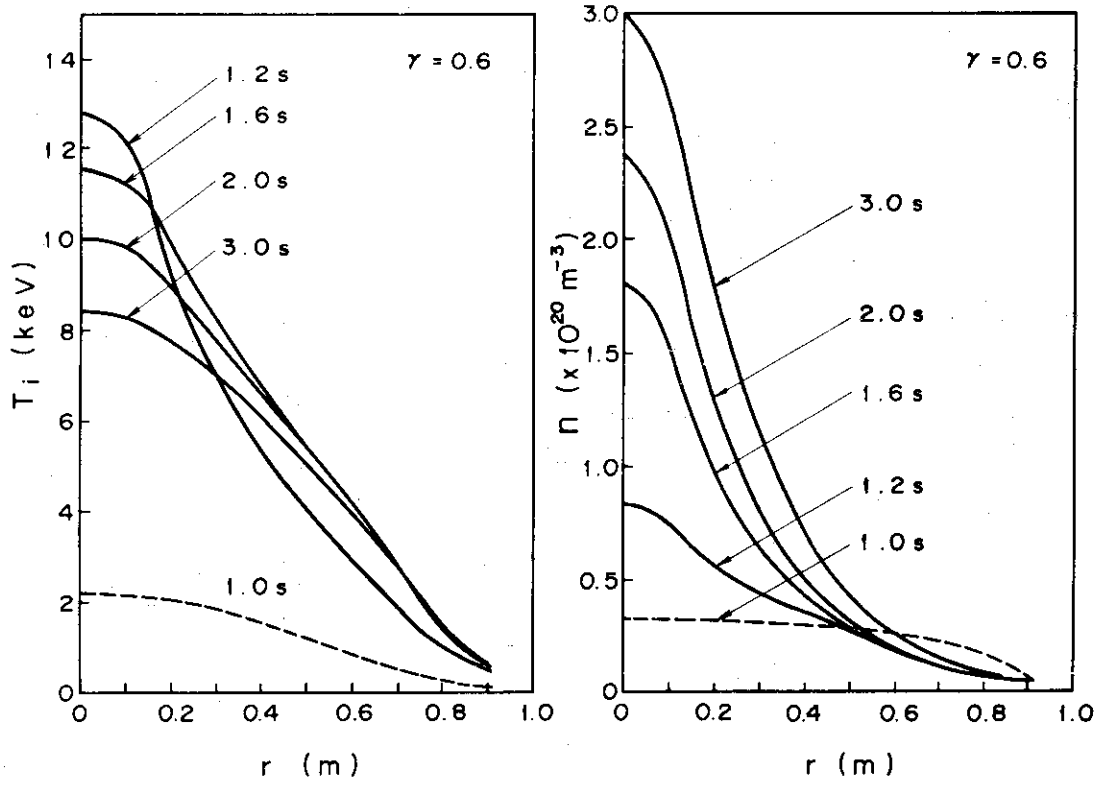

Fig. IX.7.1-4 Radial distributions of ion temperature and ion density for a recycle ratio of γ=0.6 in NBI heating phase.

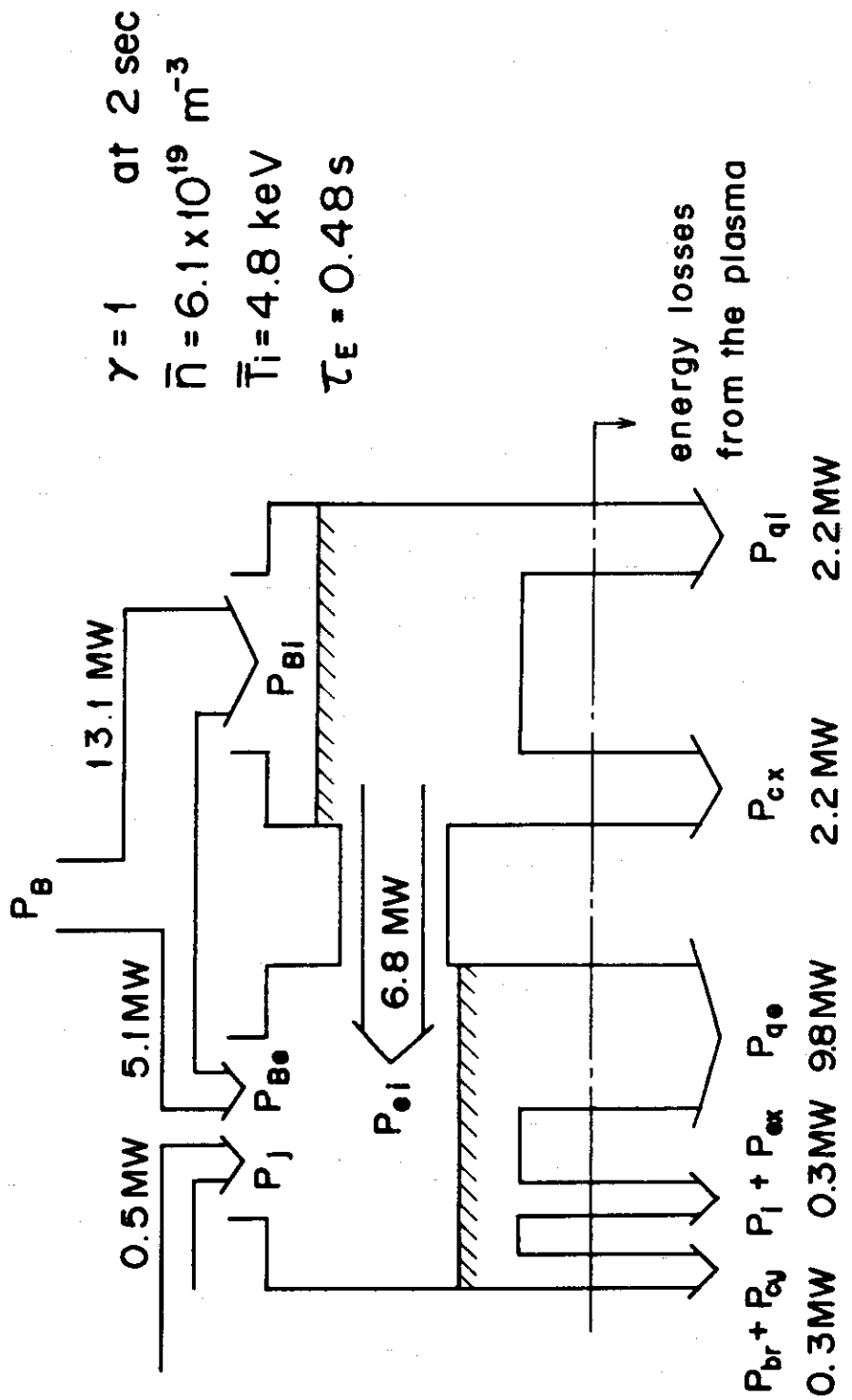

Fig. IX.7.1-5 Schematic drawing of power balance in JT-60 for a recycle ratio of γ=1.0 P_j: joule heating power, P_B: additional heating power by neutral beam injection, P_{Be}: P_B to electron, P_{Bi}: P_B to ion, P_{cy}: synchrotron radiation loss, P_{br}: bremsstrahlung radiation loss, P_{ex} and P_i: excitation and ionization losses by impurities, P_{cx}: charge exchange loss, P_{qe} and P_{qi}: conduction and convection losses of electron and ion, P_{ei}: energy transfer between electron and ion,

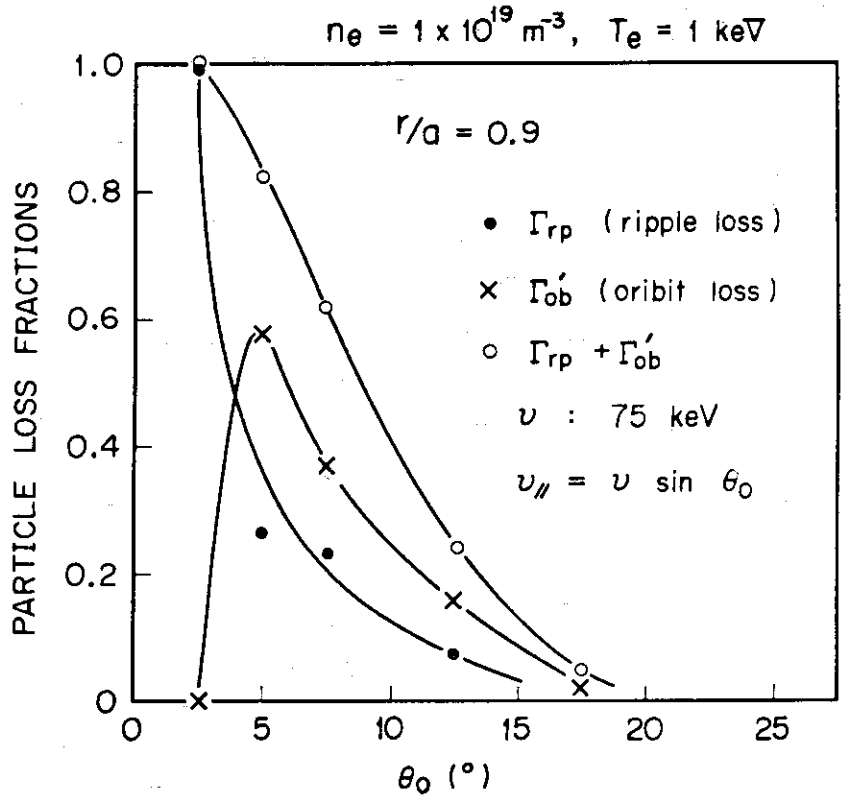

Fig. IX.7.2-1 Ripple associated particle loss fraction as functions of the initial pitch angle of fast ions.

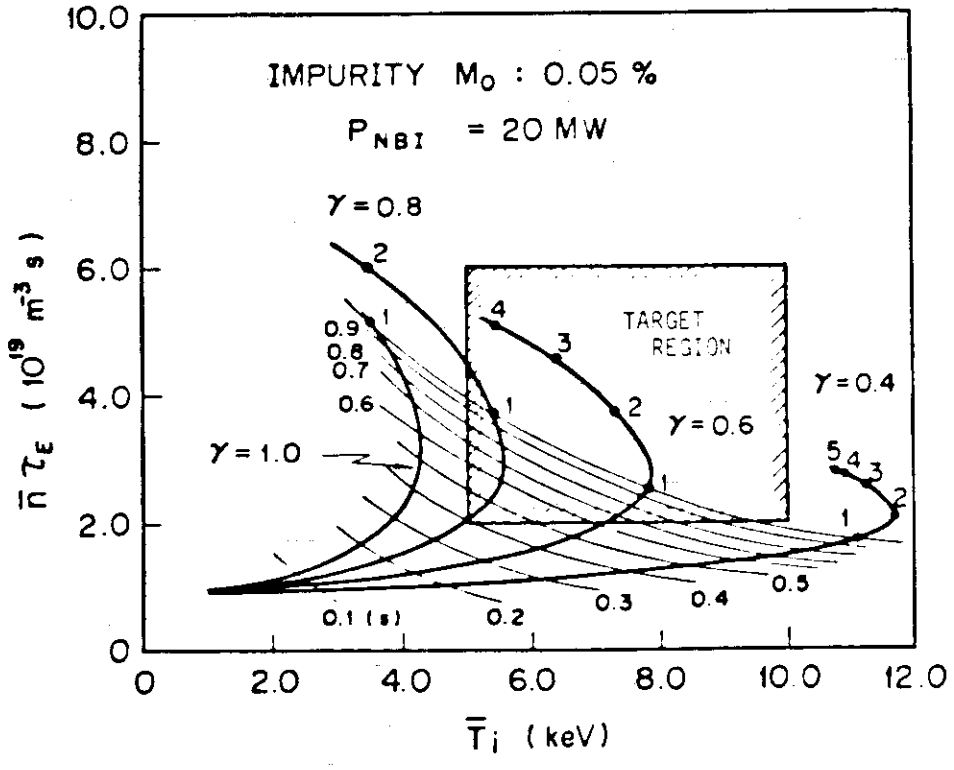

Fig. IX.7.2-2 Time evolution of plasma parameters for respective recycle ratio γ=0.4, 0.6, 0.8 and 1.0.

X. DEVELOPMENT OF A NONCIRCULAR TOKAMAK

1. Introduction

The research program on the noncircular cross section tokamak of JAERI was revised by the Fusion Council in 1978. In the old program, the design of JT-4[1] was pursued which is a tokamak of medium size (R_p=1.45 m) with D shaped cross section plasma and axisymmetric divertors. In the revised program, both an experimental research in Doublet III of General Atomic at San Diego and that in JFT-2M (see II-5.) are pursued instead of JT-4. The former will be carried out as one of the Japan-U.S. cooperation and the latter JFT-2M will be constructed as a device successing JFT-2.

2. Research program in the experiments on D shaped plasmas in Doublet III

Doublet III is a noncircular tokamak with major radius of 1.43 m and splittable D shaped toroidal field coils which are almost the same size as JT-4. The detail of Doublet III is described in Ref. 4). The bird's eye view of Doublet III machine is shown in Fig. X.1-1. A D shaped plasmas also with the same size as JT-4 can be produced in the upper half of Doublet III as shown in Fig. X.1-2. The parameters of D shaped plasmas in Doublet III are shown in Table X.1-1. The parameters are upgraded in 1982 and high power neutral beam injection heating with as much as more than 20 MW. The main objective of the Japanese effort in the joint program is to investigate the upper limit of plasma beta value in D shaped plasmas.

The research program is divided into three periods: Joule heating experiment, 1st phase NBI experiment and 2nd phase NBI experiments (or upgrade experiments). The main objective in the Joule heating experiment is to establish the plasma control technique of D shaped plasmas and to obtain high plasma density for getting high efficiency of NBI heating. The plasma-beam interactions and plasma-wall interactions are investigated in the 1st phase NBI experiment, and the plasma diagnostics will also be established.

The JAERI team dispatched to GA carries out the experimental program on D shaped plasmas under its own leadership using about half of the experimental machine time. And the joint program in Doublet III is reviewed and determined by the Doublet III Steering Committee which consists of JAERI and the United States Department of Energy.

The program in Doublet III will be carried out in cooperation with universities.

References

1) JT-4 Group: JT-4 Program, JAERI-M 6666 (August, 1976), 265 pp, (in Japanese)

2) Kitsunezaki, A., Seki, S., Saito, R., Matsuda, T., Yokomizo, H., and Yoshikawa, M.: JT-4 Program, Proc. of International Symposium on Plasma Wall Interaction, (Permagon Press, 1977)

3) JT-4 Group: Report on the Design of JT-4, JAERI-M 7853 (August, 1978), 52 pp

4) Callis, R.W.: Doublet III Baseline Design Description, GA-A13996 (June 1976)

Table X.1-1 Parameters of Doublet III

Major radius		1.43 m
Minor cross section		
Horizontal half width	(a)	0.45 m
Vertical half width	(b)	0.63 m
Ellipticity	(b/a)	∿1.4
Toroidal field		2.6 T (4.0 T)
NBI heating power		7.2 MW (21.6 MW)
Flux swing		5 V.s (10 V.s)

( ): up grade

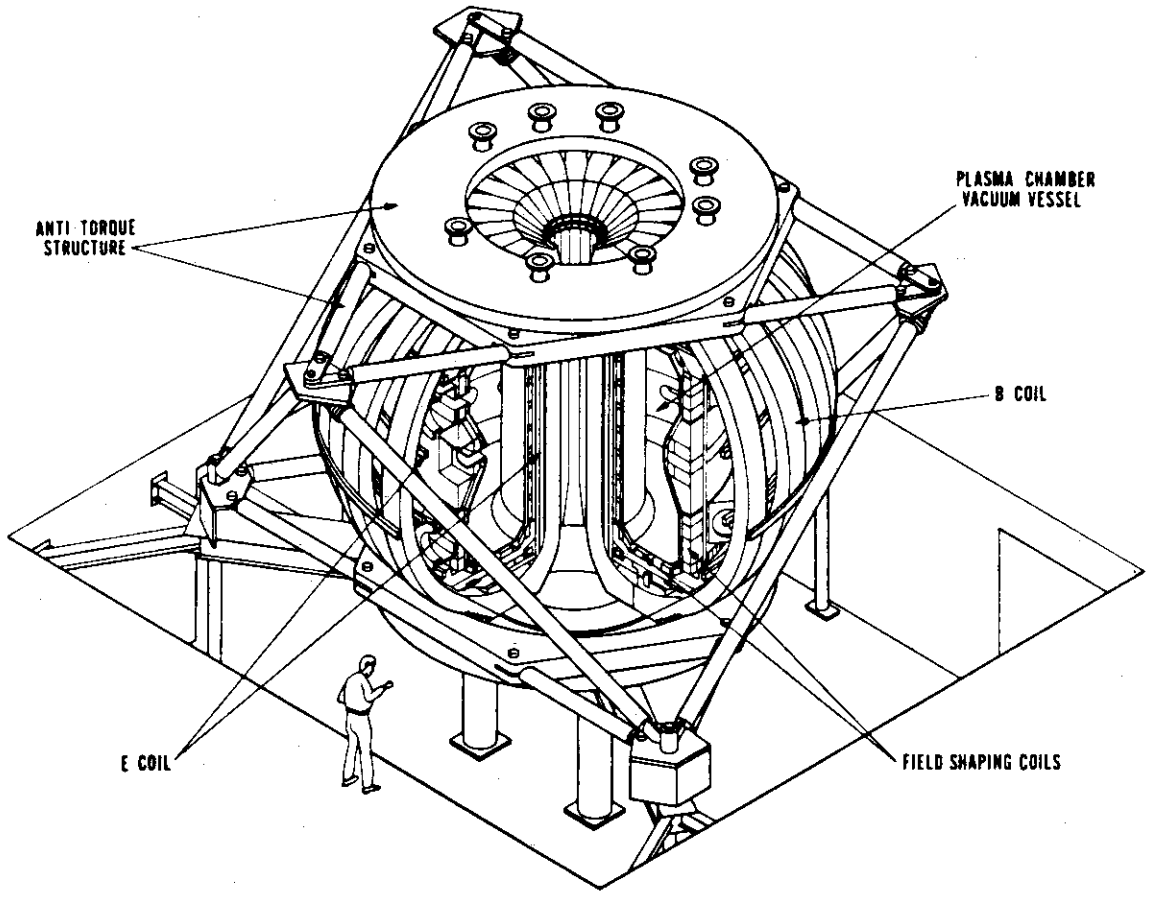

Fig. X.1-1 Schematic of Doublet III

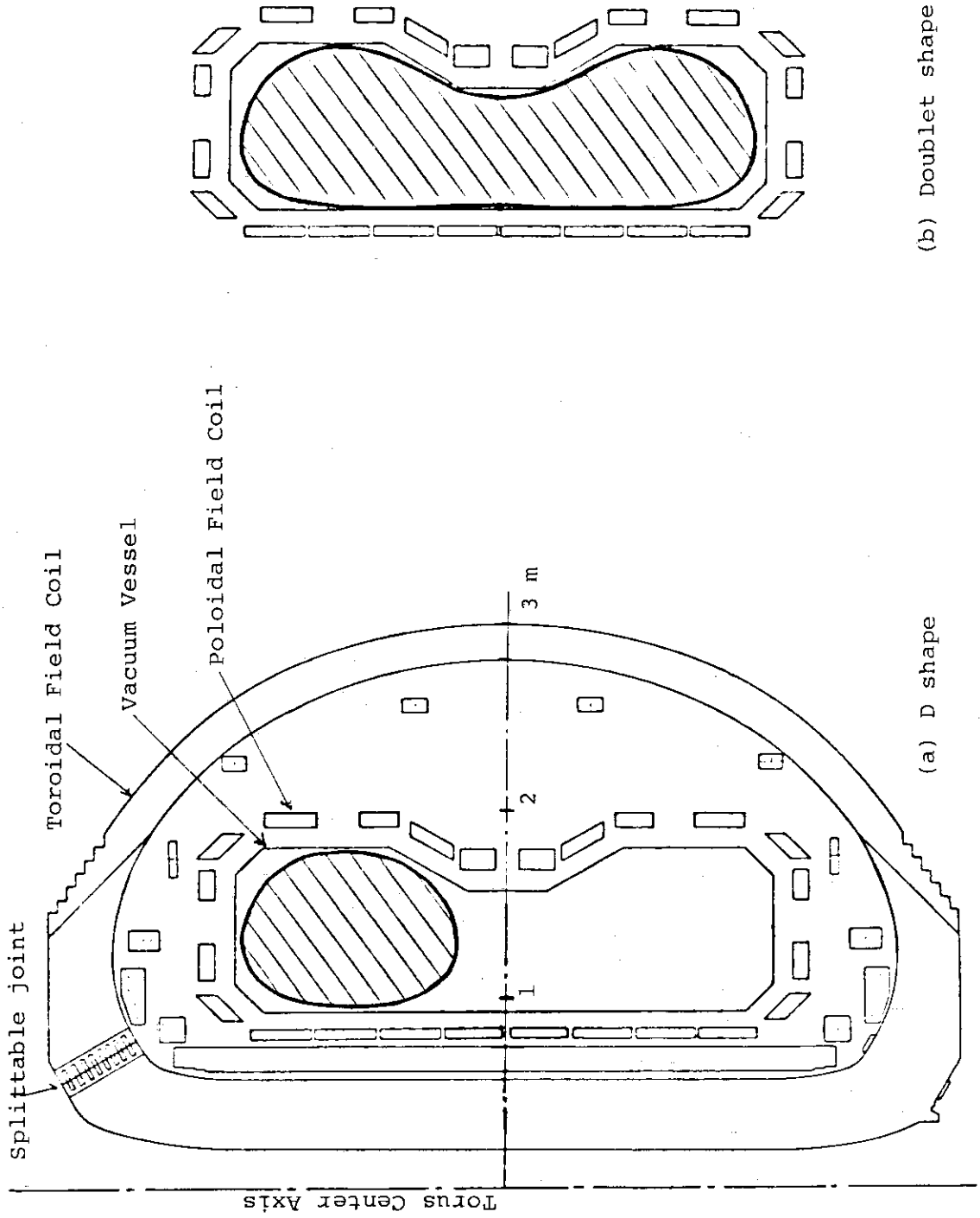

Fig. X.1-2 Cross section of Doblet III

XI. DEVELOPMENT OF THE NEXT LARGE TOKAMAK MACHINE

1. Design Study of Plasma Engineering Test Facility (PETF)

1.1 Scope of PETF

The first big step along the development schedule toward the tokamak reactor was made by construction of JT-60. As the second step, Plasma Engineering Test Facility (PETF) should be accomplished for the definite perspective about realization of fusion power in the beginning of the next century. Japan Atomic Energy Commission has settled the accomplishment of PETF, hopefully by 1990 and even at the latest by 1994 in its long range development program.

From the engineering point of view, the next machine should furnish all essential technologies for maintaining reactor relevant plasma. The technologies concerning to resources such as tritium and real energy multiplication with high duty cycle will be imposed on in the further future machine, that is, Experimental Power Reactor.

Recently, PLT of Princeton Plasma Physics Laboratory succeeded in reaching the central plasma ion temperature up to about 6 keV without unstable phenomena although collisionless plasma deeply entered the region of the trapped ion mode region. The energy confinement time still obeys the experimental ALCATOR scaling at $\tau_E \propto \sqrt{q_a}\ \bar{n}\ a^2$ similarly to other existing tokamak machines.

The proportionality coefficient for the experimental scaling at PLT can be expected to be improved by the factor of two at JT-60 by some countermeasure against impurity contamination. Thus, the results of PLT encourages JT-60 to realize one of its targets of $\tau_E \simeq 0.5 \sim 1.0$ sec. If it is accomplished, the possibility to reach the self-ignition condition at the next generation machine will be very high with the realistic machine size.

However, tokamak plasma physics at sufficiently high temperature for dominant fusion reactions and burning control is still remained to be examined in future experiments. Therefore, at the present stage, we had better initiate design work with the plasma parameters reduced from the experimental ALCATOR scaling aiming to reach the self-ignition condition and put emphases in designing one the integrated test of essential relevant plasma engineering to created the reactor plasma such as superconducting magnet or tritium technologies at a single realistic size machine.

By this machine, the reactor relevant plasma engineering such as impurity control or long D-T burning control should be established and all technologies to realize it should be reliably integrated.

1.2 Outline of PETF

JAERI begain the design study of PETF in April, 1978. It was initiated from physical investigation to obtain perspectives to reach self-ignition. In parallel, the hardware conceptual studies were initiated by the contracts with Mitsubishi Atomic Power Industry Inc., Nippon Atomic Industry Group and Hitachi, Ltd. Two design options were imposed. One of them is an option for superconducting material of toroidal field coils, that is, NbTi or Nb_3Sn. The other is about employment of poloidal magnetic limiters. Design study was carried under the condition that it must be possible to be constructed by the present technical level or the expectable level at five years later. Common use of the motor generator system with JT-60 enforced PETF small duty cycle.

The basic concept of PETF was settled in February, 1978. It major parameters are summarized in Table XI.1.2-1. The cross section view of PETF is shown in Fig. XI.1.2-1. Some major characteristics of PETF are as follows:

1. The aspect ratio is determined to achieve self-ignition condition by NbTi toroidal field coils.
2. Poloidal field coils are conventional and their number is kept the minimum to keep easy assembly and disassembly. All of them except magnetic limiter coils are located outside of toroidal field coils.
3. It has magnetic limiters at top and bottom of D-shape plasma and their magnetic limiter coils are located outside of the vacuum vessel.
4. The vacuum vessel has double-wall structure to suppress tritium leakage. Uniform structure along the toroidal direction reduces electromagnetic force. The structure is also contrived to release thermal expansion.
5. Poloidal field coils are grouped into blocks and controlled independently in composite manner both for plasma current start-up and plasma shape-position control.

1.3 Physical considerations of PETF

In determining the plasma and device parameters which enable us to examine the ignition condition, the following three major criteria must be investigated; (1) confinement scaling laws, (2) additional heating, (3) impurity control.

1) Confinement Scaling Laws

Present empirical scaling laws (ALCATOR scaling law) give rather pessimistic predictions to the future large tokamaks, unless they are improved by at least a factor of 2. When they are thus improved, we can expect several seconds of τ_E at most, but it will be difficult to attain several tens of second under the technological and cost restrictions.

2) Additional Heating

Accordingly, large heating power will be necessary to overcome poor τ_E. However, extremely large power of above 100 MW cannot be expected in PETF. Therefore, a plasma temperature of 7 $\sim$ 10 keV seems to be attainable because of available τ_E value, realistic heating power and expectable α-particle heating power.

Among the additional heating methods, what can be designed realistically at present is the neutral beam injection using positive ions. Not so high beam energy, probably less than 200 keV, is desirable to obtain the required heating power. Thus, excessively large minor radius and high plasma density must be excluded in order to avoid the surface heating of the plasma.

3) Impurity Control

Impurity control still becomes serious problem in the future large tokamaks. It is because neutral beam injection heating power per unit volume decreases as the device size becomes large or the plasma density becomes high, while the energy loss per unit volume due to impurities does not depend on the device size for the same impurity concentration. Furthermore, since the plasma temperature will be raised and the discharge time will be prolonged, the sputtering and the evaporation of the limiter and first wall materials will inevitably be increased. Therefore, unfortunately we cannot help employing the poloidal magnetic limiter to avoid the evaporation and to shield the impurity influx.

In addition, as practical problems, it is important to take account of the technological and cost restrictions in determining the plasma and

device parameters. In the present design study, we have principally pursued the compactness of the device, retaining the possibility to attain the ignition condition.

The followings are basic principles and assumptions adopted in this design study.

1) Empirical na^2 scaling laws, in which their numerical coefficients are improved by a factor of 2 ($\tau_E = 1.1 \times 10^{-20} na^2$), is employed. There are several possibilities for this improvement. They are (i) impurity control, (ii) improvement of ion's energy confinement in higher temperature plasmas, (iii) noncircular effect.

2) D-shaped plasma is employed to raise toroidal beta value.

3) Aspect ratio is about 4.5 to maximize $n\tau_E$ value and concurrently to minimize plasma volume under the condition of constant beta value.

4) Average ion temperature is set to be about 7 keV to attain a required $n\tau_E$ value under minimum beta value, and also to avoid the excessive burden in additional heating.

5) Neutral beam injection heating using positive ions is employed for the additional heating method. Deuterium is to be injected. Injection energy is 200 keV to avoid the surface heating. Required injection power to ignite the plasma is 50 ∿ 70 MW.

6) Allowable impurity concentration will become smaller by an order of magnitude than in the present day tokamaks, while impurity production tends to increase in higher temperature and longer pulse length plasma. Thus, severe impurity control will be required. Poloidal magnetic limiter, of which coils are installed outside the vacuum chamber and graphite wall and limiter with careful temperature control is the first candidate to meet this requirement.

7) In addition to this, some measure for plasma boundary temperature control will be required to avoid the erosion of wall and limiter material.

8) Time scale of thermal instability in burning phase is several times of energy confinement time, so that required burning time for burn control is 30 ∿ 60 seconds. Particular mechanism for ash exhaust is not installed, since the accumulation of helium ash is 10 ∿ 20 %.

References

1) Sugihara, M., Kasai, M. and Hiraoka, T.: Ignition Approach by Neutral Beam Injection Heating in Impurity Contaminated Tokamak Reactors, Jr. Nucl. Sci. & Techn., 16[5], pp 305-315 (May 1979).
2) Hiraoka, T., Tazima, T., Sugihara, M., Kawai, M., Shinya, K. and Sakamoto, H.: Conceptual Studies of Plasma Engineering Test Facility, JAERI-M 8198 (April, 1979).

2. IAEA-INTOR study

IAEA organized International Workshop of INTOR (International Tokamak Reactor) by recommendation of IFRC. Deligates of Workshop are four tokamak advanced countries, Japan, U.S.A., U.S.S.R. and E.C. Its first Session was held in February, 1978. INTOR is a tokamak machine anticipated as a next generation machine to succeed large tokamak machines now under construction. JAERI initiated its study in October, 1978 and could reach a consistent concept called INTOR-J by cooperation of Divisions of Thermonuclear Fusion Research, Large Tokamak Development, Nuclear Fuel Research, Health Physics, Reactor Engineering, High Temperature Engineering and Physics.

Table XI.2-1 summarizes its major parameters. The machine configuration is shown in Fig. VIII.2-1. INTOR-J has characteristic features to achieve long D-T burning by a compact machine. All of its poloidal field coils including poloidal divertor coils, are located outside of the toroidal field coils. It has a large hot blanket area of Li_2O cooled by helium gas.

To INTOR concept study, experiences at JT-60, PETF and JXFR are effectively reflected. Concept studies of INTOR will continue in the fiscal year of 1979 with the progress of INTOR Workshop activities.

Table XI.1.2-1 PETF main parameters

Operation		
Expected operation span		10 years
Total number full power		8×10^4
Pulse repetition period		1200 sec.
Burning flat top period		30 - 60 sec.
Peak fusion power		260 MW
Average fusion power (60 sec. burning)		13 MW
Plasma rise time	up to 1 MA	0.5 sec
	up to max.	4.0 sec.
Plasma		
Major radius		6.2 m
Minor radius	vertical	2.1 m
	horizontal	1.4 m
Plasma volume		338 m^3
Elliptical elongation		1.5
Triangularity		0.5
Aspect ratio		4.43
Toroidal field at axis		4.8 T
Plasma current		4.9 MA
Safety factor, q_a		2.5
Average plasma temperature		7 keV
Average plasma density		1.6×10^{20} m^{-3}
Confinement time		5.6 sec
Poloidal beta		3.0
Toroidal beta		4.0 %
Permissible Z_{eff}		1.2
Tokamak System		
Distance from plasma inner surface to the straight part of the inner perimeter of toroidal field coil		1.1 m
Out-most distance of toroidal field coil form the tokamak axis		11 m
Assembly structure		Octant assembly

Anticipated assembly		5 times
Vacuum vessel neutron wall loading		0.5 MWm^{-2}
Total neutron flux at peak		3×10^{14} cm^{-2} sec^{-1}
14 MeV neutron flux at peak		4×10^{13} cm^{-2} sec^{-1}
Total neutron dose		2.6×10^{21} cm^{-2}
Heat load	magnetic limiter plate (with flux swinging)	200 Wcm^{2}
	liner	6 Wcm^{-2}

Plasma Chamber

Vacuum vessel	Stainless steel double-wall structure
Material limiter	Pylolitic carbon or molybdenum
Liner	Pylolitic carbon
Vacuum vessel coolant	He gas
One-turn resistance	0.5 m ohm
Baking temperature	400 °C
Vacuum pumping speed	50,000 l/s for 20 °C N_2
Throughput	5×10^{-4} torr·l/sec

Primary Shield

Material		multi-layer of iron, heavy concrete and lead
Thickness	inner side	60 cm
	other, upper and lower sides	90 cm

Toroidal Field Coil

Maximum field		8.3 T
Superconducting material		NbTi
Number of coils		16
Coil current		20 kA
Total ampere-turn		149 MAT
Stored magnetic energy		15 GJ
Coil shape		D-shape
Coil bore	vertical	10.0 m
	horizontal	6.3 m

Cross section	width	0.9 m
	thickness (outer side)	1.5 m
Current density	cable	20 A mm^{-2}
	over all (inner part)	8 A mm^{-2}

Ohmic Heating Coil

Coil material	Oxygen free copper (Ag-copper)
Location	Outside of toroidal field coils
Coil current	140 kA (maximum)
Maximum ampere-turn	2.8 MAT/coil block
	2.4 MAT/m (central part)
Magnetomotive force	34.4 MAT
Magnetic energy	650 MJ
Current density	10 A mm^{-2} at central coils
Plasma current raising method	Current interruption
Power supply capacity	420 MW
Power supply method	Parallel-series hybrid
Joule loss power	87 MW
Total joule loss	5.2 GJ/shot (60 sec. burning)
Flux swing	75 Vsec (double swing)

Control Coil

Coil material	Oxygen free copper (Ag-copper)
Control method	Hybrid type
Location	Outside of toroidal field coils
Number of coil blocks	10
Maximum ampere-turn	5.0 MAT
Maximum magnetomotive force	30 MAT
Stored magnetic energy	1.5 GJ
Power supply capacity	995 MVA
Total joule loss	14.7 GJ

Magnetic Limiter

Type	Poloidal limiter at the top and the bottom with flux line swinging
Location of coil	Outside of vacuum vessel
Total ampere-turn	3.6 MAT/limiter
Heat load on limiter plate	200 W cm^{-2}

Secondary Shield

Material	Concrete
Thickness	1.5 m

Tritium

Inventory	80 gr.
Estimated annual consumption	120 gr. for 30 sec. burning

Neutral Beam Injector

Injection power	50 MW
Number of port	8
Beam particle	D^+
Injection energy	200 keV
Extracted current	1700 A
Number of ion sources per port	4 (2 × 2 array)
Port cross section	50 cm (width) × 100 cm (vertical)
Net power efficiency	about 30 %
neutralization efficiency	about 20 %
direct recovery efficiency	85 %
Power supply capacity	170 MW
Pumping speed per port	about 10^6 1/sec
Throughput per port	about 100 torr·1/sec

Table XI.2-1 INTOR-J parameter

	INTOR-J (Quasi-stationary operation)
Basic parameters	
Burn time	200 s
Dwell time	<100 s
Availability	25 %
Number of pulses during lifetime	3×10^5
Major radius (R)	5.0 m
Aspect ratio (A)	4.2
Plasma radius (r_{plasma})(z=0)	1.2 m
Wall radius (r_{wall}) (z=0)	1.3 m
Elongation	1.5
Av. ion temperature (T_i)	10 keV
Av. ion density (n)	1.2×10^{20} m^{-3}
Energy confinement time (τ_E)	≥1.4 s
Effective charge (Z_{eff})	1.5 (∿2.0)
Toroidal magnetic field at axis (B_{To})	5 T
Plasma current	4.7 (∿5.9) MA
Safety factor (q)	2.5 (∿2.0)
β_T	4 %
Field ripple	±0.75 %
Heating	
Power (P)	50 (∿70) MW
Duration	∿5 s
Mode	NBI, RF as backup
Neutral beam energy (E)	(150∿) 200 keV
Impurity and particle control	
Particle confinement	∿ τ_E
Particle fluxes from plasma	2×10^{22} s^{-1}
Fueling mode	Pellet and gas puffing
Fueling rate	Max. 2×10^{21} s^{-1}
Impurity control mode	Poloidal divertor/wall lapping plasma
Toroidal field coils	
Number	12
Conductor	Nb_3Sn
Bore, height/width	9 m / 6 m
Pulsed field	0.1∿0.2 T/s
Radiation	$\sim8\times10^8$ rad (epoxy)
Poloidal field coils* (hybrid coil system)	
OH current ramp time	∿5 s
OHC conductor	SC
OHC location	Outside B_t coil
OHC max. field	±6 T
OHC max. field rise	∿4 T/s (t≤0.1 s) ∿1 T/s (0.1<t≤5 s)
EFC conductor	SC/Cu

(continued)

EFC location	Outside B_t coil
DFC conductor	SC
DFC location	Outside B_t coil
Divertor field	Spatially depending
BDC conductor	
BDC location	
Max. one-turn voltage	∿100 V

Vacuum vessel

Location-primary vessel	Inner surface of bulk shield
Material	Stainless steel
Max. temperature	∿150 °C
Coolant	H_2O
Toroidal loop resistance	0.2 mΩ

First wall

Type	Cooling panel with protection wall	
	Protection wall	Cooling panel
Thickness	∿5 mm	2 mm
Material	low 2 mat, or low Z covered refractory metal	316 SS
Coolant	None (by radiation)	He
Max. temp.-structure	∿1500 °C	∿400 °C
Av. neutron wall load (during burn)	1 MW/m^2	
Av. surface heat load(" ") 0.25 MW/m^2	0.25 MW/m^2	0.3 MW/m^2
Number of pulses/life time	3×10^5	
Number of disruptions/life time	To be determined	
Toroidal loop resistance	See vacuum vessel	
Electric power (gross)	17 MW	

Blanket (non-breeding)

Number of modules	6
Location	Inboard only
Material	316 SS
Coolant	H_2O
Max. temp. (structure)	∿200 °C
Thickness	0.3 m
Poloidal field response time	To be determined

Blanket (T-breeding)

Breeding ratio	∿0.5 (non-divertor)
Number of modules	6
Type	Cellular type
Location	Outboard only
Material, structural	316 SS
Material, breeding	Li_2O
Coolant	He
Max. temp. (structure)	∿400 °C
Electric power (gross)	∿36 MW

Bulk shield

Inboard material	SS and W-alloy
Inboard thickness	0.4 m(0.7 m, including inner blanket)

(continued)

Outboard material	SS
Outboard thickness	1 m
Coolant	H_2O/borated H_2O
Max. temperature (structure)	∿150 °C

Tritium and vacuum

Flow rate	∿10 g/h
Inventory	∿2 kg
Consumption	4.2 kg/year
Tritium cleanup time	12 hrs
Pre-shot base pressure	$\leq 10^{-6}$ torr
Initial base pressure	$10^{-7} \sim 10^{-8}$ torr

* OHC: ohmic heating coils,
EFC: equil. field coils,
DFC: divertor field coils,
BDC: breakdown field coils.

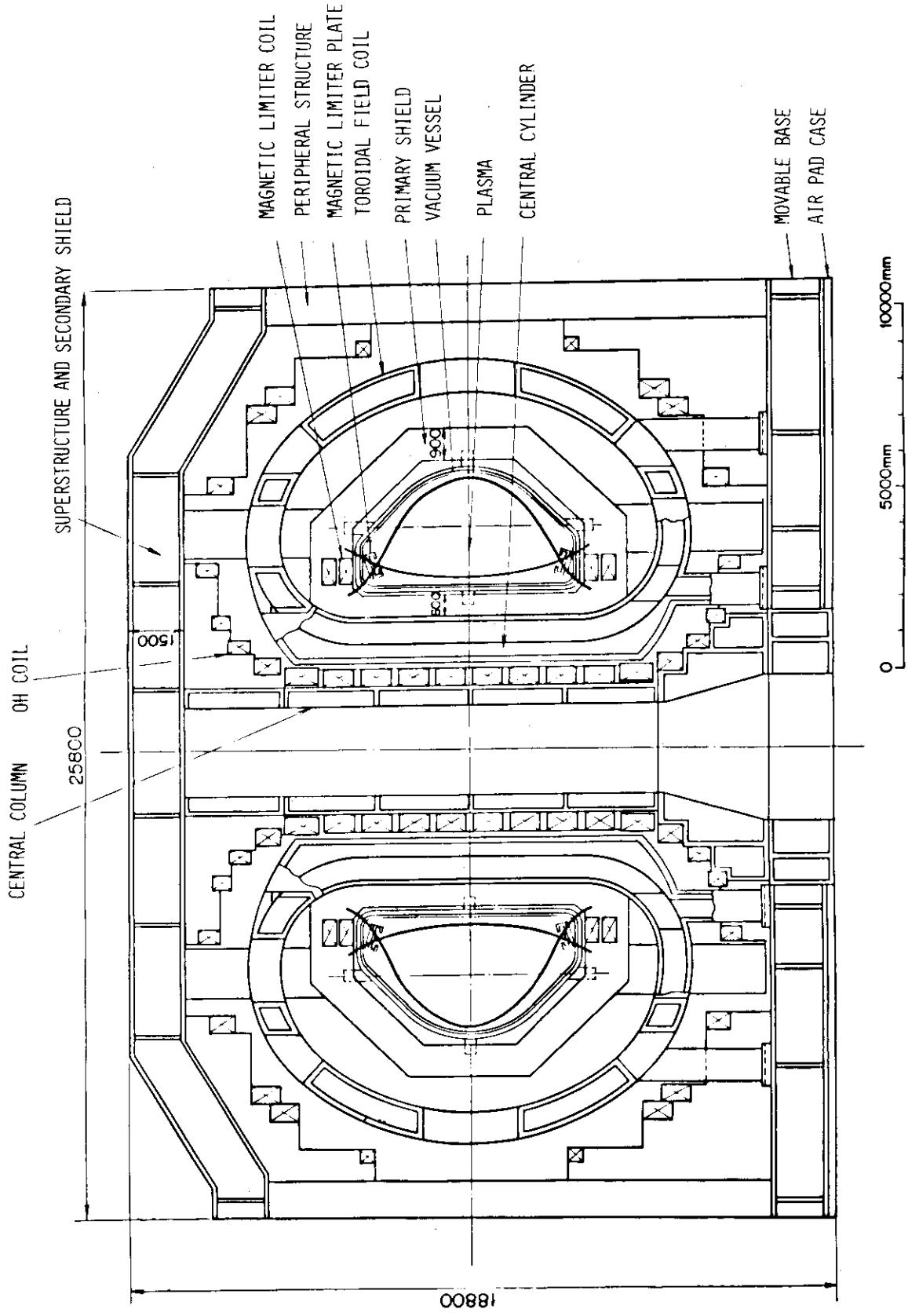

Fig. XI.1.2-1 Cross sectional view of PETF

APPENDIXES

A1. Publication List

A1. 1 List of JAERI-M Report

1) Tsuzuki, N.[*9], Nimomiya, H., Ogata, A., Aikawa, H. and Suzuki, y.: "Feedback Control of Plasma Position, Shape and Current", JAERI-M 7630 (April 1978).

2) Matsuda, M., Arakawa, Y.[**7], Horiike, H.[**5], Itoh, T., Kondoh, U.[*7], Morita, H.[*6], Ohara, Y., Ohga, T., Okumura, Y., Sakuraba, J.[*8], Shibata, T., Shirakata, H. and Tanaka, S.: "Conceptual Design of the JT-60 Neutral Beam Injection System (Interim Report)", JAERI-M 7655 (May 1978) (in Japanese).

3) Hosoda, Y., Shimamoto, S.: "Thermal Stress Analysis of Superconducting Magnet by SAP-4", JAERI-M 7675 (May 1978).

4) Okumura, O., Ohara, Y. and Ohga, T.: "Grid Heat Loading of an Ion Source in Two-Stage Acceleration System", JAERI-M 7696 (May 1978).

5) Mizuho, M., Nomura, Y., Shimizu, M., Sezaki, K., Oyamada, R.: "Experimental results of the linear heat rating capsule 72F-12J", JAERI-M 7705 (May 1978) (in Japanese).

6) Ninomiya, H. and Suzuki, Y.: "Quantitative Evaluation of Eddy Currents in the Vacuum Chamber with Tokamak Circuit", JAERI-M 7710 (June 1978).

7) Tazima, T.: "Particle and energy balances in tokamak plasma", JAERI-M 7717 (June 1978) (in Japanese).

8) Tone, T.: "Reaction-Rate Coefficients, High-Energy Ions Slowing-Down, and Power Balance in a Tokamak Fusion Reactor Plasma", JAERI-M 7769 (July 1978) (in Japanese).

9) Ohara, Y.: "Focusing by Beamlet Steering in Two-Stage Accelerator", JAERI-M 7790 (July 1978).

10) Saito, R.[*5], Seki, S., Yokomizo, H., Matsuda, T. and Kitsunezaki, A.: "Conceptual Design of a Current Transformer in a tokamak Device", JAERI-M 7810 (July, 1978) (in Japanese).

11) Mino, K.[**7] and Tone, T.: "Confinement and Energy Deposition Rate of 3.52 MeV Alpha Particles in JAERI Experimental Fusion Reactor and Demonstration Fusion Reactor Plasmas", JAERI-M 7723 (August 1978) (in Japanese).

12) Shibata, T., Matsuda, S., Shirakata, H., Saito, M.[*10] Mizuno, M.[*10] and Komiya, S.[*10]: "12,000 1/sec Cryopump for Hydrogen Gas", JAERI-M 7792 (August 1978) (in Japanese).

13) Obara, K., Abe, T., and Sone, K.: "Construction of a System for Simultaneous and Continuous Observation of Surface during Ion Bombardment", JAERI-M 7797 (August 1978) (in Japanese).

14) Yamauchi, T., Nagami, M., Sengoku, S. and Kumagai, K.: "Metal Impurity Injection into DIVA Plasmas with a Q-Switched Laser Beam", JAERI-M 7809 (August 1978) (in Japanese).

15) Nishio, S., Ohkubo, M., Kawasaki, k., Ando, T., Miki, N.: "Toroidal ripple and error field of JT-60 toroidal field coils", JAERI-M 7846 (August 1978) (in Japanese).

16) JT-4 Group : "Report on the Design of JT-4", JAERI-M 7853 (August 1978).

17) Fusion Reactor System Laboratory : "Preliminary Safety Analysis of the Reactor Cooling System for Tokamak Experimental Fusion Reactor", JAERI-M 7772 (September 1978) (in Japanese).

18) Aikawa, H., Tsuzuki, N.[*9], Kimura, T., Ogata, A., Ninomiya, H. and Suzuki, Y.: "Status on Performance of the Control System of Plasma Position and Shape", JAERI-M 7845 (September 1978).

19) Shibata, T., Okumura, Y. and Sakuraba, J.[*8] : "Cryopump of 60,000 1/sec for Hydrogen Gas", JAERI-M 7869 (September 1978) (in Japanese).

20) Sugihara, M., Kasai, M.[*4] , Tazima, T. and Hiraoka, T.: "Investigation on physical problems in the ignition approach of D-T burning plasma by one-dimentional tokamak simulation code with fixed distribution", JAERI-M 7885 (September 1978).

21) Fusion Reactor System Laboratory : "Repair and Maintenacnce Design for Tokamak Experimental Fusion Rector", JAERI-M 7825, (October 1978) (in Japanese).

22) Yamauchi, M.[*9] and Iida, H.: "Sensitivity Analysis of Neutronics Calculation in the Preliminary Design of Japan Experimental Fusion eactor", JAERI-M 7915 (October 1978) (in Japanese).

23) Sengoku, S., Azumi, M., Matsumoto, Y., Maeda, H., Shimomura, Y.: "A Condition for Scrape-off Plasma in Self-Sputtering", JAERI-M 7918 (October 1978) (in Japanese).

24) Yamauchi, T., Kumagai, K., Kawakami, T., Matoba, T. and Funabashi, A.: "Improvements of the Ruby Laser Oscillator System for Laser Scattering", JAERI-M 7931 (October 1978) (in Japanese).

25) Ohasa, K., Sengoku, S., Maeda, H., Ohtsuka, H., Yamamoto, S. et al.: "The Origin of metal impurity in DIVA", JAERI-M 7935 (Octber 1978).

26) Tanaka, S. and Shibata, T.: "Calculation of Ion Beam Species Extracted from A Hydrigen Ion Source", JAERI-M 7966 (November 1978) (in Japanese).

27) Saidoh, M., Sone, K., Yamada, R. and Ohtsuka, H.: "Simultaneous and Continuous Observation of Helium Bombarded Surfaces of Polycrystalline Molybdenum", JAERI-M 7997 (November 1978) (in Japanese).

28) Fusion Reactor System Laboratory : "Safety Analysis of Fuel Circulating System for Tokamak Experimental Fusion Reactor", JAERI-M 7964 (December 1978) (in Japanese).

29) Sakuraba, J.[*8], Ohga, T. and Shibata, T.: "Experiment of Hydrogen Beam Introduction to 60,000 1/sec Cryopump", JAERI-M 8013 (December 1978) (in Japanese).

30) Takatsu, H., Shimizu, M., Yamamoto, M., Ohta, M.: "Stress analysis of the HT-60 vacuum vessel", JAERI-M 8017 (November 1978) (in Japanese).

31) Iida, H. and Igarashi, M.[*1] : "THIDA-Code System for Calculation of the Exposure Dose Rate Around a Fusion Device", JAERI-M 8019 (December 1978) (in Japanese).

32) Takeda, T. and Tsunematsu, T.: "A numerical code SELENE to calculate axisymmetric toroidal mhd equilibria", JAERI-M 8042 (January 1979).

33) Fusion Reactor System Laboratory : "Safety Analysis of Superconducting Toroidal Field Magnet for Tokamak Experimental Fusion Reactor", JAERI-M 7963 (February 1979) (in Japanese).

34) Arakawa, Y., Akiba, M.[**2], Kondoh, U.[**7], Matsuda, S. and Ohga, T.: "Source Plasma Study of the DuoPIGatron Ion Source for JT-60 Neutral Beam Injector", JAERI-M 8088 (February 1978).

35) Takatsu, H., Shimizu, M., Okumura, M.[*3], Kawakami, M.[*3] : "Seismic analysis of the JT-60 (1) — Analysis method and eigenvalue analysis", JAERI-M 8155 (February 1979) (in Japanese).

36) Wakatani, M.[**1], Seki, S. and Kitsunezaki, A.: "Theory of High-beta Tokamaks (Stability of Ballooning Mode)", JAERI-M 8120 (February 1979) (in Japanese).

37) Nishi, M., Ando, T., Yoshida, K., Shimamoto, S.: "Measurement of Heat Transfer Characteristics and Stability Analysis of Large Superconductors", JAERI-M 8134 (March 1979).

38) Fusion Reactor System Laboratory : "Safety Analysis of Superconducting Poloidal Magnets for a JAERI Experimental Fusion Reactor", JAERI-M 8140 (march 1979) (in Japanese).

A1.2 List of Paper Published in Journals

1) Ohkubo, M., Kawasaki, K., Nishio, S., Ando, T., Ohta, M., Yoshikawa, M., Kazawa, Y.[*2], Saito, R.[*2], Matsui, A.[*2] : "Research and development of the JAERI large tokamak (JT-60), (1) Toroidal field coils", J. At. Energy Soc. Japan 20 (1978) 195 (in Japanese).

2) Ando, T., Miki, N.[*9], Ohkubo, M., Nishio, S., Kawasaki, K., Ohta, M., Yoshikawa, M., Ito, S.[*9], Sawada, Y.[*9], Takano, H.[*9]: "Research and development of the JAERI large tokamak (JT-60), (II) Poloidal field coils", ibid. 207 (in Japanese).

3) Yamamoto, M., Shimisu, M., Nakamura, H., Takatsu, H., Saigo, T.[*2], Ohta, M., Yoshikawa, M., Itoh, Y.[*2], Sato, H.[*2], Karatsu, Y.[*2], Aizawa, T.[*4]: "Research and development of the HAERI large tokamak (JT-60), (III) Vacuum vessel", ibid. 258 (inJapanese).

4) Takashima, T., Shimizu, M., Ohta, M., Minaguchi, T.[*8], Maeda, H.[*8]: "Research and development of the JAERI large tokamak (JT-60), (IV) Fast-acting movable limiter", ibid. 273 (in Japanese).

5) Takeda, T., Tsunematsu, T. and kurita, G.: "Fluid model simulations of Fusion plasmas", J. At. Energy Soc. Japan 20 (1978) 606 (in Japanese).

6) Okamoto, M. and Amano, T.[**5] : "A method to solve the impurity diffusion equation with ionization and recombination source terms", J. Comp. Phys. 26 (1978) 80.

7) Tsunematsu, T. and Takeda, T.: "A new iterative method for solution of a large-scale general eigenvalue problem", J. Comp. Phys. 28 (1978) 287.

8) Ogata, A. and Tazima, T.: "Plasma Density Control on a Tokamak", Jpn. J. Appl. Phys. 17 (1978) 753.

9) Nagashima, A.[**7], Funahashi, A., Kumagai, T., Shoji, T. and Takahashi, K.: "A 2-mm Wave Digital interferometer for Tokamak Discharges in the Upgraded DIVA", Jpn. J. Appl. Phys. 17 (1978) 1263.

10) Odajima, K., Kimura, H., Maeda, H., Ohasa, K.: "Measurement of Ion Temperature in Scrape-off Layer with Katsumata Probe", Jpn. J. Appl. Phys. 17 (1978) 1281.

11) Kasai, S., Funahashi, A., Konoshima, S., Nagami, M., Sugie, T. et al.: "Absolute Calibration of a Graging-Incidence Vacuum Monochromator by Means of Tokamak Discharges", Jpn. J. Appl. Phys. 17 (1978) 1625.

12) Kobayashi, T.*2, Tani, K., Tamura, S.: "Determination of optimum positions of the poroidal field coils of a large tokamak", Jpn, J. App. Phys. 17 (1978) 2139.

13) Ohara, Y.: "Numerical Simulation for Design of a Two-stage Acceleration System in a Megawatt Power Ion Source", J. Appl. Phys. 49 (1978) 4711.

14) Ohara, Y.: "Beam Focusing by Aperture Displacement in Two-Stage Acceleration System", Jap. Appl. Phys. 18 (1978) 351.

15) Matoba, T., Funahashi, A., Itagaki, T., Kumagai, K., Shoji, T. and Suzuki, N.: "Thomson Scattering Measurements on Ohmically Heated Plasmas in JFT-2 Tokamak", Jpn. Appl. Phys. 18 (1979) 611.

16) Matoba, T., Itagaki, T., Yamauchi, T. and Funahashi, A.: "Analytical Approximations in the Theory of Relativistic Thomson Scattering of High Temperature Fusion Plasma", Jpn. J. Appl. Phys. 18 (1979) 1127.

17) Shimomura, Y., Maeda, H.: "Divertor Experiment for Controlling Plasma-Wall Interactions", J. Nucl. Mater. 76 and 77 (1978) 45.

18) Ohtsuka, H., Yamada, R., Sone. K., Saidoh, M. and Abe, T.: "Measurement of the Sputtering Yield by Auger Electron Spectroscopy", J. Nucl. Mater. 76 and 77 (1978) 188.

19) Sone, K., Saidoh, M., Yamada, R. and Ohtsuka, H.: "Reduction of Erosion by Blistering in Molybdenum Surfaces with a Multi-Groove Microstructure", J. Nucl. Mate. 76 and 77 (1978) 240.

20) Hirayama, T., Fujisawa, N., Gomay, Y.*9, Maeno, M., Uehara, K., Shimada, M., Suzuki, N., Yamamoto, T. and Konoshima, S.: "On the origin of gaseous impurities measured by mass spectroscopy in the JFT-2 tokamak", J. Nucl. Mater. 76 and 77 (1978) 452-458.

21) Nagami, M., Maeda, H., Kasai, S., Sengoku, S., Sugie, T. et al. : "Devertor Experiment for Impurity Control in DIVA", J. Nucl. Mater. 76 and 77 (1978) 521.

22) Konoshima, S., Fujisawa, N., Maeno, M., Suzuki, N., Yamamoto, T. et al.: "Improvement of Plasma Parameters by Titanium Coating in the JFT-2 Tokamak", J. Nucl. Mater. 76 and 77 (1978) 581.

23) Tazima, T.; "First wall design consideration of JT-60", J. Nucl. Mater. 76 (1978) 594-599.

24) Matsuda, T., Kitsunezaki, A., Yokomizo, H., Saito, R.[*5] and Siki, S.: "Experimental Study on In-Situ Coating of Molybdenum", J. Nucl. Mater. 76 (1978).

25) Abe, T., Obara, K., Nakamura, H., Sone, K., Ohtsuka, H., Yamada, R., Saidoh, M. and Shimizu, M.: "Reduction of Effective Sputtering Yield by Honeycomb Structures", J. Nucl. Sci. Technol. 15 (1978) 471.

26) Shimada, R., Yanabu, S.[*9] : "DC circuit breaker for JAERI Large tokamak JT-60", J. Ins. Electrical Engineers Japan 98 (1978) 545 (in Japanese).

27) Shimada, R., Tani, K., Tamura, S.: "Excitation of plasma current in tokamak devices by inductive energy storges", J. Ins. Electrical Engineers Japan 99 (1979) 49 (in Japanese).

28) Ohkubo, K.,[**3] Ohasa, K., Matsuura, K.[**3] : "Wave Propagation to Lower Hibrid Resonance in a Magnetic Field with Shear", J. Phys. Soc. Japan 43 (1977) 642.

29) Odajima, K.: "Effects of Radial Electric Field on Drift Wave in a Weakly Ionized Plasma", J. Phys. Soc. Japan 44 (1978) 1685.

30) Sugie, T., Takeuchi, H., Kasai, S., Funahashi, A., Takahashi, K. et al.: "Ion Temperature Characteristics of Upgraded DIVA", J. Phys. Soc. Japan 44 (1978) 1960.

31) Sengoku, S., Nagami, M., Maeda, H., Kasai, S., Yamauchi, T. et al.: "Divertor Experiment for Impurity Control in DIVA", J. Phys. Soc. Japan 45 (1978) 1385.

32) Kasai, S., Funahashi, A., Nagami, M., Sugie, T. and Yamauchi, T.: "Spectroscopic Measurements of Impurities on the Upgraded DIVA Tokamak Plasma", J. Phys. Soc. Japan 46 (1979) 241.

33) Sugie, T.: "Determination of Ion Temperature Distributions from Doppler Broadenings of Impurity Lines in the Vacuum UV Region for Tokamak Discharge", J. Phys. Soc. Japan 46 (1979) 250

34) Okamoto, M., Azumi, M and Takizuka, T.: "Numerical simulation of lower hybrid wave propagation in a plasma", J. Phys. Soc. Japan 46 (1979) 1333.

35) Saidoh, M., Sone, K., Ohtsuka, H., Abe, T., Yamada, R., Obara, K. and Murakami, Y.: "Surface Erosion of the First Wall Materials Caused by Hydrogen- and Helium-Ion Bombardment", Kakuyugo-Kenkyu 39, Suppl. 2 (1978) 37 (in Japanese).

36) Ohtsuka, H.: "Some Considerations on Sputtering Yield Measurement by Auger Electron Spectroscopy", Kakuyugo-kenkyu 39 (1978) 352.

37) Tusa, T.: "On mhd characteristics of tokamak plasma", Kakuyugo-Kenkyu 39, Suppl. 1 (1978) 39 (in Japanese).

38) Tanaka, M.: "Beta limit in tokamaks", ibid. 195 (in Japanese).

39) Tuda, T.: "Drift wave instabilities", ibid. 205 (in Japanese).

40) Takizuka, T.: "Numerical study on the initial phase of a tokamak discharge", ibid. 1 (in Japanese).

41) Ohasa, K., Ikuta, K.[**3] : "Linked Min-B Configuration inside High-Shear Magnetic Surface", Nuclear Fusion 17 (1977) 473.

42) Gomay Y.[*9], Fujisawa, N., Maeno, M., Suzuki, N., Uehara, K., et al.: "Particle and Energy Fluxes Observed in the Scrape-off Layer of JFT-2 Tokamak", Nuclear Fusion 18 (1978) 849.

43) Ohasa, K., Maeda, H., Yamamoto, S., Nagami, M., Ohtsuka, H., et al.: "Ion Sputtering, Evaporation and Arcing in DIVA", Nuclear Fusion 18 (1978) 872.

44) Kimura, H., Maeda, H., Ueda, N.[*4], Seki, M., Kawamura, H. et al. : "Heat Flux to the Material Surfaces in a Tokamak", Nuclear Fusion 18 (1978) 1195.

45) Nagami, M., Maeda, H., Shiho, M., Sugie, T., Shimomura, Y., et al. : "Pulsed Methane Injection Experiment in DIVA", Nuclear Fusion 18 (1978) 1217.

46) Odajima, K., Maeda, H., Shiho, M., Kimura, H., Yamamoto, S. et al. : "Radiation Loss and Power Balance in DIVA", Nuclear Fusion 18 (1978) 1337.

47) Nagami, M., Shimomura, Y., Maeda, H., Kasai, S., Yamauchi, T. et al. : "Impurity Shielding and Sweeping-out by an Axisymmetric Divertor in DIVA", Nuclear Fusion 18 (1978) 1347.

48) DIVA Group: "Divertor Experiment in DIVA", Nuclear Fusion 18 (1978) 1619.

49) Shiho, M., Konoshima, S., Funahashi, A., Kasai, S., Sugie, T. et al. : "Spectroscopic Study of Impurities in the JFT-2 Tokamak", Nuclear Fusion 18 (1978) 1705.

50) Kasai, S., Funahashi, A., Nagami, M. and Sugie, T.: "Radiation due to Pseudo-Continuum from High-Z Impurities in Upgraded DIVA Tokamak Plasma", Nuclear Fusion 19 (1979) 195.

51) Odajima, K., Wakatani, M., Maeno, M., Fujisawa, N. : "Mode Mixing of Large Scale Fluctuations in JFT-2 Tokamak", Phys. Fluids 21 (1978) 846.

52) Uehara, K.[**8], Hagiwara, S.[**8] : "Radio-frequency plugging and heating of a magnetized sheet plasma", Phys. Fluid 21 (1978) 2316.

53) Ohtsuka, H., Kimura, H., Shimomura, Y., Maeda, H., Yamamoto. S. et al. : "Probe Measurements in the Scrape-off Layer of a Tokamak", Plasma Phys. 20 (1978) 749.

54) Someya, T.[**6], Fujisawa, N. : "Breakdown Experiment on a Tokamak", Plasma Physics 20 (1978) 1101.

55) Uehara, k.[**8], Gomay, Y.[*9], Yamamoto, T., Suauki, N., Maeno, M. et al. : "Gross Particle Confinement Characteristics by the Boundary Plasma in the JFT-2 Tokamak", Plasma Physics 21 (1979) 89.

56) Ohga, T. and Arai, T.: "Exhaust System with Turbo-Molecular Pump for Thermonuclear Fusion Experiments in JAERI", Shinkuu 21 (1978) 255 (in Japanese).

57) Murakami, Y. and Ohtsuka, H.: "Possibility of Palladium Alloy Membrane Pumps for Thermonuclear Fusion Devices", Vacuum 28 (1978) 235.

A1.3 List of Papers Published in Conference Proceedings

1) Ando, T., Yoshida, K., Shimamoto, S., Yasukouchi, K.:"Cluster Test Facility for Superconducting Tokamak Toroidal Magnet System Development", Proc. of 1978 Applied Superconductivity Conference, IEEE Trans. MAG-15, Number 1, p 63.

2) Shimamoto, S., Yasukouchi, K., Ando, T.:"Development of Multifilamentary Nb_3Sn Conductor for Fusion Research", ibid., p 406.

3) Maeno, M., Suzuki, N., Konoshima, S., Yamamoto, T., Shimada, M., et al.: "Experimental Study on Limit of the Safety Factor in JFT-2 Tokamak", Proc. of Symposium on Current Disruption in Toroidal Devices, Garching (1979).

4) Odajima, K., Nagami, M., Yamamoto, S., Ohasa, H., Sengoku, et al.: "Very Low-q Discharges Free from Major Disruptions in DIVA", ibid.

5) Takatsu, H., Yamamoto, M., Shimizu, M., Ohta, M., Saigo, T.*2, Miyama, H.*2, Sato, H.*2, Itoh, Y.*2 : "Stress analysis of vacuum vessel in JT-60", Proc. of 7th Symp. on Eng. Problems of Fusion Research, Knoxville, (1978), Vol. II, 1376.

6) Nakamura, H., Shimizu, M., Ohta, M., Aizawa, T.*4, Naitoh, T.*4., Kasai, M.*4 : "Electron beam bombardment test of JT-60 magnetic limiter plate', ibid., 1669.

7) Shimizu, M., Yamamoto, M., Takatsu, H., Saigo, T.*2, Itoh, Y.*2, Miyata, H.*2, Saito, R.*2, Takizawa, T.*2 : "Performance test of JT-60 vacuum vessel", Proc. of 10th Symp. on Fusion Technol,, Padova, (1978).

8) Ohkubo, M., Kawasaki, K., Nishi, S., Ando, T., Mitsui, M.*2, Nakai, N.*2, Kitazawa, H.*2 : "Non-destructive inspection method of brazed connection of JT-60 toroidal field coil", ibid.

9) Ninomiya, H., Ogata, A., Tanabe, Y.*9, Yamamoto, K.*9, Sawada, Y.*9 and Yamaguchi, M.*9 : "Three Dimensional Analysis of Alternating Magnetic Field in an Experimental Tokamak Machine Based on Finite Element Method",

ibid.

10) Shimada, R., Tani, K., Tamura, S., Yanabu, S.*9, Matsushita, T.*9, Murano, M.*9 : "Development of high current DC circuit breaker for large tokamak fusion device", ibid.

11) Suzuki, Y., Ogata, A., Aikawa, H., Ninomiya, H., Kimura, T., Hatakeyama, T., Iba, D., Murai, K., Takemaru, K., Kaji, A., and Iniue, K. : "Control System for JT-60", ibid.

12) Gomei, Y.*9, Fujisawa, N., Maeno, M., : "Limiter Surface Observation by AES , SEM and Infrared Techniques in the JFT-2 Tokamak", Proc. of 1st Topical Meeting on Fusion Reactor Matrials, Florida (January 1979), Paper O-2.

13) Hiraoka, T., Sugihara, M., Kasai, M.*4, and Mori, S. : "A Concept of JAERI's D-T burning test facility", Proc. of 2nd IAEA conference and workshop on fusion reactor design, Madison (1977), p 77.

14) Nagashima, T., Fujisawa, N. : "Lower Hybrid Heating Experiments in JFT-2 Tokamak", Proc. of Joint Varenna-Grenoble Int. Symp. on Heating in Toroidal Plasma, Vol. II (1978) 281.

15) DIVA Group : "Preliminary Results of ICRF Heating in DIVA", ibid.

16) Tani, K., Azumi, M., Ohtsuka, M., Kishimoto, H., Tamura, S. : "Behavior of fast ions in a large tokamak plasma during NBI heating", ibid.

17) Kishimoto, H., Shimada, R., Tamura, S., Itoh, .*9, Sawada, Y.*9, Takano, H.*9, Furusawa, T.*9, Kimura, K.*9 ;"Flywheel energy storage system for JT-60 toroidal field coil", IEEE Region Five Annual Conf. Okulahoma USA (1978).

18) Shimada, R., Tani, K., Kishimoto, H., Tamura, S., Yanabu, S.*9, Yamashita, S.*9, Ikeda, H., Sasaki, T. : "Development of high current DC circuit breaker for large tokamak fusion device", IEEE PES Summer Meeting, Los Angeles, paper A 78594-4.

19) Ohara, Y., Ohga, T. and Okumura, Y. : "Two-stage Beam Optics and Grid Loading", IAEA Technical Committee Meeting and Workshop on Injectors for Fusion Reactors, (Culham, U. K., June 1978).

20) Arakawa, Y., Kondoh, U.*7, Ohga, T., and matsuda, S. : "Source Plasma Development of the JAERI DÜoPIGatron", ibid.

21) Matsuda, S., Ohga, T., and Nishidai, J.*7 : "Cascade Mounted Power Supply System of the JAERI Injector Test Stand", ibid.

22) Matsuda, S., and Shirakata, H., : "Desigh of the JT-60 Neutral Beam Injection System and Related Current Research and Development", ibid。

23) JT-60 power supplies group : "Status of JT-60 program", 3rd IAEA Technical Committee Meeting on Engineering of Large Tokamak Experiment, Paris (1978).

24) Division of Large Tokamak Development, Division of Thermonuclear Fusion Research : "Status of JT-60", ibid.

25) Kitsunezaki, A., Seki, S., Yokomizo, H., Matsuda, T. and Yoshikawa, M. : "On the design of JT-4", ibid.

26) Kawasaki, K., Nishio, S., Ohkubo, M., Ando, T., Ohta, M., Matsui, M.*2, Kitazawa, H.*2, Saito, R.*2 : "The toroidal field coil for JT-60", Proc. of 6th Int. Conf. on Magnet Technol., Bratislava (1977) Vol. I, 81.

27) Ohkubo, M., Ando, T., Kawasaki, K., Nishio, S., Ohta, M., Ishimura, M.*9, Takano, H.*9 : "The poloidal field coils for JT-60", ibid., 86.

28) Fujii, T., Fujisawa, N., Funahashi, A., Hirayama, T., Imai, T. et al. : "Plasma Heating near the Lower Hybrid Frequency in the JFT-2 Tokamak", Proc. of 7th Int. Conf. on Plasma Physics and Controlled Nuclear Fusion Research, Insbruck, Austria 23-30, August (1978), Paper CN-A-4-2.

29) Callen, J. D.**4, Azumi, M. et al. : "Magnetic islandography in tokamaks", ibid., Paper CN-F-1-1.

30) Maeda, H., Sengoku, S., Kimura, K., Ohtsuka, H., Ohasa, K., et al. : "Experimental Study of Magnetic Divertor in DIVA", ibid., Paper CN-T-3-1.

31) Ohasa, H., Maeda, H., Yamamoto, S., Nagami, M., Ohtsuka, H. et al. : Proc. of 3rd Int. Conf. on Plasma Surface Interactions in Controlled Fusion, Culham (1978).

32) Nagami, M., Maeda, H., Kasai, S., Yamauchi, T., Sengoku, S. et al. : "Divertor Experiment for Impurity Control in DIVA", ibid.

33) Shimomura, Y., Maeda, H. : "Divertor Experiment for Controlling Plasma Wall Interactions", ibid.

34) Itoh, S.**4, Seki, Y. and Maekawa, M. : "Measurements and Calculations of Fast Neutron Spectra in a Graphite-Reflected Lithium Assembly", Proc. of 3rd Topical Meeting on the Technology of Controlled Nuclear Fusion, Santa Fe, (1978), Vol. I, 385.

35) Kasai, S. and Funahashi, A. : "Behavior of Pseudo-Continuum Emission from High-Z Impurities in DIVA and JFT-2 Tokamaks", Proc. of Joint U.S.-Japan Joint Seminar on Plasma Spectroscopy, Kyoto, (1979), Page 4.

A2. Personnel of the Center

A2.1 Number of the staff of the Divisions

	FY 1977	FY 1978	FY 1979
Regular staff*1	121	140	162
Staff on loan	22	27	20*2
Guest scientist	6	7	3*3
Scholarship fellow	30	30	5

*1 Including scientists, technicians, and secretaries.

*2 Five from Hitachi Ltd.
One from Kozo Keikaku Engineering Inc.
Two from Mitsubishi Atomic Power Ind. Inc.
Two from Mitsubishi Electric Co., Ltd.
One from Mitsubishi Heavy Ind. Ltd.
One from Nissin Electric CO., Ltd.
One from Sumitomo Heavy Ind. Ltd.
Four from Tokyo Shibaura Electric Co. Ltd.
One from ULVAC Co.
One from Hitachi Cable Co.
One from Kawasaki Heavy Ind. Ltd.

*3 One from the University of Tokyo
One from Nihon University
One from Ochanomizu University

A2.2 List of Scientific Staffs and Officers during FY 1978

Fusion Research and Development Center

MORI, Sigeru (Center Director)

(A) Division of Thermonuclear Fusion Research

OBATA, Yukio (Head)
AKAMA, Kouzou (Administrative Manager)

Plasma Theory Laboratory

AZUMI, Masafumi
KURITA, Gen-ichi
TAKEDA, Tatsuoki
TAKIZUKA, Tomonori
TANAKA, Masatoshi (Chief)
TOKUDA, Shinji
TSUNEMATSU, Toshihide
TUDA, Takashi
MINO, Kaoru **7(Scholarship fellow)

Experimental Plasma Physics Laboratory

TANAKA, Yuji (Chief)

* JFT-2

FUJISAWA, Noboru
HIRAYAMA, Toshio
KONOSHIMA, Shigeru
MAENO, Masaki
SHIMADA, Michiya
SUZUKI, Norio
YAMAMOTO, Takumi

* JFT-2a/DIVA

KIMURA, Haruyuki
MAEDA, Hikosuke
NAGAMI, Masayuki

ODAJIMA, Kazuo
OHASA, Kazumi
SENGOKU, Seio
SHIMOMURA, Yasuo
YAMAMOTO, Shin

* Diagnostics

FUNAHASHI, Akimasa
KASAI, Satoshi
KAWAKAMI, Tomohide
KUMAGAI, Katsuaki
NAGASHIMA, Akira**7(Scholarship fellow)
SHOJI, Teruaki
SUGIE, Tatsuo
TAKAHASHI, Koki
TAKEUCHI, Hiroshi
YAMAUCHI, Toshihiko

Facility Operation and Engineering Section

ANNO, Katsuto
HASEGAWA, Kouichi
HIRATSUKA, Hajime
ISAKA, Masayoshi
KAZAWA, Minoru
KIKUCHI, Kazuo
KUNIEDA, Shunsuke (Deputy Chief)
MATSUZAKI, Yoshimi
SHIBATA, Takatoshi
SHIINA, Tomio
SUNAOSHI, Hidenori
SUZUKI, Kihachiro
TANI, Takashi
TOYOSHIMA, Noboru
YOKOKURA, Kenji
YOKOUAMA, Kenji

Plasma Heating Laboratory

SHIRAKATA, Hirofumi (Chief)

* Neutral Beam Injection Heating

AKIBA, Masato**2 (Scholarship fellow)
ARAKAWA, Yoshihiro
HORIIKE, Hiroshi
ITOH, Takao
KAWAI, Mikito
KURIYAMA, Masaaki
MATSUDA, Shinzaburo
MIZUTANI, Yasuhiko*7
MORITA, Hiroaki*2
OHARA, Yoshihiro
OHGA, Tokumichi
OKUMURA, Yoshikazu
SAKURABA, Junji*8
SHIBATA, Takemasa
TANAKA, Shigeru

* Radiofrequency Heating

FUJII, Tuneyuki
IMAI, Tsuyoshi
NAGASHIMA, Takashi
UEHARA, Kazuya**8(Scholarship fellow)

Plasma Engineering Laboratory

ABE, Tetsuya
MURAKAMI, Yoshio (Chief)
OBARA, Kenziro
OHTSUKA, Hidewo
SAIDOH, Masahiro
SONE, Kazuho
YAMADA, Rayji

Superconducting Magnet Laboratory

ANDO, Toshinari
OKA, Kouichi *11
SHIMAMOTO, Susumu (Chief)
TADA, Eisuke
TSUJI, Hiroshi
NISHI, Masataka
HIYAMA, Tadao
YOSHIDA, Kiyoshi

Tritium Engineering Laboratory

MATSUDA, Yuji
NARUSE, Yuji
NUMATA, Kazuyoshi
OBATA, Yukio (Chief)
SHIMIZU, Toku
TACHIKAWA, Katsuhiro
TANAKA, Kichizo
YOSHIDE, Hiroshi

Fusion Reactor System Laboratory

IIDA, Hiromasa
IOKI, Kimihiro *4
MAKI, Koichi *2
MINATO, Akio *12
SAKO, Kiyoshi (Chief)
SEKI, Yasushi
TONE, Tatsuzo
YAMAMOTO, Takashi *3
YAMATO, Harumi *9
YANAUCHI, Michinori *9

(B) Division of Large Tokamak Development

ISO, Yasuhiko (Head)
SAITO, Jo (Administrative Manager)
SHIRAISHI, Kensuke (Principal Engineer)

JT-60 Project Office I

YOSHIKAWA, Masaji (Chief)

* Planning and Coordination Group

HIRAOKA, Toru
HIRAYAMA, Toshio
KASAI,Masao *4
SAKAMOTO, Hiroki *6
SHINYA, Kichiro *9
TAZIMA, Teruhiko
TOKUTAKE, Toshikuni

* Power Supplies Group

ARAKAWA, Kiyotsugu
HOSHINO, Katsumichi
ITOH, Sin-ichi *2
KISHIMOTO, Hiroshi
KITAHARA, Tadayuki *9
MIYA, Naoyuki**10(Scholarship fellow)
SHIMADA, Ryuichi
TAMURA, Sanae
TANI, Keiji
YOSHIDA, Hidetoshi

* Control Group

AIKAWA, Hiroshi
KANAMORI, Takahiro *2
KIMURA, Toyoaki
KONDO, Ikuo
MATOBA, Tohru
NAGASHIMA, Akira **7(Scholarship fellow)

NINOMIYA, Hiromasa
OGATA, Atsushi
SHIHO, Makoto
SUZUKI, Yasuo

* JT-4 Group
KAMOTO, Satoru *5
KITSUNEZAKI, Akio
SAITO, Ryuta *5
MATSUDA, Toshiaki
SEKI, Shogo
YOKOMIZO, Hideaki

JT-60 Project Office II

IIJIMA, Tsutomu (Chief)

* Machine Group
ANDO, Toshiro
KAWASAKI, Kozou
MIKI, Nobuharu
NAKAMURA, Hiroo
NAKAMURA, Yukiharu
NISHIO, Satoshi
OHKUBO, Minoru
OHTA, Mitsuru
SAIGO, Tsugumoto *2
SEIMIYA, Munetake
SHIMIZU, Masatsugu
TAKASHIMA, Tetsuo
TAKATSU, Hideyuki
TOYOSHIMA, Noboru
TSURUMI, Satoshi *2
YAMAMOTO, Masahiro

* Auxiliary Facilities Group
ARAI, Takashi
HIRUTA, Kazuharu
KODAMA, Kozou
KUNIEDA, Shunsuke
OGIWARA, Norio

(C) Office of Fusion Program

OHKUBO, Yoshiharu/ MATSUI, Takashi (Administrative Manager)

INOUE, Kenji

TAKEDA, Takashi

KUROSAWA, Katsuhiko

Guest Scientists

IWATA, Giichi (Ochanomizu University)

KAWAKAMI, Ichiro (Nihon University)

TUZI, Yutaka (The University of Tokyo)

On leave from

* 1 Century Research Center Co.

* 2 Hitachi Ltd.

* 3 Kozo Keikaku Engineering Inc.

* 4 Mitubishi Atomic Power Ind. Inc.

* 5 Mitsubishi Electric Co., Ltd.

* 6 Mitsubishi Heavy Ind. Ltd.

* 7 Nissin Electric Co., Ltd.

* 8 Sumitomo Heavy Ind. Ltd.

* 9 Tokyo Shibaura Electric Co., Ltd.

*10 ULVAC Co.

*11 Hitachi Cable Co.

*12 Kawasaki Heavy Ind. Ltd.

*13 Fuji Electric Co., Ltd

** 1 Kyoto Univ.

** 2 Kyushu Univ.

** 3 Nagoya Univ.

** 4 ORMAK

** 5 Osaka Univ.

** 6 Shizuoka Univ.

** 7 Tokyo Institute of Technology

** 8 Tsukuba Univ.

** 9 The University of Tokyo

**10 Nihon Univ.

A3. Budget of the Center

(unit: Million ¥)

	FY*1 1977	FY*1 1978	FY*1 1979
Scientific program	6,925.0*2	9,391.8*2	22,751.2*2
(excluding Staff & administrative cost)	16,516.2	14,335.7	25,558.7*3
Builing	410.8	1,155.5	16,900.1
Site			1,723.0

*1 From April to March.

*2 Including cashing of the financial obligation in each FY.

*3 The total financial obligation from FY 1979 to FY 1981 for the construction of part of the components of JT-60 and for the development of plasma heating systems and super conducting magnet.